ÉCOLE DE TECHNOLOGIE SUPÉRIEURE
UNIVERSITÉ DU QUÉBEC

THESIS PRESENTED TO
ÉCOLE DE TECHNOLOGIE SUPÉRIEURE

IN PARTIAL FULFILLEMENT OF THE REQUIREMENTS FOR
THE DEGREE OF DOCTOR OF PHILOSOPHY
PH. D.

BY
Farzad RAFIEIAN SICHANI

STUDY OF VIBRATIONS AND INSTABILITY IN A ROBOTIC GRINDING PROCESS

MONTRÉAL, 29 JANUARY 2014

BOARD OF EXAMINERS

THIS THESIS HAS BEEN EVALUATED

BY THE FOLLOWING BOARD OF EXAMINERS

Prof. Zhaoheng Liu, Thesis Supervisor
Department of Mechanical Engineering at École de technologie supérieure

Prof. Ilian Bonev, President of the Board of Examiners
Department of Automated Manufacturing Engineering at École de technologie supérieure

Prof. Marc Thomas, Member of the Jury
Department of Mechanical Engineering at École de technologie supérieure

Prof. Jérôme Antoni, Independent External Evaluator
Laboratoire Vibrations Acoustique at Institut national des sciences appliquées de Lyon

Dr. Serafettin Engin, External Evaluator
Pratt & Whitney Canada

THIS THESIS WAS PRENSENTED AND DEFENDED

IN THE PRESENCE OF A BOARD OF EXAMINERS AND PUBLIC

10 JANUARY 2014

AT ÉCOLE DE TECHNOLOGIE SUPÉRIEURE

ACKNOWLEDGMENT

I would like to express my sincere thanks to my supervisor, Professor Zhaoheng Liu, whose invaluable advice, directions and inspiring ideas made the successful completion of this thesis possible. The lessons I learned from his forbearance throughout my study are priceless.

My special thanks are extended to Mr. Bruce Hazel whose directions in this thesis, toward industrial needs, taught me critical thinking to conduct practical research. I am also grateful to him for having contributed the result from his years of experience into this research work.

Throughout this thesis, I have been privileged to collaborate with Professor Marc Thomas whose advices on experimental vibration analysis have significantly improved my work. Thanks for the support from the staff at DYNAMO and SCOMPI laboratories in ÉTS as well.

Various experimental contents of this thesis were conducted with the aid of the technical, engineering and brainstorming research support from the SCOMPI team at Hydro-Québec's research institute (IREQ) with whom I earned a unique team work experience. The collaborations from the Robotics and Civil Department of IREQ is appreciated in this regard. I am thankful to Jacques Michaud for his wonderful help in gearing up my experimental test rig. I built up working proficiency in French language communication through the patient friendly atmosphere of working with him.

Thanks to the Natural Sciences and Engineering Research Council of Canada (NSERC) and École de technologie supérieure (ÉTS) for the financial support of this research.

I'm indebted to my beloved family for completion of this stage in my life. I extend my warmest wishes to my sisters, Shahrzad and Shirin in their lives. Without the peace of mind provided through their warmest support, from overseas, this work could not be accomplished.

And my dearest love to friends with whom the moments of getting together had great influence during my stay in Montréal throughout the past years.

Thank you all, Farzad, October-2013.

DEDICATION

To my parents, Shahnaz Navaei and Ali Rafieian, whose unconditional love was the fuel to my drive toward this end.

STUDY OF VIBRATIONS AND INSTABILITY IN A ROBOTIC GRINDING PROCESS

Farzad RAFIEIAN SICHANI

RÉSUMÉ

La dynamique vibratoire d'un procédé de meulage robotisé est étudiée dans cette thèse. Le procédé de meulage robotisé étudié est en cours de développement à l'Institut de recherche d'Hydro-Québec (IREQ) pour des opérations de maintenance sur les équipements hydroélectriques. L'application consiste à profiler des grandes pièces à géométrie complexe avec un taux d'enlèvement de matière élevé. Cette application est différente du meulage conventionnel dans lequel une couche mince est enlevée en tant que procédure de finition. Les vibrations importantes inhérentes au procédé constituent un défi majeur pour cette technologie. Cependant, la manœuvrabilité que le robot apporte dans les opérations est parfois la seule solution réalisable pour l'usinage dans les endroits difficiles à atteindre. Les caractéristiques principales du porte-outil robotisé qui affectent sa dynamique vibratoire, telles que sa flexibilité importante et sa dynamique variant selon sa configuration sont étudiées. L'objectif est d'étudier les vibrations et l'instabilité basé sur une compréhension appropriée de la dynamique instantanée du processus d'enlèvement de matière effectué par le robot multi-corps articulé. Considérant que l'instabilité vibratoire dans l'usinage est due aux interactions entre la dynamique du processus de coupe et la dynamique de la structure du porte-outil, deux axes de recherche sont menés.

Une étude expérimentale, confirmée par des simulations numériques, est réalisée sur la dynamique vibratoire stationnaire du processus. On a observé qu'en raison de la flexibilité du robot, l'enlèvement de matière est régi par des vibro-impacts, survenant principalement à la fréquence de rotation de l'outil, entre la meule et la pièce. Une analyse angulaire des impacts cycliques dans les oscillations du procédé est utilisée pour caractériser le comportement de «coupe par impact». La fréquence de rotation instantanée mesurée de la meule est exprimée selon la position angulaire et le nombre de rotation pour suivre l'évolution dynamique du régime d'impact. Cette «carte de coupe par impact» est également utilisée pour valider une hypothèse plausible du déplacement du point de contact pour l'usure uniforme des meules. On observe que la décélération mesurée de la vitesse angulaire instantanée, comme une transitoire qui est excitée de façon impulsive par des impacts de coupe, est très bien corrélée à la puissance de meulage. L'utilisation de la mesure en temps réel de la décélération et du nombre d'impacts par tours dans la stratégie de contrôle permettra d'améliorer l'estimation du taux d'enlèvement de métal.

Un modèle de coupe par impact pour enlèvement de métal a été utilisé pour estimer la puissance de meulage nécessaire dans une tâche de meulage robotisé. D'abord, les coefficients du modèle ont été identifiés expérimentalement. Des essais de meulage robotisé ont été effectués à puissance constante. Il a été démontré qu'une entaille uniforme avec une

profondeur de coupe cible peut être réalisée en présence des oscillations d'impacts stabilisées. L'amplitude des ondulations sur la surface finie se trouve être beaucoup plus petite que l'amplitude des oscillations de la meule. Le modèle dynamique à vibro-impact contribue à l'amélioration de la productivité de la stratégie d'enlèvement de matière à taux contrôlé utilisée pour le profilage. En effet, le nombre d'itération de meulage/mesure requis pour atteindre un niveau de tolérance donné sur la surface est fonction de l'incertitude du modèle d'enlèvement de matière.

Par la suite, l'effet du phénomène de broutage régénératif sur la limite de stabilité du procédé a été étudié. L'étude a montré que la flexibilité du robot localise le problème de broutage régénératif pour meulage robotisé à l'extrême supérieur droit du premier lobe sur la charte de la stabilité. Dans cette région, la limite de fonctionnement stable est définie par de très grandes valeurs de gain. Ceci est différent de l'usinage traditionnel qui se trouve à l'intérieur de la «zone des lobes» sur le diagramme des lobes de stabilité. La dynamique d'impact cyclique de l'enlèvement de matière est utilisée pour identifier l'instabilité dans cette région. La limite de fonctionnement stable est identifiée à partir de simulations numériques des coupes par impacts. La frontière se trouve à être très proche de la limite prévue en utilisant la méthode traditionnelle d'analyse du broutage régénératif. On peut conclure que le grand gain est intrinsèque à l'usinage robotisé. La dynamique des impacts de l'enlèvement de matière due à la flexibilité du robot doit être considérée pour comprendre ces grandes valeurs de gain, ne se produisant pas dans l'usinage conventionnel. Des expériences sont effectuées pour confirmer la nouvelle formulation du problème de broutage régénératif dans le meulage robotisé.

Un deuxième axe de recherche a été mené pour mettre l'accent sur la dynamique du porte-outil robotisé. L'objectif est de fournir un modèle pour étudier l'effet de la configuration du robot sur la dynamique des vibrations et l'instabilité dans le procédé. Un modèle dynamique multi-corps à 6-DDL est développé pour le robot. L'analyse modale expérimentale sur la structure du robot a été utilisée pour valider les formes des modes et les fréquences naturelles prédites par le modèle. Une discussion traite de la façon dont l'outil de modélisation développé peut servir à l'étude d'instabilité par le couplage des modes dans l'usinage robotisé.

L'étude des vibrations et de l'instabilité dans cette thèse contribuent à la compréhension des dynamiques vibratoires qui régissent le procédé de meulage robotisé. La poursuite du développement de l'approche robotisée de profilage de précision de pièces industrielles s'appuie sur de telles bases de compréhension.

Mots-clés: Broutage d'usinage robotisé; coupe par impact, fréquence de rotation instantanée; encodeur rotatif; analyse angulaire; modèle d'enlèvement de matière; identification des paramètres; profilage de surface robotisé.

STUDY OF VIBRATIONS AND INSTABILITY IN A ROBOTIC GRINDING PROCESS

Farzad RAFIEIAN SICHANI

ABSTRACT

The vibratory dynamics of the grinding process performed by a robot arm is studied in this thesis. The robotic grinding process under development at Hydro-Québec's research institute (IREQ) for maintenance operations on hydropower equipment is a high material removal rate task used for profiling large parts and complex geometries. The profiling application is unlike conventional grinding in which, a thin layer of material is removed as a finishing procedure. One major hurdle for this technology is the significant vibrations inherent to the process. However, the maneuverability that the robot brings into the operations makes it, sometimes, the only practical solution for machining in hard-to-reach areas. The main features of the robotic tool holder which affect its vibratory dynamics, i.e. the robot's high compliance and its configuration-dependent dynamics are studied. The objective is to investigate vibrations and instability based upon appropriate understandings of the instantaneous dynamics of the material removal process performed by the articulated multi-body robot arm. Since vibrational instability in material removal is caused by the interactions between the dynamics of the cutting process and the tool holder's structural dynamics, two lines of research are conducted accordingly.

An experimental investigation substantiated by numerical simulations is carried out on the steady vibratory dynamics of the process. Due to the compliance of the robot arm, material removal is found governed by vibro-impacts, occurring mainly at the spindle's rotational frequency, between the cutter and the workpiece. The "impact-cutting" behavior is characterized through angular analysis of the cyclic impacting oscillations. The measured instantaneous rotational frequency of the spindle during robotic grinding is mapped into a representation suited for monitoring the dynamic evolutions in the impacting regime. The "impact-cutting map" was also used to validate a plausible hypothesis for uniform disk wear when exhibiting an impact-cutting operation. The measured drop in the instantaneous angular speed, as a transient which is excited impulsively by the cutting impacts, was found well correlated to grinding power. The practical significance of this latter result is considered as to integrate the real-time measurement of the speed drop and the number of impacts per spindle revolutions into the robot control strategy in order to improve the metal removal estimation.

In a following step, an impact-cutting model for metal removal was used to estimate the grinding power required for a grinding task performed by the robot. Constant coefficients of the model were first identified experimentally. Robotic grinding tests were performed while setting the target grinding power in the control strategy based upon the impact-cutting model. It was demonstrated that a uniform cut with a target rate of metal removal and a target cutting depth can be achieved in presence of stabilized impacting oscillations. The waviness amplitude on the finished surface is found to be much smaller than the amplitude of vibro-

impact oscillations. The knowledge about vibro-impact oscillations present in the process helps improving the strategy of controlled material removal rate employed in the robot control strategy. The iterative procedure of grinding/profile scanning to reach the desired tolerance level on the surface can be improved based upon the estimation of the material removal rate by the impact-cutting model.

The limit of stable impact cutting due to regenerative chatter was investigated next. The investigation resulted into understanding that the high compliance of the robot arm locates the problem of robotic grinding regenerative chatter on the far upper right of the first lobe on the stability chart. In this region, the limit of stable operation is defined by very large gain values. This is different from traditional machining which is located inside the "lobes zone" on the stability lobes diagram. The cyclic impacting dynamics of material removal is invoked to investigate instability in this region. The limit of stable operation is identified from numerical simulations of impact-cutting. The boundary is found to be very close to the margin predicted using the traditional approach for regenerative chatter analysis. It is concluded that the large gain is typical for robotic grinding. The impacting dynamics of material removal due to robot compliance must be considered to understand such large gain values, never occurring in conventional grinding. Experiments are performed to substantiate the new understanding regarding the problem of regenerative chatter in robotic grinding.

A second line of research was focused on the robotic tool holder's structural dynamics. The goal was to provide a modeling tool for an investigation of the effect of robot's configuration-dependent dynamics on vibrations and instability in the process. A 6-DOF multi-body dynamic model was developed for the robot manipulator. Experimental modal analysis on the robot structure was used to validate the mode shapes and natural frequencies predicted by the model. A discussion is provided about how the developed modeling tool can serve an investigation of mode-coupling chatter in robotic machining.

The study of vibrations and instability in this thesis contribute into understanding the vibratory dynamics that govern the robotic grinding process. Further development of the robotized technology for precision profiling of industrial parts relies on such understanding bases.

Keywords: Robotic machining chatter; Impact cutting; Instantaneous rotational frequency; Rotary encoder; Angular analysis; Material removal model; Parameter identification; Robotized surface profiling.

TABLE OF CONTENTS

Page

LIST OF TABLES

LIST OF FIGURES

Page

NOMENCLATURE

a_i	DH parameter associated to link (*i*) of the robot (m)
A_0	cross-sectional area of the cut (m^2)
$\left[\boldsymbol{A}_i\right]$	transformation matrix from link (*i*) to (*i-1*)
b	dead zone (m)
c_t	damping coefficient of tool holder $(N \cdot s/m)$
C_{power}	cost of fitting the model on measured power $(\%)$
$[\boldsymbol{C}]$	joints' damping matrix for the robot $(N \cdot s/m)$ or $(N \cdot s/rad)$
d_i	DH parameter associated to link (*i*) of the robot (m)
dt	integration time step (s)
dx	width of a differential element (m)
dX	resolution of graphic delineation along X (μm)
dY	resolution of graphic delineation along Y (μm)
D	damping coefficient of the Impact-Pair $(N \cdot s/m)$
$[\boldsymbol{D}]$	robot's inertia matrix $(N \cdot s^2/m)$ or $(N \cdot s^2/rad)$
e	eccentricity (m)
E	grinding wheel (cutter) width (m)
E_c	energy per impact (J)
E_r	rotational kinetic energy (J)
f	instantaneous rotational frequency (Hz)
f_{cl}	counter clock's frequency (Hz)
f_d	feed direction of the grinding task
f_{ml}	mean line rotational frequency (Hz)
f_{mp}	mapped rotational frequency (Hz)
f_n	robot's first mode natural frequency (Hz)
f_{rst}	piecewise linear restoring force function (N)
f_{rstL}	linear restoring force function (N)
f_{rstN}	nonlinear restoring force function (N)
F	force (N)
F_a	alternating external force (N)
F_c	cutting force (N)
F_e	edge force (N)
F_{ex}	external force (N)
F_m	mean external normal force (N)
F_N	instantaneous normal grinding force (N)
$\overline{F}_N$	average normal grinding force (N)
$\overline{F}_{N,E}$	error in the average normal grinding force (N)
$\overline{F}_{N,m}$	measured average normal grinding force (N)
F_T	instantaneous tangential grinding force (N)
$\overline{F}_T$	average tangential grinding force (N)

$\bar{F}_{T,m}$	measured average tangential grinding force (N)
$\{\boldsymbol{g}\}$	vector of gravitational generalized force (N)
G	real part of the receptance frequency response function (m/N)
h	depth of cut (m)
h_0	target depth of cut (m)
$h_{0,m}^X$	measured depth of cut at X (m)
H	imaginary part of the receptance frequency response function (m/N)
H_i	height of the rectangular prism assumed as link (i) of the robot (m)
i	spindle revolution index
I	infeed distance (mm)
$[\boldsymbol{I}_i]$	tensor of inertia for link (i) of the robot expressed in its attached frame $(kg \cdot m^2)$
J	moment of inertia $(kg \cdot m^2)$
$[\boldsymbol{J}]$	jacobian matrix of the robot
$[\boldsymbol{Jv}]$	link's sub-Jacobian matrix for transformation of linear velocities
$[\boldsymbol{J\omega}]$	link's sub-Jacobian matrix for transformation of angular velocities
k_c	cutting force coefficient (N/m^2)
k_e	edge force coefficient (N/m)
k_t	stiffness coefficient of the tool holder (N/m)
K	stiffness coefficient of the Impact-Pair (N/m)
K_p	process stiffness (N/m)
$[\boldsymbol{K}]$	joints' stiffness matrix for the robot in (N/m) or (N/rad)
l	spring length (m)
l_i	length of link (i)
lt	lateral direction of the grinding task
L_i	length of the rectangular prism assumed as link (i) of the robot (m)
m	filter length $(revolutions)$
m_i	mass of link (i) for the robot (kg)
m_t	equivalent mass of the tool holder (kg)
m_u	unbalance mass (kg)
M	equivalent mass of the Impact-Pair (kg)
M_I , M_{II}	masses of the Impact-Pair (kg)
n	number of samples per revolution
n_c	number of impacts per revolution
n_{cl}	number of clock's counts per pulse period
nr	normal direction of the grinding task
n_{tst}	number of tests
N	rotational frequency (Hz)
N_m	measured rotational frequency (Hz)
$\{\boldsymbol{O}_i^j\}$	position vector for the origin of frame (i) expressed in frame (j) (m)
p	grinding wheel profile (m)

$\{\boldsymbol{p}\}$	angular displacements of rotors' actuators (deg)
P	grinding power (W)
P_E	error in grinding power (W)
P_m	measured grinding power (W)
$\overline{P}_m$	mean measured grinding power (W)
P_m^X	measured grinding power at X (W)
$\left[\boldsymbol{P}_c\right]$	position of center of masses for the six links of the robot (m)
q_i	robot's i^{th} degree of freedom
$\{\boldsymbol{q}\}$	robot's configuration (m) or (deg)
$\{\boldsymbol{Q}\}$	vector of generalized forces (N)
$\{\boldsymbol{r}_{c,i}\}$	position vector for the center of mass of link (i) (m)
R	grinding wheel radius (m)
R_0	rear radius of the grinding wheel $(x=0)$ (m)
$R_{0,m}$	measured rear radius of the wheel $(x=0)$ (m)
$\left[\boldsymbol{R}_i\right]$	rotation matrix from link (i) to the base frame
S	measured signal
S_{chip}	surface of the uncut chip (m^2)
S_f	filtered signal
S_m^X	groove's cross-sectional area measured at X (m^2)
t	time (s)
T	revolution period of the grinding wheel (s)
$\left[\boldsymbol{T}_i\right]$	transformation matrix from link (i) to base frame (0)
v_{fd}	feed speed of the robot (m/s)
$\{\boldsymbol{v}_{c,i}\}$	vector of linear velocity of the centre of mass for link (i) of the robot (m/s)
$\{\boldsymbol{v}_i^j\}$	vector of linear velocities for the origin of frame (i) expressed in frame (j) (m/s)
V	volume of the rectangular prism assumed as link of the robot (m^3)
V_{chip}	volume of the uncut chip (m^3)
V_s	peripheral speed of the grinding wheel (m/s)
w	width of cut (m)
w_0	target width of cut (m)
W_i	width of the rectangular prism assumed as link (i) of the robot (m)
x	coordinate along the grinding wheel width (m)
x_0	base frame coordinate for the robot
X	longitudinal coordinate of the groove (m)
y	position coordinate of the robot (m)
y_0	base frame coordinate for the robot
y_{ave}	average robot's displacement (m)
y_E	position coordinate of the robot's base (m)
y_{std}	standard deviation of robot's displacement (m)

Y	traverse coordinate of the groove (m)
z_0	base frame coordinate for the robot
Z	normal coordinate of the groove (m)
Z_d	wear rate of the grinding wheel (m^3/s)
Z_w	material removal rate (m^3/s)
$Z_{w,m}$	measured material removal rate (m^3/s)
$Z_{w,m}^X$	measured material removal rate at X (m^3/s)
$\{\boldsymbol{Z}_i^0\}$	axis of joint (i) expressed in the base frame
α	normalized slope (N/m)
α_i	DH parameter associated to link (i) of the robot (deg)
β	proportional damping coefficient
δ	deflection (m)
δ_I , δ_{II}	displacements of the Impact-Pair (m)
Δ	wheel's advance per revolution (m)
Δl	pre-compression (m)
Δy_B	position displacement of the robot (m)
ε	chip thickness (m)
$\bar{\varepsilon}$	average chip thickness (m)
ξ	damping ratio of the robotic holder (%)
η	phase difference between undulations on the machined surface (deg)
θ	cutting angle (rad)
θ_0	cutting angle at the wheel's rear ($x = 0$) (rad)
λ	overlapping factor
μ	friction coefficient
ρ	ratio of cut
τ	passing period of the cutter (s)
φ	angular position of the grinder shaft (rad)
Φ	receptance frequency response function (m/N)
$\{\Psi\}_i$	robot's eigendirection for the vibratory degree of freedom associated to the i^{th} articulation
ω	rotational frequency (rad/s)
$\bar{\omega}$	mean line rotational frequency (rad/s)
ω_c	chatter frequency (rad/s)
$\{\boldsymbol{\omega}_{c,i}\}$	vector of angular velocities of the centre of mass for link (i) of the robot
$\{\boldsymbol{\omega}_i^j\}$	vector of angular velocities for the origin of frame (i) expressed in frame (j) (m/s)
ω_d	robot's first mode damped natural frequency (rad/s)
ω_n	robot's first mode natural frequency (rad/s)
ω_{T01-}	NI-I transition frequency (rad/s)
ω_{T01+}	I-NI transition frequency (rad/s)
Ω	rotational frequency (rpm)

INTRODUCTION

The elastic components in a machine tool structure respond to internal and external forces of the machining operation with finite deformation amplitudes. Lack of dynamic stiffness in the machine tool, the tool holder, the cutting tool and the workpiece material causes free, forced and self-excited vibrations in response to perturbations. Robotic tool holders, employed recently in the manufacturing sector, provide holding mechanisms typically two to three orders of magnitude more compliant than the rest of the chain. Moreover, modal properties of the articulated multi-body robot structure, unlike the conventional tool holder, vary substantially as the robot undergoes through the machining trajectories accessing awkward locations. Tremendous decrease in the dynamic stiffness and its configuration-dependent modal characteristics make the problems of vibrations and instability of particular concern in robotic machining. Machinists should then plan their tasks in presence of significant vibration amplitudes even if stability is guaranteed. Vibration problems encountered in a machining operation performed by a robot arm are more severe compared to CNC machining.

The high force task of machining is not much developed for robotic tool holders. Instead, robots provide maneuverability into machining operations which cannot be performed by traditional CNC machines on complex geometries, large parts or in hard-to-reach areas. This has come at the cost of tool holders with two distinct characteristics being (i) substantial compliance, and (ii) configuration-dependent structural dynamics. The vast literature about vibrations and instability in machining operations since the beginning of the 20^{th} century has not focused on the vibratory dynamics that result from these particular properties. That is because even within the modern industries which are heavily dependent on robots, machining products constitute less than 5% of robotic sales (Chen and Dong, 2013). Robots were not believed to be able to replace CNC machine tools but they are emerging as a viable alternative depending on the required surface finish. There exist applications where a robotized approach for the task of material removal is one of the best practical solutions available. An example of such cases is the robotic grinding application under development at

Hydro-Québec's research institute (Hazel et al., 2012b) which is used in this study. The new application is being developed in order to robotize the field maintenance tasks and construction work on hydropower equipment. The tasks of material removal address issues such as cavitation damage and cracking. They are usually performed in awkward locations or hard-to-reach areas and on large/complex geometries. The robotization of such tasks saves the great costs of disassembly for off-site repairs. Also, within the manufacturing sector, turbine runner manufacturers have succeeded to automatize the machining of the blades with very large 5-axis CNC machines, but the welding and grinding operations are still performed manually. A major difficulty in robotizing the grinding application has been the inherent significant vibrations during the process. To deal with this challenge, a strategy of controlled material removal rate is employed rather than position control which is generally used in rigid machine tools performing conventional grinding. The strategy relies on an average model of the vibratory oscillations in the cutting force during material removal.

Including the vibratory dynamics in the planning of the tasks for robotic processes appears to be necessary if productivity in robotic machining processes is to be enhanced. Chatter, which is always a limitation to productivity and part quality, remains an important topic in the robotized manufacturing research as well. The persistent relevance has always been due to the complexity of the phenomenon which makes its understanding nontrivial. The intuitive approach is to understand the steady vibratory oscillations present in the material removal process first, and then, to investigate the mechanisms of instability. Therefore, a study of robotic machining chatter should be established on the basis of the vibratory dynamics specific to a robotic tool holder.

Objective of this Work

The objective of this work is to understand the vibratory dynamics specific to the robotic grinding process under study in order to investigate instability based upon appropriate understandings of the governing vibrational behavior. Ultimately, the line of research will result into chatter predictive models which will be employed to predict unstable conditions

during the grinding tasks performed by the robot manipulator. Without chatter predictive models, task planning involves conservative selection of cutting parameters through trials and errors resulting into loss of productivity. Modeling tools, experimental procedures and understandings which are developed to reach this objective can be implemented into the control strategy of the robotic machining operation under study in order to improve the accuracy of the robotized material removal tasks.

The research work is conducted on a robotic grinding process specifically. However, the principal understandings developed throughout the work can be extendable for other robotic machining operations.

Organization of the Thesis

Two separate lines of research are conducted in this study toward reaching the objective mentioned in the previous section. Given the fact that chatter is the issue of unstable interactions between the *dynamics of the cutting process* and the *tool holder's structural dynamics*, these two research aspects are considered accordingly. The main emphasis is though put on the vibratory dynamics of the cutting process affected by the substantial compliance of the robot arm through the work presented in Chapters 2, 3 and 4. The configuration-dependent structural dynamics of the robotic tool holder is studied in Chapter 5.

Following this introduction, Chapter 1 presents a review on some available literature about machining with flexible manipulators and addresses the critical issues encountered in this field. The robotic machining technology used for this study is also presented. The chapter finishes by a brief description about the problem of chatter in machining as it is the required background for the reader of this thesis.

In Chapter 2, the instantaneous *cutting process* is studied through modeling and experimental validations in order to understand the vibratory regime which results from the substantial

compliance of the grinder robot. Cyclic impacting oscillations of the cutter during material removal (impact cutting) are captured with the help of the experimental setup and the procedures developed in this chapter. The setup employs the methodology of angular sampling to locate the interruptions of the cut and to investigate the governing dynamics. Variation in the measured instantaneous rotational frequency of the spindle during the cutting impacts, at every revolution, is correlated to the grinding power. The significance of such real-time measurement during grinding is that it can be used as feedback to control the rate of the material being removed. However, one missing element is a model which formulates the grinding force or power to be delivered at the spindle for achieving a target material removal rate, in presence of the sustained impacting oscillations in the process.

A model for the grinding power based upon the impact-cutting behavior is presented in Chapter 3. First, to complement the experimental study presented in Chapter 2, a conceptual analogy is drawn between the impact-cutting behavior and the vibro-impact dynamics of the classical generic impact pair. This is to assure that the dynamic behavior is an inherent characteristic of the process. With this understanding and the averaged impact-cutting model for grinding power considered into the control strategy of the robotic grinding task, this chapter investigates whether metal removal at a target material removal rate or to a target depth of cut is possible given the unavoidable severe vibrations inherent to the process. The capability of the impact-cutting model to predict grinding power in the real practice of the robot is validated as long as stable grinding conditions are guaranteed.

Regenerative self-excitations that originate from the cutting process within the impact-cutting material removal are studied in Chapter 4. Vibro-impact motions of the grinding disk introduce discrete kinematics into the dynamics of the grinding process under study. This makes the grinding operation different from conventional grinding which has continuous kinematics and involves irregularities. The cutting impacts which occur mainly once per spindle revolution and remain quasi-stationary regarding their angular position bring regular kinematics into the cutting process. Stability of metal removal, which is thus carried out more similar to the flutes of a milling cutter, is analysed with the help of the stability lobes diagram

used generally for milling operations. The process is simplified by a SDOF dynamic model of the robotic holder. A single delay term that accounts for the self-excitation from the overlapping cutting impacts once per spindle revolution is considered. An appropriate perspective for the problem of regenerative chatter in robotic machining is drawn by using the specific vibratory dynamics of the process, i.e. the impacting oscillations. An experimental investigation is also carried out to support the part of the study presented in this chapter. This is the first step toward predictive models for avoiding regenerative chatter in the robotic grinding process under study.

The second line of research, focused on the robotic *tool holder's structural dynamics*, is presented in Chapter 5. The objective is to develop the modeling tool and the needed insight for vibration analysis of a robot arm with varying vibratory dynamics caused by its extensions and compressions when accessing awkward locations along machining trajectories. Traditional modal analysis is extensively employed in the studies of vibrations and instability for machining. Nevertheless, unlike the fairly invariant structure of a CNC machine tool holder, modal properties of a robotic holder vary substantially. A multi-body dynamic model is developed in this chapter for the varying articulated structure of the robot arm. The model is validated through experimental modal analysis by measurement of the natural frequencies and mode shapes. A discussion is provided about defining eigendirections for the robot structure to replace the functionality of mode shapes in conventional modal analysis. Instability due to self-excitations caused by the exchange of vibration energy between structural modes can be well investigated using this proposed approach.

Contributions and industrial impacts of the thesis are summarized at the end and some recommendations are made about how this research work can be continued in future.

CHAPTER 1

Background and Literature Review

1.1 Machining with Flexible Manipulators

The manufacturing procedure for many industrial parts includes cleaning, pre-machining, machining for high tolerance surfaces, painting and assembly. Robotization of these operations became desirable firstly in order to avoid manual operations in extremely noisy, dusty and unhealthy environments. However, there exist instances where machining is not even possible using the conventional CNC machine tools. Machining of large parts or parts with complex geometries are examples of such instances. Due to variations and irregularities of machining trajectories, these are considered as high-cost difficult-to-change capital investments for a CNC machine tool cell where a robotic machining cell becomes the immediate viable alternative. In a robotic machining process, a light-weight cutter or grinder is held by an articulated robot arm. Material removal is achieved by the rotating cutting tool while the robot end effector ensures that the tool follows a programmed trajectory in order to work on complex curved surfaces. However, more than 80% of the processes developed for industrial robots are about material handling and welding (Zhang et al., 2005). Machining processes are high force tasks in which the physical contact of the cutter with workpiece material causes large deformation errors on the robot arm. The process of metal removal requires a process-specific force to be exerted in order to establish the shear deformation of work material and remove the chip. Constant conservative feed-rate and depth of cut is the solution of robot machinists to reduce vibrations during the operation. Few robots have been reported successful to perform machining.

Some practical issues on a milling application performed by an industrial robot are discussed in (Marui et al., 1988c). An analytically based stiffness model of a robot structure in its

workspace for the special needs of a machining application is presented by (Abele, Weigold and Rothenbucher, 2007). Dynamic interactions of a flexible multi-body model for the robot structure with a process model for a milling application is presented in (Marui et al., 1988a). The purpose has been to predict the tool displacement caused by the process forces. Research on robotic deformation compensation is mainly about gravity compensation and deflection compensation. Not much attention has been given to process-force induced robot deformation (Zhang et al., 2005). Modeling and experimental identification of the robot within its working space is used by (Zhang et al., 2005) to estimate and compensate for the real time deformations and improve the overall machining accuracy. A tool angle adjustment method in a grinding application with a small robot is introduced by (Akbari and Higuchi, 2000; Akbari and Higuchi, 2002). Using real-time force control, (Matsuoka et al., 1999) studies the characters of a robot in milling to avoid large process forces. Much effort has been made by force control. The idea was to move the robot by the information of contact forces (Ferretti, Magnani and Rocco, 1999). Regarding process development (Abele, Weigold and Kulok, 2006) uses high speed cutting to reduce the process forces so that the load on the structure is minimized. Stability investigation of the process has also been done in a few recent studies (Pan et al., 2006; Pan and Zhang, 2007). Critical issues and challenges about using a robotic arm as the tool holder to perform machining are reviewed by (Wang, Zhang and Pan, 2006).

1.1.1 The SCOMPI[1] Robot

Despite serious challenges that exist about vibration and instability in robotic machining processes, the maneuverability that robots bring into the operations makes them, sometimes, the only practical solution for machining. The robotic machining technology which is used in this study (Hazel et al., 2012b) provides maneuverability in order to automate the in-situ maintenance work on hydroelectric equipment. The 6-DOF robot called “SCOMPI” shown in

[1] **S**uper **COMP**act **I**REQ

Figure 1.1.a was developed at Hydro-Québec's research institute, IREQ[2]. It uses a *lightweight structure* ($\approx 30\ \ kg$) which is much lighter than the average robot used for machining ($\approx 200\ \ kg$) to provide a portable solution for field machining tasks, thus avoiding the costs of dismantling parts and minimizing shutdowns. The manipulator's unique kinematic design uses a *track-based installation* for its first prismatic joint rather than being installed on a rigid grounded shoulder like the robots used in factory lines. The track may be straight, circular or a series of circular sections so that such feature provides a *track-long extended working envelop* to gain access for machining awkward locations. Such intervention works as welding, grinding or machining which workers cannot do in these locations are done by the fully extended arm and with the help of its track-based kinematics. Several field repair and construction procedures on large hydropower equipment are under development

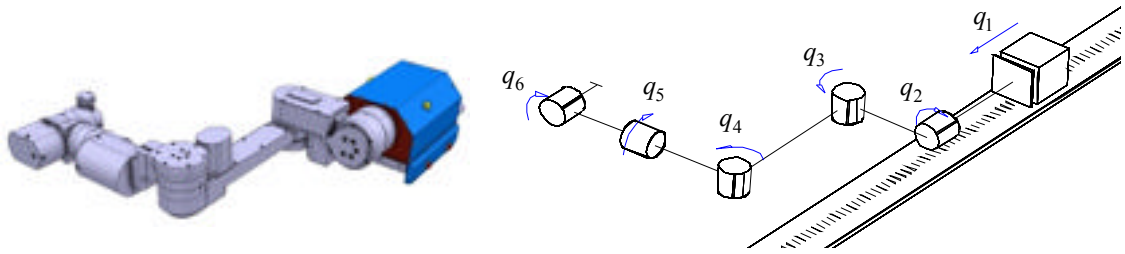

(a) Track-based kinematic architecture of SCOMPI with 6-DOF

(b) Grinding between the blades of a Fransic turbine runner

Figure 1.1 The SCOMPI robot

[2] Institut de recherche d'Hydro-Québec

with this robotic machining technology (Hazel et al., 2012a). Grinding tasks performed by SCOMPI are demanding jobs that involve heavy material removal aimed at modifying parts' dimensions (Hazel et al., 2012a) rather than generating glossy surfaces only. The task shown in Figure 1.1.b is about reshaping the blades of old-design Francis turbine runners to correct fluid flow problems (Giroux et al., 2008). Such maintenance operation involves thickening of the blades at some sections by overlay welding and thinning at other sections by grinding. There exist instances that 18 *mm* depth of material over a 1 m^2 area needs to be removed by the robotic grinding process through several iterations reaching typical material removal rates around 4-5 kg/h. In applications of the robot for refurbishment of head gate components (Gagné et al., 2010), few millimeters of material are removed over an area of 10 *m* length, 200 *mm* width. The problems of vibration and instability encountered during machining with this robot are even more serious compared to the average machining robot. This is the price to pay for being capable to machine in hard-to-reach areas while using a portable robotic solution as well.

Robotic machining has been reported by many researchers to be more prone to severe chatter vibration problem as compared to CNC machining. There are not guidelines or rules of thumb for robot machinists to set up their task in a way to avoid chatter. This has resulted into the frustrated trial and error effort spending a lot of time to find the appropriate chatter-free machining operation setup, which may sometimes even be at the expense of loss of productivity.

1.2 Machining chatter

The well-known problem of machining chatter is briefly described in the current section. Machining chatter is the issue of self-excited vibrations in the process of removing material resulting into unwanted machining conditions such as excessive noise, disproportionate tool wear and breakage or poor surface quality. There exist an extensive literature about investigation and avoidance of chattering conditions in machining started by the early studies of (Arnold, 1946), (Hahn, 1953) and (Doi and Kato, 1956). A comprehensive mathematical

model and analysis of the problem was first given by (Tobias and Fishwick, 1958) and (Tlusty and Polacek, 1963). The excitation energy under the chattering condition comes from the cutting process itself. Several mechanisms of self-excitation have been recognized throughout years of research continued until very recent studies (Quintana and Ciurana, 2011; Siddhpura and Paurobally, 2012). A classification of these mechanisms distinguishes frictional, regenerative, mode coupling and thermo-mechanical chatter (Wiercigroch and Budak, 2001). Among all, instability due to the regeneration of surface waviness and the mode-coupling instability are considered as two dominant mechanisms.

1.2.1 Regenerative Chatter

Overlapping cuts exist in almost all machining operations. The tool is always cutting a surface which was already cut during the previous tool passes. Regeneration is the feedback mechanism between subsequent cuts as shown schematically by the illustration in Figure 1.2. Oscillations of the cutting tool leave undulations on the machined surface. The excitation due to the cutting force F_c depends on the instantaneous chip thickness h. The uncut chip thickness h_0 is modulated by the oscillations of the cutting tool in the current and previous passes $y(t)$ and $y(t-\tau)$ with τ being the passing period of the cutter (delay term). The phase difference η between the undulations left on the surface cause perturbations in the

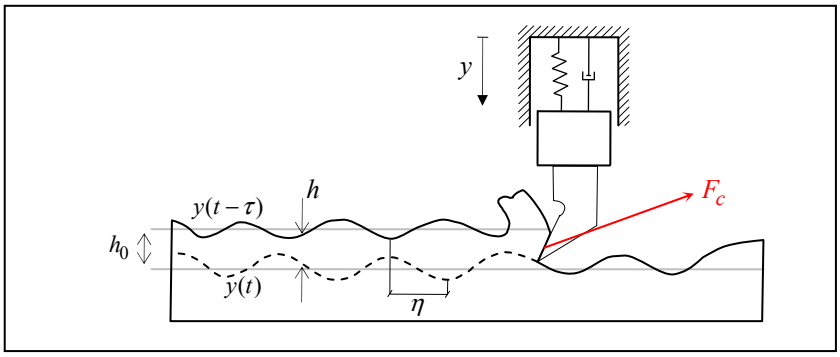

Figure 1.2 Regeneration of surface waviness in machining

cutting force which results from chip removal. Under certain conditions of the cutting operation, perturbations in the cutting force can grow exponentially and as a result, the vibration response to cutting force excitation becomes unstable. Numerous researchers such as (Altintas and Budak, 1995) have formulated the interactive dynamics resulting into such unstable conditions in machining with the help of linear delay differential equations (DDE). The formulation combines the dynamics of the cutting process with the tool holder's structural dynamics. Solving the DDE, the borderline of stability is plotted versus the spindle speed of the operation in charts known as "stability lobes diagram". As shown in Figure 1.3, in the stability lobes diagram, the borderline of stable operation is plotted versus a cutting parameter such as the width or the depth of cut. These charts are considered as guidelines for machinists in order to setup the working point for the task in the white region below the lobes where cutting is predicted to be stable.

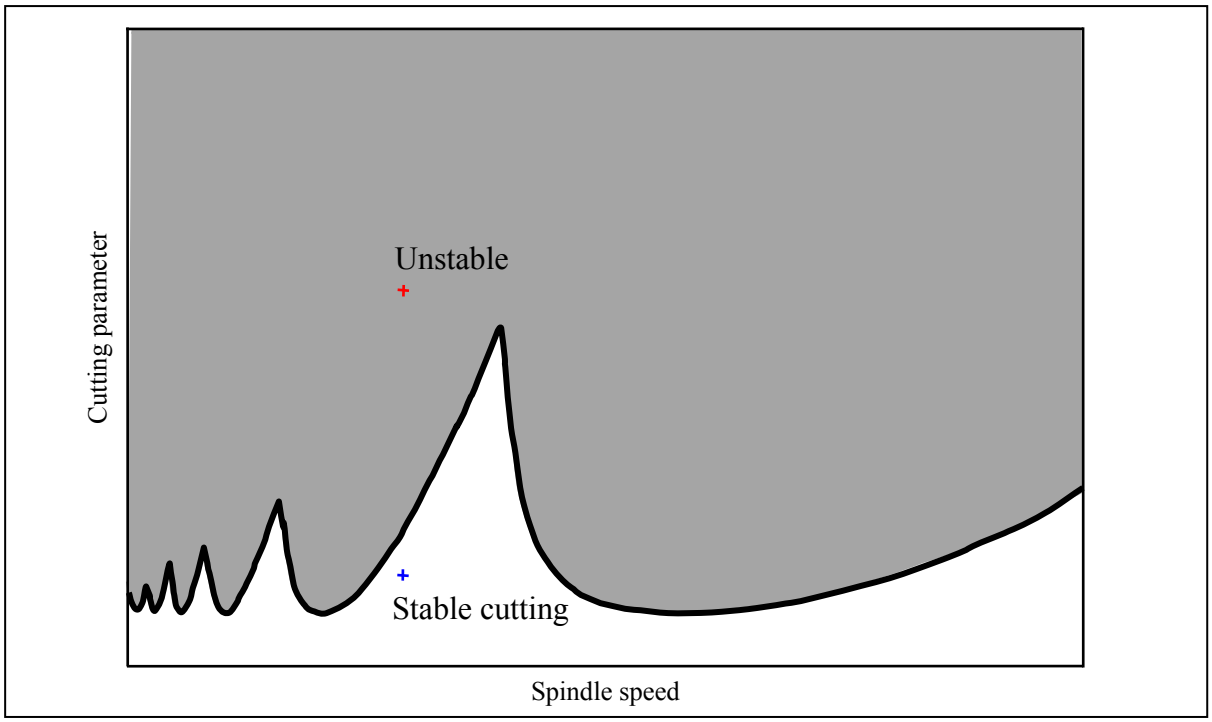

Figure 1.3 Stability lobes diagram for regenerative chatter in machining

1.2.2 Mode Coupling Chatter

The mechanism of mode-coupling instability in machining occurs in vibratory systems which are assumed to have at least two degrees of freedom. It was first introduced by (Tlusty and Polacek, 1963) as the "positional coupling" principle causing self-excitation in machining operations. The effect is briefly described in this section.

In the cutting operation shown in Figure 1.4, the system is assumed including two natural vibratory modes along directions *I* and *II*. The vibrations of the system along one direction occurs with a phase shift relative to the vibrations along the other direction. The result is that the cutting tool which is connected to the vibratory system, moves on an eliptical path. This has also been observed experimentally (Hahn, 1953). Let's assume that the oscillations in the cutting force F_c is proportional to the vibrations along the normal direction y to the workpiece. Considering the moving direction as depicted on the ellipse shown by Figure 1.4, during the first half of the move from point A to B, the movement direction of the tool tip is in the opposite direction of the cutting force. This means energy is dissipated from the vibratory system during this part. Within the second half cycle though, the cutting force has a projection in the same direction as the movement of the tip. This means energy is delivered into the system during this half. Given the fact that during the second half the cutter is

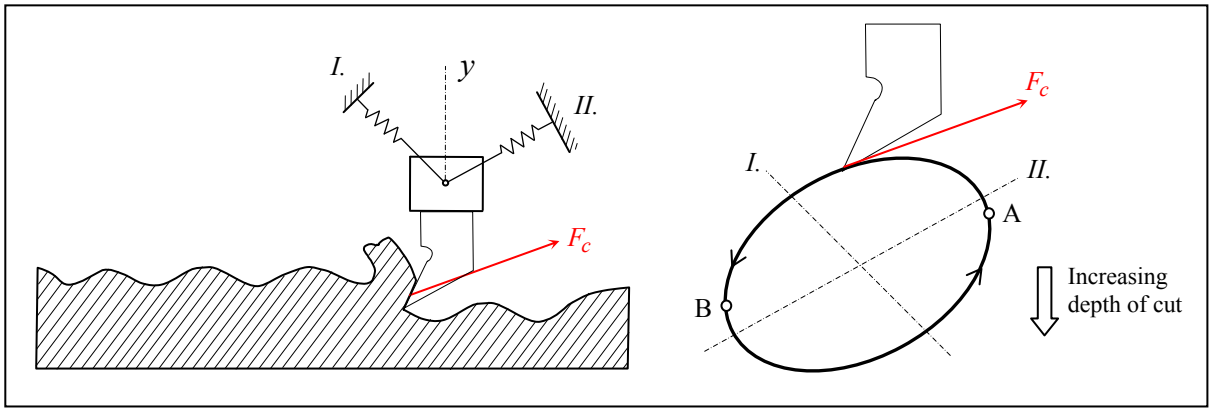

Figure 1.4 Mode-coupling instability in machining adapted from (Tlusty and Polacek, 1963)

removing greater depths of material, the work done is bigger and the resultant in one oscillation cycle is that energy is exerted into the system. It is therefore obvious that orientation of the natural vibratory modes of the system with respect to the direction of the cutting forces is very important regarding the self-excitations due to the mode-coupling effect. The layout of these directions with respect to the direction of the cutting force defines if the system becomes unstable caused by the mode-coupling effect.

1.2.3 Forced vibration

In self-excited vibrations with mechanisms such as regeneration or mode-coupling, as described in Sections 1.2.1 and 1.2.2, the alternating force which sustains the motion depends on the motion itself. That means the force magnitude is a fuction of the cutter's vibratory deflection and if the motion stops, the alternating force disappears. Another type of vibration involved in metal cutting is caused by the forces which are independent of the cutter's motion and persist if the vibratory motion stops. These are forced vibrations caused by the perturbing forces present in the mechanical system such as forces due to the rotary operation, forces induced by hydraulic devices integrated into the machine or floor vibrations. For the case of grinding, vibrations caused by the unbalance and eccentricity of the wheels are the fundamental perturbing forces of the rotary operation.

From the brief introductions about the two mechanisms of slef-excitation in the preceding sections, it can be seen that vibrational instability in machining is investigated based upon appropriate understanding of the vibrations that govern the steady regime of metal removal. To study regenerative instability, one should first have enough knowledge about the vibration locus of the cutter's end during the steady regime of material removal. For an investigation of mode coupling instability, vibratory modes of the machine tool structure should have been identified first. In this thesis, first, the steady vibratory dynamics of the robotic grinding process is investigated through Chapters 2 and 3. In Chapter 4, the mechanism of regenerative chatter affecting the steady vibrations of the operation is studied. The part of the

work which is presented in Chapter 5 is focused on the vibratory dynamics of the multi-body articulated structure of the robotic tool holder in machining.

CHAPTER 2

Angular Analysis of the Cyclic Impacting Oscillations

In this chapter, the instantaneous cutting process performed by a grinder robot arm is investigated with the help of modeling and experimental verifications. The purpose is to elaborate the effect of the substantial compliance of the tool holding mechanism, i.e. the robot arm, on the dynamics that govern the process of material removal.

2.1 Introduction

The tool holder, in a machining task, assures that the cutting tool follows the programmed trajectory of machining. In the meantime, it also provides restoring forces in order to counterbalance the cutting force which is established inside the zone of contact. Once this balance is violated, disengagement of the cutter with the workpiece takes place and the cut gets interrupted. In CNC machining, the elements in the machine tool-tool holder-cutting tool-workpiece chain have the same order of magnitude stiffness. Therefore, the capacity for providing a counterbalancing force at the contact zone is high. Contact is thus almost always maintained as long as large unstable vibrations are not met. For a robotic arm though, this force capacity is very small as compared to the amount of force required for removing material. The limit is dictated by the compliant restoring mechanism of the robot arm which is composed of articulated bodies. Compliance of a robot is reported mainly due to its joints' compliances (Zhang et al., 2005). This is caused by the elasticity of gear transmission systems used for the articulations. Dependent on the type of the robot and its size, gears' compliance can contribute from 50% to 75% of the overall robot's compliance (Abele, Weigold and Rothenbucher, 2007). Also, in the parallel mechanism of a CNC machine, the off-axis flexibilities of articulated joints are constrained by the effect of other chains and the closed-loop mechanism is stiff in overall. In the open kinematic structure of a serial robot though, the chain becomes progressively less rigid with multi-body components added. This

also contributes to the very compliant restoring mechanism of a robot for the high-force task of machining. A typical articulated robot has a stiffness usually less than $10^3\ kN/m$, while a standard CNC machine very often has stiffness greater than $50\times10^3\ kN/m$ (Zhang et al., 2005). In the case of the SCOMPI robot used for this study, the stiffness value is around $20\,kN/m$. Robotic tool holders are thus, one to three *orders of magnitude* more compliant than the conventional CNC machine tools, inherent to their structure. This makes robotic machining a striking example of intermittent cutting because a robot can hardly afford the counterbalancing force required at the cutting zone due to its limited force providing capacity.

Interruption of the cut is an issue of great concern in the study of the dynamics of material removal because it introduces nonlinearity into the system dynamics and results into non-uniform metal removal. Researchers have developed different methodologies to deal with it. The interruption phenomenon is recognized as the basic nonlinearity in machining chatter (Tlusty and Ismail, 1981) and a traditional approach is to deal with it in numerical simulations by setting the cutting force to zero when the tool moves out of the cut. Modern cutting operations involve conditions where the degree of such nonlinearity is increased and the tool cuts the material for only small fractions of the spindle period. High-speed machining of contoured surfaces, near-net-shape flexible components and difficult-to-machine materials are examples of such operations (Davies et al., 2000). A generalized analytical approach is proposed (Bayly et al., 2003; Davies et al., 2000; Davies, Pratt and Dutterer, 2002; Szalai and Stepan, 2006) by denoting a parameter $0<\rho<1$ which represents the ratio of time spent cutting to not cutting during a spindle period. The stability of interrupted cutting is then investigated for scenarios both of continuous operation ($\rho\approx1$) and of highly interrupted operation ($\rho\approx0$). In this chapter, interruptions of the cutting process are investigated experimentally with respect to the instantaneous angular position of the spindle. This enables us to correlate the intermittence in the cutting operation with the machine cycle, i.e. the spindle revolution and draw conclusions about the governing dynamics. The angular analysis technique has been used successfully in a large number of

applications to observe faults in rotating machines with discrete events during rotations (Girardin, Rémond and Rigal, 2010; Remond and Mahfoudh, 2005; Stander and Heyns, 2005; Yang et al., 2001). The technique is applied in this study to detect and locate the angular position of the discrete cutting events per spindle revolution.

In the following section, dynamic modeling and numerical simulation of the robotic grinding process is presented in order to explain, theoretically, the governing dynamics of the material removal process. In Section 2.3, the test setup and material used for verifying these governing dynamics are described. The techniques of angular sampling and analysis with the measurement of instantaneous rotational frequency which are the key features implemented in the test setup are described in this section. The experimental approach is then evaluated in Section 2.4 regarding its capability to detect and locate the discrete cutting events of an imposed interrupted cutting operation. Robotic grinding experiments are then studied in Sections 2.5 and 2.6 using the experimental setup developed. The work presented in this chapter is mainly focused on experimental characterization of the cutting dynamics performed by the compliant robot arm. Dynamic modeling and analysis is thus simplified to a SDOF representation.

2.2 Impact-Cutting Material Removal in Robotic Grinding

Details of a typical robotic grinding task are studied in this section to illustrate the distinctive vibratory dynamics of the process theoretically.

2.2.1 SDOF dynamic model

A SDOF representation of robotic grinding with a flexible arm is shown in Figure 2.1. The robot holds the cutting tool, *approaches* the workpiece along coordinate y_B and positions the grinding wheel (see Figure 2.1.b). Traverse grinding is then performed through robot travel in feed direction fd parallel to the wheel axis (see Figure 2.1.a). Restoring and damping

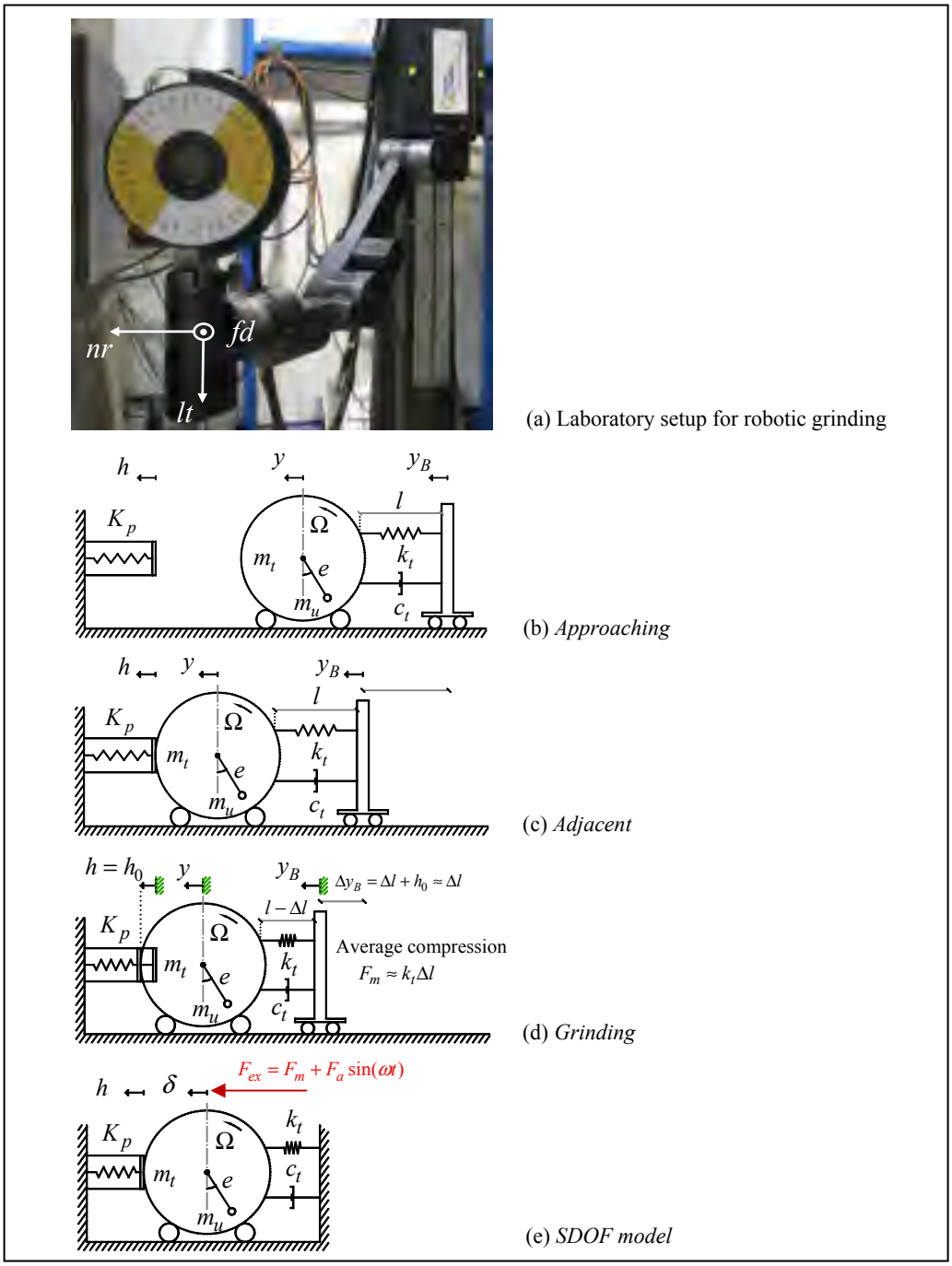

Figure 2.1 Machining with a flexible robot

forces from the holding mechanism to maintain the cut are provided by the articulated links at any configuration during the movement. These forces are modeled by spring and damper elements k_t and c_t. Inertial resistance of the entire robot-grinder chain is represented by an

equivalent mass m_t. External alternating forces F_a during machining include mainly the unbalance force if other perturbations from the rotating grinder are ignored. Perturbation in the process is therefore modeled as an unbalance mass m_u with eccentricity e and rotational frequency Ω.

The grinding wheel is placed *adjacent* to the workpiece surface by the robot (see Figure 2.1.c). During the steady state, the robot provides a push through displacement Δy_B to remove depth h_0 of material. Restricted by the workpiece surface, the constant push results in compression along the flexible links and joints. Figure 2.2 plots the controlled displacement of the robot's end-effector from its original location at the workpiece surface starting about $10mm$ above the surface for a typical grinding task. On average, a deflection of the robot of around $15mm$ is needed to remove material to depth $h_0 = 0.27mm$. To appreciate the difference between robotic grinding and conventional grinding with a CNC machine, consider the order of magnitude of the material removed versus this deflection of the holder. This distinguishing factor is represented in the SDOF model as pre-compression Δl in the tool-holding spring element during steady-state *grinding* (see Figure 2.1.d). Since $\Delta l >> h_0$, the pre-compression of the robot can be assumed as $\Delta y_B = \Delta l + h_0 \approx \Delta l$. Pre-compression is maintained throughout the task with oscillations due to external alternating forces and cutting force superimposed. It may therefore be replaced by an equivalent mean

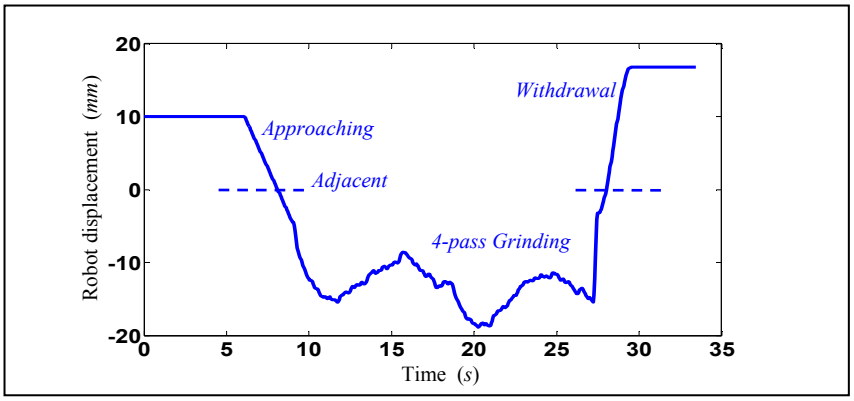

Figure 2.2 Deflection measured in 4-pass robotic grinding

force F_m exerted on the cutting tool if equilibrium is defined at steady state. Such a system subjected to mean and alternating forces of the cutting operation is shown in Figure 2.1.e. Cutting force will then be an internal force that appears inside process stiffness spring element K_p.

2.2.1.1 Cutting force

The force required to remove material to depth h_0 defines process stiffness spring element K_p. Abrasive grits of a grinding wheel distributed over its surface are individual cutters that perform the cut and remove the chip of metal with thickness ε from the workpiece surface (see Figure 2.3.a). Grits have random shapes but in average, they can be considered as cutters with negative rake angles (Kita, Ido and Hata, 1978). These cutting edges are distributed through random patterns over the surface of the wheel which has the width E. The cutting operation that is carried out by these cutting edges is simplified as if done by an equivalent cutter of width E and with negative rake angle as illustrated by Figure 2.3.b. Tangential and normal cutting forces on such a cutter have two components (Altintas, 2000d). The first is the edge force, which is assumed proportional to cutter width E, where constant k_e represents the friction force per unit width. The second is the shearing force that deforms the material out of the workpiece and is assumed proportional to the uncut chip's cross-sectional area $E\varepsilon$ through cutting coefficient k_c. This modeling approach is typically used for the flutes of the milling tools. Normal cutting force is then formulated as follows:

$$F_N = F_e + F_c = \frac{1}{\mu}(k_e E + k_c E \varepsilon) \tag{2.1}$$

where E is the wheel width, ε is the chip thickness and μ is the friction coefficient. An estimate of the process stiffness spring element is then given by the ratio of the force required to cut the chip of material over the chip thickness.

$$K_p = \frac{F_c}{\bar{\varepsilon}} = \frac{1}{\mu}\left(\frac{k_c E \varepsilon}{\varepsilon}\right) = \frac{1}{\mu} k_c E \tag{2.2}$$

2.2.1.2 Piecewise Linear Restoring Force Function

Since edge force F_e does not contribute to shearing the material, it does not depend on the depth of cut for a cutter of constant width. It appears as soon as the cutting edges of the grits (or the width of the equivalent cutter in Figure 2.3.b) initiate the cut. It should not therefore contribute to process stiffness spring element K_p of the model in Figure 2.1.e. A piecewise

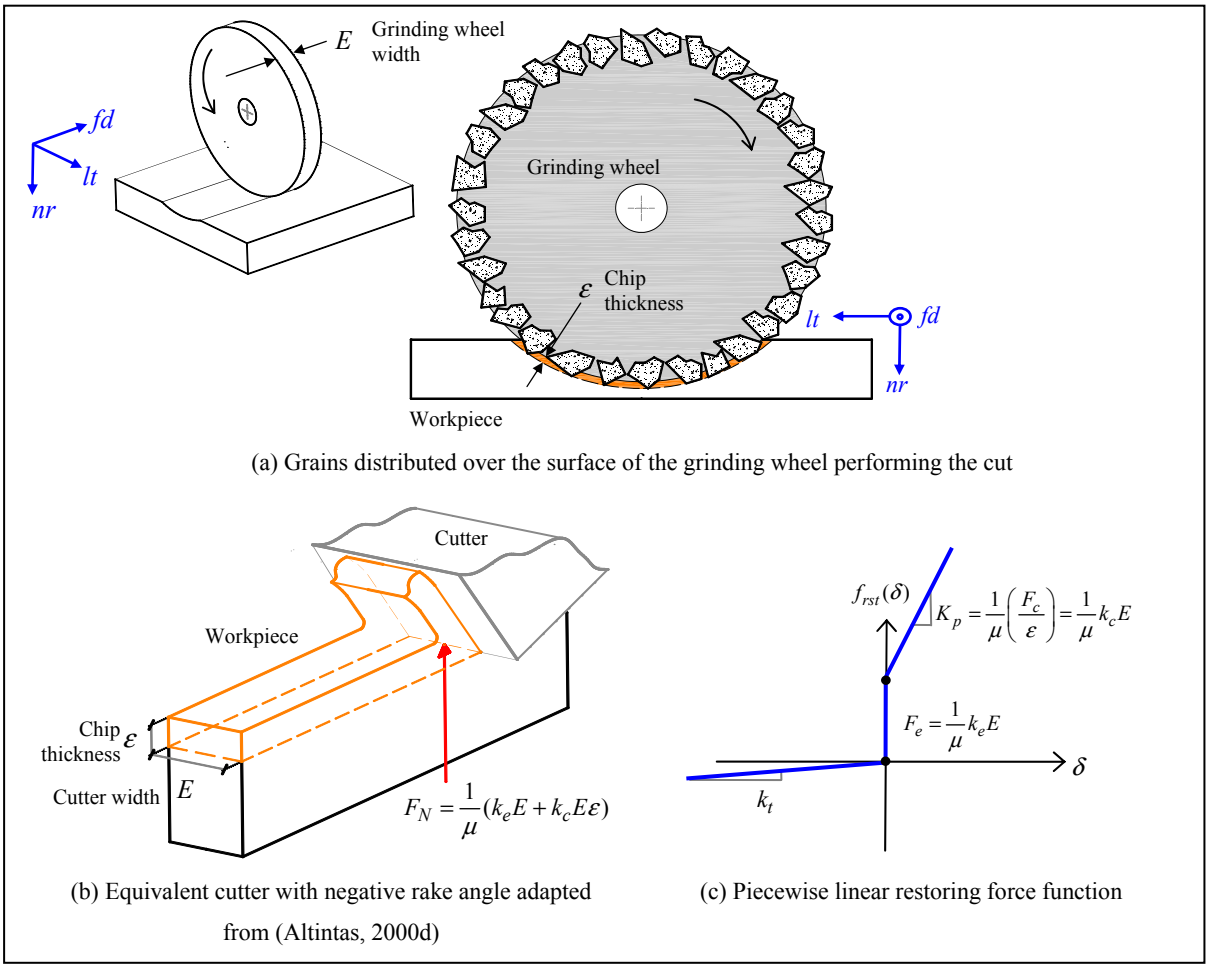

(a) Grains distributed over the surface of the grinding wheel performing the cut

(b) Equivalent cutter with negative rake angle adapted from (Altintas, 2000d)

(c) Piecewise linear restoring force function

Figure 2.3 Average cutting force in traverse robotic grinding

linear restoring force function may now be established for the dynamic equation that governs the SDOF model (see Figure 2.3.c). This function governs three sources of forcing in the dynamic response: restoring force due to dynamic compression (not pre-compression) of holding spring k_t, cutting force to shear off the material and edge friction force. The function is formulated such that the spring element k_t only pushes the cutter into the cutting zone to counterbalance the cutting force and never pulls it out in order to resemble the real practice more accurately.

2.2.2 Cyclic Impacting Oscillations

The dynamic response to external forces of the operation is studied to find the steady-state vibration behavior. The equation for robot deflection δ normal to the workpiece surface is then:

$$m_t\ddot{\delta} + f_{rst}(\delta) + c_t\dot{\delta} = F_m + F_a \sin(\Omega t) \quad \text{where} \quad f_{rst}(\delta) = \begin{cases} F_e + K_p\delta & if \quad \delta \geq 0 \\ k_t\delta & if \quad \delta < 0 \end{cases} \tag{2.3}$$

Typical parameters of a grinding task and properties of the first mode for the robot structure from experimental modal testing (See Chapter 5) are set for this model. Figure 2.4 shows the simulated time- and frequency-domain response using the Runge-Kutta integration method with time step $dt = 1\times10^{-5}\,s$ and typical parameters for the grinding operation. $\delta = 0$ corresponds to the instants when the wheel touches the workpiece surface. The steady-state response of this system is clearly far from the linear sinusoidal response commonly assumed even though the system is excited by a pure sine function. The cutting tool, for almost 98% of the cycles of its steady-state response (revolutions) is not doing its cutting job. It stays in the cut ($\delta > 0$) for a very short time and during small angular displacements. The cut is then interrupted and the grinding wheel spends the rest of its steady-state cycle out of the cut. The response shows at times one and at other times several impacts per revolution of the wheel ($T = 0.01s$). Steady-state cutting consists of impacts occurring once or twice per revolution of the wheel. Non-harmonic responses are also appearing as amplitude modulations of the harmonic response. One of these amplitude modulations evidently visible is the one that

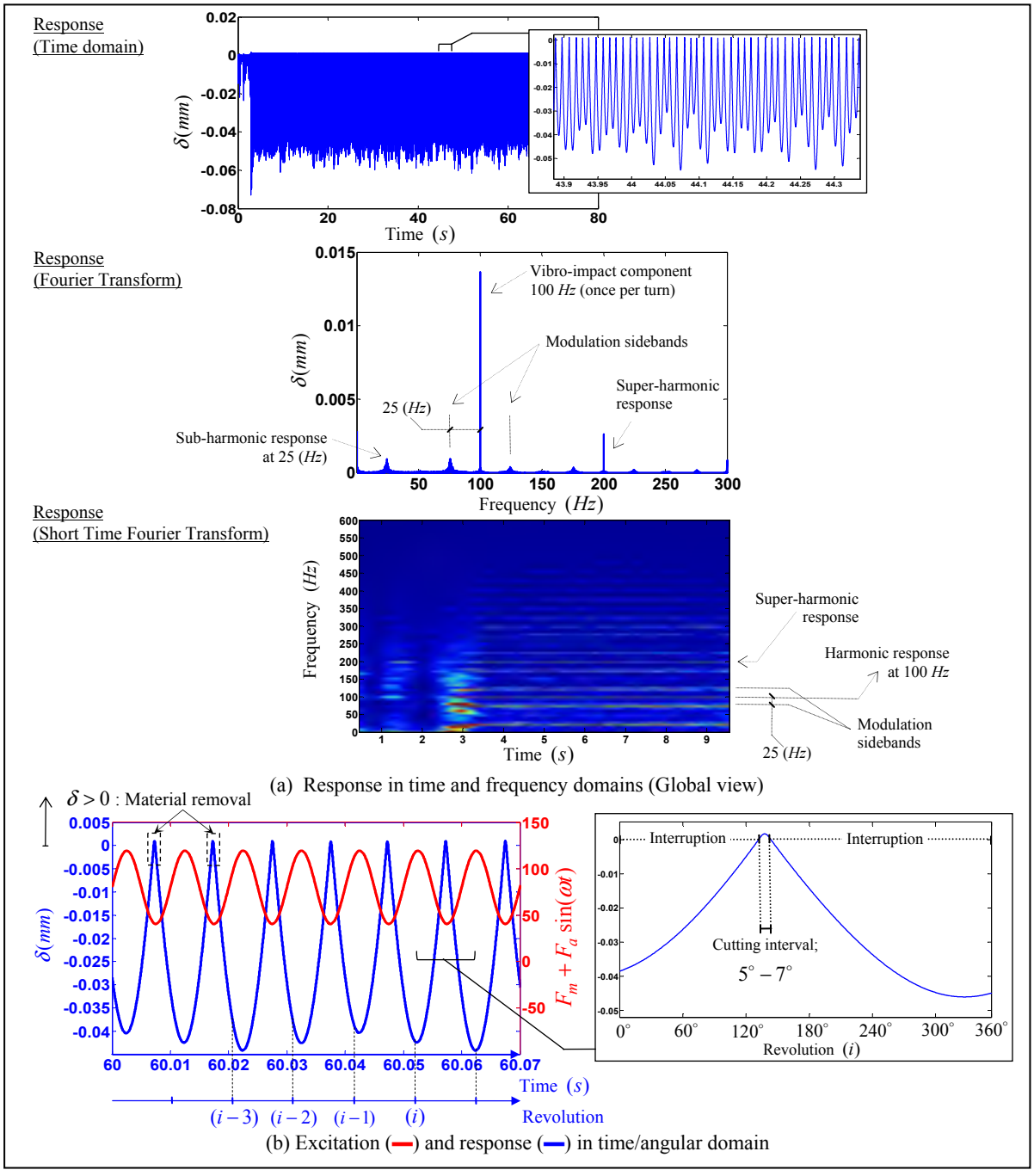

Figure 2.4 SDOF response using typical parameters:
$k_e = 163\,kN/m$, $k_c = 4911\times10^3\,kN/m^2$, $f_n = 4Hz$, $k_t = 17.2\,kN/m$, $m_t = 27kg$, $\xi = 0.1$,
$F_m = 80N$, $m_u = 0.2kg$, $e = 0.5mm$, $\Omega = 6000rpm$, $E = 6.8mm$, $\varepsilon = 0.02mm$, $\mu = 0.33$.

happens every 4 or 5 cycles. That means every 0.04 or 0.05 *s* which is about 25 *Hz*. To see if the modulation at 25 *Hz* is a steady component, the response in frequency domain is

investigated. The FFT plot of the response shows that harmonic vibro-impact response at 100 *Hz* is the most dominant component of the response. Multiple harmonics like the one at 200 *Hz* are also present. The sub-synchronous component at every 4-5 cycles corresponding to 25 *Hz* is also present and seems to be a steady component looking at the STFT plot. It appears as modulation sidebands separated by 25 *Hz* around the multiple harmonics. The harmonic response at $100Hz$, the main component of the response, is the event that repeats once per revolution of the wheel. The excitation force is also plotted over the response to confirm that conditions have reached a steady state. Under steady-state conditions, because the excitation frequency is much higher than the robot's natural frequency, excitation and response become out of phase. An angular phase shift close to 180° is evident between the position of the cutting impact and the driving force being the unbalance perturbation.

This analysis explains how steady-state material removal is achieved through recurrent impacts. The high ratio of cutting forces to restoring forces from the compliant robot results in such behavior. The stable solution of the oscillating cutter, like any natural mechanism, is the one with minimum mechanical energy. The average stiffness of the oscillator with the piecewise linear restoring force function is given by the relative amount of time (over one revolution) that it spends in one stage versus the other. The system tends to minimize the amount of time it spends in the stage with high stiffness and therefore a cut is always followed by an interruption of the longest possible duration. The impacting oscillation has a frequency which is commensurate to the frequency of the driving force and interruption of the cut is a dynamic effect that would occur regardless of discrete cutting kinematics.

2.2.3 Angular Position of a Cutting Impact

The grinding disk is an impacting oscillator that moves out of phase with perturbations present in the process as illustrated in the video shown by Figure 2.5.a (see the supplementary material to play the video). That means there is always about a 180° phase

difference between the angular position of a cutting impact and the phase of the perturbing forces. This is a characteristic behavior in the operation under study since the rotational frequency $N \approx 100Hz$, or equivalently the excitation frequency, is much larger than the natural frequency of the robotic holder ($N >> f_n$) in typical robotic grinding tasks. Overlaying the simulated response and the excitations confirms this reasoning (see Figure 2.5.b). An inherent unbalance of the disk resulting either from its eccentricity or non-uniform distribution of material superimposes on the imbalance due to wear of the wheel at each cutting impact. The flattening of the disk due to wear caused by a cutting impact is like a negative mass unbalance, and it can be considered as an unbalance mass located 180° away from the angular position where the impact takes place. Therefore, sequential impacts

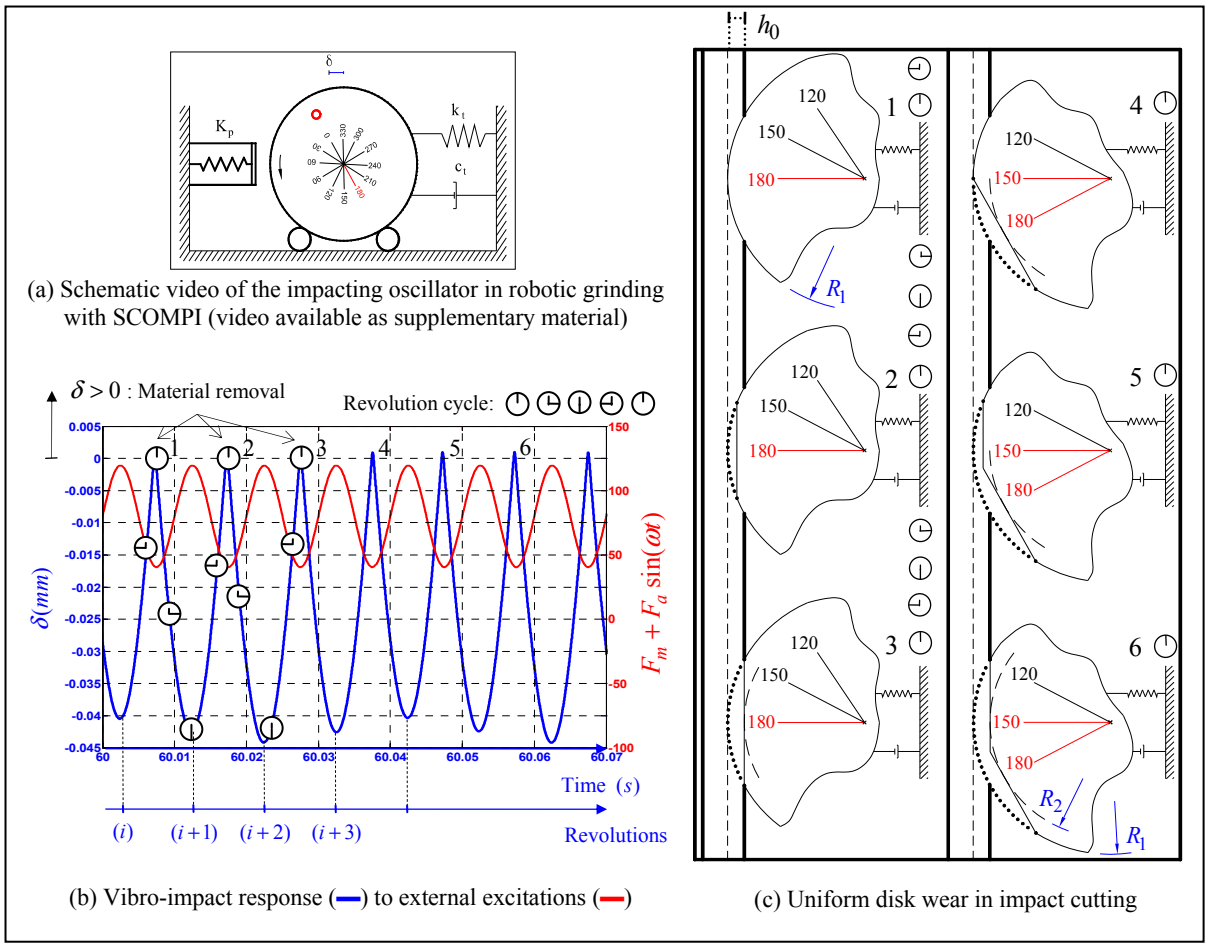

(a) Schematic video of the impacting oscillator in robotic grinding with SCOMPI (video available as supplementary material)

(b) Vibro-impact response (—) to external excitations (—)

(c) Uniform disk wear in impact cutting

Figure 2.5 Angular position of cutting impacts and uniform disk wear in robotic grinding

successively increase the resultant unbalance mass located 180° away and consequently increase the response amplitude.

The measured vibration amplitude at the rotational frequency ($0.1-0.4mm$, peak to peak) is in the same order of magnitude as the depth of removed material (h_0 in Figure 2.5.c). It is then reasonable to think that the angular position of the cutting impacts remains stationary until the vibration amplitude becomes smaller than the amount of wear on the wheel. At that instant, the wheel starts impacting at another angular position, which may be simply assumed adjacent to the former location. With this mechanism, the wheel wears down uniformly from a larger radius R_1 to smaller radius R_2. The instantaneous views in Figure 2.5.c are a visual simplification of this concept. They must be considered together with the sequence of points shown on the cycles of vibro-impact response in Figure 2.5.b. The sequence of 5 states, with a rotating clock marked on the response, corresponds to revolution cycles indexed by variable i. Starting from the i^{th} revolution, imagine that the first impact occurs as shown in view (1) while the radius of the disk is R_1. The angular position of the impact at 180° is out of phase with the inherent unbalance of the disk. Then until the next impact, the wheel bounces off the surface (illustrated by the sequence of 5 states) and then touches the workpiece at the same angular position, where flattening occurs due to wear. The flattening at the area of impact acts like an unbalance mass added 180° away and results in an increase in vibration amplitude. The scenario repeats and the next impact, shown in view (3), results in an amount of wear on the wheel as large as the vibro-impact amplitude (assuming for illustrative purposes that three impacts result in this amount of wear). At that instant, some other place on the disk starts touching. In views (4), (5) and (6), that place is simply assumed to be the adjacent angular position 150°. This is only one plausible explanation of how the wheel might wear down uniformly from R_1 to R_2 while it goes through an impact-cutting regime of material removal. To understand the dynamics of transitions in the angular position of cutting impacts and also the number of impacts per spindle revolution, methods of nonlinear analysis should be employed to replace the concept explained in this section.

Within the scope of this chapter, an experimental methodology is developed to capture the impacting oscillations during material removal (impact cutting) in real practice. Angular analysis is performed to reveal the cyclic nature of the transients in such process.

2.3 Test Setup and Material

Figure 2.6 shows the test setup used for the experiments presented in this chapter. A SCOMPI robot holds a grinder, mounted with the grinding wheel normal to the workpiece plane. The grinder is moved along the feed direction over the plate, with a vertical infeed of $5mm$ so as to grind the entire workpiece surface. The experiments are performed at different rotational frequencies ω. Average normal force F_m is maintained around $100N$ in all experiments by adjusting the target grinding power P in the robot's control system. In the control system of SCOMPI, an estimate of the grinding mechanical power is obtained based on the current, rotational speed and temperature of the electric grinder and considering the power losses (Tahvilian et al., 2013). The grinding mechanical power delivered to the spindle is regulated versus the target grinding power. Normal force and grinding power are related as:

$$P = \mu F_m R_{0,m} \omega \tag{2.4}$$

where μ is an empirical friction coefficient, which is estimated around 0.3 by measuring the average normal and tangential grinding forces, and $R_{0,m} = 113mm$ is the measured disk radius.

The setup is equipped with an IDT high-speed digital camera of the Y4 series with a CMOS sensor. The camera is capable of capturing 1-megapixel video images at up to $5{,}100fps$. Three $750W$ halogen lamps rated at $17{,}000$ lumens fitted inside 7-inch Fresnel lenses are used for lighting. Lights are powered by a 3-phase electric source to avoid $60Hz$ variation of light intensity and thus focus enough continuous light on the cutting zone. An angular marking is attached to the grinding wheel so that in the video captures of the grinding operation, it will be easier to identify the instants were material removal is being performed.

2.3.1 Angular Sampling and Measurement of Instantaneous Rotational Frequency

A DT9836 data acquisition card capable of receiving an external trigger source is used for the measurement of vibration and instantaneous angular speed signals. The purpose is to acquire samples of data on the basis of a trigger source which is synchronized with the angular displacements of the grinder's shaft during revolutions (angular sampling). Measured data samples will be then correlated to precise angular positions of the shaft which is reproducible at each revolution. This enables us to track the instantaneous cutting process in the angular domain and investigate the dynamics that govern the interruptions of the cutting process.

The grinder is specially equipped with an angular optical encoder attached to the grinder shaft. Output of the optical encoder, i.e. the 1000 square-wave pulses per revolution, is used as the external clock for the data acquisition system. Resolution of the encoder is divided by two to reduce the number of samples acquired per revolution. Eventually, 500 square-wave pulses are generated at equidistant angular displacements of the spindle during each revolution within the grinding operation. This signal is used as the trigger source for data acquisition on all channels. The measurement channels include tri-axial vibrations from an accelerometer and the speed signal from the rotary encoder. Samples of data will be then captured in the angular domain rather than in the time domain, simply meaning on constant intervals of angle rather than on constant intervals of time. Due to using this method, sections of $n = 500$ samples in the acquired signals will correspond to the revolution cycles of the machine. Thereupon, instead of representing the vibration and angular speed measurements versus time, these signals will be shown with respect to angular positions of the shaft or equivalently versus the revolution numbers of the spindle.

The encoder signal is also used to obtain the angular speed using the *elapsed time method*, by counting the number of pulses of a high-frequency clock between two encoder pulses (Li et al., 2005). The method is based on measuring the elapsed time between the rising edges of a square-wave pulse that is generated synchronous with angular displacements of the rotating

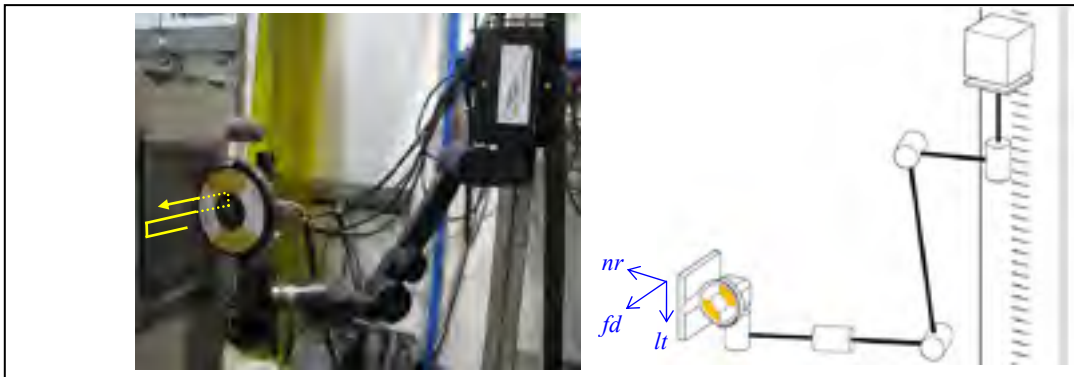

(a) Laboratory setup to perform traverse grinding with SCOMPI (fd : feed, nr : normal, lt : lateral)

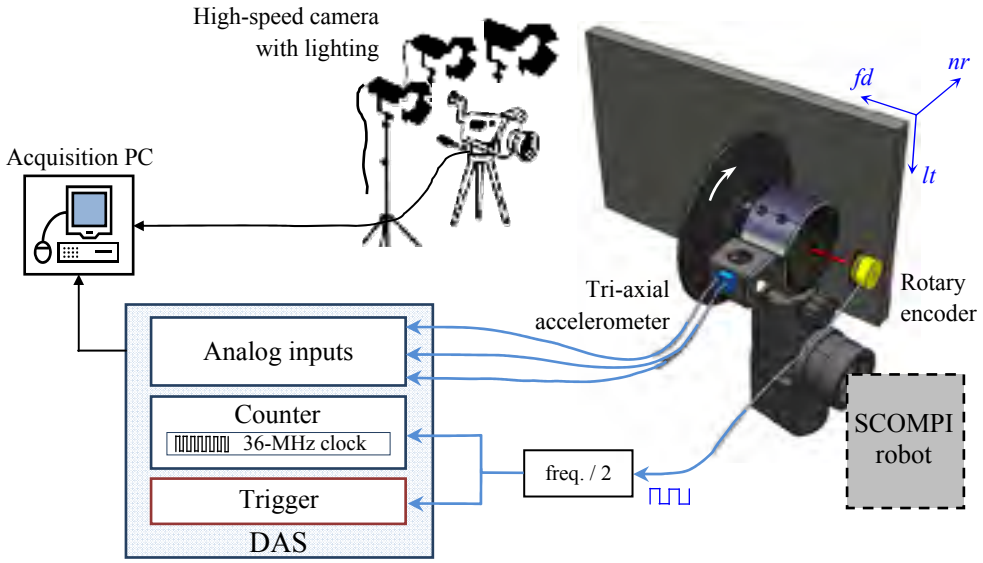

(b) Data acquisition system

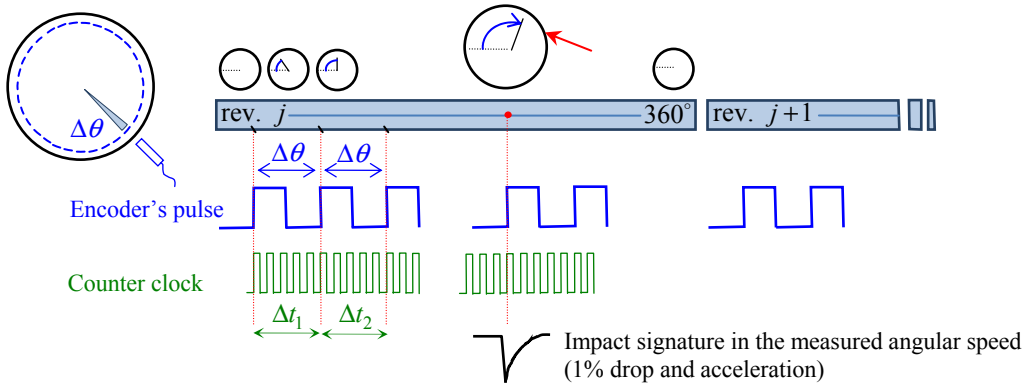

(c) Measurement of instantaneous angular speed and the angular sampling methodology

Figure 2.6 Test setup using the angular sampling technique

shaft. A square-wave pulse that is generated n times per revolution is in fact coding the angular speed of the shaft at these instants by its n pulse periods. The signal used for the

trigger source ($n = 500$) is used here once more. A counter available on the acquisition card uses a high frequency $f_{cl} = 36MHz$ clock to count the time between the rising edges of the square-wave pulses. An interrupt service routine resets the counter at each rising edge. Therefore, the instantaneous rotational frequency f at each instant can be calculated from the clock's count n_{cl} corresponding to a pulse period as,

$$f = \frac{f_{cl}}{n \cdot n_{cl}} \tag{2.5}$$

The main advantage of angular sampling is the ease of synchronous averaging, which is a powerful method to enhance the detection of cyclic phenomena in mechanical operations (Antoni et al., 2004; Braun, 1975). An intuitive description of a synchronous averaging process is that data samples separated by exact period are averaged. This results into attenuation of components which are not synchronous with this period while periodic components, synchronous with this period, remain unchanged. A *running synchronous (angular domain) average* (Braun, 2011) is used in this study since data samples are acquired in the angular domain rather than the time domain. The averaging procedure is expressed by the following equation:

$$S_f(\theta_{j,i}) = \frac{1}{m} \sum_{c=i-m+1}^{i} S(\theta_{j,c}) \tag{2.6}$$

where $S_f(\theta_{j,i})$ is the filtered signal for the sample at position θ_j of revolution i, and m is the length of the filter. $S(\theta_{j,c})$ is the sample of the measured signal at position θ_j of revolution c. Measurement of instantaneous angular speed and the angular sampling methodology is schematically shown in Figure 2.6.c. For the experiments presented in this chapter, angular speed is analyzed to detect cyclic oscillations of the grinding wheel during material removal. As shown in Figure 2.6.c, a signature of cutting impacts in the measured rotational frequency is expected as a fast drop and acceleration which repeats on the basis of the revolution cycle. The advantage of using the angular sampling technique is that measurement samples and thus the impact signature can be correlated to a precise angular position during each revolution cycle. Vibration signals and high-speed camera images are

used to substantiate the behavior of the robot estimated from angular speed observations. The equipment used for these experiments are listed in Table 2-1.

Table 2-1 Equipment used to perform Tests (1-7)

Equipment	**Specifications**	**Accessories**
B&K triaxial accelerometer, Type 4326	Sensitivity: $X = 0.341$; $Y = 0.326$ $Z = 0.319\ pC/ms^{-2}$	B&K charge amplifiers (3), Type 2635. $10\,mV/ms^{-2}$ output, $2Hz - 100kHz$ frequency range
QPhase optical encoder, Type QD145	TTL output, Resolution 1,000 lines per revolution	Frequency divider circuit
IDT high-speed digital camera, Y4 series	1-megapixel video images at up to 5,100 fps	$750W$ halogen lamps (3) rated at 17,000 lumens, 7-inch Fresnel lenses for continuous lighting, Acquisition PC
DT9836 data acquisition module	Sampling triggered by an external clock	Acquisition PC
Abrasive product	Cylindrical, self-dressing, aluminum oxide wheel with resin bonding (*NORZON III*)	
Grinding tool	Permanent magnet electrical grinders, $2kW$ and $2.5kW$	SCOMPI control system regulating grinding power
Tool holder	SCOMPI robot, 6-DOF	
Workpiece material	$300\times300\times25mm$ plates (A36 steel)	

2.4 Evaluation of the Experimental Methodology

The test setup described in the previous section is designed to detect and locate the discrete cutting events of an impacting nature in robotic grinding. Prior to testing the approach in real practice, experiments were conducted in which cutting impacts at a given angular position of the grinding disk were certain. This checks the capability of the setup to detect high-frequency repeating impacts before taking the next step and trying it in real robotic grinding experiments.

A typical grinding disk was shaped with water cutting to have a bump about 5 *mm* high as shown in Figure 2.7. The height was selected to be about one order of magnitude larger than the typical measured vibration amplitude at the rotational frequency in grinding experiments. This was to ensure that a grinding experiment with this disk would involve impacts between the wheel and the workpiece at this angular position. A balancing protrusion (difficult to see

in Figure 2.7) was also made 180° away from the bump to satisfy the plane balance. The disk was covered with angle markings highlighting the bump in red. The circumference of the disk was painted white to track the angular positions where the disk touches the workpiece during grinding. Parameters of the robotic grinding task performed using the disk with a bump are listed in Table 2-2.

Table 2-2 Robotic grinding test with an imposed impact-cutting behavior

Test	Grinding power $P(W)$	Nominal speed $\Omega(rpm)$	Feed speed $v_{fd}(mm/s)$	Disk	Grinder	Task
(1)	2000	6000	60	*NORZON III* (shaped to have a bump)	*2kW*	Single-pass grinding

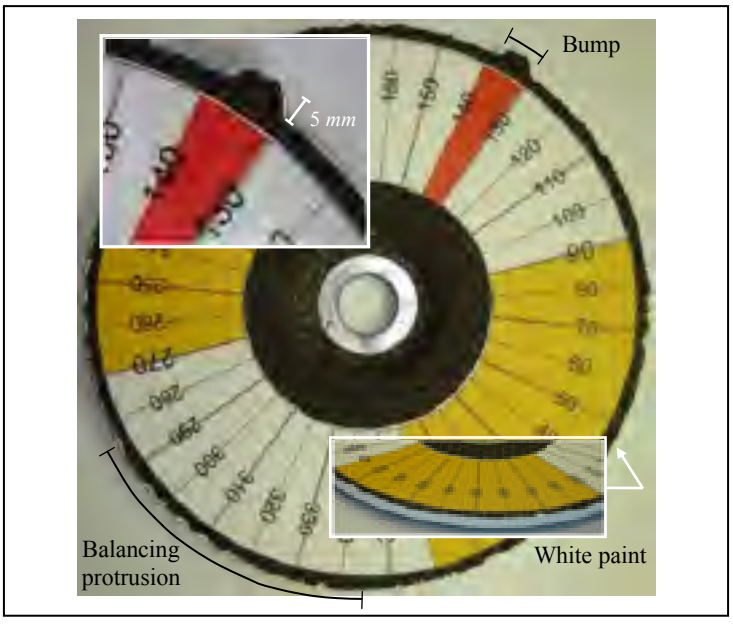

Figure 2.7 Disk with angle markings, bump, balancing protrusion and edge painted white

2.4.1 Paint Removal

The bump on the disk was completely worn down in this test. The painted edge of the disk was showing that the disk has touched the workpiece surface at the angular position of the bump as well as other places around. First the pattern of the paint removed around the circumference of the disk after grinding was checked. Figure 2.8 shows that the paint was totally untouched at about half of the angular positions around the wheel's circumference. This clearly illustrates the non-continuous nature of the cut. Moreover, it strongly suggests that interruptions are cyclic in the grinding period; otherwise, paint would have been removed almost everywhere. Based on the pattern of paint removed, it may be concluded that impact cutting with two impacts per revolution has taken place. A phase difference of about 220° is seen between the average angular positions of the cyclic cutting impacts.

2.4.2 High-speed Camera Observations

The high-speed video recorded from just before beginning the grinding task is shown in Figure 2.9 (see the supplementary material to play the video). Grinding starts by impacts between the bump and workpiece material. Cutting impacts take place at the angular position in red on the disk. When the task begins, there are times when the wheel bounces off the

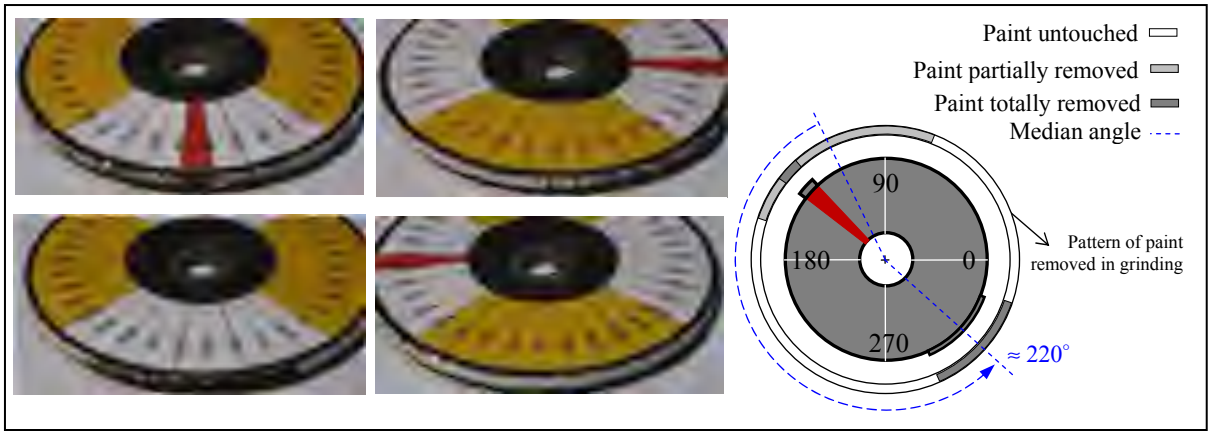

Figure 2.8 Paint removal after single-pass robotic grinding

Figure 2.9 High-speed video (2500 *fps*) of imposed cutting impacts (video available as supplementary material)

surface after a cutting impact and revolves several times before it touches the surface again. The robotic process follows a "seeking power" state at the onset of grinding. This means that after ramp-up to full nominal rotational speed and free rotations for a while, the robot moves the rotating disk toward the surface and seeks the initial contact, as measured by grinder power consumption. It then increases the amount of normal grinding force through displacement of its articulation until grinder power consumption reaches a threshold around $600W$, after which traverse grinding is launched by robot travel in the feed direction (see Figure 2.10). Cutting impacts in the seeking power state are then separated by several revolutions since the restoring force provided by the robotic holder has yet to reach its desired value. This is not a typical grinding task but it serves the purpose of verifying whether the test setup is capable of detecting high-frequency repeating impacts taking place at known angular positions.

The wearout of the bump takes place almost at the beginning of the seeking power state. The seeking power state, as shown in Figure 2.10, lasts about 200 revolutions (from revolution number 800 to 1000). Careful observation of the high speed video and counting the number of revolutions show that it takes about 60 revolutions (from revolution number 800 to 860) for the bump to wear out very quickly and then a new regime of impacting behavior starts. In this phase, which continues until the end of the task, impacts take place almost twice per revolution of the disk. They mainly occur once at the angular position of the balancing protrusion and a second time at an angular position adjacent to the bump, removed in the preceding phase. This pattern continues until near the end of the grinding task.

To summarize, the full-length video shows a major regime with one, two or zero impacts per revolution of the disk. Impacts start taking place one/zero times per revolution at the angular position of the bump until it wears down in a short time (see Phase 1 in the video presented by Figure 2.9). Then, a major regime of one/two/zero impacts per revolution begins at the angular position of either the balancing protrusion or adjacent to the bump (almost on the two white sectors of the disk, see Phase 2 in the video presented by Figure 2.9). These observations match very closely the pattern of paint removed (shown in Figure 2.8) and will now be compared to the speed and vibration measurements.

2.4.3 Angular Speed / Vibration Measurements

The overview of angular speed and vibration measurements in Figure 2.10 is detailed in Figure 2.11. Detailed views (a) and (b) show the angular speed and vibration measurements for about 180 revolutions at the beginning of the experiment. The peaks in the angular speed measurements and their equivalents in tri-axial vibration measurements correspond to the instants of initial impact between the bump on the disk and the workpiece material. They show that the discrete cutting events are well captured with the test setup. As detailed in view (c), cutting impacts are detected as a fast drop and gradual acceleration in the measured angular speed signal corresponding to accelerometer measurements showing impulsive responses. Cutting impacts around revolutions 920, 926, 931 and 936 are clearly visible in

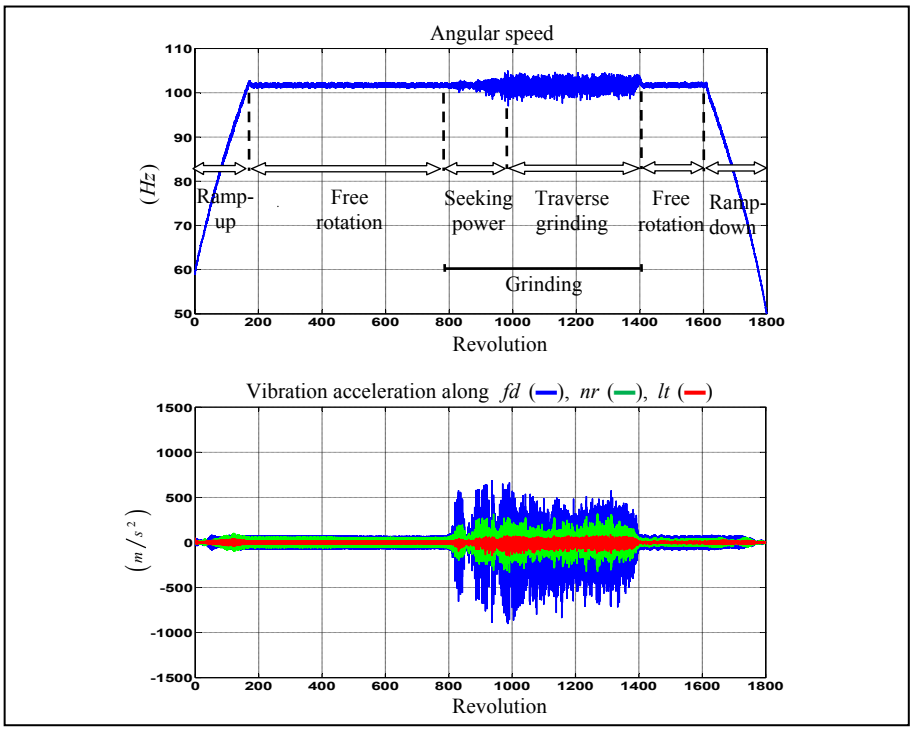

Figure 2.10 Triaxial vibrations (feed fd, normal nr, lateral lt) and rotational frequency in single-pass grinding (overview)

both detailed views (c) and (d). Interruptions of the cut for several revolutions between successive impacts in the seeking power phase, observed in the high-speed video, are also confirmed convincingly in detailed views (c) and (d). Inherent perturbations of the rotating grinder (e.g., unbalance) cause a harmonic response, as shown in detailed view (e), over which responses to cutting impacts are superimposed. The major challenge in this technique is to achieve high precision for the angular speed signal measurement shown in detailed view (f). The variation of about 1% in measured angular speed around its mean value is an unwanted phenomenon with several potential causes like the misalignment of the grinder's shaft with the external shaft on which the encoder is installed. The measurement precision achieved, about 1%, is very close to the target for detecting cutting impacts. Even the strong cutting impacts caused by the artificial bump and protrusion, shown in detailed view (c), could sometimes be masked with only this level of precision. Several tests were performed to find the probable sources limiting precision. It was found that alignment of the shaft of the

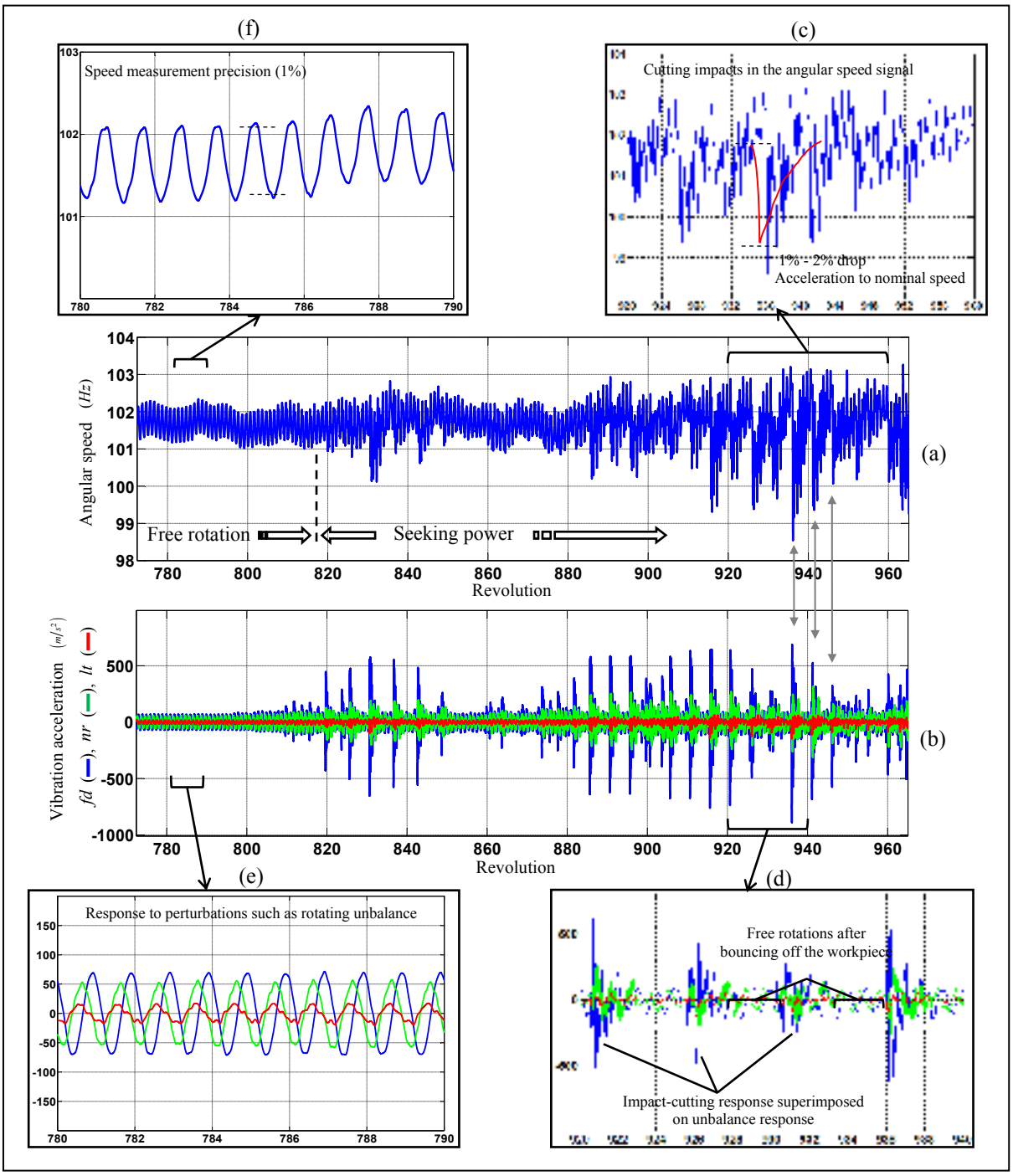

Figure 2.11 Detection of high-frequency repeating impacts in robotic grinding (detailed views)

external optical encoder with the grinder's shaft is the most probable factor limiting the precision of the readings.

2.4.4 Impact-cutting Map

The bump and the balancing protrusion in Test (1) are used to guarantee known angular positions for cutting impacts. The high-speed video taken during grinding and the pattern of paint removed, as explained in earlier sections, confirmed that cutting impacts occurred at the expected angular positions. In this section, the angular positions are again determined, now by processing the angular speed signal recorded during the test, as shown in Figure 2.10 and detailed in Figure 2.12. Using angular sampling methodology in data acquisition is of benefit since it is insensitive to variations of angular speed due to cutting impacts. Using the technique assures that $n = 500$ samples of data correspond to one revolution cycle. Moreover, the data samples are acquired by the trigger launched synchronously with the rising edges of the square-wave signal output from the encoder. These facts add an extra piece of information to the data plotted in Figure 2.10, i.e., the angular position of the wheel corresponding to each data sample. This information is lost in 2D representations and can be viewed only when the same data is mapped into 3D. The procedure to obtain such a map from the measured angular speed signal is summarized in Figure 2.12 with the help of three illustrations using the same data. Measured rotational frequency was low-pass filtered to suppress high-frequency oscillations irrelevant to the machine cycle. Furthermore, a running synchronous average filter of $m = 5$ cycles length was applied and removed most of the non-cyclic events from the signal. The result is what is shown as the instantaneous rotational frequency f in Figure 2.12.a. Revolution cycles 964, 965 and 966 are highlighted in the same colors in the three illustrations of Figure 2.12 to help follow the mapping procedure visually. Mean line variations in the average angular speed denoted by f_{ml} are also plotted in Figure 2.12.a over instantaneous variations. Figure 2.12.b-c show how using angular sampling helps in locating the angular position of the drops and accelerations in the speed signal. Samples of data $f^{j,i}$ in revolution i are acquired over equal angular increments ($\Delta\theta^1 = \Delta\theta^2 = \cdots = \Delta\theta^n$) rather than equal time increments ($\Delta t^1 \neq \Delta t^2 \neq \cdots \neq \Delta t^n$). Therefore, a given number of samples ($n = 500$) corresponding to one revolution can be reshaped into a

3D or color map representation like the one illustrated in Figure 2.12.c for the highlighted revolutions 964 to 966.

The reshaped data makes it possible to compare the dynamics of speed variation on the platform of a cycle that remains unchanged through machine operation. The cycles, being the 360° angular displacements of the disk laid next to one another, indicate whether the drops

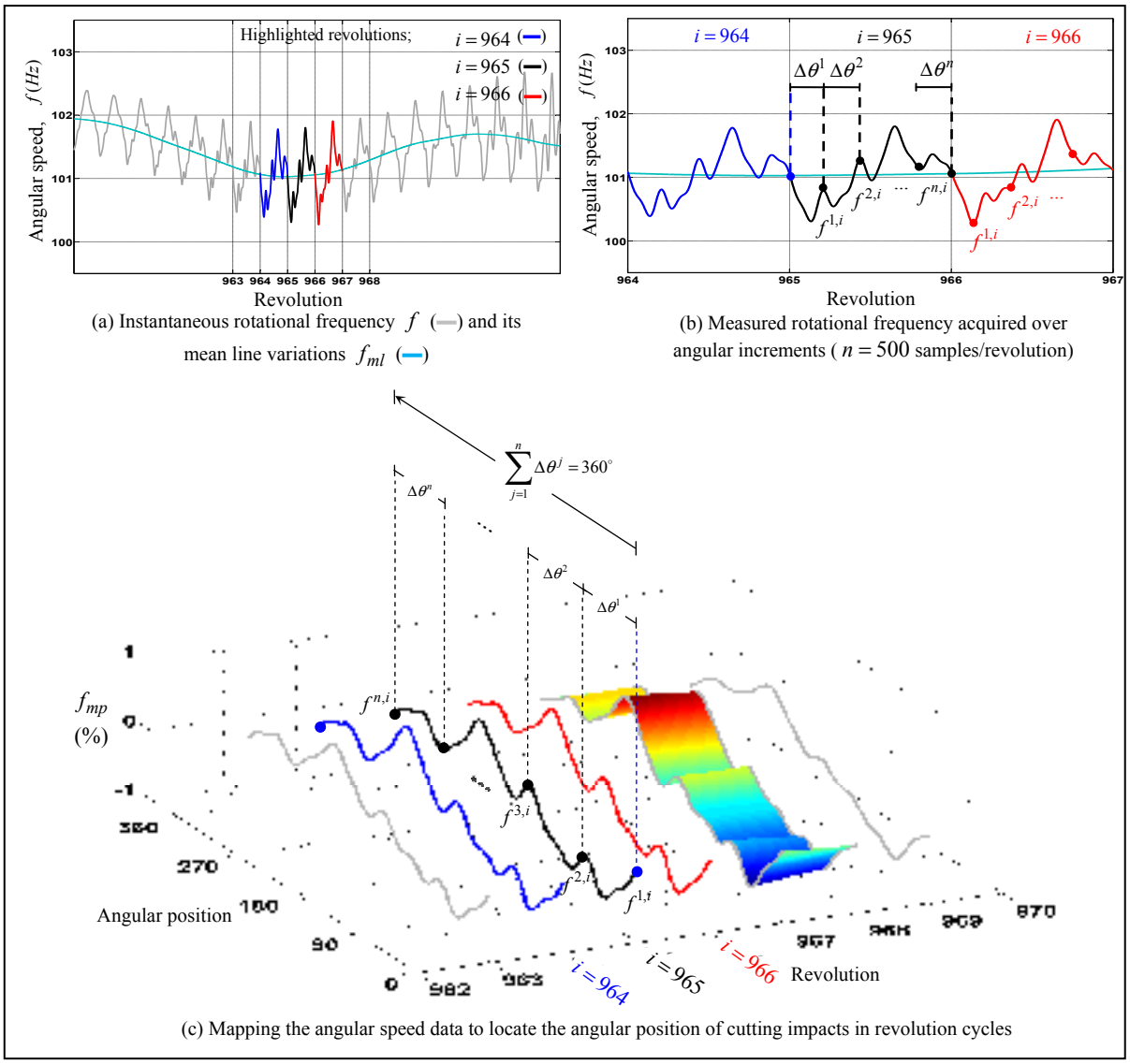

(a) Instantaneous rotational frequency f (—) and its mean line variations f_{ml} (—)

(b) Measured rotational frequency acquired over angular increments ($n = 500$ samples/revolution)

(c) Mapping the angular speed data to locate the angular position of cutting impacts in revolution cycles

Figure 2.12 Impact-cutting map from the speed signal

and accelerations in speed due to the discrete cutting events follow any regular pattern. Mean line variations of the speed, probably caused by the control system of the robot, and their effect are removed from this process by using the percentage of change when data samples are mapped into their new shape. The mapped rotational frequency is computed as the percentage change in the instantaneous rotational frequency from the mean line.

$$f_{mp}^{j,i} = \%f^{j,i} = \frac{f^{j,i} - f_{ml}^{j,i}}{f_{ml}^{j,i}} \times 100 \tag{2.7}$$

Figure 2.13 maps the angular speed data for revolutions 600 to 1500. This contains the grinding portion of the experiment with some free rotations before and after grinding. A major regime with almost two impacts per revolution appears clearly in the mapped data. This agrees perfectly with the high-speed video. Since mapping is done on data that is the cyclic average over 5 revolutions, those interruptions of the cut that lasted for about 3 to 5 revolutions (see Figure 2.11.d) are resolved into the revolutions with the impacting behavior.

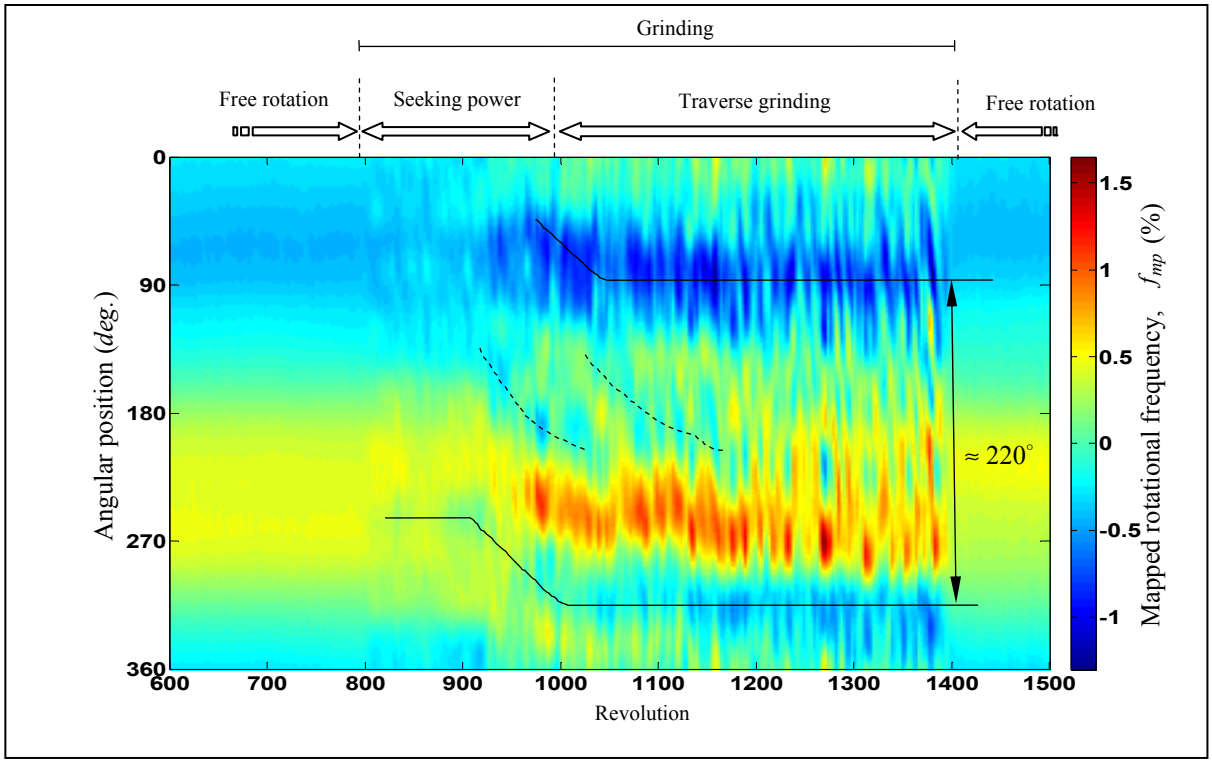

Figure 2.13 Impact-cutting map from the speed signal based on the experiment with the bump showing (—) a major regime of 2 impacts/revolution and (…) minor oscillations

The major impacting regime starts at 800 revolutions, corresponding to the impacts of the bump with the workpiece shown in Figure 2.10. Then, exactly as seen in the video represented by Figure 2.9, impacts start taking place adjacent to the angular position of the bump. In a short while, impacts reach their major regime of 2/revolution, once on the balancing protrusion and once adjacent to the bump. This behavior is also clearly visible in the map. Minor oscillations in Figure 2.13 are probably due to either small cutting impacts or measurement precision, as discussed earlier. Given current measurement system quality, it is difficult to distinguish between a probable minor impacting regime and oscillations caused by the measurement system. The phase difference of about 220° between the two impacts per revolution, which exists throughout the main portion of the grinding task, matches very closely the pattern of paint removed, as shown in Figure 2.8. This provides solid evidence that the setup and mapping tool are capable of locating the angular position of the high-frequency repeating impacts.

2.5 Robotic Grinding Experiments

The setup and the technique developed in the earlier sections of this chapter were used in real robotic grinding experiments with SCOMPI. Tests were performed at several nominal rotational speeds, as listed in Table 2-3, using the parameters of a typical field task. Grinding was performed in 2 passes, each 30 *cm* long to ensure that steady conditions are achieved. Testing was done at rotational speeds in the range of 4000-6500 *rpm* because SDOF dynamic analysis found the fundamental frequency of the impacting behavior to be at the rotational frequency.

Measurement of angular speed in these experiments has the following two main objectives:

- Firstly, to observe the dynamics of material removal in the operation under study in order to know whether the intermittent cutting operation performed by a flexible robot is of a cyclic impacting nature per revolution (impact-cutting behavior).

- Secondly, to learn how the angular position of cutting impacts changes while grinding. Cyclic impacts are discrete cutting events that result into local wear around the wheel. Unless the angular position of these cutting events moves around the wheel, uniform wheel wear, as evident from practice, may not be achieved. A plausible hypothetical mechanism was explained in Figure 2.5 and its existence is investigated in the experiments presented in this section.

Mechanical installation of the optical encoder was improved slightly in these experiments compared to Test (1) regarding the alignment of the shafts and the support of the encoder (see Figure 2.6). This improved measurement precision to about 0.3% was sufficient for what is to be detected in these experiments.

Table 2-3 Robotic grinding tests to investigate the impacting oscillations of material removal

Test	Grinding power $P(W)$	Nominal speed $\Omega(rpm)$	Feed speed $v_{fd}(mm/s)$	Disk	Grinder	Task
(2)	1477	4000	80	*NORZON III* (6.8*mm* width, 113*mm* radius)	2.5*kW*	2-pass grinding
(3)	1662	4500				
(4)	1846	5000				
(5)	2031	5500				
(6)	2215	6000				
(7)	2400	6500				

Figure 2.14 shows the measured rotational frequency in Test (2) performed at 4000 *rpm*. All tests include ramp up of the grinder to nominal speed, free rotations of the grinding disk as the robot approaches the workpiece surface, two grinding passes, free rotations while the robot draws the disk back from the surface and ramp down until the wheel stops rotating. The overview in Figure 2.14.a shows the measured angular speed over the complete sequence and a sample image from the two overlapping grinding passes. Detailed views over the two-pass grinding interval clearly indicate that material removal is performed through an impacting

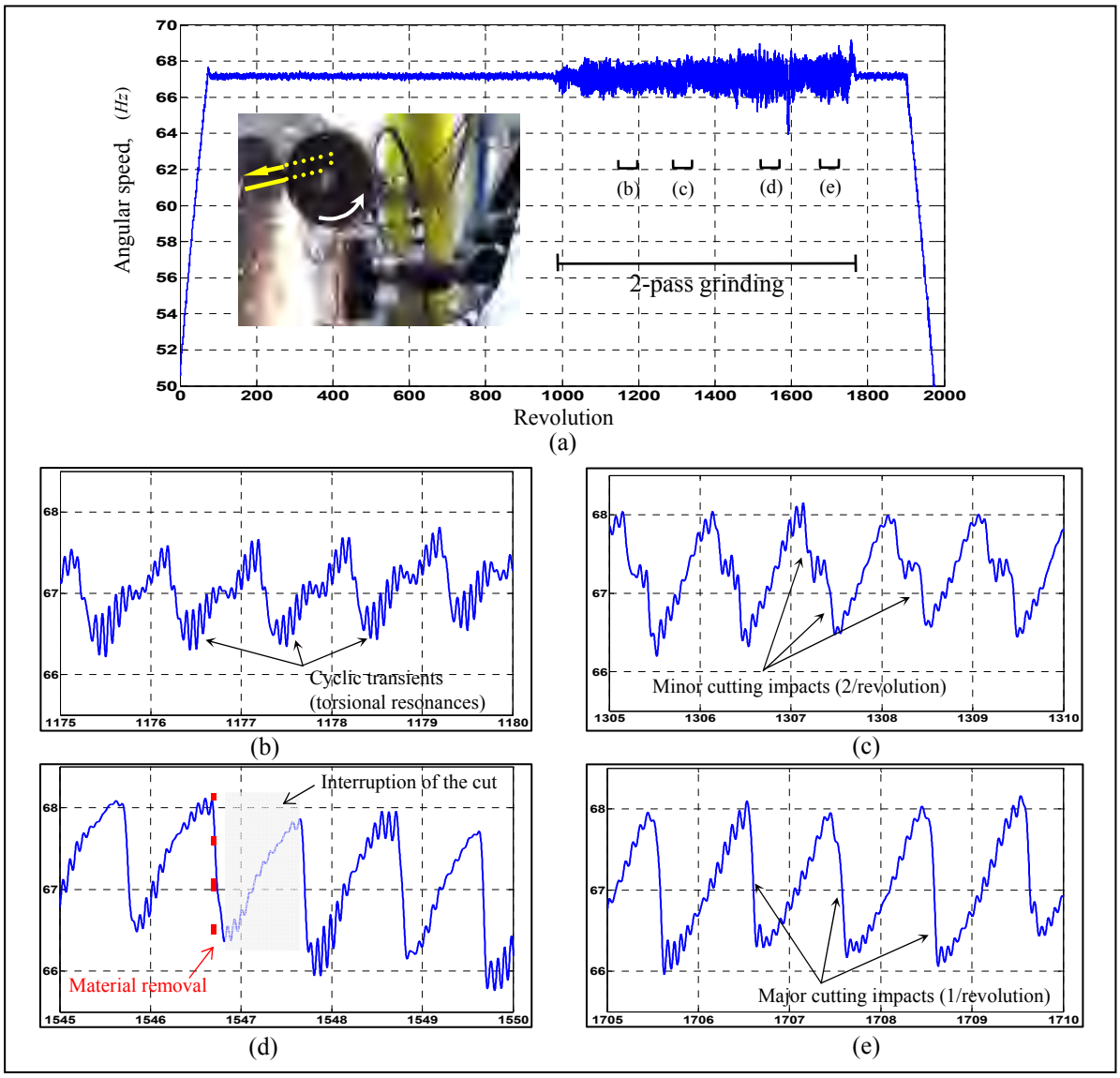

Figure 2.14 Discrete cutting events from rotational speed measurements in Test (2) at 4000 *rpm*

regime. A fast drop in speed corresponds to engagement of the disk with workpiece material as the torque caused by the cutting force has a rapid decelerating effect on rotational speed. Following the short interval of material removal, the wheel bounces off the surface and the cut is interrupted. As shown in Figure 2.14.d, the interruption period comprises the main portion of revolution cycles as the rotating disk accelerates to its nominal speed.

Figure 2.15 shows a similar behavior measured in Test (6), which is performed at 6000 *rpm* and is the practical rotational speed in disk grinding with SCOMPI. Cyclic impacts excite a system resonance which is found in the range of 800-900 *Hz* and is most probably the torsional resonance of the grinder's shaft. This is confirmed by several tests and a torsional dynamic model of the grinder which is under development through some internal research work. The system's response to impact-cutting excitations starts with the drop in angular speed during the interval of material removal and continues by resonance until the following cutting impact. These cyclic transients (see Figure 2.14.b-d) are unavoidable due to the vibro-impact dynamics governing the process. However, they provide a valuable source of information about the mechanical system and are very well captured using the test setup.

Figure 2.16 shows the impact-cutting maps plotted on the measured speed signal from Tests (2) to (7). The methodology used to create these maps was developed and verified in Test (1), i.e., the experiment performed using the disk with a bump and balancing protrusion (see Section 2.4.4). The so-called "impact-cutting map", derived from the measured rotational frequency, was capable of demonstrating the angular position of the discrete cutting events. These events occurred at known angular positions imposed by the shape of the disk. High-

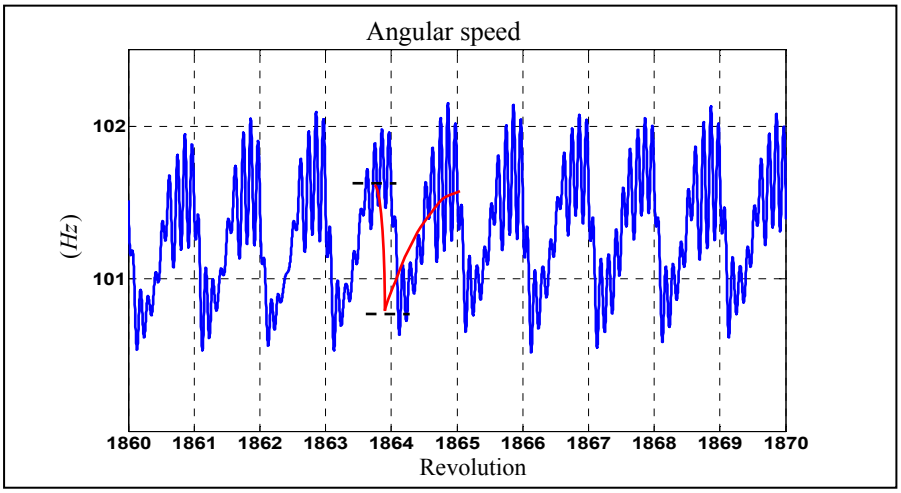

Figure 2.15 Discrete cutting events from rotational speed measurements in Test (6) at 6000 *rpm*

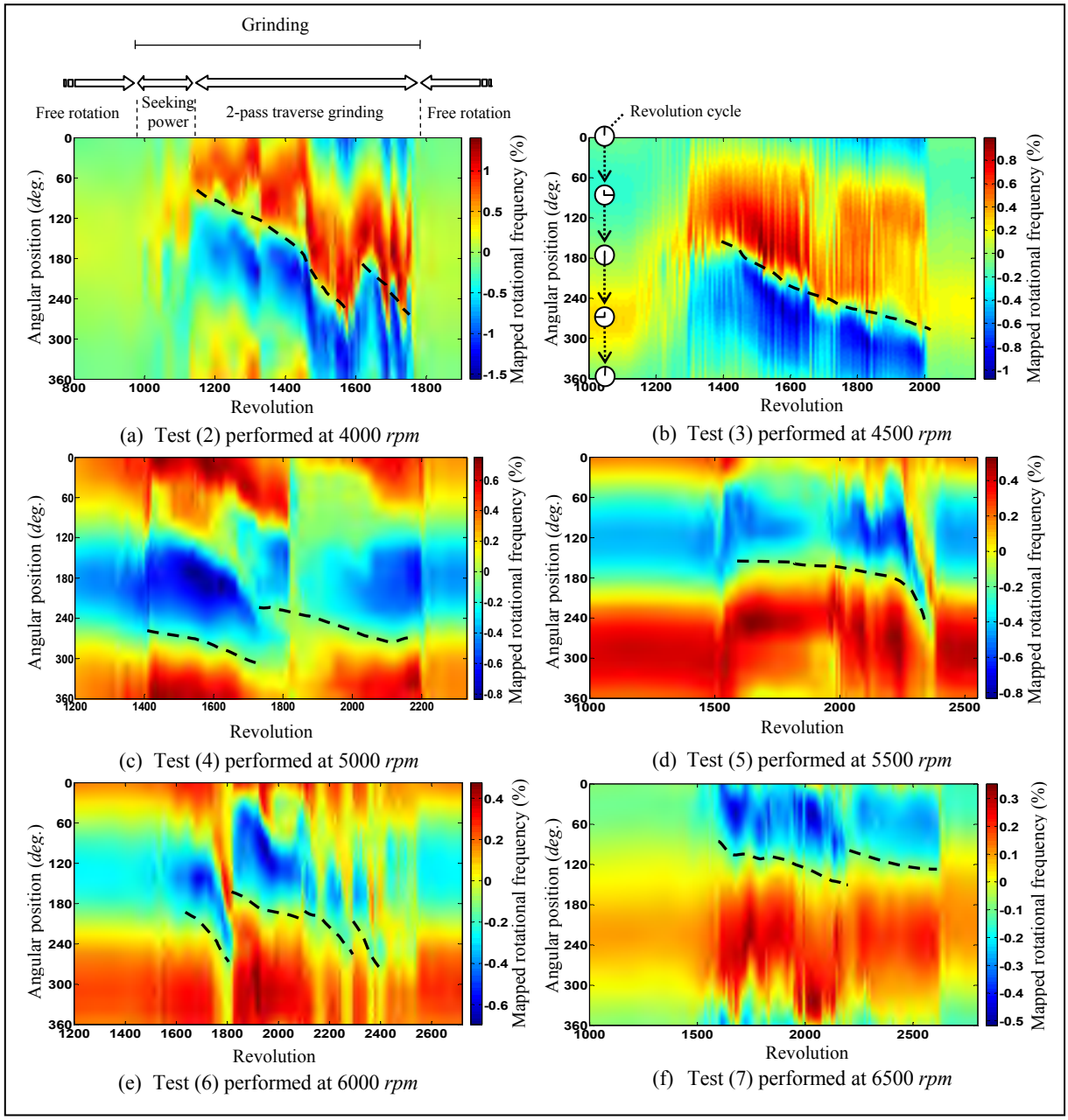

Figure 2.16 Impact-cutting maps showing the moving angular position of cutting impacts

speed video images and the pattern of paint removed provided solid evidence of the dynamic changes in these occurrences, which the map further confirmed. The tool is used in this section for typical robotic grinding experiments with a regular grinding disk. Revolution cycles of the disk during 2-pass grinding are plotted using color maps (see Figure 2.16.b).

The mapped color represents the percentage change in the measured angular speed with respect to the mean line. Maps are plotted on the speed signal low-pass filtered and averaged over $m = 5$ cycles. The major impacting regime of material removal taking place once per revolution is clearly visible from these maps. The maps, especially at the lower speeds of 4000 and 4500 *rpm*, show that the angular position of the cutting impacts moves around the circumference of the disk. This can be concluded given the inclined borderline between the blue and red regions in the maps. The line sweeps angular positions around the circumference of the disk. This indicates that the major deceleration-acceleration event due to cutting impacts has moved around the disk in a 2-pass grinding period (see the broken lines in Figure 2.16). This confirms the explanation proposed in Section 2.2.3 (see Figure 2.5) about how an impact-cutting regime of material removal might exist at the same time as the disk wears down uniformly.

Comparing the maps from different experiments suggests that at lower rotational speeds, the angular position of the cutting impacts moves more quickly around the wheel. For the two-pass grinding tasks illustrated in the maps of the experiments at 6000 and 6500 *rpm*, the position remained almost unchanged. One hypothesis that might explain this is that at lower rotational speeds, the wheel makes a larger advance per revolution while it is bouncing off the surface and when it contacts the surface again it removes a bigger chunk of material. Assuming that wheel wear is proportional to the amount of material removed, this means that at lower rotational speeds, local wear of the wheel at the impacting position is greater. Then, based on the mechanism explained in Section 2.2.3, the impacting position starts moving after fewer revolutions compared to higher speeds. This hypothesis must be investigated further once the setup is linked to sufficient computing power so that long grinding tasks can be monitored using this technique. Long-run experiments will also ensure that irregularities caused by the nature of the grinding process have similar effects across the tests being compared.

2.6 Correlation between Angular Speed Variation and Metal Removal

Cutting impacts excite several structural modes repeatedly. In general, resonating modes disturb the measurement system but are unavoidable. However, transient response to impact excitations could also be a source of information for system identification. For instance, the proposed test setup could capture these cyclic transients during the dynamic robotic grinding process and use this as feedback about the material removal process in order to fine-tune process parameters in real time. One useful source of feedback is the drop in angular speed caused by cutting impacts. It can be correlated to the amount of energy used for removing chips of metal through the impacting regime. The chart in Figure 2.18, a summary view of the maps in Figure 2.16, plots the percentage drop in angular speed measured during the major impacting regime for each test versus estimated values. The drop in angular speed in a test can be calculated based on an understanding of the physical process. The energy required to remove a chip of material through a cutting impact E_c is calculated considering the average grinding power P and the average number of impacts per turn n_c as,

$$E_c = \frac{2\pi P}{\bar{\omega} \cdot n_c} \tag{2.8}$$

where $\bar{\omega}(rad/s)$ is the mean line rotational frequency.

The rotational kinetic energy of the grinding disk E_r at this angular speed $\bar{\omega}$ is,

$$E_r = \frac{1}{2} \cdot J \cdot \bar{\omega}^2 \tag{2.9}$$

where J is the moment of inertia of the disk.

Rotational kinetic energy of the disk after each cutting impact decreases as a consequence of the drop in angular speed $\Delta\omega$ caused by the impact. Figure 2.17 shows a typical measurement of instantaneous angular speed together with its mean line variation from Test (3) performed at 4500 *rpm*. It is noted that the drop in speed caused by the cutting impact $\Delta\omega = 7\,rad/s$ is much smaller than both the maximum speed before the impact

$\omega_{\max} = 478\,rad/s$ and the average rotational frequency $\bar{\omega} = 475\,rad/s$. The variation in angular speed due to a cutting impact is about 1% of the mean speed. Since $\Delta\omega << \bar{\omega}$, the drop in rotational kinetic energy caused by $\Delta\omega$ is calculated by ignoring $\Delta\omega^2$ and assuming $\bar{\omega} \approx \omega_{\max}$ using the following equation:

$$\Delta E_r = \frac{1}{2} \cdot J \cdot \left[\omega_{\max}^2 - (\omega_{\max} - \Delta\omega)^2 \right] \approx J \cdot \bar{\omega} \cdot \Delta\omega \tag{2.10}$$

ΔE_r is the change in kinetic energy of the rotating disk and is equivalent to the energy consumed per cutting impact E_c from Equation (2.8) as,

$$J \cdot \bar{\omega} \cdot \Delta\omega = \frac{2\pi P}{\bar{\omega} \cdot n_c} \tag{2.11}$$

An estimate of the drop in angular speed per cutting impact is therefore given by,

$$\Delta\omega \approx \frac{2\pi}{J} \frac{P}{n_c \cdot \bar{\omega}^2} \tag{2.12}$$

The moment of inertia for the disk was calculated to be close to 0.0046 $kg \cdot m^2$. The number of impacts per revolution was selected as $n_c = 1.5$ to account for both the minor and major impacting regimes present in the experiments. Nominal rotational speeds and grinding power for Tests (2) to (7) were used as $\bar{\omega}$ and P in Equation (2.12). Calculated values of the drop in speed from Equation (2.12) are transformed into percentage values using the average angular speed of the corresponding experiment and are plotted versus the measured values in Figure 2.18. The measured values are read from the color bars of the impact-cutting maps in Figure 2.16. The small difference between measured and calculated values is because the measured values are read from the impact-cutting maps. The mapped speed signal, already filtered and averaged over 5 cycles, indicates smaller drops than the original signal. The close fit between the calculated and measured patterns shown in Figure 2.18 means that the experimental methodology described in this chapter is capable of detecting and characterizing the cyclic nature of the impact-cutting behavior at different rotational speeds. Moreover, the measured drop in angular speed correlates very well to the grinding power and is an indicator of the rate of material removal. The significance of this result is that the setup

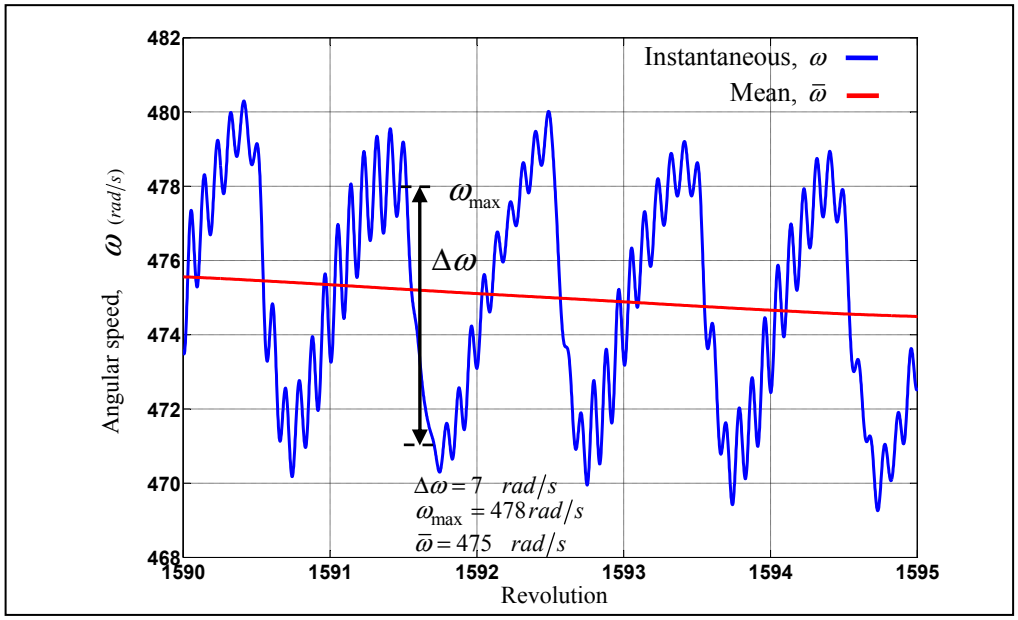

Figure 2.17 Typical values of $\bar{\omega}$, ω_{max} and $\Delta\omega$ during a cutting impact from measured rotational frequency in Test (3) at 4500 *rpm*

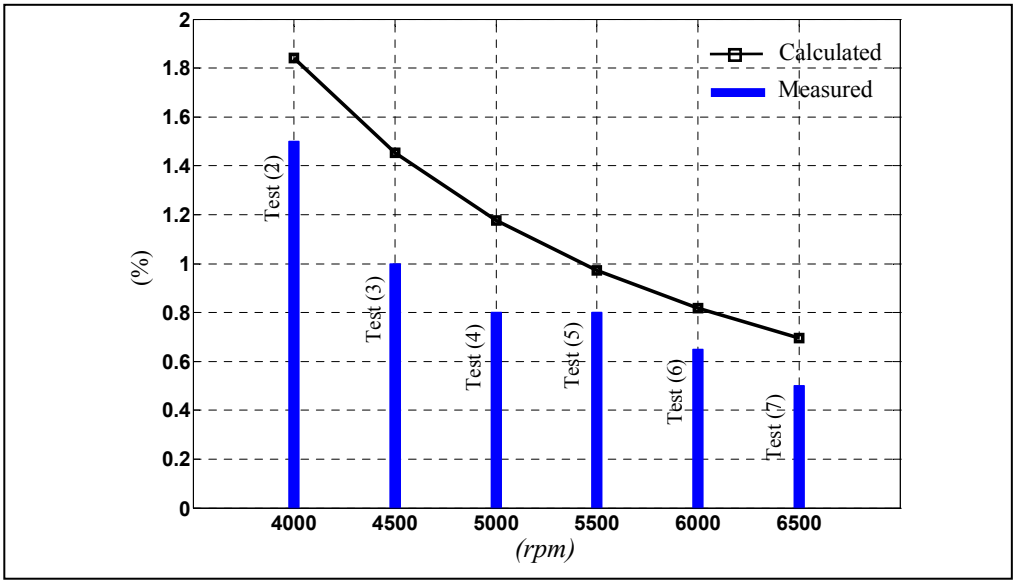

Figure 2.18 Percentage drop in speed during the impacting regime for the tests listed in Table 2-3

provides ongoing measurements of this transient at each revolution cycle. SCOMPI's control strategy, which is based on regulating the grinding power to control the material removal rate, could use this feedback to improve the robotic grinding task. Also, the number of

impacts per spindle revolutions can be extracted from this real-time measurement to be used in the control system for obtaining the instantaneous rate of metal removal during the task.

2.7 Summary

In this chapter, the instantaneous dynamics of the cutting process performed by a grinder robot was investigated experimentally. The vibratory behavior observed in experiments was substantiated with numerical simulation of a simplified SDOF dynamic model of the robotic grinding process. It was found that the *substantial compliance of the robotic holder makes robotic machining an interrupted cutting operation with cyclic impacting characteristics*. Dynamic analysis suggests that the discrete cutting events take place within a very short interval of the spindle period and for the rest of the revolution, the cut is interrupted. Material removal resembles a high-frequency impacting mechanism that repeats on a cyclic basis. An experimental approach was developed to detect and study the impacting dynamics of material removal (impact cutting).

The grinder was especially equipped with an optical rotary encoder. The encoder's signal was acquired using the angular sampling technique and a running cyclic synchronous average was applied to remove the non-cyclic contents from it. Measured instantaneous rotational frequency of the spindle confirmed the existence of an impact-cutting operation taking place mainly once per spindle revolution.

Data acquired on the angular basis was mapped into a representation where revolutions during a robotic grinding experiment could be compared regarding the angular position of the cutting impacts. It was found that the impact position moves around the wheel as was expected from an understanding of the dynamics involved. A plausible hypothesis for *uniform disk wear in presence of the impact-cutting material removal process was verified experimentally*.

The developed experimental methodology was proved capable of capturing the instantaneous variation in the spindle's angular speed during each cutting impact. *The measured drop in angular speed was very well correlated to the grinding power which can be an indicator of the material removal rate.* The setup can provide ongoing measurements of this transient at each revolution cycle. Practical significance of this result is that such information can be fed back into the robot control strategy as an instantaneous measure of the rate of material removal in order to optimize the iterative robotic grinding procedure. To this aim, an appropriate model of the process is needed which formulates the grinding power based on task parameters and the rate of material removal under the impacting oscillations of the cutter.

Impact-cutting model for material removal together with experimental verifications are addressed in the next chapter.

CHAPTER 3

Vibro-impact Dynamics of Material Removal in Robotic Grinding

3.1 Introduction

The accuracy of machine tools must be greater than the tolerances of the manufactured parts. The tolerance of machined parts, or equivalently, the precision of the machine tool is affected by the positioning accuracy of the tool holder and the relative structural dynamic deformations between the cutting tool and the workpiece. When it comes to robotized machining though, dynamic deformations of the robotic tool holder structure are of much more concern as compared to the issue of positioning accuracy.

In industrial robotic tasks such as spot welding or material handling, an articulated multi-body arm holds an end effector while a path generation algorithm controls the displacement of the multi-body mechanism. The purpose is to reach the end-effector point at a series of previously taught positions located on the programmed trajectory (see Figure 3.1.a). Vibration responses of the system are excited by the displacement of the bodies or due to the low-force task being performed at the end-effector point. Vibration energy transfers mainly to the most compliant structural mode, which is the low-frequency mode correlated to the flexible articulations along the degrees of freedom. These transient vibrations damp out after some time and today's robots can reach their taught positions repeatedly with very small error values. However, positioning accuracy does not suffice when such a robot performs a *cut* along these taught points rather than just reaching them. A human arm with a cutter would require a ruler to cut along a line on a metal sheet since it is necessary to compensate for deviations caused by the contact forces. Cutting along a series of points using a robotic tool holder is not achieved simply by setting the cutter's end point to a series of positions

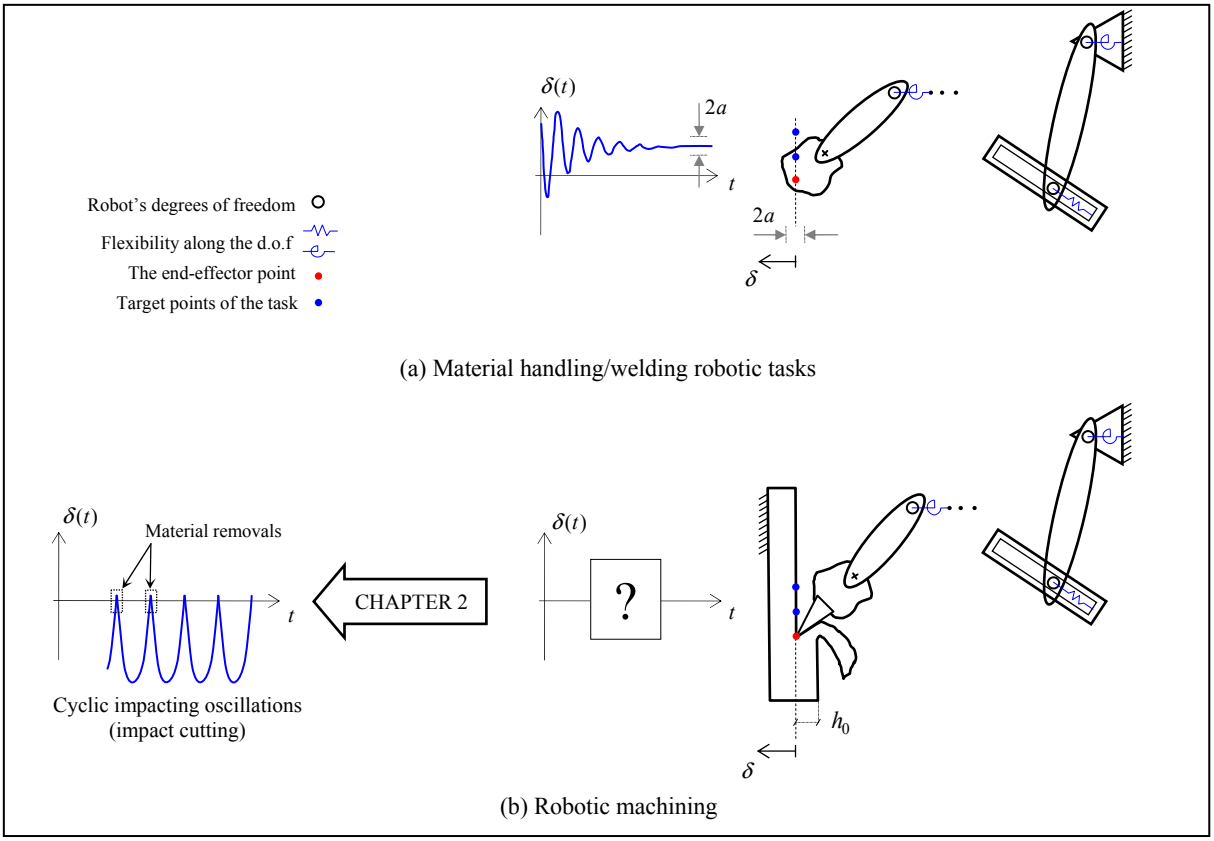

Figure 3.1 Vibration dynamics in an industrial robotic task

located at depth of cut h_0 (see Figure 3.1.b). The process that the robot performs to reach the surface of the workpiece is completely different from the cutting it must perform to remove material to depth h_0. Material removal largely depends upon the steady vibratory dynamics of the cut, a subject not well studied for robotic machining operations. The work presented in Chapter 2 revealed the steady vibrations (dynamic deformations) of the cut in the robotic grinding operation under study as cyclic impacting oscillations, i.e. the impact-cutting behavior (see Figure 3.1.b).

For heavy material removal tasks, cyclic interruptions of the cut become a sound behavior due to the large cutting force established inside the zone of contact. The few success stories reported in the literature on robotic grinding, polishing and deburring (Dai, Yuen and Elbestawi, 1993; Huang et al., 2002; Kunieda and Nakagawa, 1985; Lin and Lü, 2005; Liu,

Ulrich and Elbestawi, 1990; Ren, Kuhlenkötter and Müller, 2006; Takeuchi, Ge and Asakawa, 1993), cover tasks aimed at generating a glossy, smooth surface rather than heavy material removal tasks. The high-force task of machining is relatively neglected for robotic tool holders in the available literature on robotic developments. In the schematic shown in Figure 3.1.b, heavy material removal is equivalent to target points deep inside the material. An interactive dynamic procedure takes place due to the large cutting force which is required for deforming the chip out of metal. *Oscillations of the end-effector point are usually larger than the positioning accuracy of the robot or the required surface waviness*. Therefore, the control system cannot manage to remove the desired depth of material using the strategy of position control as done in CNC machining or robotic applications of welding and material handling. Instead, it needs a control strategy which can compensate for the deviations caused by the cutting forces. The robotic grinding operation used in this study employs the strategy of controlled material removal rate (CMRR) coupled with a measurement system for this purpose (Hazel et al., 2012b). The required depth of cut for the target profile is derived from an initial measurement on the surface. During the cutting operation performed by the robot arm, a controlled force is applied in the normal direction. To control the depth of cut, a model is used to relate the material removal rate to controllable process variables such as force or power. A modeling tool is used for this purpose which incorporates the vibratory dynamics of the process into its formulation. To remove a uniform depth of material, the robot needs to reach a series of points located on the cutter's end vibration trajectories, as opposed to points taught along the end-effector's motion trajectory. The work presented in this chapter aims at verifying if uniform cut with acceptable surface waviness is possible using the robotic grinding operation under study and in presence of high-amplitude vibratory oscillations in the process.

Cyclic interruptions of the cut are studied from the view angle of vibro-impact dynamics in Section 3.2 by drawing an analogy between the impacting oscillations of the cut and the generic classical impact pair. The objective is to substantiate, in a generic conceptual sense, the vibro-impact behavior which was explored in Chapter 2 for the robotic grinding process. Grinding force and power are then formulated based on the impacting dynamics of the cut

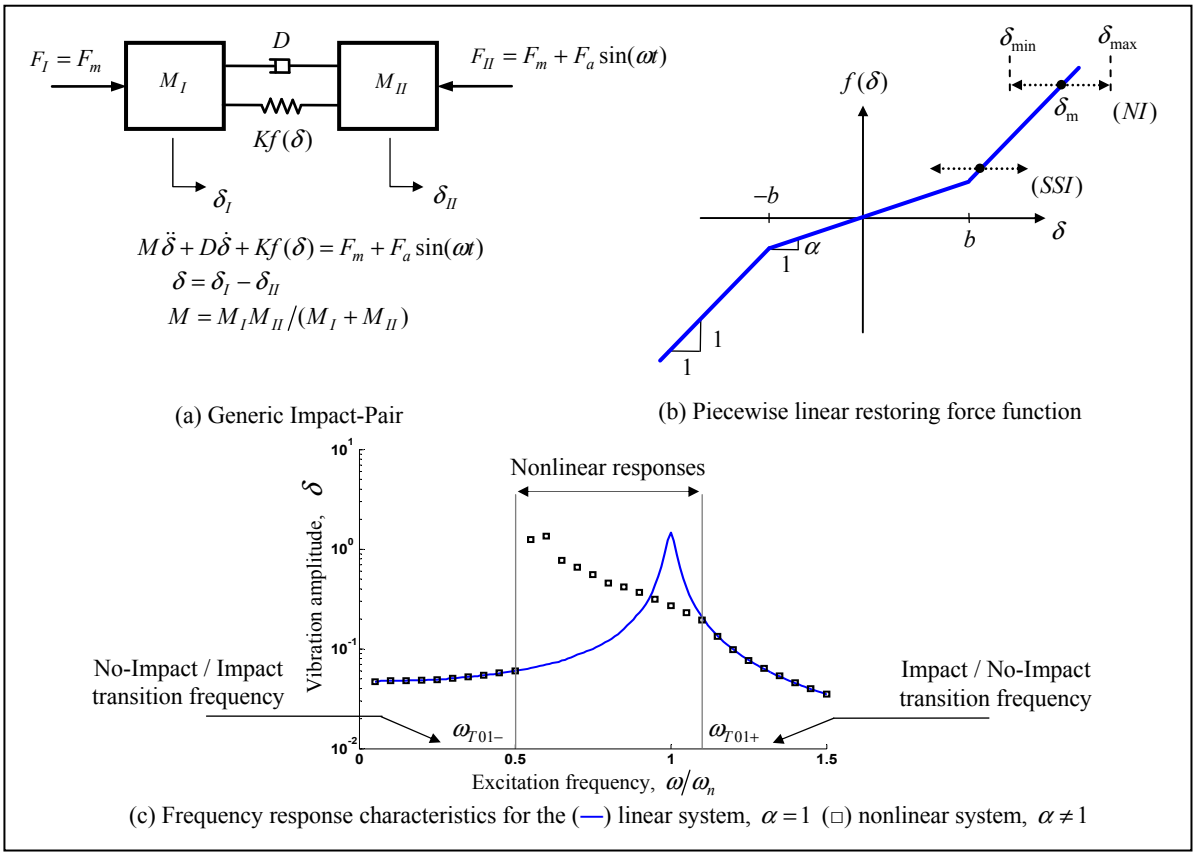

Figure 3.2 Vibro-impact dynamics adapted from (Comparin and Singh, 1989)

and task-related parameters in Section 3.3. The so called "impact-cutting" model for material removal, integrated into the robot control strategy, is then validated through several tests. The test setup which was initiated for the experiments presented in the previous chapter is further developed, as described in Section 3.4. The tests presented in this chapter provide further evidences from the impacting oscillations in the process and validate the impact-cutting model for material removal during robotic grinding experiments.

3.2 Nonlinear Frequency Response Characteristics

The experimental approach presented in the previous chapter allows detecting and characterizing the sequential impacts at the contact zone between the cutter's end and the

workpiece in robotic grinding. Impacts in the contact interfaces are a strong source of nonlinearity in structural dynamics. An extensive discussion on the existence and stability of vibro-impact responses is given by (Comparin and Singh, 1989) for the generic mechanical representation of an Impact-Pair (see Figure 3.2.a). The equations of motion for the IP are represented by two coupled non-linear second order differential equations. The system is semi-definite and therefore the number of degrees of freedom can be reduced by one. Two bodies, M_I and M_{II}, are held against one another by a mean force F_m. Alternating forces are modeled with a sinusoidal function as $F_a \sin(\omega t)$. The general form of the piecewise linear restoring force function $f(\delta)$ in Figure 3.2.b covers several possibilities for the contact dynamics of an operation under study. For example, $\alpha = 0$ covers a mechanical system with a dead-zone stiffness and $\alpha = 1$ corresponds to the classical linear vibration problem. Several possibilities for such a generic system are investigated and the frequency response characteristics of the nonlinear system are compared to the linear case. The study shows that oscillations of the two bodies relative to one another around the mean value δ_m and between $\delta_{\min}$ and $\delta_{\max}$ can exhibit a no-impact (*NI*) or single-sided-impact (*SSI*) behavior (see Figure 3.2.b) depending on system parameters. Vibro-impact responses are found as a characteristic behavior when looking at the frequency response function (FRF) of a nonlinear system ($\alpha \neq 1$). The region illustrated in Figure 3.2.c over the linear FRF is where the nonlinear system deviates from linear responses and exhibits impacting oscillations. For a given set of parameters, if the excitation frequency falls in a specific range ($\omega_{T01-} < \omega < \omega_{T01+}$), one impact occurs per cycle; otherwise, if either $\omega < \omega_{T01-}$ or $\omega > \omega_{T01+}$, the response is like that of the linear system with no impacts per cycle.

This section draws an analogy between the generic Impact-Pair and the SDOF model of our system (see Figure 2.1.e) to understand whether high-frequency repeating impacts between the grinding wheel and workpiece are inherent to the task under study. The piecewise linear restoring force function of Figure 2.3.c was replaced by a bilinear function for this analogy. Both edge and cutting forces (F_e and F_c) should then be accounted for by spring element

K_p. Instead of using Equation (2.2) to estimate process stiffness, the total normal cutting force in Equation (2.1) is then used and divided by the depth of cut.

$$K_p = \frac{F_N}{h_0} = \frac{F_e + F_c}{h_0} \tag{3.1}$$

Applying this simplified formulation for K_p, the SDOF dynamic model is numerically solved over a wide frequency range using two different restoring force functions (see Figure 3.3a). The linear function $f_{rstL}(\delta) = (k_t + K_p)\delta$ that represents continuous grinding with no interruption and a bilinear non-smooth function to simplify the piecewise linear $f_{rst}(\delta)$ in Equation (2.3) as,

$$f_{rstN}(\delta) = \begin{cases} K_p\delta & if \quad \delta \geq 0 \\ k_t\delta & if \quad \delta < 0 \end{cases} \tag{3.2}$$

where K_p is now determined using Equation (3.1) to account for both edge and cutting forces. System parameters are selected to resemble those of a typical robotic grinding task.

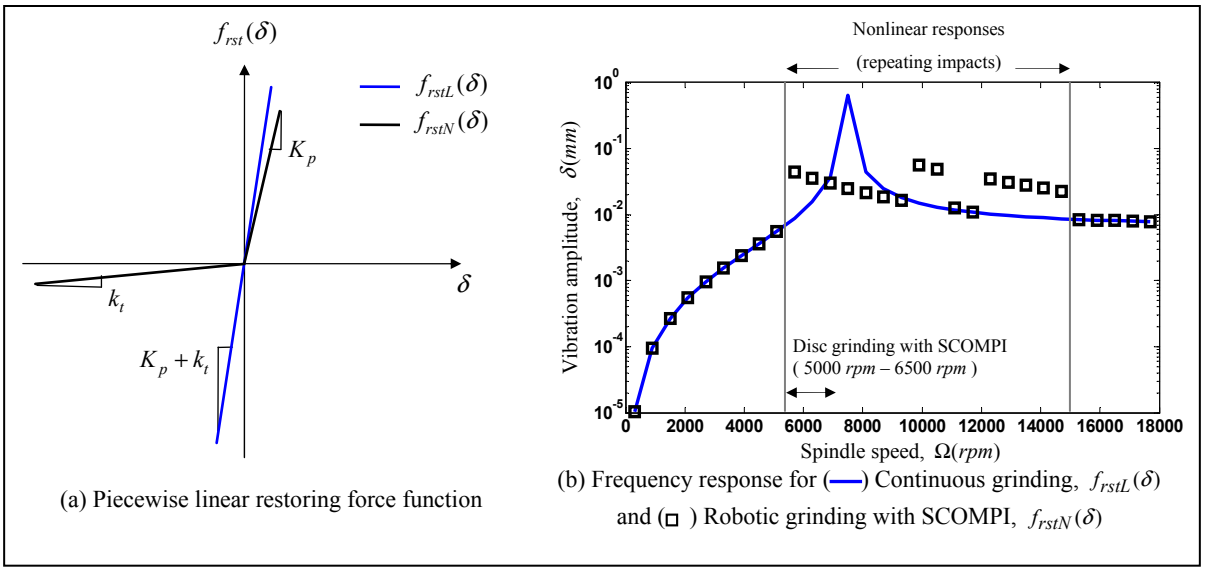

(a) Piecewise linear restoring force function

(b) Frequency response for (—) Continuous grinding, $f_{rstL}(\delta)$ and (□) Robotic grinding with SCOMPI, $f_{rstN}(\delta)$

Figure 3.3 Qualitative investigation of the permanent regime of material removal using typical parameters: $f_n = 6Hz$, $m_t = 33kg$, $k_t = m_t\omega_n^2 = 46.9\,kN/m$, $\xi = 0.1$, $\Delta l = 8mm$, $h_0 = 0.2mm$, $\varepsilon = 0.024\times10^{-3}\,mm$, $E = 6.8mm$, $m_u = 0.6kg$, $e = 0.5mm$, $\mu = 0.2744$, $k_e = 163\,kN/m$, $k_c = 4911\times10^3\,kN/m^2$

Proportional damping $c_t = 2m_t\xi\omega_n$ is assumed. The mean external force provided by the holding mechanism is approximated by $F_m = k_t\Delta l$. Removing material with the same chip thickness is considered at all rotational speeds. Runge-Kutta integration method with time step $dt = 1\times10^{-5}\,s$ is used to simulate the vibration response. The standard deviation of the response amplitude for both systems is plotted versus the excitation frequency in Figure 3.3.b. This frequency response gives a qualitative understanding of the dynamics governing grinding with a compliant arm as the holding mechanism. The frequency range of $5000rpm - 6500rpm$, which is the range of practice when grinding with 9-inch *NORZON III* wheels, falls in the range of vibro-impact responses for the non-smooth system governed by the nonlinear restoring force function. Grinding with the wheel is not possible at rotational speeds out of this range, wheel cohesive forces precluding higher speeds.

The qualitative analysis in this section suggests that the steady vibrations in robotic grinding *inherently* involve cyclic impacting oscillations. Continuous cutting would only occur if the cutter was held by a holder as stiff as the process, i.e., the linear case in Figure 3.3.a. The non-smooth nonlinearity in this system is an inescapable challenge that arises when machining includes an articulated open-chain multi-body structure, i.e., a robot arm. The robotic arm in the holder-grinder-wheel-workpiece chain is a highly compliant part, unlike the rest of the chain. The vibro-impact behavior in material removal is thus rooted in an inherent system property. The cutter's vibratory displacement during the interruption period of vibro-impact cycles, however, does not leave waviness on the ground surface because material removal is performed only during the small contact interval of vibro-impact cycles, i.e., during the cutting impacts. Even though the wheel bounces off the surface for a considerable amount, it touches the surface almost around the same height through successive cutting impacts and therefore the waviness amplitude left on the ground surface is small. Grinding power to be delivered at the spindle to remove material through the discrete cutting events of such an impacting regime should thus be calculated based on this understanding.

3.3 Impact Cutting Model

In the previous section, by means of a single degree of freedom model, cutting impacts once per revolution of the grinding wheel were found as the governing regime in the process of material removal when robotic grinding with SCOMPI. Mechanics of removing material through a cutting impact was first proposed in an earlier stage of the ongoing research (Hazel et al., 2012b) and is further explored in the current section of this chapter. The impact-cutting model for material removal formulates the force which is developed inside the cutting zone when an impact occurs. Grinding power is then established based on this model. The experimental section of this chapter will indicate the successful application of this model in robotic grinding tests to achieve acceptable waviness on the ground surface in presence of high-amplitude impacting oscillations.

3.3.1 Kinematics of a Cutting Impact

Traverse grinding groove geometry for a cylindrical grinding wheel performing a perpendicular cut on a flat plate is shown in Figure 3.4. Assuming a constant feed speed, v_{fd}, and volumetric metal removal rate, Z_w, one can calculate the target depth, h_0, width, w_0, and cross-sectional area, A_0 of the groove.

$$h_0 = R_0\left(1-\cos\left(\frac{\theta_0}{2}\right)\right) \approx \frac{R_0\theta_0^2}{8} \tag{3.3}$$

$$w_0 = 2R_0\sin\left(\frac{\theta_0}{2}\right) \tag{3.4}$$

$$A_0 = \frac{Z_w}{v_{fd}} \approx \frac{R_0^2\theta_0^3}{12} \tag{3.5}$$

R_0 is the radius of the wheel and θ_0 is the cutting angle both at the rear side ($x=0$) of the grinding wheel. Once steady-state grinding is in progress, both rear and front of the wheel start to wear out. We can then assume that a constant radial wear out of the wheel over its entire width, E, is maintained ($dR(x)/dt = const.$). Such an assumption would thus result in

a constant wheel profile, $p(x)$ for the steady state of the cut. Given a known wheel profile $p(x)$, groove's geometry can be expressed as functions of x along the width of the wheel (see Figure 3.4.b-c).

$$R(x) = R_0 - p(x) \tag{3.6}$$

$$\theta(x) = 2\cos^{-1}\left(1 - \frac{h(x)}{R(x)}\right) \tag{3.7}$$

$$h(x) = h_0 - p(x) \tag{3.8}$$

$$w(x) = 2R(x)\sin\left(\frac{\theta(x)}{2}\right) \tag{3.9}$$

Using the basic geometry of the groove we can consider two consecutive positions of the wheel separated by one revolution to find the chip of material removed during a cutting impact. It is the shaded area in Figure 3.5.a between the profile of the wheel in current and previous revolutions which is also demonstrated in 3D by Figure 3.5.b. To determine $p(x)$, we need to propose a model for wheel's local (along x) wear out as a function of the local metal removal rate. For a cylindrical grinding wheel of radius R_0, the rate of radial wear out, $\dot{R}$ can be expressed as a function of the volumetric wearout rate, Z_d for the wheel. The model is valid when the cut angle $\theta_0 = 2\sqrt{2h_0/R_0}$ is small and the advance per revolution of the wheel is much smaller than its width ($\Delta << E$). To determine $p(x)$, a model is proposed for wheel's local wear as a function of the local (along x) metal removal rate. For a cylindrical grinding wheel of radius R_0, the rate of radial wear, $\dot{R}$ can be expressed as a function of the volumetric wear rate, Z_d for the wheel.

$$\dot{R} = \frac{Z_d}{2\pi R_0 E} \tag{3.10}$$

To maintain a permanent regime for the cut, $\dot{R}$ should be constant over the width of the wheel and consequently Z_d should also be constant. Assume local wheel wear Z_d to be proportional to the local material removal rate Z_w. The profile of the wheel can then be found considering a constant material removal rate along the width of the wheel as follows.

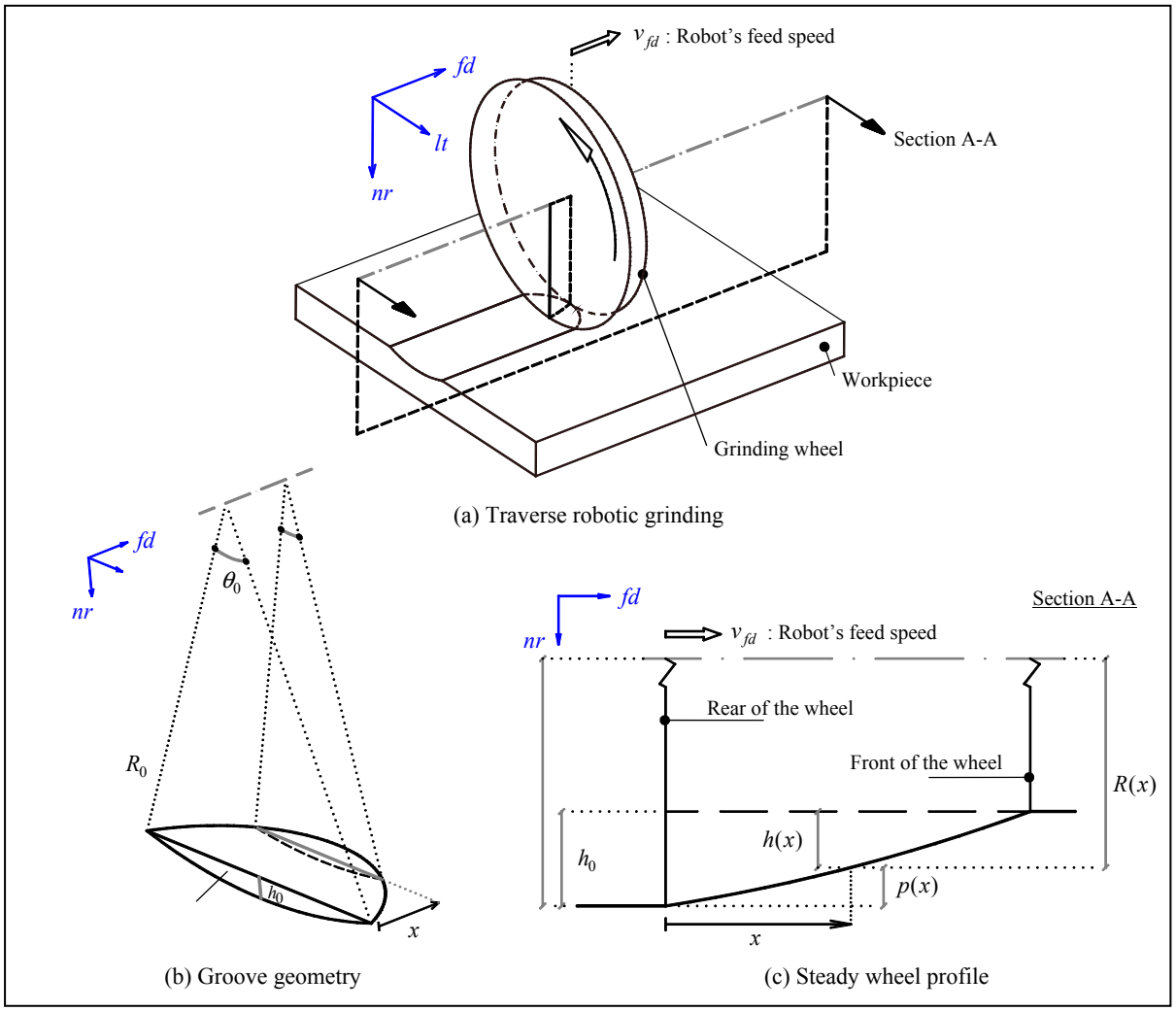

Figure 3.4 Kinematics of traverse robotic grinding adapted from (Hazel et al., 2012b)

The uncut chip can be considered as being composed of differential elements to be removed by individual grains (see Figure 3.6). A volumetric metal removal rate Z_w, for a constant feed speed v_{fd}, dictates the cross-sectional area of the groove to be $A_0 = Z_w / v_{fd}$. To distribute this rate of metal removal uniformly along the width of the wheel, we implement a constant 'cross-sectional area per unit width' for the differential elements of the cut. The elements having constant cross-sectional area will be therefore removing the same amount of material because they have the same width, dx. This will dictate the depth of cut $h(x)$, to increase as the cut angle $\theta(x)$ decreases throughout the elements. For each element, the

cross-sectional area per unit of its width can be written as $\frac{dh(x)}{dx}R(x)\theta(x)$ where $R(x)\theta(x)$ is the width of the element at x and $dh(x)R(x)\theta(x)$ gives the cross-sectional area of the element. For the uncut chip, this can be calculated as the cross-sectional area of the groove divided by the width of the wheel, $\frac{Z_w}{v_{fd}E}$. The following differential equation for the depth of the cut should then be maintained all over the width of the wheel.

$$\frac{dh(x)}{dx}R(x)\theta(x) = \frac{Z_w}{v_{fd}E} \tag{3.11}$$

As long as $\theta(x)$ is small and consequently $h(x) << R(x)$, one can approximate the length of the differential elements as $R(x)\theta(x) \approx R_0\theta(x)$. It ccan also be approximated considering the triangle of contact for each differential element. Width of the cut, the bottom side of this triangle, is equal to the element's length, $w(x) \approx 2\sqrt{R_0^2 - (R_0 - h(x))^2} \approx 2\sqrt{2R_0h(x)}$. Therefore, we can conclude.

$$R(x)\theta(x) \approx 2\sqrt{2R_0h(x)} \tag{3.12}$$

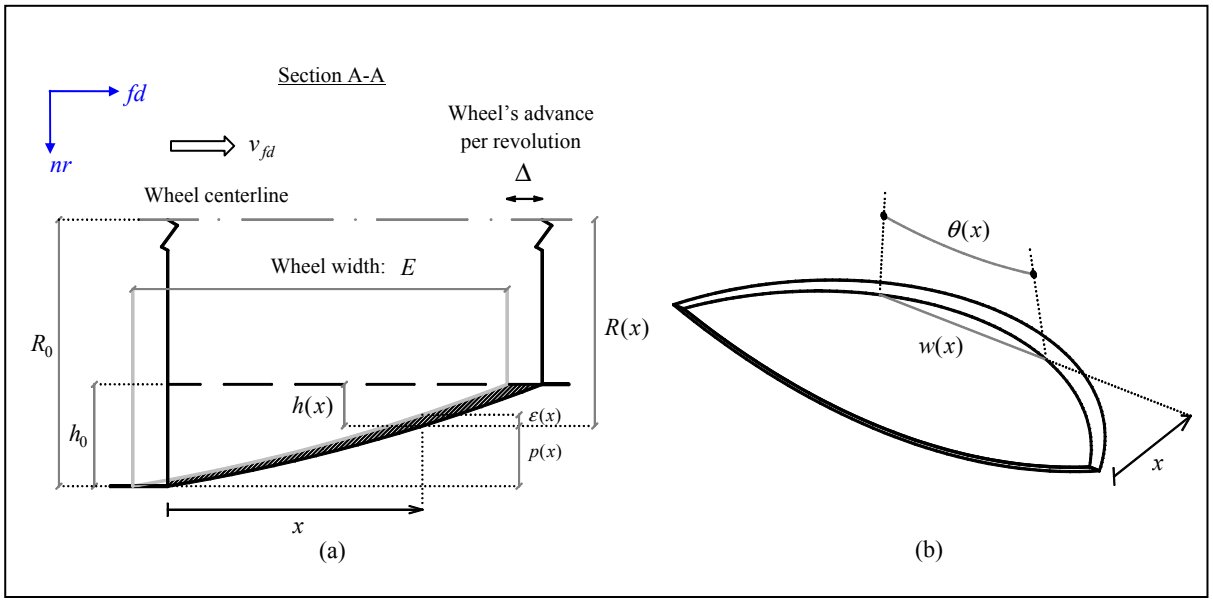

Figure 3.5 The uncut chip

Substituting this approximated length for the element into Equation (3.11), one can integrate this equation from $h(x)$ to $h(E)=0$ using the method of separation of variables.

$$\int_{h(x)}^{h(E)=0} 2\sqrt{2R_0 h(x)}\,dh = -\int_{x}^{x=E} \frac{Z_w}{v_{fd}E}\,dx \tag{3.13}$$

It therefore gives good approximation for the profile of the wheel under steady-state conditions as,

$$h(x) = h_0(1-x/E)^{2/3} \quad \text{where} \quad h_0 = \left(\frac{3}{4\sqrt{2R_0}}\frac{Z_w}{v_{fd}}\right)^{2/3},\ h(0)=h_0 \ \text{ and } \ h(E)=0 \tag{3.14}$$

With a rotational frequency $N(Hz)$ for the wheel, the advance it makes per revolution with a constant robot's feed speed v_{fd} will take $dx/v_{fd} = 1/N$ seconds to take place. Considering the chip thickness shown in Figure (3.6) as $\varepsilon(x) = h(x) - h(x+dx) = dh(x)$ and replacing it into Equation (3.11) where we were assuming constant chip cross-sectional area along x would result into the following equation after separating variables.

$$R(x)\theta(x)\varepsilon(x) = \left(\frac{Z_w}{v_{fd}E}\right)dx = \frac{Z_w}{EN} \tag{3.15}$$

In the above $R(x)\theta(x)$ is replaced using Equation (3.12) and the depth of cut from Equation (3.14). These will be all valid under the conditions of $\Delta \ll E$ and small $\theta(x)$. Equation (3.15) is then solved for the chip thickness to give,

$$\varepsilon(x) = \frac{Z_w}{2EN\sqrt{2R_0 h(x)}} = \frac{1}{EN}\left(\frac{Z_w^2 v_{fd}}{12R_0}\right)^{\frac{1}{3}}\left(1-\frac{x}{E}\right)^{-\frac{1}{3}} \tag{3.16}$$

Kinematics of the cut for traverse grinding with a robot was represented throughout this section. Depth and width of the cut, $h(x)$ and $w(x)$ and the chip thickness, $\varepsilon(x)$ were given as functions of the geometrical coordinate x along the width of the grinding wheel.

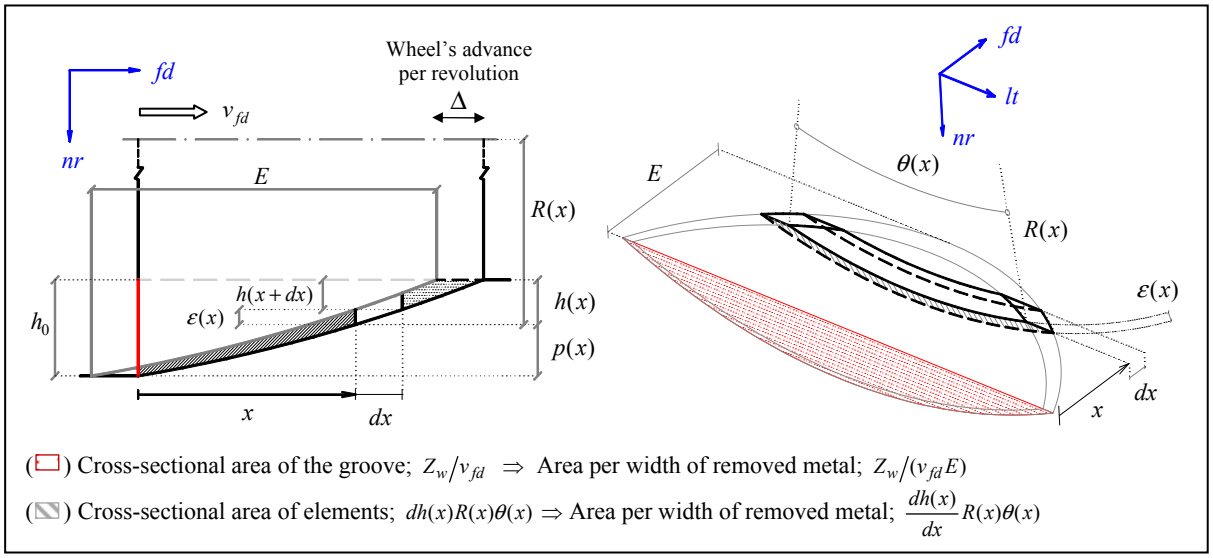

Figure 3.6 The uncut chip and differential elements

3.3.2 Impact-Cutting Dynamic Force Model

This section formulates the instantaneous cutting force required for removing the desired chip of material shown in Figure 3.5.b through a cutting impact. Using the kinematics developed in the previous section, an innovative approach is used to account for the impacting nature of the cut. It is assumed that the chip is removed by an imaginary notch as it progresses beneath the surface of material (see Figure 3.7). The notch starts immersing into material as soon as the wheel initiates the contact with the work piece once per revolution. The immersion of this notch will remove the material by exerting tangential cutting forces. The tangential cutting force is zero when the immersion is about to start ($\varphi = -\theta_0/2$). The very bottom of this immersion, where the imaginary notch is removing the maximum depth of material ($\varphi_2 = 0$), corresponds to the maximum cutting force during one complete revolution. The cutting force will then start descending from here after and gets back to zero when the wheel is about to bounce from the workpiece surface ($\varphi = +\theta_0/2$). Defining φ as the angular position of the grinder's shaft or the immersion angle of the notch, one can then represent x as the subsurface length of this notch. That will make x no more a time-

independent geometrical coordinate as before, but a variable which is a function of the angular position of the rotating grinding wheel. Then, for a subsurface length of x from the notch corresponding to the cut angle $\theta(x)$ and the immersion angle $\varphi(x)=\theta(x)/2$, one can use Equation (3.3) and express the depth of cut from Equation (3.14) as follows.

$$h(x)=\frac{R_0\varphi(x)^2}{2}=\frac{R_0\theta(x)^2}{8}=\left(\frac{3}{4\sqrt{2R_0}}\frac{Z_w}{v_{fd}}\left(1-\frac{x}{E}\right)\right)^{\frac{2}{3}} \tag{3.17}$$

From Equation (3.17), the length of the subsurface notch, x can be expressed as a function of the immersion angle, φ which makes the subsurface length also a function of time.

$$x(\varphi)=E\left(1-\frac{1}{12}R_0^2\frac{v_{fd}}{Z_w}\left|\theta(x)\right|^3\right)=E\left(1-\left|\frac{\varphi(x)}{\theta_0/2}\right|^3\right) \tag{3.18}$$

The subsurface length of notch is now expressed for any instant of time corresponding to an angular position, $\varphi=\Omega t$. Tangential cutting force can then be calculated at this instant considering the length and area of the cutting notch. A lateral force coefficient, $k_e(N/m)$ is multiplied by the subsurface length of the notch, and a cutting coefficient, $k_c(N/m^2)$ is multiplied by the area of the immersed notch to establish the instantaneous tangential cutting force equation as follows.

$$F_T(\varphi)=k_e x(\varphi)+\int_0^{x(\varphi)}k_c\varepsilon(x)dx \quad \text{for} \quad -\theta_0/2<\varphi(x)<+\theta_0/2 \tag{3.19}$$

Equation (3.19) can be evaluated considering Equations (3.16) and (3.18) by assuming $\theta_0/2\approx\sqrt{2h_0/R_0}$ to give the instantaneous tangential and normal cutting forces during one cutting impact.

$$F_T(\varphi,h_0)=\left[k_eE\left(1-\left|\frac{\varphi}{\sqrt{2h_0/R_0}}\right|^3\right)+k_c\frac{v_{fd}}{N}\left(h_0-\frac{R_0\varphi^2}{2}\right)\right]g(\varphi) \tag{3.20}$$

$$F_N(\varphi,h_0)=\frac{1}{\mu}F_T(\varphi,h_0) \tag{3.21}$$

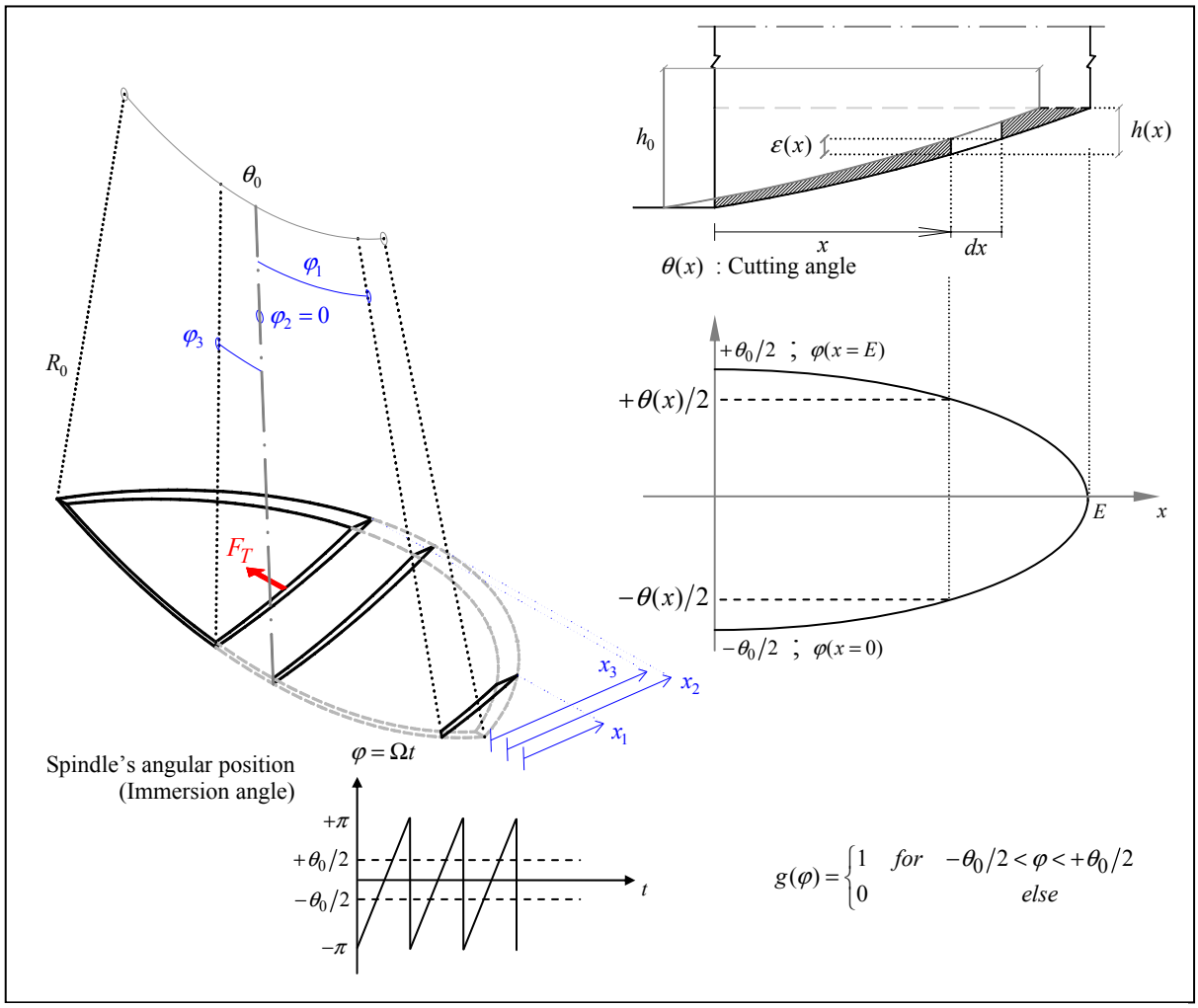

Figure 3.7 Impact cutting at a given angular position of the grinder shaft

in where $g(\varphi)$ is a windowing function to put the force to zero when the wheel is not in contact with the surface.

$$g(\varphi) = \begin{cases} 1 & for \quad -\sqrt{2h_0/R_0} < \varphi < \sqrt{2h_0/R_0} \\ 0 & else \end{cases} \tag{3.22}$$

E is the width of the wheel, h_0 is the target depth of cut, R_0 is the radius of the grinding wheel at its rear side, v_{fd} is the robot's feed speed, N (in hertz) is the rotational frequency, μ is the friction coefficient and φ is the immersion angle of the notch at any instant of time as illustrated in Figure 3.7. In Figure 3.8, typical parameters are used to plot the normal impact-cutting grinding force during one revolution of the grinding wheel versus its angular

position based on Equation (3.21). The edge and cutting force coefficients used for this figure is identified experimentally as will be explained in Section 3.4.4.

Average grinding forces along normal and tangential directions are obtained by integrating the impact-cutting force in Equations (3.20) and (3.21) over one cycle of steady-state response. The cycle is assumed to be one complete rotation of the grinding wheel based on the experimental observations in Chapter 2. This assumption was also justified by the qualitative study presented in this chapter about the vibro-impact dynamics present in the operation.

$$\bar{F}_T(h_0) = \frac{1}{2\pi}\int_0^{2\pi} F_T(\varphi, h_0) = \frac{1}{2\pi}\sqrt{\frac{h_0}{R_0}}\left(k_e \frac{3}{\sqrt{2}} E + k_c \frac{v_{fd}}{N}\frac{4\sqrt{2}}{3} h_0 \right) \tag{3.23}$$

$$\bar{F}_N(h_0) = \frac{1}{\mu}\bar{F}_T(h_0) \tag{3.24}$$

An intuitive check on the formulations obtained for the average grinding forces is to verify their trends with respect to the amount of removed metal. The surface and volume of the uncut chip are indicative measures of the required edge and shear forces respectively. The contact surface and volume of the uncut chip are estimated using the approximations in Equations (3.5), (3.3), (3.12) and (3.14) and by considering the wheel's advance per rotation $\Delta = v_{fd}/N$ as,

$$S_{chip} = \int_0^E \int_{-\theta(x)/2}^{+\theta(x)/2} R(x) d\varphi dx = \int_0^E R(x)\theta(x) dx = \frac{3}{\sqrt{2}} E\sqrt{R_0 h_0} \tag{3.25}$$

$$V_{chip} = A_0 \Delta = \frac{4\sqrt{2R_0 h_0}}{3}\frac{v_{fd}}{N} h_0 \tag{3.26}$$

Using Equations (3.25) and (3.26), one can express the average tangential or normal grinding force proportional to the contact surface and volume of the uncut chip as,

$$\bar{F}_N(h_0) = \frac{1}{2\pi\mu R_0}(k_e E S_{chip} + k_c V_{chip}) \tag{3.27}$$

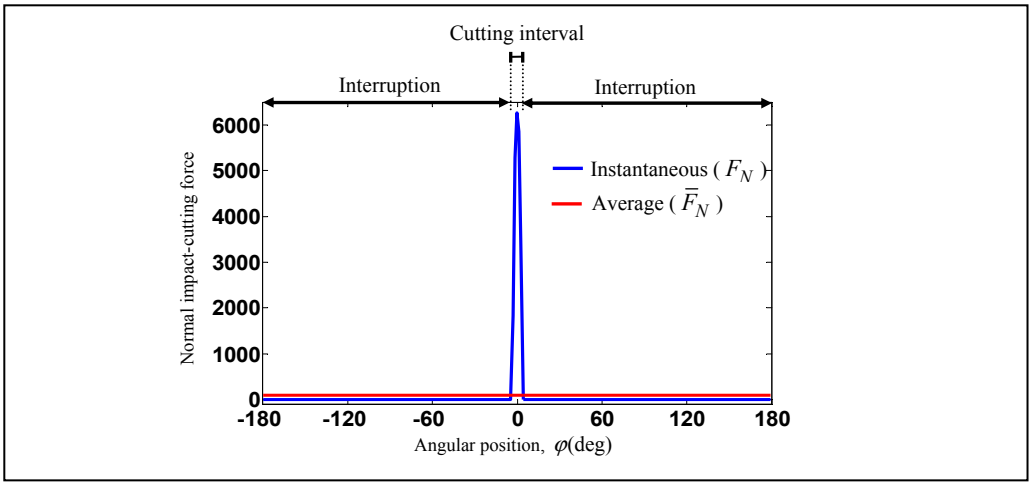

Figure 3.8 Instantaneous impact-cutting force $F_N(\varphi, h_0)$ and the average grinding force $\bar{F}_N(h_0)$ required to remove the uncut chip ($h_0 = 0.2mm$, $E = 7.6mm$, $R_0 = 100mm$, $\mu = 0.33$, $k_e = 163\,kN/m$, $k_c = 4911\times10^3\,kN/m^2$, $v_{fd} = 80\,mm/s$, $\Omega = 6000rpm$)

Equation (3.27) shows a reasonable trend between the amount of the material removed (contact surface and volume of the uncut chip) and the predicted cutting force which is established inside the cutting zone. In Figure 3.8, the average normal grinding force is plotted over its instantaneous value during one revolution of the wheel.

3.3.3 Grinding Power versus the Metal Removal Rate

The grinding power required to remove metal can be calculated using the average tangential grinding force multiplied by the wheel's peripheral speed $V_s = 2\pi R_0 N$. It can then be correlated to the material removal rate using the kinematics of the cut as follows:

$$P = k_e E N \frac{3}{4}\left(\frac{12R_0 Z_w}{v_{fd}}\right)^{\frac{1}{3}} + k_c Z_w \tag{3.28}$$

The formulated grinding force and power developed so far are for single grooves in a steady-state impact-cutting operation. The formulation can be extended to reciprocal (back-and-forth) traverse grinding where grooves are juxtaposed on a flat surface to profile large surface areas. Grinding power is then a function of infeed distance I, i.e., the distance between the

adjacent grooves juxtaposed to cover the entire workpiece surface. Details of derivation can be found in (Hazel et al., 2012b) and the final equation used here is:

$$P = k_e EN \frac{3}{4}\left(\frac{I}{2} + \sqrt{2R_0\left(\frac{Z_w}{v_{fd} I} + \frac{I^2}{24R_0} \right)} \right) + k_c Z_w \tag{3.29}$$

Equations (3.28) and (3.29) will be used in Sections 3.4.4 and 3.5 to compare the predicted grinding power with measured values in robotic grinding tests (single and juxtaposed grooves).

3.4 Experimental Validation of the Impact-Cutting Model

Cyclic impacts were found as the mechanism of material removal when grinding is performed by a compliant robot arm as presented in Chapter 2. Considering the regime of vibro-impact present in the process, cutting force and grinding power were formulated based upon such impacting dynamics in the preceding sections of the current chapter. Parameters of the impact-cutting model for material removal are identified experimentally in the sections that follow. Robotic grinding tasks are performed while setting the target grinding power in the robot control strategy based on this model. It is illustrated that a uniform cut is possible in presence of high amplitude vibro-impact oscillations in the material removal process.

3.4.1 Test rig, Material and Experimental Procedures

The laboratory setup which was established for the first part of this thesis, presented in Chapter 2, is further developed for the experimental study presented in the current chapter. The schematic in Figure 3.9 is showing the main components used for conducting the robotic grinding experiments with this test rig. A SCOMPI robot holds a grinder which is mounted with a grinding wheel. Robot holds the grinding wheel perpendicular to the surface and travels along the feed direction fd while it also makes traverse displacements along the lateral direction lt to perform single or multi-pass grinding tasks on the workpiece material

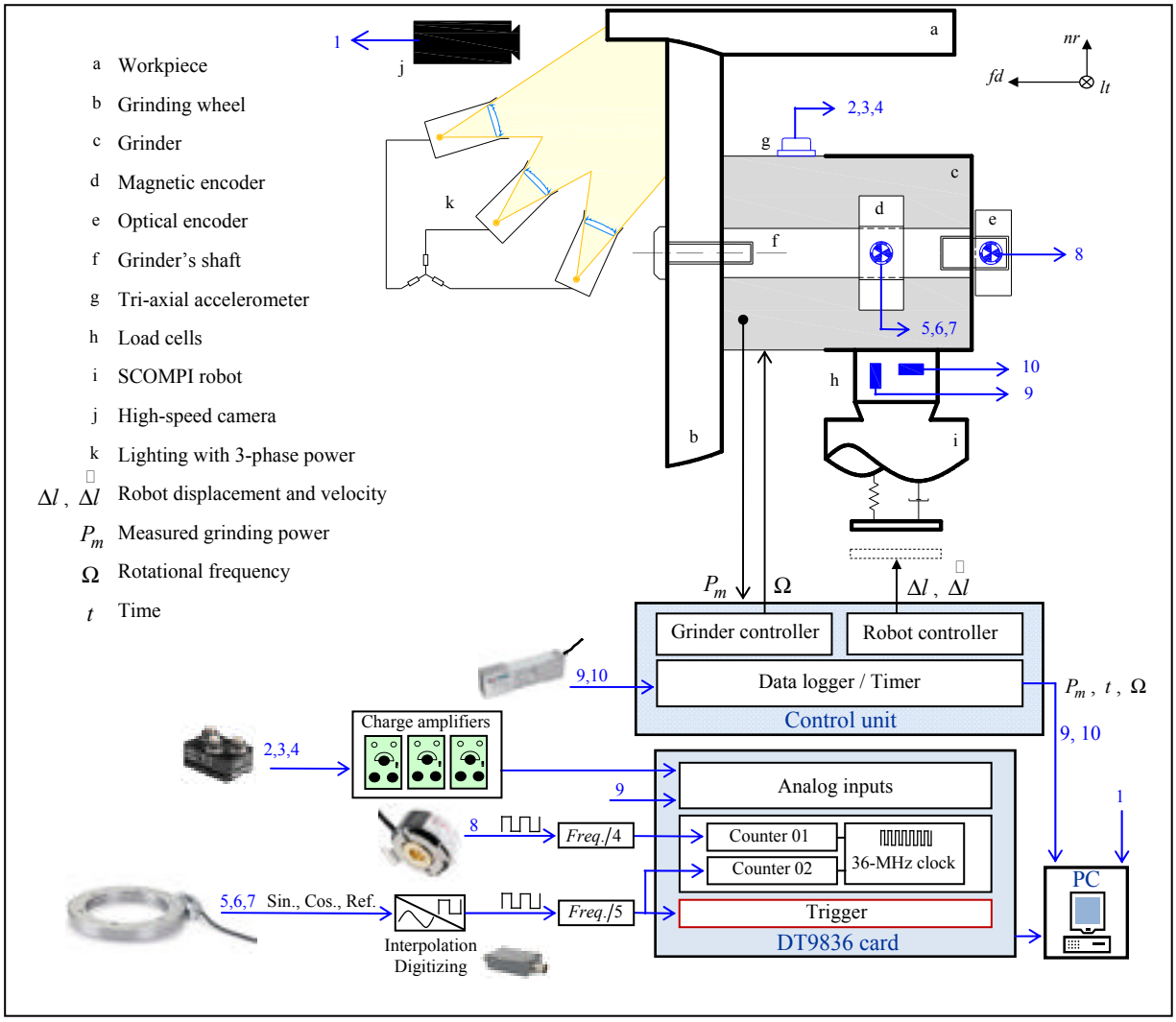

Figure 3.9 Experimental setup and data acquisition system

(see Figure 3.10). The control unit of SCOMPI monitors the average grinding power P_m measured every $0.05s$ during the process and regulates it according to a target value defined by the task. To regulate the grinding power, robot controller moves the robot by a calculated distance and velocity at each instant along surface normal. The grinder controller controls the rotational frequency of the grinder to maintain it at a nominal value defined by the task.

Robot's control mechanism is simplified in Figure 3.11. Given a target depth of cut h_0 and the task related parameters, the target material removal rate Z_w is calculated based on the

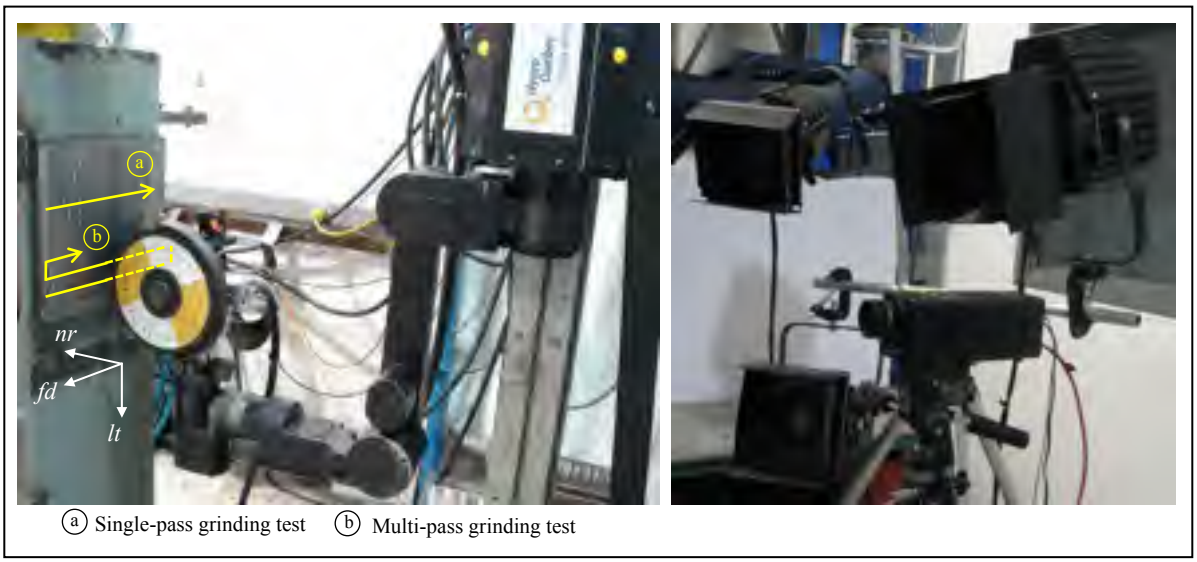

Figure 3.10 Robotic grinding test rig with high-speed camera and lighting

kinematics of the cut. For example, in the case of single groove grinding experiments, Equations (3.3) and (3.4) can be used for this purpose. Target grinding power is then calculated based upon the impact-cutting model of the material removal process. During the task, the target grinding power P is compared to the consumed power of the grinder P_m monitored by the control unit. Error in grinding power P_E is equivalent to an error in average normal grinding force $\bar{F}_{N,E}$ correlated by the rotational frequency ω, radius of the wheel R_0 and an empirical friction coefficient μ. The error in normal force is compensated by moving the robot and consequently the grinder by a certain displacement Δl and velocity $\dot{\Delta l}$. The required displacement and velocity are calculated based on an empirical SDOF compliance model for the robot structure.

Two strain gauge load cells are installed between the robot and the grinder to give an estimate of the average normal and tangential grinding forces. Several monitored parameters during the task are logged by a data logger from which the monitored grinding power P_m, robot displacement Δl, average normal and tangential grinding forces, rotational frequency Ω and the corresponding time vector t are input into the data acquisition system.

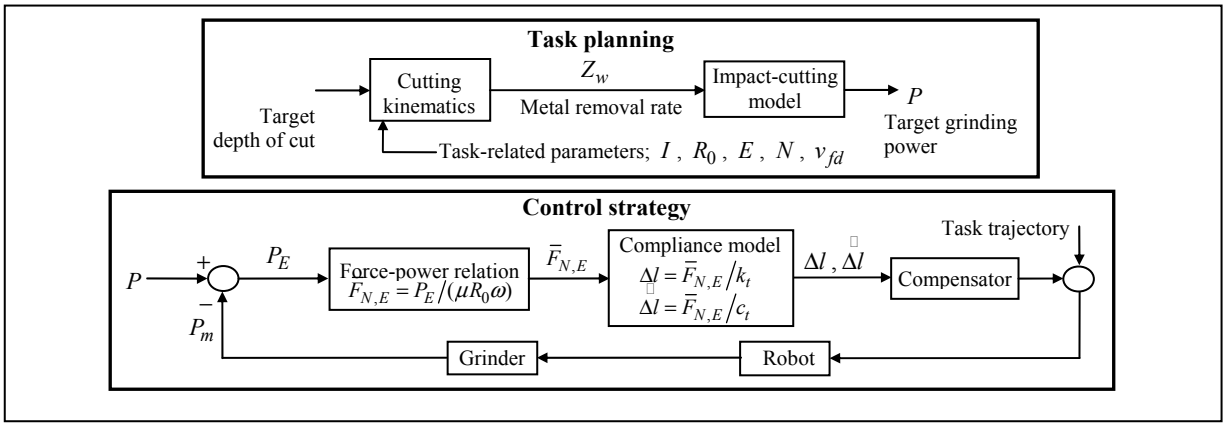

Figure 3.11 Simplified control mechanism of SCOMPI in robotic grinding

The setup is equipped with an IDT high-speed digital camera as explained in Section 2.3. An angular marking is attached to the grinding wheel so that in the video captures of the grinding operation, it will be easier to identify the instants were material removal is being performed.

A balance with $0.1g$ resolution is used to weigh the workpiece specimens once before and once after multi-pass grinding tests. The purpose is to measure the amount of material removed during the tests.

Vibration and angular speed signals are measured using a DT9836 data acquisition card capable of receiving an external trigger source. The purpose is to capture these data in sync with the spindle's angular displacements. Data acquisition based on the angular sampling methodology was explained with more details in Section 2.3.1 using an optical rotary encoder installed on the spindle with the help of an auxiliary extension shaft. The grinder is further equipped with a Heidenhain magnetic encoder which is installed on the spindle directly. The modular magnetic encoder includes a scale drum which is installed on the shaft of the grinder. The drum is composed of a graduation carrier with 600 magnetic line counts. Passages of magnetic lines in front of a scanning head with magneto-resistive sensors generate sine and cosine wave outputs. These outputs are received by an IBV 101 interpolation and digitizing electronics box which generates a 5-fold square-wave pulse at the TTL level from the sine and cosine wave inputs. The signal which is therefore generated

3000 times per revolution is passed through a frequency divider circuit which divides its frequency by 5. Eventually, 600 square-wave pulses are generated at equidistant angular displacements of the wheel during each revolution within the grinding operation. This signal is used as the trigger source for data acquisition on all channels. Using this method, a block of 600 samples in the signals acquired corresponds to one spindle rotation cycle. Instead of representing these measurements versus time, they are thus shown versus angular positions of the shaft or equivalently versus fractions of a revolution.

The instantaneous rotational frequency of the wheel is measured, as detailed in Section 2.3.1, by two sensors simultaneously to double check using the elapsed time method. The signal used for the trigger source from the Heidenhain magnetic encoder and a similar output from the QPhase optical encoder are used as square-wave pulses for this measurement. The optical encoder outputs square-wave pulses 250 times per revolution through a divider circuit. The two counters on the acquisition card use a $36-MHz$ clock to measure the time between rising edges of square-wave pulses based on which the instantaneous angular frequency of the shaft is obtained.

3.4.1.1 Topographical Investigation of the Ground Surfaces

Surface profiles of the grooves created in single-pass grinding experiments are measured using a profilometer. The experimental investigation aims verifying signatures of the impacting behavior on the ground surface profile. Furthermore, it is used to quantify the robotic grinding task and identify the parameters of the impact-cutting dynamic force model.

The Altisurf530 machine shown in Figure 3.12 is used for topographical measurement of the grooves. Workpiece specimens on which several grooves were grounded through single-pass grinding experiments are put on the machine for precise profile measurement of each groove individually. The machine has a table that holds the workpiece plate and moves it along X and Y directions such that grooves' profiles can be scanned by a CL4-MG35 optical sensor. The optical sensor, adjusted on the Z axis, uses the Confocal Spectral Interferometry (CSI)

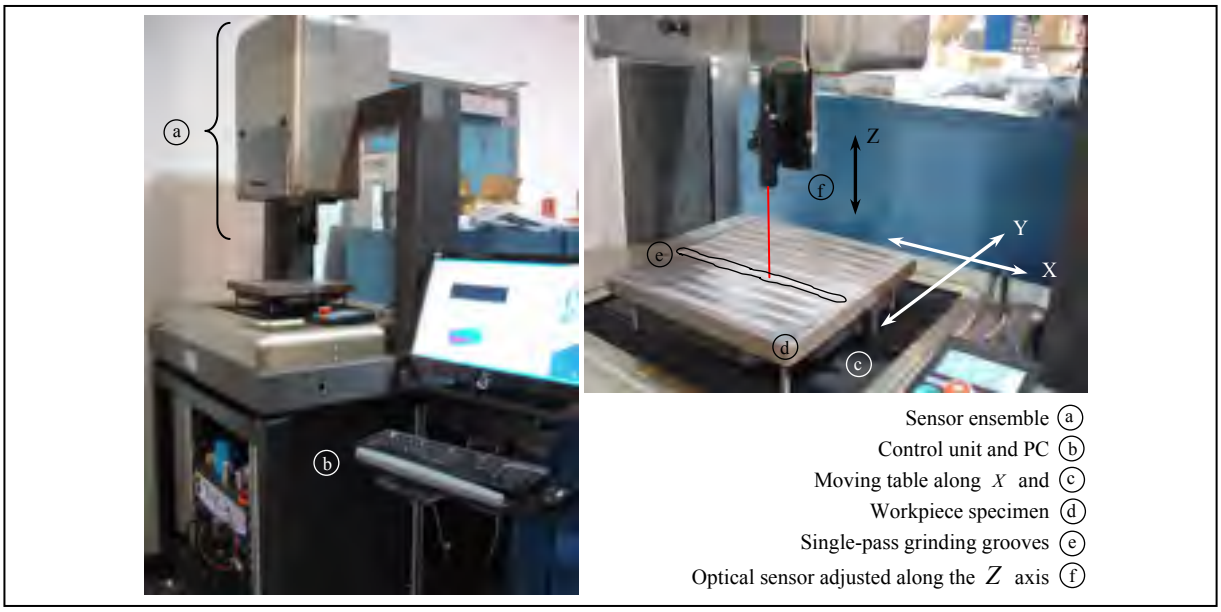

Figure 3.12 AltiSurf 530 machine

method to give accurate measures of the topography of the ground surfaces with extremely high resolutions.

Two scans with different resolutions are performed on each groove as depicted in Figure 3.13.a. The detail scan is performed on a small zone close to the end of the pass where steady grinding conditions are most certainly achieved. Graphic delineation of the surface along groove's longitudinal axis is performed with a very fine resolution $dX = 10\mu m$. That is because the purpose of the detail scan is to study the probable signature of the cyclic impacting behavior on the ground surface. Such investigation is carried out by correlating the scanned lines (see Figure 3.13.b) to the parameters of the robotic grinding task performed by robot's travel along the feed fd direction (groove's longitudinal axis X).

The global scan is performed on the entire groove. The objective of this scan is to quantify the single-pass robotic grinding task in an offline manner. That means extracting in-process parameters of the material removal process once the groove has been created. Specifically, at each location X along the groove's longitudinal coordinate, the maximum depth of cut $h_{0,m}^{X}$ and the material removal rate $Z_{w,m}^{X}$ is measured from this scan (see Figure 3.13.c). The

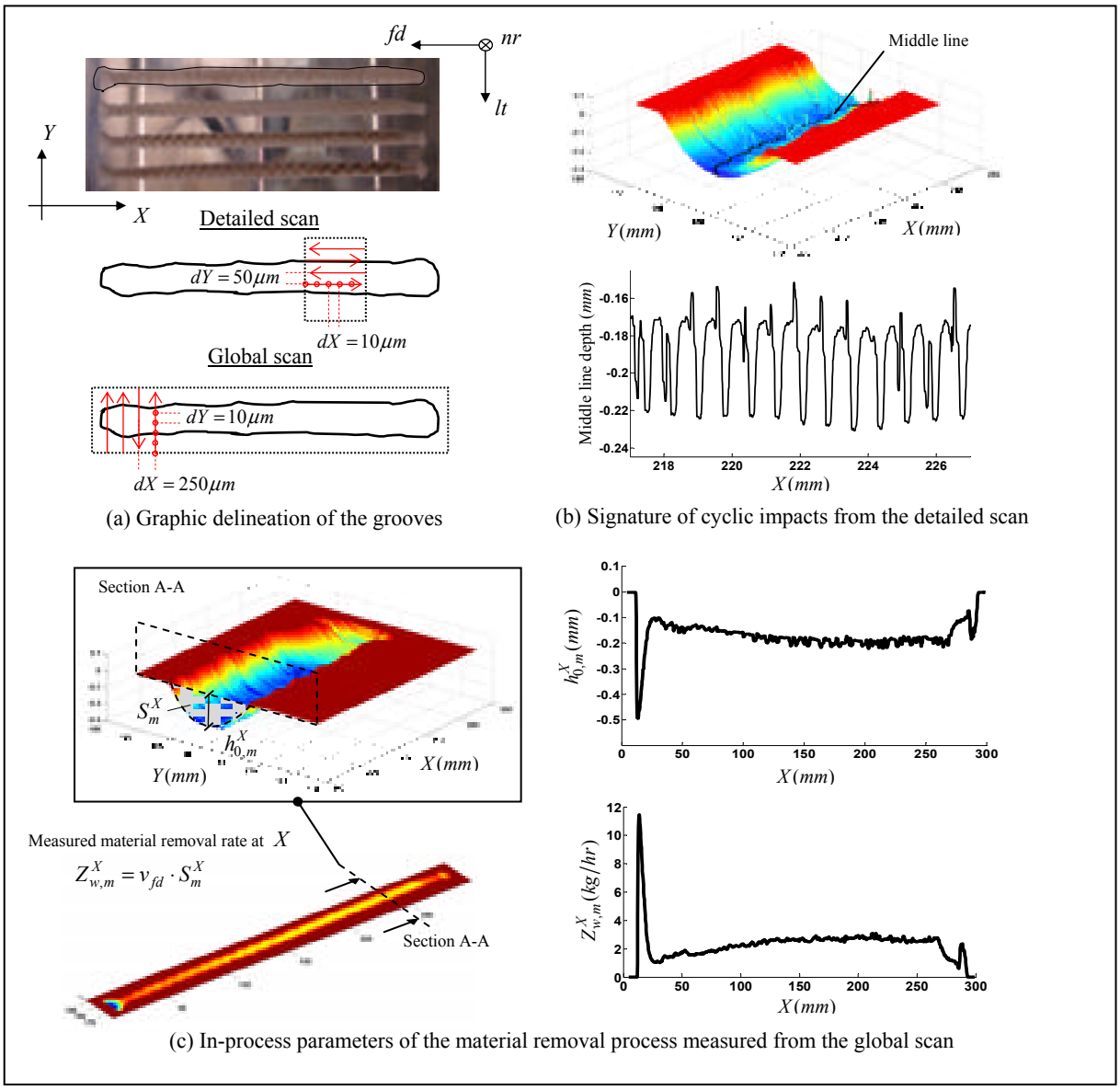

(a) Graphic delineation of the grooves

(b) Signature of cyclic impacts from the detailed scan

(c) In-process parameters of the material removal process measured from the global scan

Figure 3.13 Topographical inspection of the grooves created by single-pass grinding tests

material removal rate is estimated by multiplying the cross-sectional area of the groove S_m^X with the nominal feed speed v_{fd} of the test. Cross-sectional area of the groove S_m^X is calculated by numeric integration of the lines which have been scanned with a very fine resolution $dY = 10\mu m$. Using this offline approach, variations of the depth of cut and the material removal rate can be measured versus the groove's longitudinal coordinate as

depicted in Figure 3.13.c. The list of the equipment used with their specifications and accessories ispresented in Table 3-1.

Table 3-1 Equipment used in the setup shown in Figure 3.9

Equipment	**Specifications**	**Accessories**
B&K triaxial accelerometer, Type 4326	Sensitivity: $X = 0.341$, $Y = 0.326$, $Z = 0.319\ pC/ms^{-2}$	B&K charge amplifiers (3), Type 2635. $10\ mV/ms^{-2}$ output, $2Hz - 100kHz$ frequency range
QPhase optical encoder, Type QD145	TTL output, Resolution 1,000 line counts	Frequency divider circuit
HEIDENHAIN modular magnetic encoder	TTR ERM2404 Scale drum, 600 line counts AK ERM2480 Scanning head IBV101 Interpolation/digitizing electronics (square-wave output signal at TTL level with 5-fold interpolation)	Frequency divider circuit
Tedea-Huntleigh	Model 1042, two-beam single-point load cell, Sensitivity: $0.01V/N$	Signal conditioning
IDT high-speed digital camera, Y4 series	1-megapixel video images at up to 5,100 fps	$750W$ halogen lamps(3) rated at 17,000 lumens, 7-inch Fresnel lenses, Three-phase electric power
DT9836 data acquisition module	Sampling triggered by an external clock	
AltiSurf 530 profilometer	$30cm \times 30cm$ stage, Precision: $0.5\mu m$	CL4-MG35 optical sensor (Spot size diameter= $8\mu m$, Lateral resolution= $4\mu m$, Measuring range= $4mm$), Control unit, Acquisition PC, Altimap acquisition software
Abrasive product	Cylindrical, self-dressing, aluminum oxide wheel with resin bonding (*NORZON III*)	
Grinder	Permanent magnet electrical grinder, $2.5kW$ Bosch HF electrical grinder, model HWS88/230, $2.2kW$	SCOMPI control system regulating grinding power
Tool holder	SCOMPI robot, 6-DOF	
Workpiece material	$300 \times 300 \times 25mm$ plates of A36 carbon steel $300 \times 300 \times 25mm$ plates of 1045 carbon steel	
Mettler balance	Model PM30000-k, Weighing capacity= $32kg$, Readability= $0.1g$	

3.4.2 Tests

Robotic grinding tests performed using the setup described in the previous section are listed in the current section. These include single and multi-pass grinding tests with several measurements which were carried out either before, during or after the experiments using the equipment and procedures described in the previous section. These measurements will be used interchangeably for several purposes in the sections that follow.

3.4.2.1 Single-pass Robotic Grinding Tests

A series of six single-pass robotic grinding tests, i.e., Tests 8–13 are performed. Each lasts about $4s$ and creates a groove on the workpiece along the feed direction fd (see Figure 3.10). Table 3-2 gives for each test the nominal values for target grinding power and rotational frequency, as well as general specifications for all tests. Instantaneous rotational frequency, tri-axial vibrations, average normal grinding force and grinding power are measured during the tests. A high-speed camera is also used to capture video images in the middle of the tests in order to observe the impacting behavior. After the tests, topographical measurements are made from the ground surface of the grooves created.

Table 3-2 Single-pass grinding tests to investigate the vibro-impact dynamics in robotic grinding

Parameter / Nominal value	**Tests**					
	8	9	10	11	12	13
Grinding power (W)	2500	2292	2083	1875	1667	1458
Rotational speed (rpm)	6000	5500	5000	4500	4000	3500
Grinder: *Permanent magnet electrical grinder,* $2.5kW$; Workpiece material: *1045 carbon steel*; Nominal feed speed: $60mm/s$; Grinding wheel diameter: $230mm$; Grinding wheel width $6.8mm$.						

3.4.2.2 Multi-pass Robotic Grinding Tests

A series of ten successive multi-pass grinding tests, each about 5 minutes long, are performed iteratively on one workpiece specimen using one grinding wheel. These long-run experiments are to study average properties of the operation and to validate the impact-cutting model over successive grinding iterations. Validity of the impact-cutting model over successive grinding iterations which result into wearout of the wheel and workpiece is verified by these tests. During each test, grinding is performed over the whole surface of the workpiece through back-and-forth travel of the robot along the feed direction and infeed displacements along the lateral direction (see Figure 3.10). Juxtaposed grooves created during each test constitute one layer of material that is removed from the workpiece surface. Table 3-3 gives the measurements taken during each of these tests, i.e., Tests 14–23, and general specifications. The workpiece is weighed and the wheel diameter measured before and after each test. During each test, average values of the monitored grinding power, rotational speed, normal and tangential grinding forces, and the duration of each test are obtained from the logged data. An empirical friction coefficient μ is determined from such tests and used to correlate normal and tangential grinding forces.

$$\mu = \frac{1}{n_{tst}} \sum_{j=14}^{23} \frac{\overline{F}_{T,m_j}}{\overline{F}_{N,m_j}} \tag{3.30}$$

where i is the test number and n_{tst} is the total number of tests. $\overline{F}_{T,m}$ and $\overline{F}_{N,m}$ are the measured average tangential and normal grinding forces for each test. The friction coefficient obtained from Tests 14–23 is $\mu = 0.2744$.

Table 3-3 Multi-pass robotic grinding tests to investigate the impact-cutting model for material removal

Parameter / Measurement	**Test**									
	14	15	16	17	18	19	20	21	22	23
Weight of the workpiece (g)	15309.9	14720.2	14007.2	13626.2	13016.1	15983.9	15033.2	14299.9	13558.7	12782.9
Wheel diameter (mm)	227	224	216	214	208	199	192	181	174	153
Duration of the test (s)	358.55	713.65	358.55	358.55	358.55	358.55	358.55	358.55	358.55	358.55
Grinding power (W)	1901.9	1362.68	2446.6	1631.4	2174.9	1908.8	1908.6	2450.7	1908.1	2446.6
Rotational speed (rpm)	6329.5	6374.01	6270.6	6350.8	6287.7	6324.1	6333.9	6257.8	6330.5	6253.9
Normal grinding force (N)	98.8	81.93	109.9	97.8	108.5	108.3	113.8	118.9	116.3	119.1
Tangential grinding force (N)	24.10	20.31	33.7	25.6	31.1	25.4	26.6	37.4	29.5	42.9
Grinder: *Bosch HF electrical grinder,* $2.2kW$; Workpiece material: *A36 carbon steel*; Grinding wheel diameter before tests: $230mm$; Weight of the workpiece before tests: $15793.8g$; Infeed distance: $6mm$; Nominal feed speed: $80\,mm/s$, Grinding wheel width: $6.8mm$.										

3.4.3 Experimental Evidences of the Impact-Cutting Behavior

The main theme of this chapter is to validate the impact-cutting model for material removal. The core dynamic behavior based on which this model is established, i.e. the cyclic impacting oscillations of the cutter were experimentally characterized in Chapter 2 with the help of the experimental setup initiated. In the current section of this chapter, once more, some experimental evidences are provided to support the existence of such behavior in the robotic grinding tests used in this part of the work. Given the fact that the test setup is further developed as compared to its initial version and test conditions have therefore changed, this also provides additional evidence on the existence of vibro-impact dynamics in the robotic grinding process under study independent from test conditions.

3.4.3.1 High-speed Camera Observations

One of the high-speed video sequences recorded in the middle of the grinding passes performed in Tests 8–13 is provided as supplementary material for the image shown in Figure 3.14 (see the supplementary material to play this video). Close inspection of such video images confirms the existence of vibro-impact behavior in steady-state operation.

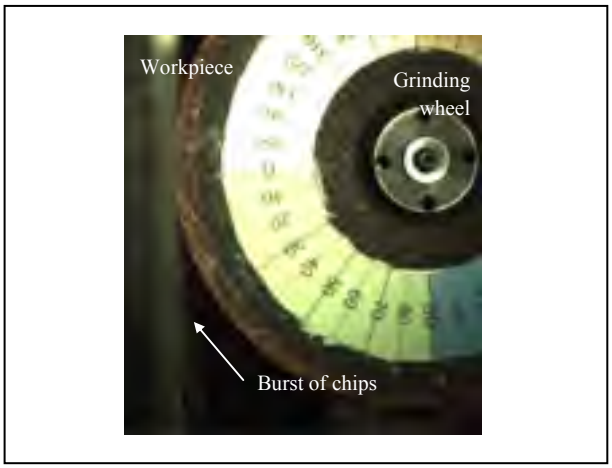

Figure 3.14 High-speed video recorded in the middle of the grinding pass (video available as supplementary material)

Bursts of chips, which indicate that cutting impacts are occurring, almost always appeared during the steady regime of the cut. However, the number of impacts per revolution of the wheel and the angular position of the impacts change. High-frequency impacts between the wheel and the workpiece clearly do occur on a regular cyclic basis.

3.4.3.2 Vibration/Instantaneous Rotational Frequency Measurements

Figure 3.15 gives an overview of the tri-axial vibrations and instantaneous rotational frequency measured in Test 13. The robotic grinding process starts by ramping up the wheel's rotational speed to its full nominal value. After free rotations for a while, the robot moves the rotating wheel toward the workpiece and seeks the initial contact, as measured by grinding power consumption. In the "seeking power" phase which follows, the robot increases the amount of normal grinding force through displacement of its articulation until grinding power consumption reaches a predefined threshold. Traverse grinding is then launched by robot travel along the feed direction. Once a single grinding pass is performed, the robot withdraws the wheel from the surface and after a number of free revolutions, the rotational speed ramps down and the wheel eventually stops. This sequence is shown in the overview of the measured rotational frequency in Figure 3.15, which also plots the

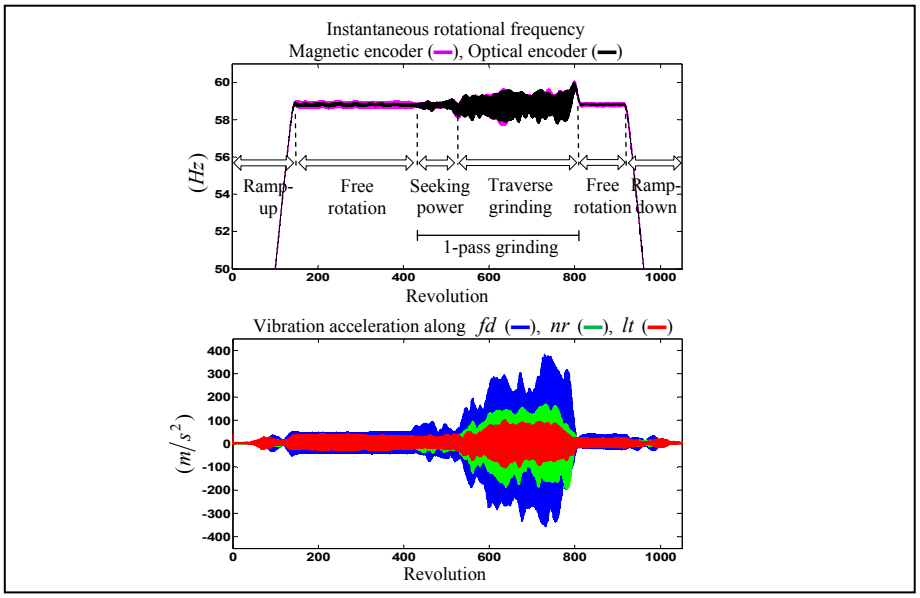

Figure 3.15 Overview of the measured instantaneous rotational frequency and tri-axial vibrations in Test 13 at 3500 *rpm* (typical of single-pass robotic grinding tests)

corresponding tri-axial vibration measurements. All single-pass experiments, i.e., Tests 8–13, follow these same steps.

The measured instantaneous rotational frequency from Tests 8–13 is investigated carefully in detailed views. Figure 3.16.a shows one such detailed view, during the steady grinding step in Test 11. A fast drop and then acceleration from the mean line rotational frequency appear clearly during every revolution period. The phenomenon is detected by both the magnetic and optical encoders, which are arranged differently on the grinder's shaft and produce independent signals. The fast drop corresponds to the interval when material is being removed and the grinding wheel is in contact with the workpiece. The acceleration to the mean line rotational frequency takes place when the wheel bounces off the surface and the cut is interrupted. Cutting impacts are therefore clearly visible from this measurement. The major challenge of this measurement is the torsional resonance of the shaft due to impulsive excitations as seen in Figure 3.16.a. This resonance differs in amplitude between the two encoders because of their location on the shaft. Efforts were made in modeling and testing to

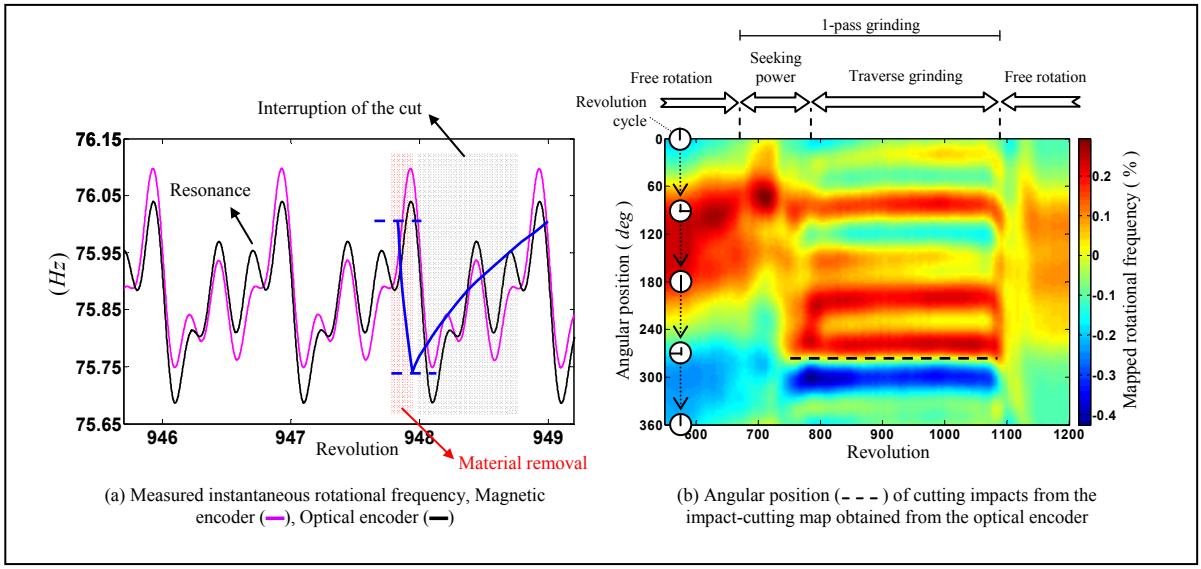

(a) Measured instantaneous rotational frequency, Magnetic encoder (—), Optical encoder (—)

(b) Angular position (- - -) of cutting impacts from the impact-cutting map obtained from the optical encoder

Figure 3.16 Impacting dynamics of material removal from the measured instantaneous rotational frequency in Test 11 at 4500*rpm*

identify such resonance and minimize its effect on the quality of measurements. The signal for measured instantaneous rotational frequency could be color mapped to generate "impact-cutting maps" from these measurements since angular sampling was used for data acquisition (see Section 2.4.4). With this "impact-cutting map", the angular position of cutting impacts in revolution cycles can be compared throughout the entire task as shown in Figure 3.16.b. The dark blue region on the map with a thin transition to a red region indicates that during Test 11, cutting impacts occurred at almost the same angular position.

Tri-axial vibrations measured in Tests 8–13 correlate very well to the instantaneous rotational frequency with respect to cyclic impacts. This correlation is shown in Figure 3.17 for part of Test 8. During the 20 revolution cycles in this figure, the fast drop and rise detected by the two encoders is correlated to a sharp peak in vibration measurements along three directions.

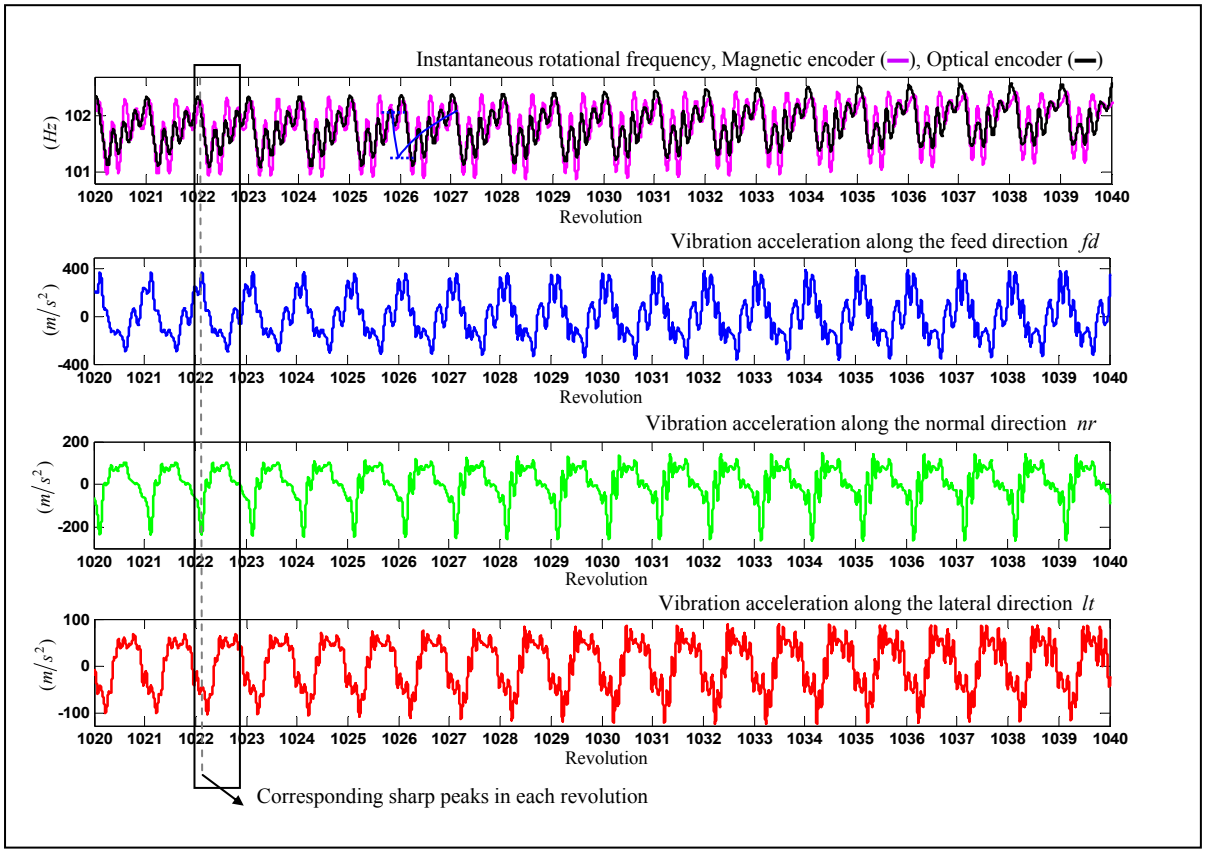

Figure 3.17 The cyclic impacting oscillations from tri-axial vibrations and instantaneous rotational frequency measured in Test 8 at 6000*rpm*

3.4.3.3 Surface Profile Measurements

Grooves created in Tests 8–13 were inspected topographically to find any probable signature from the impacting oscillations of the cutter on the ground surface profile. As shown by both photographed and scanned images in Figure 3.18.a from Test 9, patterns of regular slots along the grooves' longitudinal axis were present in the ground surface profile. These slots were mainly spaced at a distance very close to the wheel's nominal advance per revolution Δ. Two examples of the middle lines from the detailed scans of grooves produced in Test 8 and Test 11 are shown in Figure 3.18.b. It is concluded that the impacting oscillator cuts a deep slot when its rear grit hit the ground surface once per revolution of the wheel.

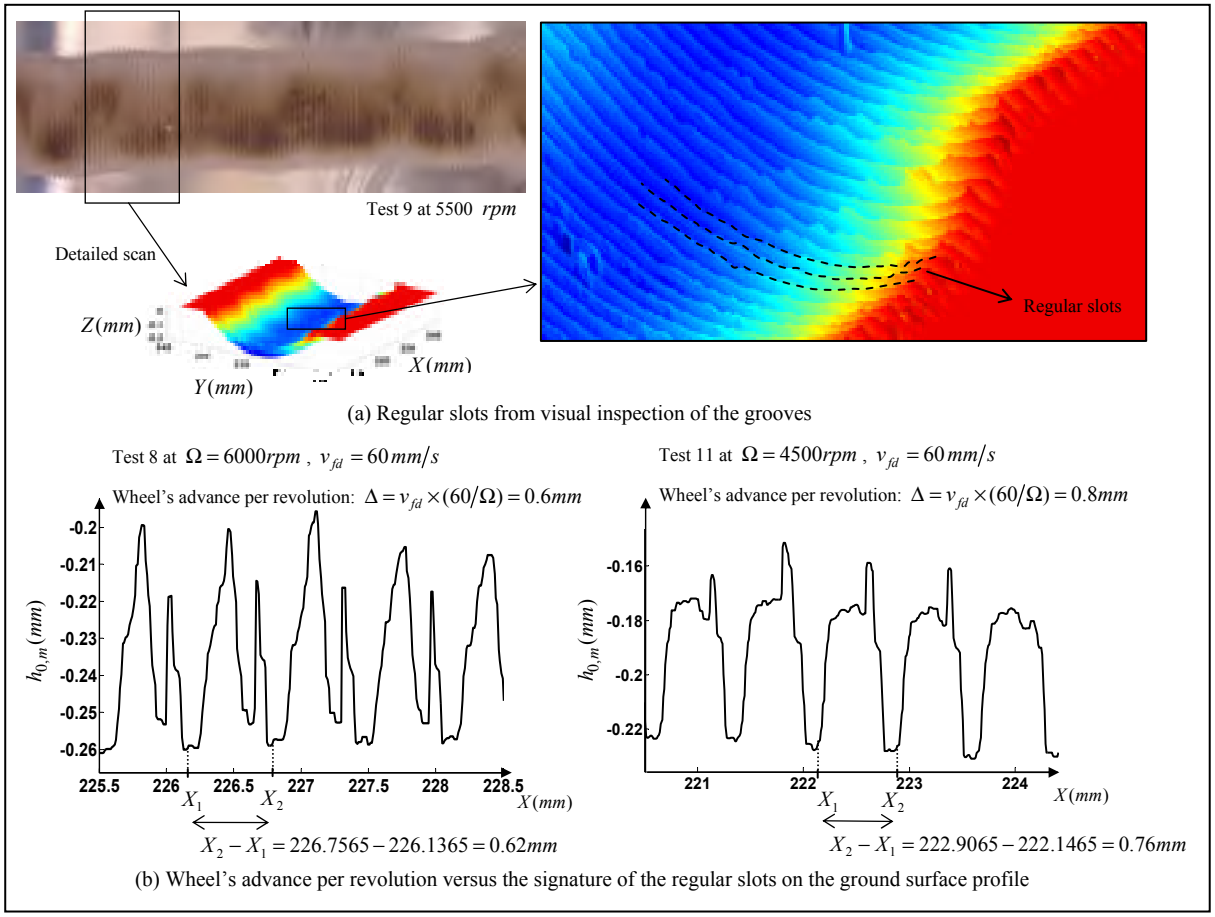

Figure 3.18 Signature of the impacting dynamics on the ground surface profile

3.4.4 Experimental Identification of Parameters

Vibro-impact dynamics was the principal vibratory behavior upon which grinding force and power were formulated. Parameters of the impact-cutting model, the edge and cutting force coefficients k_e and k_c in Equation (3.20), are determined in this section from grinding power measurements taken during the ten long-run multi-pass grinding tests, i.e., Tests 14–23. A cost function is defined as the variation coefficient of the root mean square of the difference between the measured and predicted grinding power over the cloud of ten tests,

$$C_{power} = \frac{1}{\overline{P}_m}\sqrt{\frac{\sum_{j=14}^{23}\left[P_j - P_{m_j}\right]^2}{10}} \times 100 \tag{3.31}$$

where index j refers to the test number. Measured grinding power P_m for each test is obtained from Table 3-3 and its mean value $\overline{P}_m$ over the group of ten observations is used for normalization. Predicted grinding power is calculated using the measured average rotational frequency N_m, material removal rate $Z_{w,m}$ and grinding wheel radius $R_{0,m}$ in these tests (see Table 3-3). Equation (3.29) developed for the required grinding power in creating juxtaposed grooves is then used as,

$$P_j = k_e E N_{m_j} \frac{3}{4}\left(\frac{I}{2} + \sqrt{2R_{0,m_j}\left(\frac{Z_{w,m_j}}{v_{fd} I} + \frac{I^2}{24R_{0,m_j}}\right)}\right) + k_c Z_{w,m_j} \tag{3.32}$$

The weight of the workpiece measured before and after each test and the duration of each test are used to obtain material removal rate $Z_{w,m}$. The measured radius of the wheel before and after each test are averaged to obtain grinding wheel radius $R_{0,m}$. Nominal values in Table 3-3 are used for feed speed v_{fd}, infeed distance I and grinding wheel width E. The cost function is plotted in Figure 3.19.a over a reasonable domain for k_e and k_c. Its global

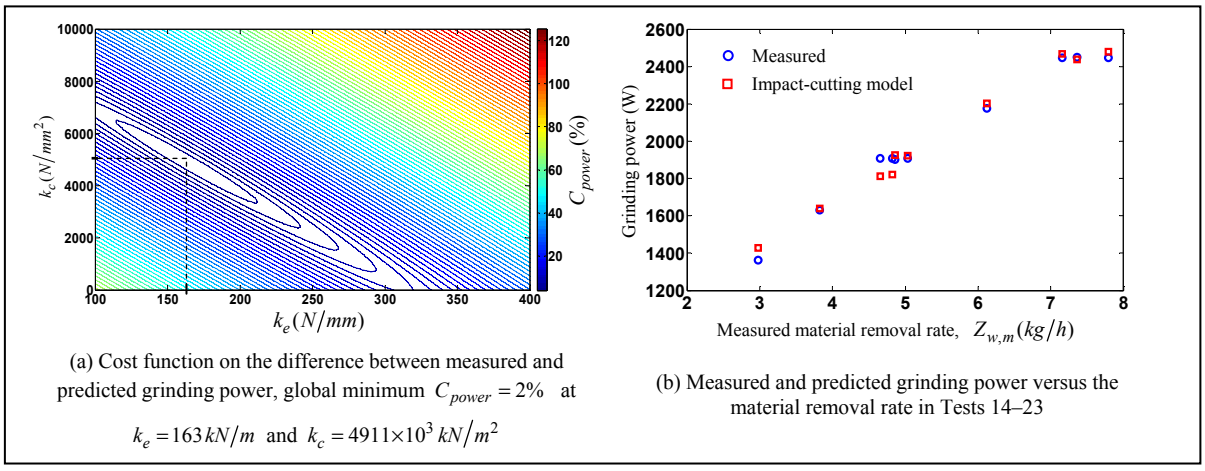

(a) Cost function on the difference between measured and predicted grinding power, global minimum $C_{power} = 2\%$ at $k_e = 163\,kN/m$ and $k_c = 4911\times10^3\,kN/m^2$

(b) Measured and predicted grinding power versus the material removal rate in Tests 14–23

Figure 3.19 Experimental determination of the edge and cutting force coefficients, k_e and k_c

minimum is found at $k_e = 163\,kN/m$ and $k_c = 4911\times10^3\,kN/m^2$ with an error value of around 2%. This means that the impact-cutting model with this set of parameters determined could predict grinding power for the cloud of ten experiments within 2% error. For further clarification, Figure 3.19.b shows the measured grinding power versus the measured material removal rate in these tests compared to predicted values from the impact-cutting model.

The impact-cutting model provides a very close fit with the observations from long-run tests performed iteratively using one workpiece specimen and one grinding wheel undergoing considerable wear in the course of the tests. Several other experiments, not reported in this thesis, have shown very similar results despite varying setup conditions. For the same type of workpiece material and abrasive product, the impact-cutting model can be made to fit experimental observations just by tuning such task-related parameters as wheel radius and feed speed. Conventional empirical models used for grinding are dependent upon the particular conditions of the experimental setup and are thus of limited practical use (Malkin and Guo, 2008). Grinding in general, is the least understood material removal process (Moerlein, 2007). In contrary to other material removal processes which can be characterized by limited number of variables, even a simple grinding process requires at least 12 empirical variables to be described (Shin, Chen and Kumara, 1992). Such models are mainly built on a statistical basis and are usually applicable to one specific setup. To be used under different conditions, their parameters must be determined accordingly. This is mainly due to the inherent irregularity of grinding, which also changes over time and also due to the empirical nature of these models rather than being based on the physical merits involved in the process. The approach behind the impact-cutting model benefits from the regular basis of the discrete cutting events, similar to a milling cutter with constant flutes and therefore invariant kinematics and cutting conditions. This makes the model, once determined for a wheel-workpiece set of material, readily applicable to a wide range of grinding operations performed by the robotic arm, provided the major impacting regime of material removal is maintained. Numerous successful field robotic grinding tasks (Hazel et al., 2012a) have used this impact-cutting model under a controlled material removal rate strategy.

3.5 Comparison between the Measured and Target Depth of Cut

The objective of using the impact-cutting model in task planning is to calculate the grinding power that must be delivered at the spindle to achieve a target depth of cut and rate of material removal. The cutter's end reaches the points located at depth h_0 while it is inevitably subjected to move along the trajectories of vibro-impact oscillations. This vibratory motion is taken into account by the impact-cutting model when calculating the grinding power required to remove an uncut chip specific to a cutting impact. This section investigates whether the robotic grinding process could have reached the cutter's end point to the calculated points located at the target depth of metal (see Figure 3.1.b).

Tests 8–13 listed in Table 3-2 are used. In each test, the monitored grinding power is set equivalent to the material removal rate measured along the groove's longitudinal coordinate X from the global scan. Figure 3.20 shows this procedure for Test 10. From each test indexed as j, samples $(k = 1-50)$ of the measured grinding power $P_{m_j}^{X_k}$ along the groove are considered in sync with samples from the measured material removal rate $Z_{w,m_j}^{X_k}$. The cost function for fitting the impact-cutting model on this set of 300 observations will be then defined as,

$$C_{power} = \frac{1}{\overline{P}_m}\sqrt{\frac{\sum_{j=8}^{13}\sum_{k=1}^{50}\left[P_j^{X_k} - P_{m_j}^{X_k}\right]^2}{300}} \times 100 \tag{3.33}$$

where $\overline{P}_m$ is the mean value obtained from all observations. The predicted power at position X_k of the groove created in the j^{th} test is given by,

$$P_j^{X_k} = k_e EN\frac{3}{4}\left(\frac{12R_0 Z_{w,m_j}^{X_k}}{v_{fd}}\right)^{\frac{1}{3}} + k_c Z_{w,m_j}^{X_k} \tag{3.34}$$

Nominal values from Table 3-2 are used for grinding wheel width E, radius R_0 and feed speed v_{fd}. The cost function is plotted in Figure 3.21.a over a reasonable domain for k_e and k_c. Its global minimum is located at $k_e = 280\,kN/m$ and $k_c = 4331\times10^3\,kN/m^2$ with an error value of around 13%. The two parameters of the impact-cutting model represented by Equation (3.28) are updated accordingly with these values, which are in the same order of magnitude as their values determined in the same way through long-run tests in Section 3.4.4. Grinding power P is then expressed as a function of depth of cut h_0 using the updated model. Samples of measured grinding power along the grooves' longitudinal coordinate in Tests 8–13 are then used with this expression to find the depth of cut. The results predict the points that the end of the oscillating cutter exhibiting vibro-impact dynamics would reach once per revolution of the wheel. Figure 3.21.b plots predicted depths for Test 10 versus measured depths of cut from the global scan. The model is clearly able to calculate the grinding power which must be delivered at the spindle such that the end-effector point to reach a set of target positions at the depth of cut in the presence of vibro-impact oscillations. Note that the surface waviness with an amplitude around $0.05mm$ is achieved despite

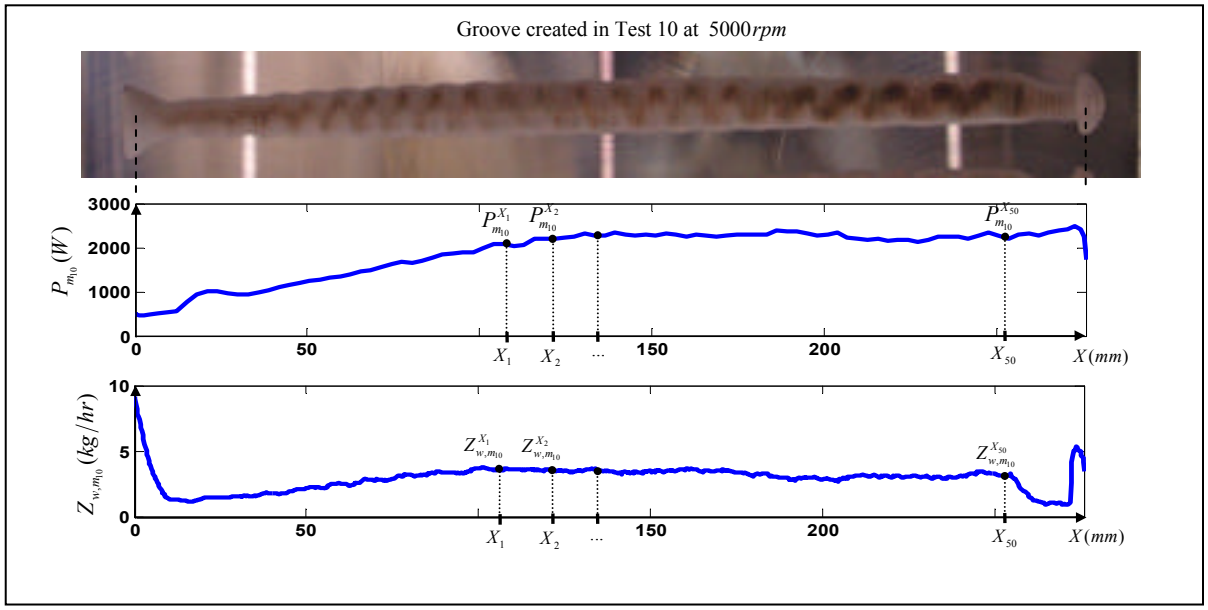

Figure 3.20 Measurements of grinding power and material removal rate along the groove's longitudinal axis

significant unavoidable vibrations. Figure 3.21.c is the frequency domain representation of the vibrations measured in Test 10 in the direction normal to the workpiece. The dominant structural response at the rotational frequency has a peak-to-peak vibration amplitude of about $0.25mm$ as shown, while the amplitude of the waviness left on the ground surface is less than $0.05mm$ (see Figure 3.21.b). Dynamic deflections of the tool holder in machining are thus five times larger than the tolerance of the machined part. In other words, the surface waviness ground by the robotic process can be limited to an acceptable range despite severe vibrations of the robot arm.

The discrepancies in the predicted depth of cut and parameters determined are partially due to the inherent irregularity of grinding compared to other machining operations with definite cutting kinematics. There also exist uncertainties due to changes in the dynamic regime of material removal. Even though the regime of cutting impacts, once per revolution, is the

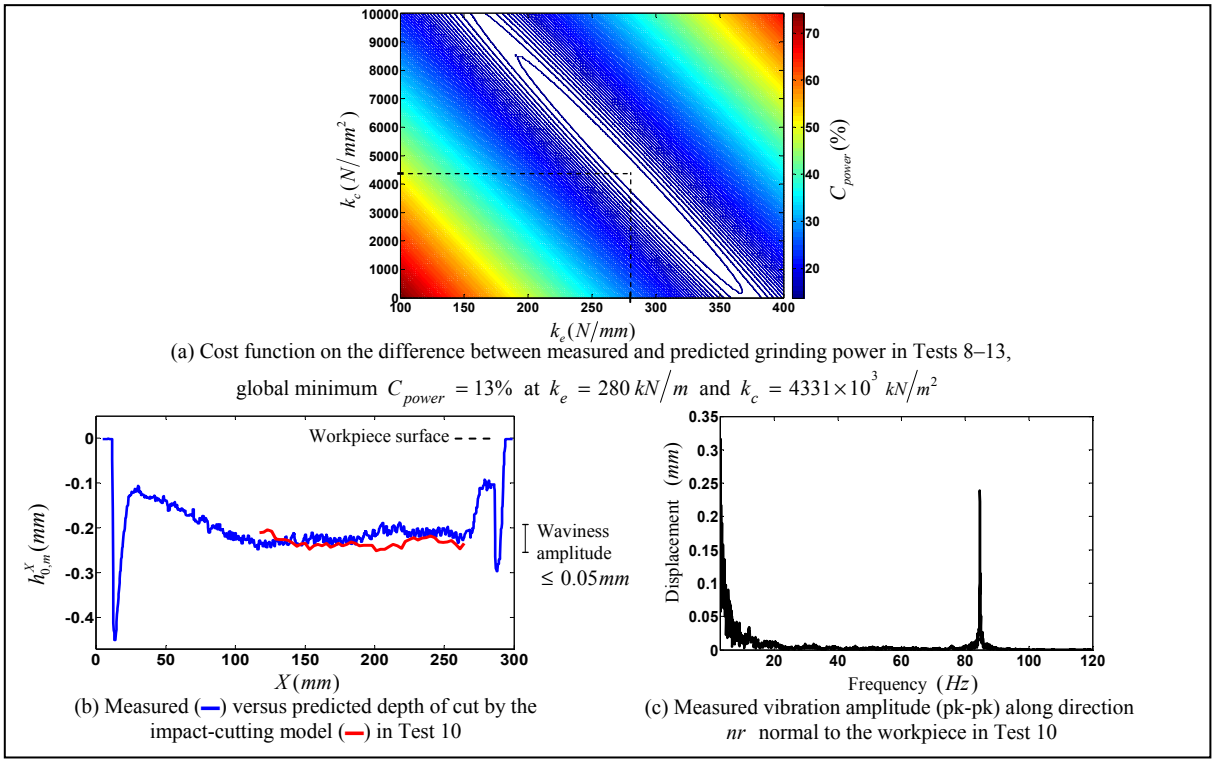

Figure 3.21 Application of the impact-cutting model to achieve a target depth of cut in robotic grinding

major factor governing the dynamics of the process, variations in the number of impacts per revolution are possible. When the impact-cutting model is fitted over observations from representative long-run tests, these variations have less effect and cause smaller errors compared to single-pass grinding tests. In the practice of the robot, to compensate for such discrepancies, the strategy of controlled material removal rate based on the impact-cutting model is coupled with a precise measurement system that scans the profile of the ground surface and compares it to the task's desired profile. Robotic grinding and surface profile measurement is then carried out in an iterative approach to reach the tolerance which is required. In each iteration, the target for material removal is set to approximately 80% of the excess material. Through successive iterations, as the thickness of the excess material decreases, grinding wheels with finer grit size are selected. The sequence is repeated until the desired tolerance of the ground surface is achieved. Typically, five to six iterations are needed to reach a tolerance level of $0.1mm$.

3.6 Summary

Dynamic deformation of the cutting tool in the robotic grinding operation under study was found have cyclic impacting characteristics as presented in the previous chapter. In the current chapter, first, a conceptual analogy was drawn between the impacting nature of the cutting process and the vibro-impact dynamics of the generic impact pair. As confirmed by this qualitative analysis, the process of material removal is interrupted and governed by vibro-impacts between the workpiece and grinding wheel, which mainly repeat at the spindle's rotational frequency. This ascertain that *the impact-cutting behavior present in the robotic grinding operation is inherent to the mechanical operation.*

A modeling tool was then introduced to formulate the grinding force and consequently the required grinding power based on the impacting dynamics of material removal (impact cutting). Parameters of this impact-cutting model, employed in robot control strategy, were experimentally identified. The impact-cutting model provided a very close fit with the observations from representative long-run robotic grinding tests performed iteratively.

Several field applications of the robot, which are not reported in this thesis, have shown very similar results despite varying setup conditions. *The impact-cutting behavior confirmed by modeling and experiments in this study provides the understanding basis* which is employed in the strategy of controlled material removal rate in the robotic grinding operation under study. The practical significance in using the impact-cutting model is that it incorporates physical parameters from the impacting dynamics of the cut such as the number of cutting impacts per revolutions. Real-time measurement of such parameter can be combined with this model to estimate the material removal rate during the process dependent on the dynamic regime of metal removal. This information can be used in the robot control strategy. Appropriate knowledge from the vibratory dynamics of material removal increases the confidence level when task planning to remove the excess material in robotized surface profiling.

Next, a detailed investigation was carried out on individual grooves created during single-pass robotic grinding tests. The purpose was to verify the capability of the robotic grinding operation to achieve a uniform cut, i.e. a cut with a target depth, a target rate of metal removal and an acceptable surface waviness left on the ground surface. *It was shown that even in presence of significant vibro-impact oscillations in the process, acceptable tolerance levels can be achieved on the machined part.* Numerous robotic grinding tasks aimed at very fine tolerances on the finished surface are reported successful using such control strategy coupled with an accurate measurement system that scans the ground surface profile in an iterative measuring/grinding approach. In each iteration, the target for material removal is set to a percentage of the excess material and the ground surface profile is measured afterwards with the help of a precise measurement system. Through successive iterations, as the thickness of the excess material decreases, grinding wheels with finer grit size are selected. The sequence is repeated until the desired tolerance of the ground surface is achieved.

The steady vibratory dynamics present in the robotic grinding process was explored in Chapters 2 and 3. In the next chapter, the issue of vibrational instability caused by the regenerative effect is investigated under the impacting regime of material removal.

CHAPTER 4

The Problem of Regenerative Chatter Revisited for Robotic Grinding

4.1 Introduction

Throughout the previous chapters, the cyclic impacting nature of the cut in robotic grinding with SCOMPI was explored. It was shown that even in presence of these high-amplitude vibro-impacts between the grinding wheel and the workpiece, an acceptable surface waviness can be achieved on the ground surface. However, there exist conditions when the undulations left on the machined surface, referred to as chatter marks by the common sense, become unacceptable. Figure 4.1 is showing an example of such ground surfaces. Since robots were employed in machining processes, severe chatter problem has been reported about their application. Low frequency chatter, vibrations of the entire robot structure, variation of chatter limits at different locations in the robot workspace are some characteristics of this challenging issue for robot machinists. Robotic engineers spend a considerable amount of

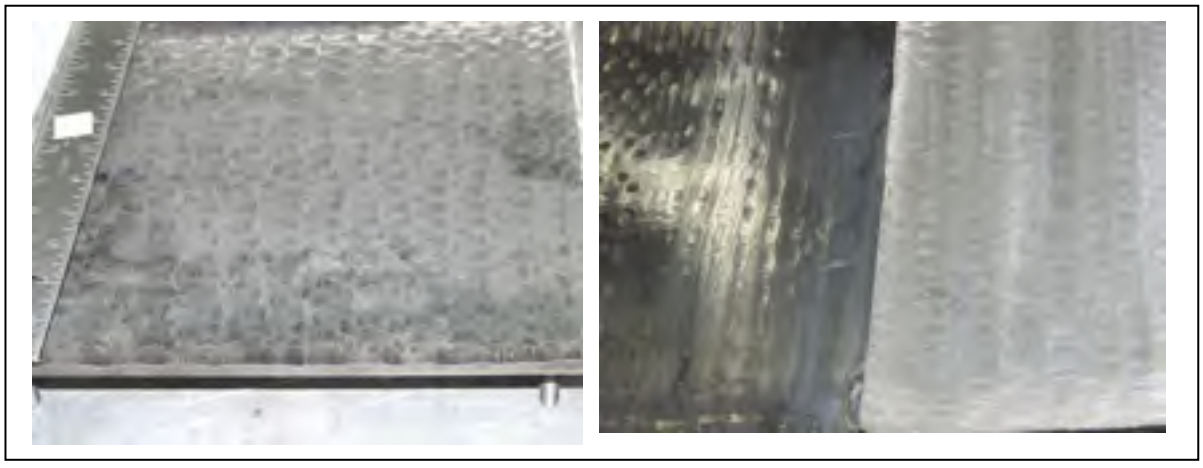

Figure 4.1 Chatter marks on the ground surface under certain conditions of robotic grinding with SCOMPI

time and effort to find their golden chatter-free setup. If the sheer luck of finding such setup is not met, they have to sacrifice productivity by selecting conservative cutting parameters for their machining tasks. The extensive research work carried out on conventional machining chatter has not yet focused on the emerging utilisation of robot arms for machining tasks. The rule of thumb guidelines and understandings used by conventional machinists to avoid chatter do not help robot machinists. In general, the problem of chatter vibration in metal cutting is a complex issue. The mechanisms of self-excitation are nontrivial, they are many and the simultaneous occurrence of vibrations caused by all these mechanisms is very probable. Researchers never get direct access to the cutting zone and they can only use measurements obtained outside of this zone in order to get evidences of the chattering behavior based upon which unstable conditions are studied. It is only after decades of research on machining chatter that CNC machinists claim the regenerative effect as the main cause of vibrational instability in metal cutting. The research on robotic machining chatter is very young to provide such conclusive remark. However, as industrial robot manufacturers realize the potential of robotic machining, researchers have started to bridge this gap. To our knowledge, (Pan et al., 2006) has initiated an investigation on this issue by studying the fundamentals of the problem of vibrational instability for a compliant robot arm. The study mainly focuses on the mechanism of mode coupling instability for a robotic tool holder. Instability due to the regeneration mechanism for a robot arm that performs machining is only briefly discussed. The current chapter of this thesis deals with the problem of regenerative chatter for a compliant robot arm. From the practice of SCOMPI, it is observed that the chattering situation is made worse by a greater overlap of grinding trajectories and grinding multiple layers on top of one another. This suggests the probable existence of a self-exciting mechanism regenerating itself through the dynamics of the cut, i.e., the “regenerative chatter”.

Regeneration is the feedback mechanism between successive cuts. It is recognized as the main source of vibrational instability in machining operations (Tlusty and Polacek, 1963; Tobias and Fishwick, 1958). Overlapping cuts exist in the majority of cutting processes and therefore, it is the main source of vibration amplification in material removal. As compared

to other types of chatter, regeneration has the dominating effect based on the experimental studies such as (Kaneko et al., 1984) and (Marui et al., 1988b). A straightforward method based on the feedback control theory is introduced by (Merritt, 1965) to analyse the regenerative effect in machining as a closed-loop interaction between the tool holder's structural dynamics and the dynamics of the cutting process. The method has become very well adopted within the machining community and many researchers such as (Altintas, 2000b) and (Olgac and Hosek, 1998) have established their work based on a similar approach. In this section, the traditional approach is revisited to investigate the problem of regenerative chatter in the grinding process performed by the compliant robot arm under study. The previous chapters of this thesis dealt with the steady vibro-impact dynamics present in the robotic grinding process caused by the compliance of the robot. Vibro-impact motions of the grinding disk introduce discrete kinematics into grinding dynamics. The grinding operation is thus different from conventional grinding which has continuous kinematics and involves irregularities. The impacting regime of material removal in the robotic grinding operation under study brings regular kinematics into the process. The cutting impacts which occur once per turn and remain quasi-stationary regarding their angular position resemble the cutting events in a milling process performed by a cutter with known kinematics. Thereupon, the stability chart established in this section for the robotic grinding operation follows the methodology which is mainly used for milling operations. The purpose is to investigate the problem of regenerative instability, charted by stability lobes diagram, when the cutting process is performed by a compliant robot.

Dynamics of the cutting process is directly coupled to the dynamics of the holder structure. To have a measure of the dynamics of the holder structure, the receptance frequency response function of the tool holder is measured through modal testing. The robotic tool holder of this study was therefore put into the average configuration of a typical grinding task to be performed on $30cm \times 30cm$ workpiece specimens. Modal parameters of the first structural mode of the robot were extracted by exciting its end-effector with an instrumented hammer (PCB 086C04) along normal to the surface. The direct response of the holding mechanism is measured using a tri-axial piezoelectric accelerometer (PCB 356B21). Modal

Impact module of an LMS Test.Lab vibration analyser is used to identify the dynamic properties of the robot for a typical configuration. As results from the measured data, the damped natural frequency is $\omega_d = 4.8(Hz)$ and the damping ratio is $\xi = 3(\%)$. The measured receptance frequency response and the corresponding phase angle are shown in Figure 4.2. Contribution of this most flexible mode along surface normal can be represented by the SDOF dynamic model of the robot structure (see Figure 2.1e) as,

$$m_t\ddot{\delta}(t) + c_t\dot{\delta}(t) + k_t\delta(t) = F_N(t) \tag{4.1}$$

The dynamic compliance for this lumped-parameter model representing the robot structure with one degree of freedom is written in the Laplace domain as,

$$\frac{\delta(s)}{F_N(s)} = \frac{1}{m_t s^2 + c_t s + k_t} = G(s) + jH(s) = \Phi(s) \tag{4.2}$$

In Equation (4.2), $\Phi(s)$ is the receptance frequency response function of the structure as measured through modal testing on the robot's end effector. $G(s)$ and $H(s)$ are the real and imaginary parts of this function.

The resultant cutting force is related to the depth of cut by the dynamics of the cutting process. The steady-state cutting process is usually represented by a simple model for the normal cutting force as,

$$F_N = K_p h \tag{4.3}$$

in where K_p is the rigidity of the cut. The dynamic depth of cut, h, includes a desired value, h_0, plus a term to account for regenerative self-excitation.

$$h = h_0 + \lambda\left[\delta(t) - \delta(t-T)\right] \tag{4.4}$$

In the above, $\delta(t)$ and $\delta(t-T)$ are the displacements of the tool holder along surface normal in the current and previous cuts separated by one complete rotation, T is the revolution period and λ is the overlap factor. The transfer function representing the dynamics of the machining process can then be,

$$\frac{h(s)}{h_0} = \frac{1}{1 + K_p \lambda (1 - e^{-sT}) \Phi(s)} \tag{4.5}$$

The limit of stable cutting at $s = j\omega_c$ is formulated by (Altintas, 2000b) based on the characteristic equation in Equation (4.5) where ω_c is the chatter frequency. It gives a marginal value for the process stiffness as,

$$K_{p,\lim} = \frac{-1}{2\lambda G(\omega_c)} \tag{4.6}$$

Based on Equation (4.6), instability happens for $G(\omega_c) < 0$ because K_p should be a positive value. That means the onset of instability corresponds to frequencies greater than the natural

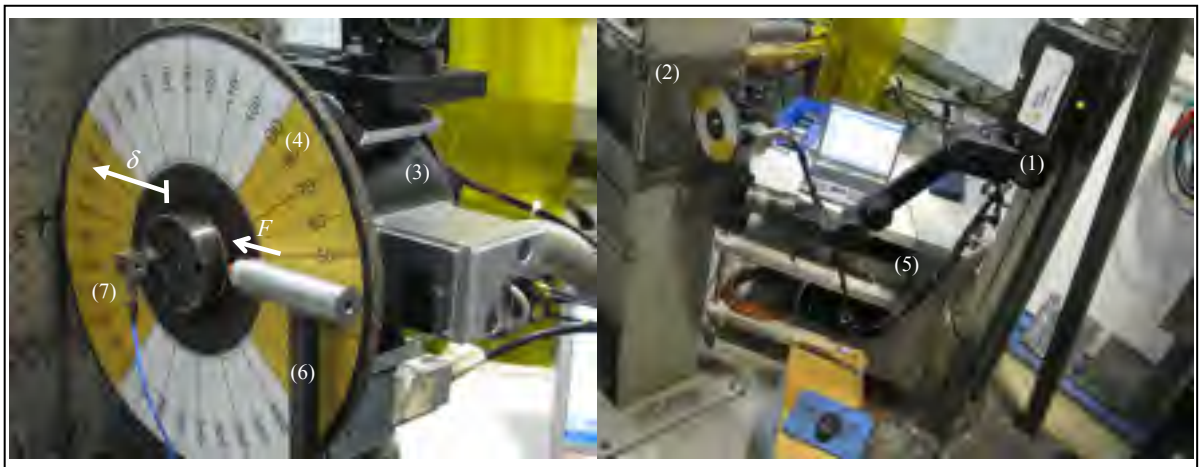

1. Robotic tool holder structure
2. Workpiece
3. Grinding tool
4. Grinding disk (cutter)
5. Vibration analyser
6. Impact hammer
7. Tri-axial accelerometer

(a) Setup for modal testing on the robotic structure

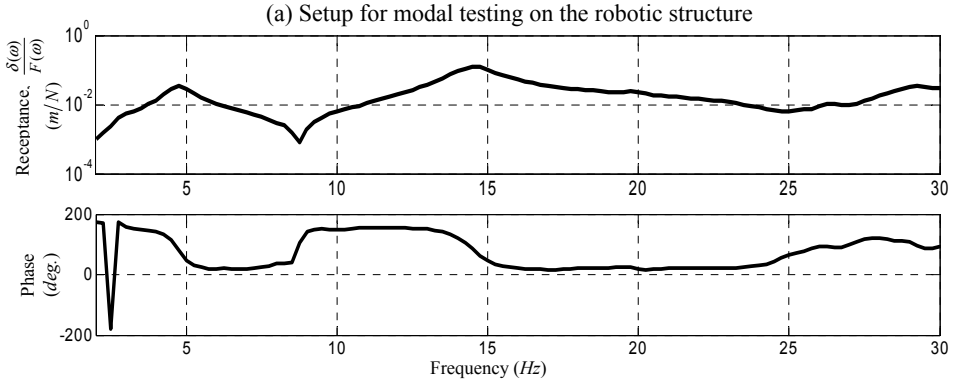

(b) Measured receptance frequency response and phase angle on the robotic tool holder structure

Figure 4.2 Impact testing on the robot's end-effector in an average grinding configuration

frequency of the robotic holder. The stability chart in Figure 4.3 is generated using Equation (4.6) and with the modal parameters of the SDOF equation described by Equation (4.1) and assuming $m_t = 21kg$. In grinding with SCOMPI, operational angular speeds are in the range of 6000-18000(*rpm*) and the natural frequency of the arm is generally smaller than 10 *(Hz)*. This feature distinguishes the problem of regenerative instability for a robotic holder from a conventional machine tool. To our knowledge, almost all of the existing research works about conventional machining chatter deal with the problem of instability which is located inside the "lobes zone" on the stability chart (see Figure 4.3). A discussion is provided on the problem of machining chatter at the two extremes of the stability lobes by (Ganguli, Deraemaeker and Preumont, 2007) but they have also not considered the region out of the lobes zone on this chart. A machining robot is located on the far upper right of the lobes zone where very large gain values $\lambda K_{p,\lim}/k_t$ are needed to cause instability (see Figure 4.3). Unlike robot machining, the stiffness of the machine-tool, tool holder, cutting tool and the workpiece are about the same order of magnitude in a conventional CNC machining operation. This intuitive feeling is well confirmed by looking at the lobes zone of the chart in Figure 4.3 where the ratio of the rigidity of the cut over the tool holder stiffness is less than unity $\lambda K_{p,\lim}/k_t \leq 1$. The few existing literature on robotic machining chatter have entirely overlooked this problem. (Pan et al., 2006) discuss this problem very briefly in their paper and interpret the large gain values as an unlimited stable cutting zone and conclude that regenerative self-excitation may not be the source of instability when using a robot for machining. A first look into a stability chart similar to Figure 4.3 plotted for a machining robot might give this misleading impression that robot machining is performed at higher angular speeds compared to conventional CNC machining. However, this is counter-intuitive since there exist CNC machining operations at very high angular speeds such as 20000 (*rpm*). The fact is, when this chart is plotted for a compliant robot that performs machining, it is the lobes zone which gets shrinked to the left side as compared to the location of the working point for the machining operation. The relative position of the working point with respect to the lobes zone on the stability chart plotted for robot machining should be compared with its equivalent on a similar chart plotted for a rigid CNC machine.

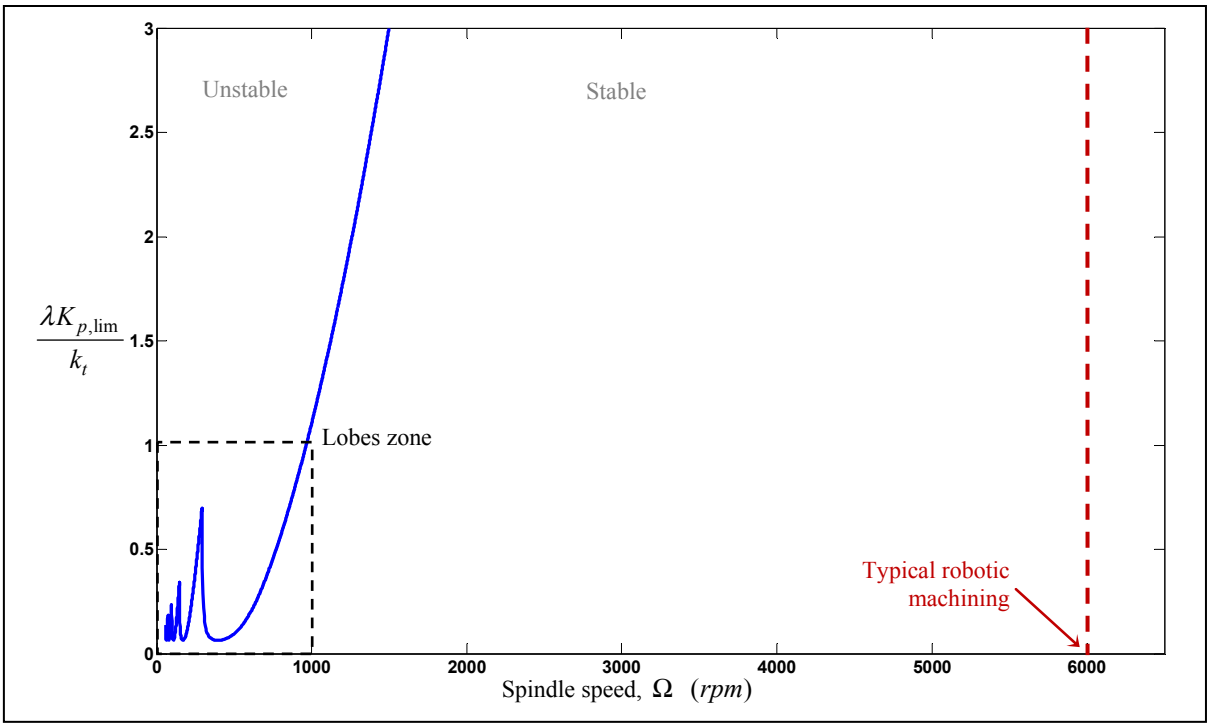

Figure 4.3 Robotic machining on the stability chart

A new perspective for the problem of regenerative chatter in robotic machining was elaborated through this section. The goal of this chapter is to understand if the stable cutting zone under the stability borderline can be considered as extensive for the practice of a compliant robot in machining. Since the large gain values for a machining robot are never experienced in conventional operations, the characteristic behavior for the operation under study, i.e. the cyclic impacting dynamics of material removal (impact cutting) from previous chapters is invoked to investigate instability in this region with more details.

4.2 Impact-Cutting Regenerative Chatter

The interaction between the dynamics of the cutting process and the dynamics of the tool holder structure is governed by Equations (4.2), (4.3) and (4.4). The interdependence is shown by the block diagram in Figure 4.4. The dynamic depth of cut, i.e. $h(s)$ in Equation (4.4), is the feedback tie in this self-exciting mechanism. The regenerative feedback path due

to overlapping cuts and the feedback of vibration displacement are the sources that constitute the self-excitation energy in the material removal process. Steady-state behavior of the cut is represented by $F_N = K_p h$ as a linearized model of the dynamics involved in the process of removing metal. One of the early studies who analyzed the steady dynamics of the cut by such model is (Merchant, 1944). In the Merchant's equation, the constant coefficient is called the static directional cutting stiffness or simply the cutting stiffness. It is a coefficient determined by the workpiece material and the tool geometry. There is not much involved from the cutting dynamics into this approach of modeling the resultant cutting force. However, using the linearized model for the resultant cutting force is very common in order to simplify the dynamics of the cutting process for the traditional analysis of regenerative chatter in machining. Cutting process dynamics have been studied by many researchers such as (Das and Tobias, 1967; Doi and Kato, 1956; Kegg, 1965; Shumsheruddin and S., 1962; Smith and Tobias, 1961). In our study, through the work presented in Chapter 2, the cyclic impacting nature of material removal (impact cutting) was introduced as an important characteristic of the dynamics involved in the cutting process caused by the tremendous compliance of the robot arm (small k_t). In Chapter 3, material removal through cutting impacts was studied with the help of an impact-cutting dynamic force model (F_N, Equation (3.21)). Through the discussion of regenerative vibrational instability in the current chapter, the conventional linearized model for the cutting process dynamics will be customized to

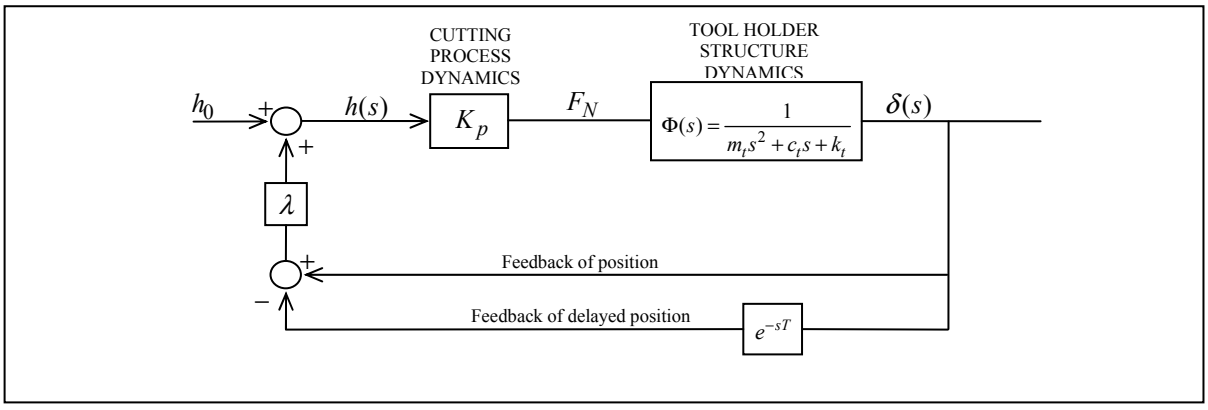

Figure 4.4 Regenerative chatter as a feedback loop

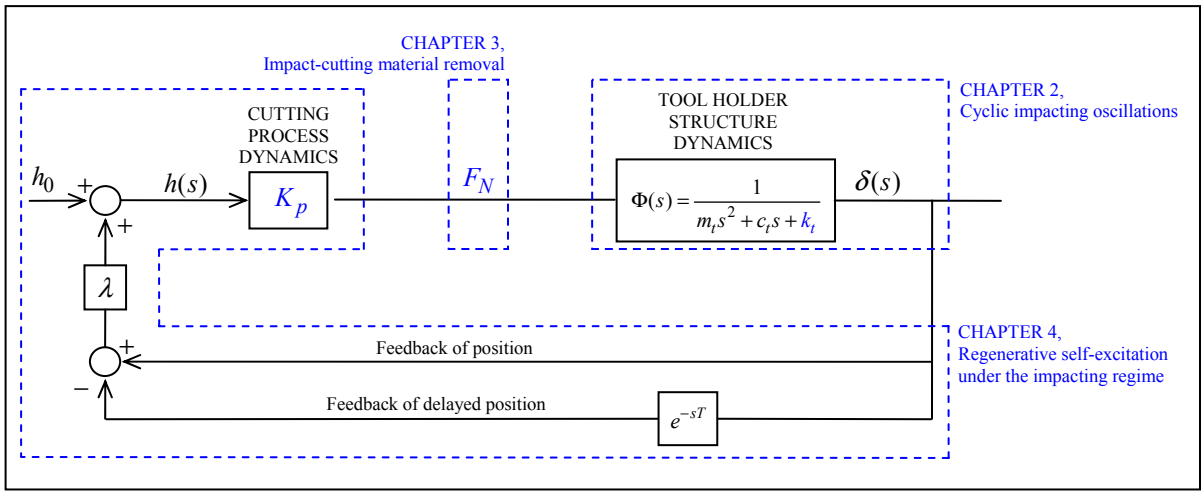

Figure 4.5 Revisiting the problem of regenerative chatter for robotic grinding

account for the impacting nature of the cut. Given the fact that the theme behind the whole work presented in this thesis is about the problem of chatter vibration in robotic grinding, Figure 4.5 is showing how the classical problem is revisited for robotic grinding through the liaison of understandings from different chapters.

4.2.1 Stabilized Impact Cutting

The tool holder's structural response to impact-cutting excitation is simulated in this section using a SDOF dynamic model for the robot. The purpose is to verify if the dynamic behavior of the system excited by this impulsive forcing function resembles a typical robotic grinding task performed by SCOMPI. The SDOF dynamic model shown in Figure 4.6.a represents the system at rest equivalent to the state represented by Figure 2.1.c. The system is excited by the instantaneous impact-cutting forcing function $F_N(\varphi, h_0)$ as in Equation (3.21). The angular position φ in this equation is replaced by $\varphi = \omega t$ (see Figure 3.7) in order to transfer into the time domain for numerical integration of the motion equation as,

$$m_t \ddot{\delta}(t) + c_t \dot{\delta}(t) + k_t \delta(t) = F_N(t, h_0) \tag{4.7}$$

A set of typical parameters is set for the robotic grinding task as $f_n = 6.6Hz$, $k_t = 17.2\,kN/m$, $m_t = 10kg$, $\xi = 0.1$, $c_t = 2m_t\xi\omega_n$, $\Omega = 6000rpm$, $R_0 = 115mm$, $E = 6.8mm$, $v_{fd} = 80\,mm/s$ and $\mu = 0.33$. Edge and cutting force coefficients $k_e = 148\ \ kN/m$ and $k_c = 5910\times10^3\ \ kN/m^2$ were identified from a comprehensive set of experiments which included robotic grinding tests using several different types of grinding products and under varying conditions. The identification methodology was the same as what was explained in Section 3.4.4 using a subset from these tests. Figure 4.6 shows the system's simulated response when removing three different depths h_0 of material through cutting impacts. The response

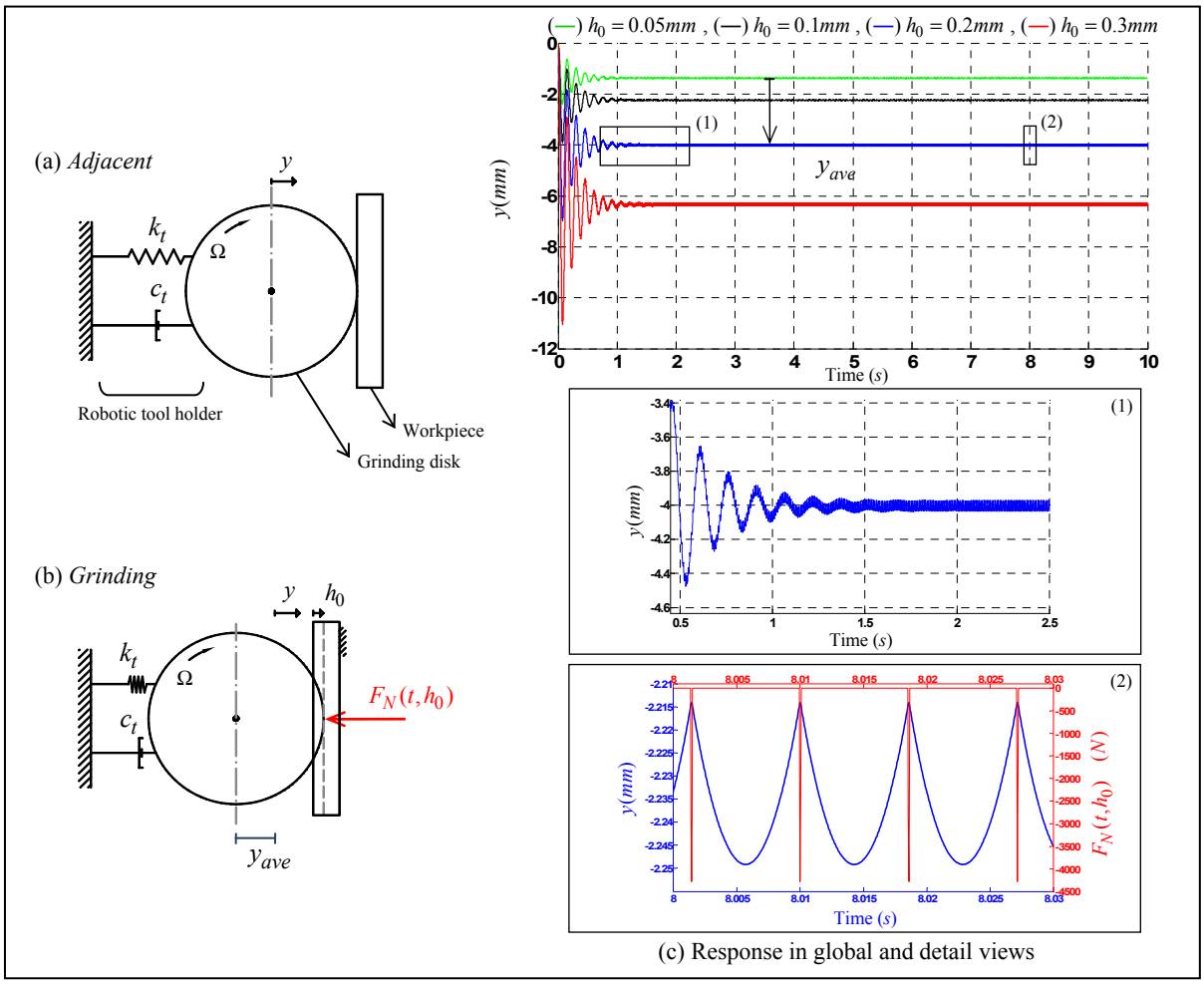

Figure 4.6 Stabilized tool holder's structural response to impact-cutting excitation

indicates natural frequency oscillations at the beginning as expected. When transients damp out, the harmonic response to the sequential impulsive force becomes steady around an average displacement y_{ave} which is found very close to the practice of the SCOMPI robot (see Figure 2.2 for an example). The detail view (2) in Figure 4.6.c shows that the dynamic response to the sequential impacting force stabilizes at a constant level. This means even though the wheel is bouncing from the surface once per revolution, it touches the surface at the same height in the following revolution as long as steady state is achieved. Therefore, conceptually, even if the cutter is a cyclic impacting oscillator due to being held by a compliant robot arm, removing a constant depth of material can be achieved. The work presented in Chapter 3 confirmed this fact with experimental verifications.

The average displacement y_{ave} that takes place under the impulsive excitation (see Figure 4.6.b) is equivalent to the compression Δl of the articulated bodies shown in Figure 2.1.d. The average value of the dynamic responses in Figure 4.6.b indicates that for cutting greater depths h_0 of material, the robot should provide larger pre-compression along its flexibilities. A further step in the development of the concept of impact cutting would be to include the self-excitation mechanisms. Studying the effect of self-excitation will identify how far it is possible to perform a cutting operation by a flexible robot and through repetitive impacts.

4.2.2 Unstable Impact Cutting

Regenerative self-excitation, caused by overlapping cuts, is the issue of growing cutting forces due to the growth of a cutting parameter. Similar to the discrete cutting events performed by the flutes of a milling tool, overlapping cutting impacts also cause regenerative self-excitation as illustrated in Figure 4.7.a. The dynamic depth of cut is defined as:

$$h = h_0 + \lambda\left[y(t) - y(t-T)\right] \tag{4.8}$$

The effect of steady vibro-impact oscillations appears in h by the desired depth of cut h_0 being removed through an impact-cutting regime as described in Section 4.2.1. Impacting

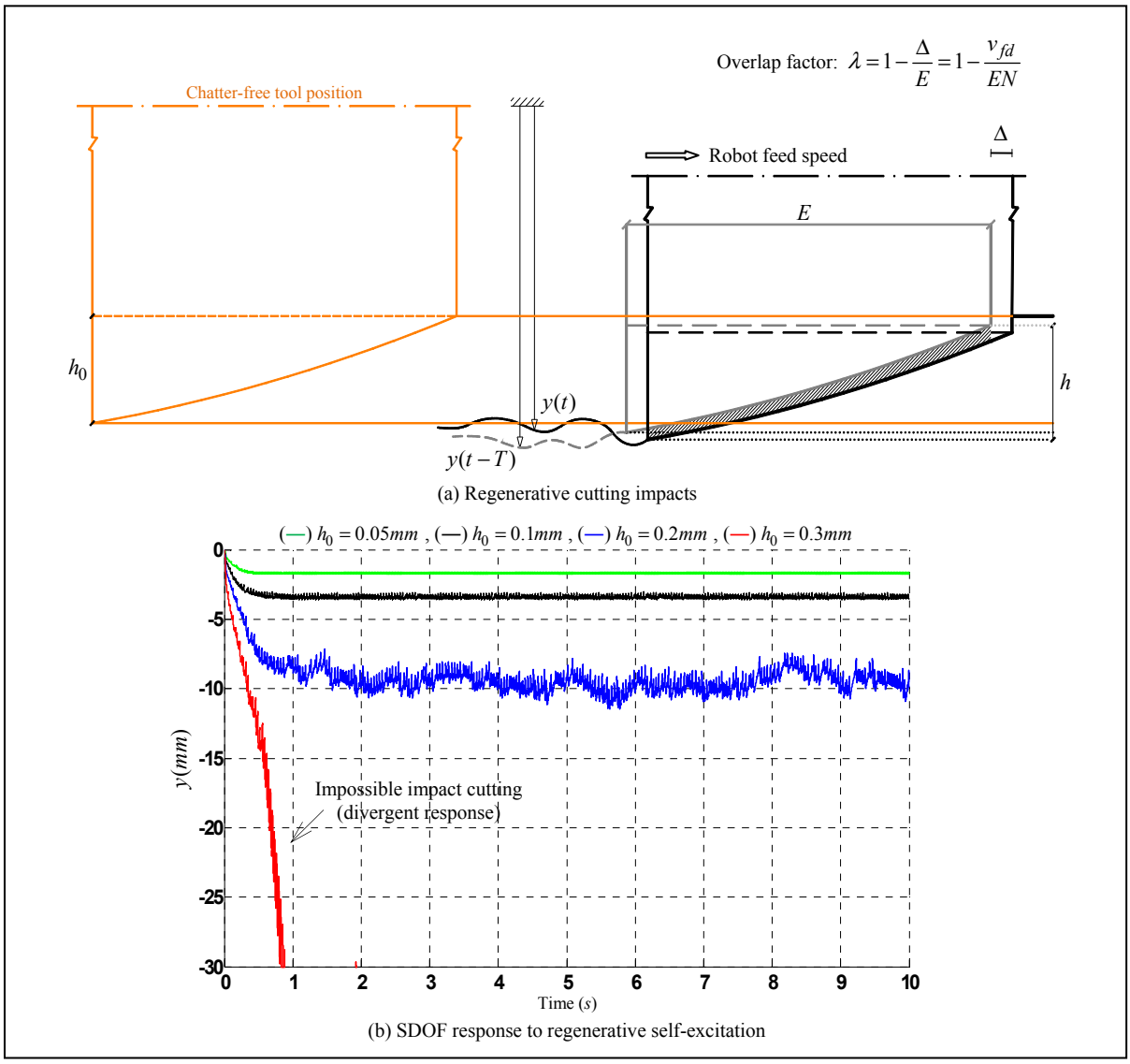

Figure 4.7 Unstable impact cutting

oscillations at the same height remove a constant depth h_0 from the surface of the workpiece. The regenerative term modulates the desired depth of cut considering $y(t)$ and $y(t-T)$, the present and past vibration amplitudes of the tool in the normal direction separated by one rotation of the grinding wheel in where T is the time delay. The overlap factor, λ, is the percentage of overlapping of two successive impacts. It is a function of the tool's advance per impact, Δ, and the width of the wheel, E. The dominant mode of one impact per

revolution of the grinding wheel is used in this study such that $\Delta = v_{fd} / N$, where N (Hz) is the angular speed of the wheel:

$$\lambda = 1 - \frac{\Delta}{E} = 1 - \frac{v_{fd}}{EN} \tag{4.9}$$

The overlap factor is $\lambda = 0.89$ if the parameters used to simulate the stabilized cutting operation are considered. Figure 4.7.b shows the response to regenerative impact-cutting force for the same values of the desired depth of cut h_0 as in Figure 4.6. Responses in this figure are obtained by numerical integration of Equation (4.7) when the excitation term $F_N(\varphi, h_0)$ is replaced by $F_N(\varphi, h)$.

For small values of h_0, the simulation results show that the cutting operation is stable, the cutting impacts stay regular and a uniform depth of material is removed from the surface. By increasing the desired depth of cut, the impact forces grow in a regenerative manner and the response becomes divergent. At the limit of stable responses in Figure 4.7.b impacts start becoming irregular. Eventually, cutting through impacts becomes impossible for higher h_0 values as seen in this figure. This is when the holder is not capable of restoring itself into the original position in response to the exerted energy into the system by one cutting impact and within the time interval it has until the following cutting impact.

4.3 Discussion on the Margins of Stable Cutting

Machining stability is studied by investigating the deformation errors caused by the cutting force (Altintas, 2000c). Likewise, robotic holder's response to the proposed impact-cutting excitation was found reasonable in Sections 4.2.1 and 4.2.2. It was demonstrated that even in presence of a vibro-impact dynamic response with a significant vibration amplitude, the response can stabilize around reasonable average deflections ($y_{ave} = 5 - 10mm$). Removing a constant depth of material with an acceptable surface waviness at each cutting impact under such conditions is therefore guaranteed (see Chapter 3 for experimental confirmation as well). Once the regenerative mechanism was invoked into the dynamic equation of motion,

simulated responses depicted the exponential growth of cutting force excitation in the machining operation as intuitively expected. In this section we discuss the margins of stable machining under the impact-cutting regime and compare it to the conventional approach for chatter analysis. The impetus for this work came when it was observed that vibrations when using SCOMPI in field operations could be alleviated by adjusting process-related parameters. Divergent vibrations about to disrupt the robot's task were easily suppressed by slight changes to cutting parameters. However, conventional regenerative chatter theory predicts an extensive stable cutting zone for a low natural frequency robot because the robot works on the far upper right of the first stability lobe (Pan et al., 2006)(see also Section 4.1).

4.3.1 Numerical Simulation of the Impact-Cutting Responses

The divergent impact-cutting response shown in Figure 4.7.b for $h_0 = 0.3mm$ never occurs in practice. Real grinding exercises with the robot remain way far from such margin. A realistic divergence criterion was therefore defined which resembled the practice of robotic grinding with SCOMPI. The criterion observed the mean y_{ave} and standard deviation y_{std} of the time domain response to impact-cutting excitation. y_{ave} is a measure of the holder's deflection while grinding (see Δl in Figure 2.1.d). y_{std} indicates the nonlinear response amplitude including all frequency components (super- and sub-harmonics) rather than a single frequency component corresponding to the excitation frequency. The margin of stability was identified at each spindle speed by increasing the desired depth of cut h_0 and verifying the simulated time domain response of the dynamic equation of motion for if $y_{ave} < -20mm$ or $y_{std} > 0.3mm$. Other system parameters used in the numerical simulation of the system's dynamics together with the results of simulation are shown in Figure 4.8.

The margins indicate the limiting depths of cut until which grinding through a permanent regime of impacting is possible. It is evidently concluded from this analysis that regenerative self-excitation limits the scope of stable impact-cutting and the marginal values of the depth

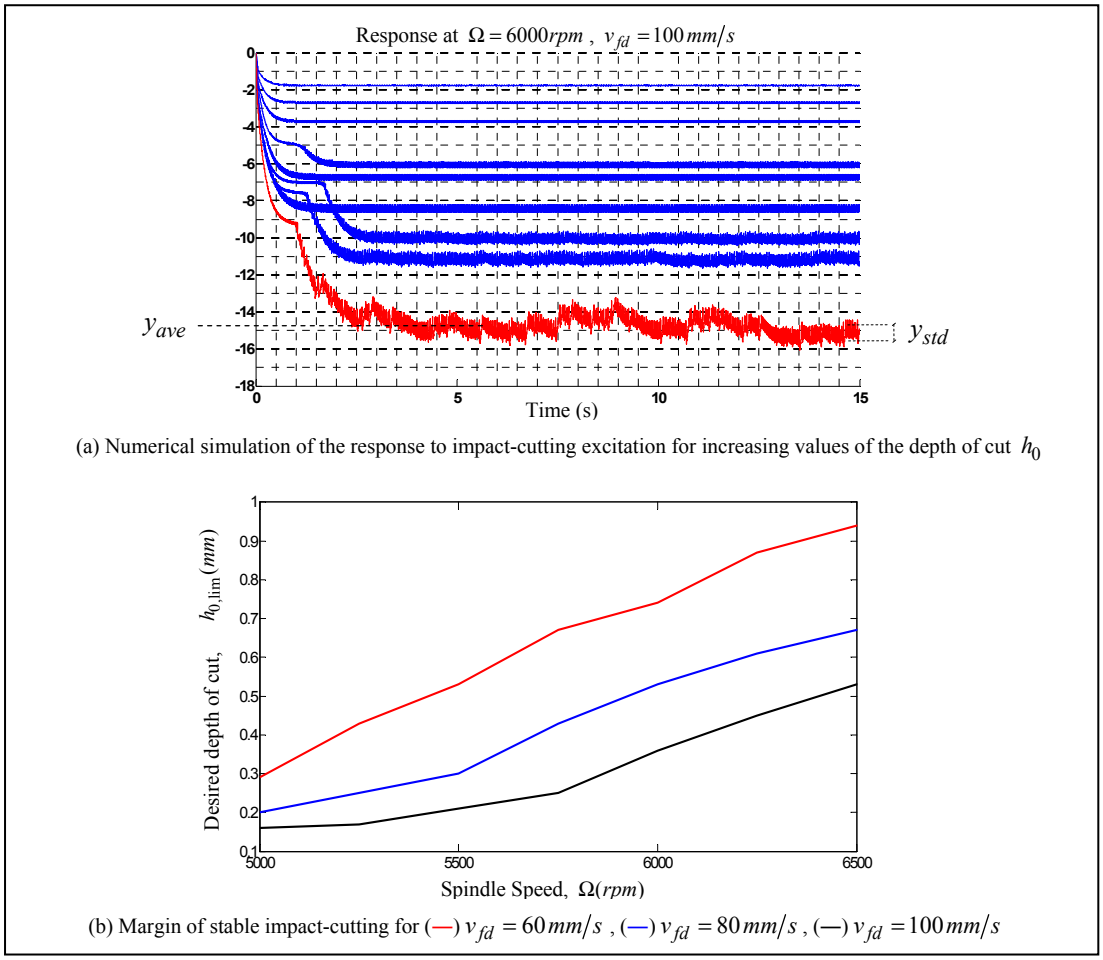

(a) Numerical simulation of the response to impact-cutting excitation for increasing values of the depth of cut h_0

(b) Margin of stable impact-cutting for (—) $v_{fd} = 60\,mm/s$, (—) $v_{fd} = 80\,mm/s$, (—) $v_{fd} = 100\,mm/s$

Figure 4.8 Practical margins of stable grinding with SCOMPI from numerical simulation ($\omega_d = 4.8Hz$, $m_t = 21kg$, $\xi = 0.0306$, $R_0 = 100mm$, $E = 7mm$, $k_e = 148\,kN/m$, $k_c = 5910\times10^3\,kN/m$, $\lambda = 0.9$)

of cut ($< 1mm$) are very small. We have found these values very close to the real practice of robotic grinding with SCOMPI. While this strongly suggests the existence of regenerative chatter in our operation, the following section compares this approach with the conventional approach for chatter analysis.

4.3.2 Linearized Impact-Cutting Model

In the new perspective drawn for the problem of regenerative chatter in robot machining through Section 4.1, it was demonstrated that conventional chatter analysis predicts very

large values for system gain at the margin of stability. The question was raised as how these large values of system gain should be interpreted. Given the fact that such large values have never been experienced in conventional machining, does it mean regenerative self-excitation cannot drive a robotic machining operation toward unstable cutting conditions ? This section gives a simple non-confirmative answer to this question by using the understandings from the previous chapters of this thesis integrated into the traditional approach for chatter analysis.

It should be clarified at this point that the significance of this investigation is not mainly about determining numerical values for the margin of stable machining. Stability lobes are the practical rule-of-thumb guides for machinists to setup a chatter-free task. They are the handy tool to deal with the nontrivial challenge of chatter in machining. The lobbed, tangent and asymptotic borderlines on these stability charts (see Figure 4.9) are progressively more important from the practical point of view (Merritt, 1965). Researchers deal with the lobed borderline because they are interested in exploring as much details as possible from the physics of regenerative self-excitation. However, the asymptotic and lobed borderlines define the limit for stable cutting within less than one order of magnitude difference in conventional machining (see the lobes zone in Figure 4.3). That is why, practically, it might be preferable to use the asymptotic borderline even if productivity is sacrificed. This is the ordinary usage

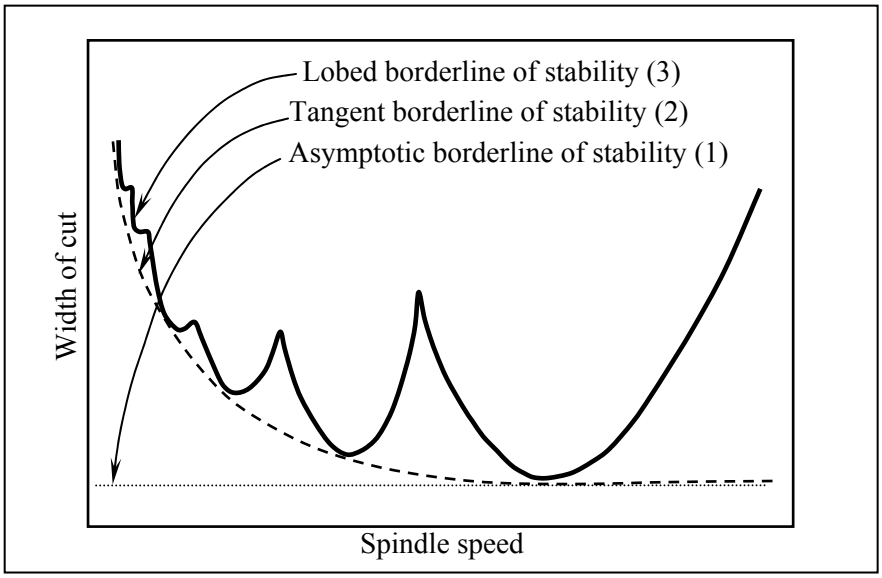

Figure 4.9 Practical importance of the borderlines of stability in machining taken from (Merritt, 1965)

of stability charts by machinists unless maximum material removal rates are crucial. Considering the location of the problem of robotic machining on these charts, such practice may not be exercised by robot machinists. The loss of productivity due to selection of cutting parameters below the asymptotic borderline seems to be tremendous. On the other hand, if robot machining is to be exercised close to the lobed borderline, based on the traditional chatter analysis which uses a linear model for the cutting force excitation, counter-intuitive large values for the cutting parameter are met. Numerical simulations of the impact-cutting operation in the previous section though, predicted reasonable values for the stable limit of grinding operation performed with a compliant robot. A linearized impact-cutting model is used in this section to compare the limits of stable cutting predicted in the previous section with the conventional analysis where cutting force is generally assumed as $F_N = K_p h$. The impact-cutting force in Equation (3.21) is averaged over a cycle of steady-state response assumed to be one complete rotation of the grinding wheel. This assumption is made referring to the experimental observations in Chapters 2 and 3 from the cyclic impacting oscillations during material removal occurring once per spindle revolution.

$$\bar{F}_N(h) = \frac{1}{T}\int_0^T F_N(\varphi, h) = \frac{1}{2\pi\mu}\sqrt{\frac{h}{R_0}}\left(k_e \frac{3}{\sqrt{2}} E + k_c \frac{v_{fd}}{N}\frac{4\sqrt{2}}{3} h\right) \tag{4.10}$$

Using the above means we assume that the cut is being performed continuously over all angular positions around wheel's circumference. However, this linearization does not ignore completely the impacting nature of the process. The excitation energy which is input to the holding mechanism with this average force model is equivalent to that from a cutting impact which occurs during a very small portion of the vibration cycle. An equivalent rigidity of the cut can then be formulated with this linearized model.

$$K_p = \left.\frac{\partial \bar{F}_N(h)}{\partial h}\right|_{h=h_0} = \frac{1}{2\pi\mu}\sqrt{\frac{1}{h_0 R_0}}\left(k_e \frac{3}{2\sqrt{2}} E + k_c \frac{v_{fd}}{N} 2\sqrt{2} h_0\right) \tag{4.11}$$

The rigidity of an impact-cutting operation that removes h_0 depth of material is therefore formulated as a function of the task parameters. Margins of stable impact-cutting can be then compared to the values predicted by the conventional chatter analysis. The results presented

in Figure 4.8.b for $v_{fd} = 80\,mm/s$ were once more simulated while an extra step was added to the procedure. Limiting values of the depth of cut, $h_{0,\lim}$ found from numeric simulations were translated into equivalent process stiffness values, $K_{p,\lim}$ using the formulation proposed for an impacting operation in Equation (4.11). Thereupon, system gain ($\lambda K_p / k_t$) was compared to predicted values from conventional linear approach as shown in Figure 4.10.

The existing literature on machining chatter is focused inside the lobes zone of the stability chart. That is because conventional machine tools provide rigid tool holders with their stiffness in the same order of magnitude as the rigidity of the cut. Equivalently stated, a gain of $\lambda K_p / k_t \le 1$ is typical in conventional machining. Using a robotic holder, we found that our study is located outside of the lobes zone and on the far upper right of the first stability

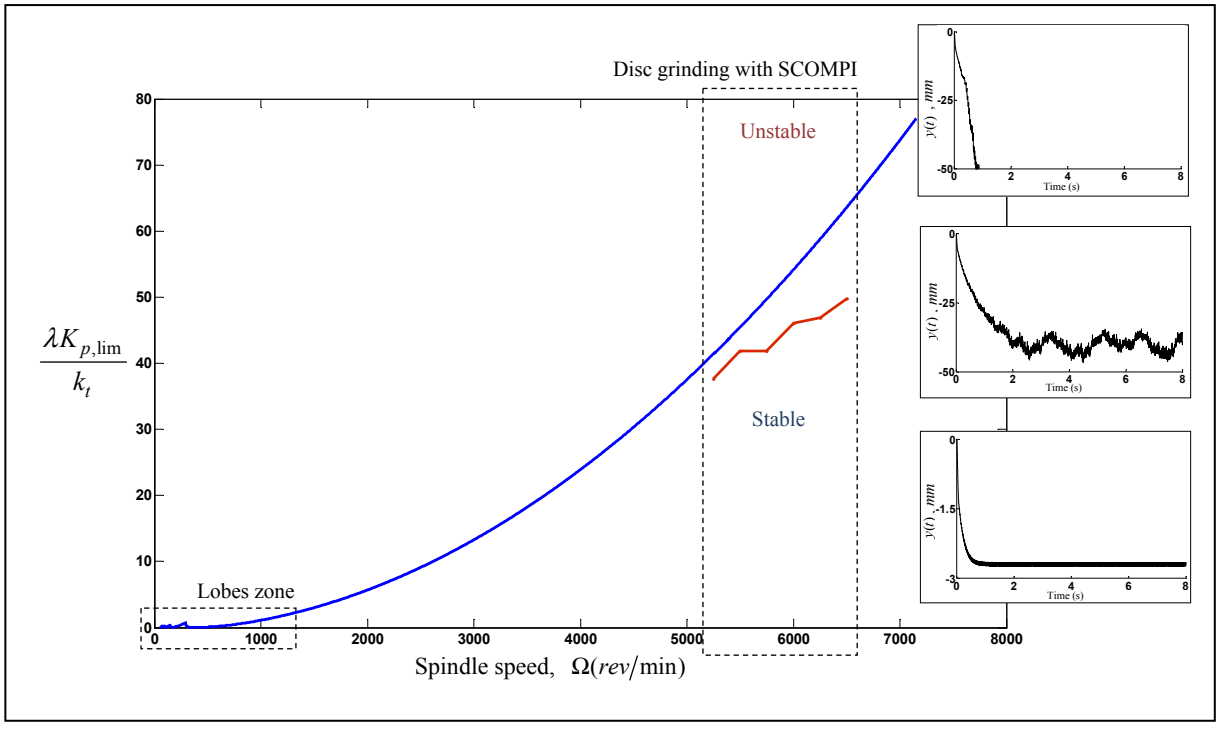

Figure 4.10 Marginal gain values for robotic grinding with SCOMPI from (—) Conventional chatter analysis (—) Impact-cutting regenerative chatter analysis

lobe where only large gain values may put the cutting process into unstable conditions. However, the results summarized in Figure 4.10 prove that the predicted high gain values are in fact presenting the usual practice of a compliant robot that performs grinding. The margins of stable cutting predicted from numeric simulation of an impact-cutting operation are found very close to those predicted by the conventional approach. This suggests the existence of regenerative chatter instability in the application under study. In other words, it indicates that the large values for the marginal gain, which are not experienced in conventional machining, are typical for the machining practice of a compliant robot arm.

4.4 Experimental Results

In the earlier sections of this chapter, the stable/unstable zone defined by the lobed borderline of stability around where a machining robot is located on the stability chart was discussed. A series of robotic grinding experiments are presented in the current section in order to demonstrate the existence of regenerative chatter in the practice of a machining robot and thus substantiate the discussion of the earlier sections qualitatively. The experimental setup and the procedures which were described in Section 3.4.1 are used to carry out the tests used for this section as well.

4.4.1 Tests

The tests presented in this section are single-pass robotic grinding experiments similar to what was described in Section 3.4.2.1 and shown schematically in Figure 3.10. The experimental series is planned such that some tests will be located under the stability borderline, in the stable zone, and some above, in the unstable zone. For the purpose of planning, nominal values which are set for the Tests 14-24 as listed in Table 4-1 are used. These nominal values are used to calculate the limit of stable cutting in terms of the process stiffness $K_{p,\lim}$ for each test. Average normal force F_m is maintained around $123N$ in all

experiments by adjusting the target grinding power P in the robot's control system. Normal force and grinding power are related as,

$$P = \mu F_m R_{0,m} \omega \tag{4.12}$$

where μ is an empirical friction coefficient, which is estimated around 0.3 by measuring the average normal and tangential grinding forces, and $R_{0,m} = 107mm$ is the measured disk radius. Robot's travel speed is set to $v_{fd} = 60\,mm/s$ in all experiments. The target cutting depth in each test is then given by using Equation (3.24) while setting $\bar{F}_N = 123N$ and solving to find h_0. The location of each test on the stability chart can then be demonstrated by predicting the rigidity of the cut under the impacting regime in that experiment using Equation (4.11) with the empirical coefficients $k_e = 148\,kN/m$, $k_c = 5910 \times 10^3\,kN/m$ and $k_t = 19.88\,kN/m$ which were used for numerical simulations in Section 4.3.1 as well. Figure 4.11 is showing the predicted positions for Tests 14-24 on the stability chart which was established in Section 4.3.2 (see Figure 4.10). As can be seen in this figure, Tests 14-18 are predicted, based on the linearized impact-cutting model, to be performed in the stable zone on the stability chart and Tests 19-24 within the unstable zone.

Table 4-1 Single-pass grinding tests to demonstrate the existence of regenerative chatter

	Tests										
Nominal values	14	15	16	17	18	19	20	21	22	23	24
Grinding power (W)	2500	2292	2083	1875	1667	1458	1250	1042	833	625	417
Rotational speed (rpm)	6000	5500	5000	4500	4000	3500	3000	2500	2000	1500	1000
Predicted values											
Depth of cut (mm)	0.32	0.31	0.29	0.28	0.26	0.24	0.22	0.2	0.18	0.15	0.12
Rigidity of the cut, K_p (kN/m)	387	408	434	463	499	544	600	675	779	939	1225
Grinder: *Permanent magnet electrical grinder,* $2.5kW$; Workpiece material: *1045 carbon steel*; Nominal feed speed: $60\,mm/s$; Grinding wheel diameter: $107.5mm$; Grinding wheel width $6.8mm$.											

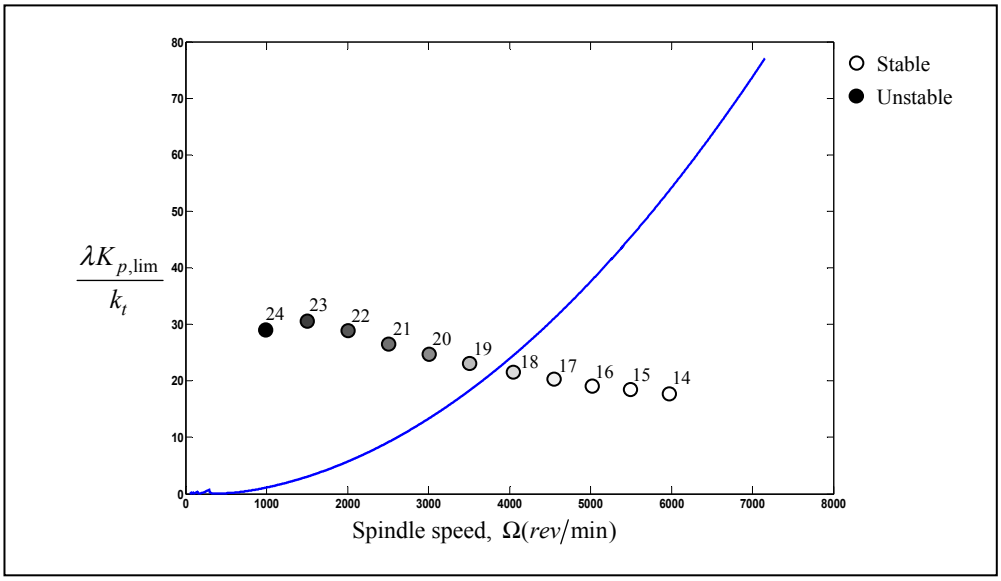

Figure 4.11 The working point for Tests 14-24 on the stability chart

A qualitative measure of the finished surface is captured after each robotic grinding test. A detail scan, as described in Section 3.4.1.1, is performed on the grooves created during tests. The middle lines of these scanned images are extracted (see Figure 3.13.b) for further investigation of surface waviness on the ground surfaces.

4.4.2 Experimental Evidence from the Stability Margin

In Section 3.4.3.3, it was demonstrated that cutting impacts leave a pattern of regular slots on the grooves created during robotic grinding tests. As long as the stabilized regime of impact-cutting is maintained, waviness of the finished surface stays regular and within an acceptable range as shown in Section 3.5 and Figure 3.21. Deterioration of surface finish is an indication of chatter in machining by the common sense. Figure 4.12.a is showing photographed images from the grooves created in Tests 14-24 together with some selected scanned images. As can be seen, the regular signature of impacting oscillations of the cutter in Tests 14-18 is evidently visible on both photographed and scanned images. These tests were located in the stable zone were stabilized impact-cutting behavior is expected. For Tests 19-24, which are located in the unstable zone of the stability chart, it is observed by visual inspection that the

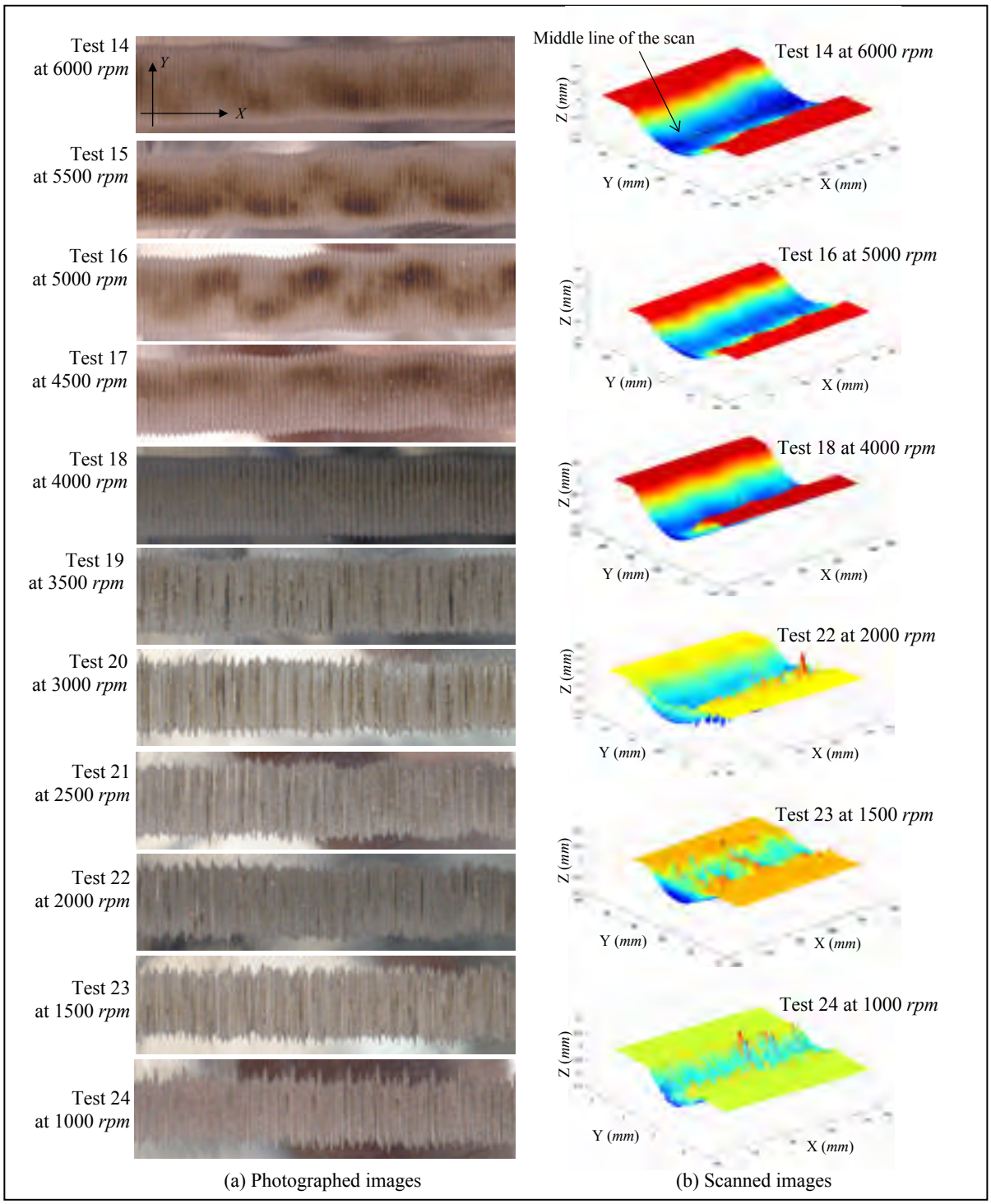

Figure 4.12 Visual inspection of the grooves created in Tests 14-24 for surface deterioration

finished surface has become irregular. This can be easily seen from both photographed and scanned images in Figure 4.12. In order to show this more clearly, Figure 4.13 is showing the

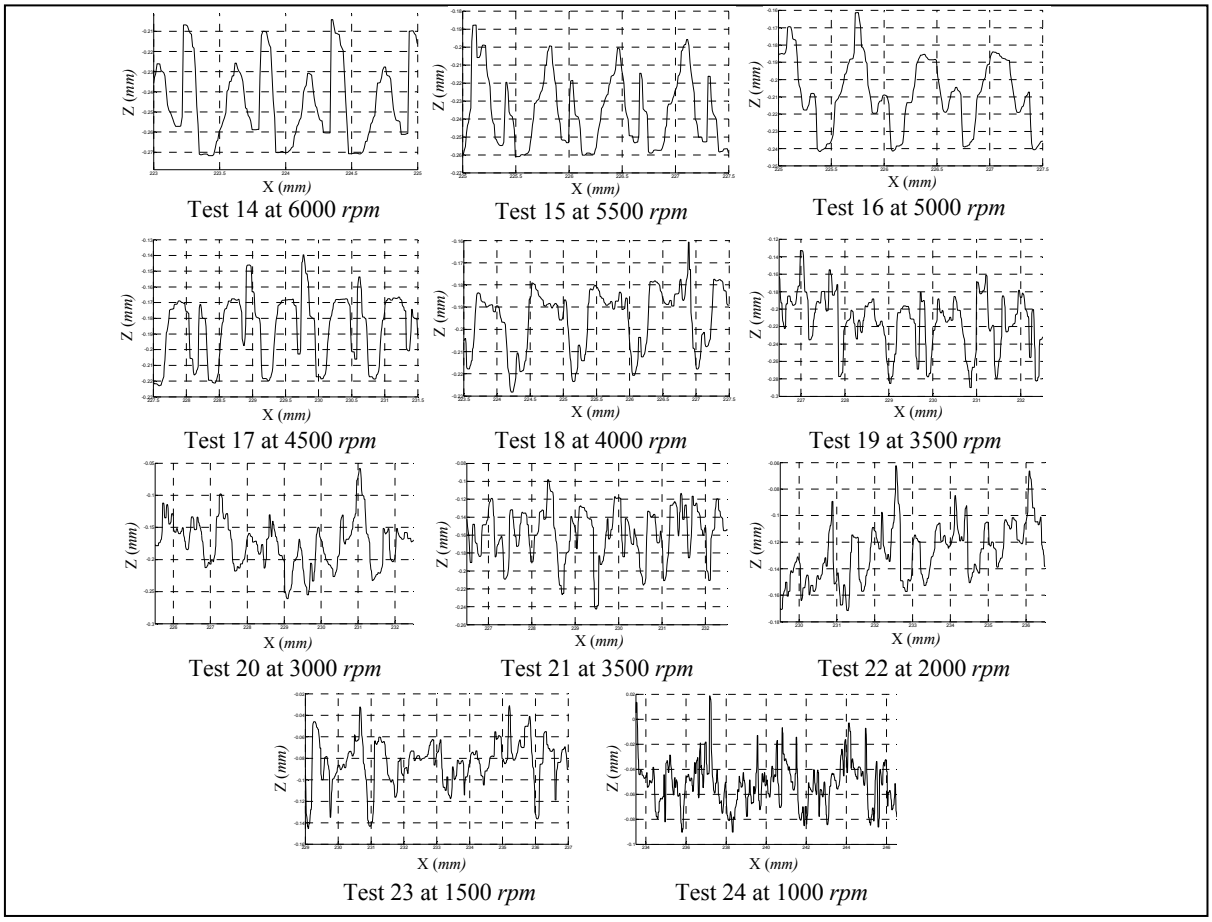

Figure 4.13 Deterioration of the regular impact-cutting pattern caused by regenerative chatter in Tests 14-24

middle line of the detail scan performed on the ground surface profile through tests 14-24. The regular pattern of the slots left by the impacting oscillations of the cutter is mostly visible in Tests 14-18. As the Tests 18-24 are carried out toward the unstable zone, the middle line starts to become irregular and it is hard to recognize a clear signature from the regular impacting regime of material removal on the ground surface. This is in a very good agreement with visual inspections and prediction of the margin of stable operation.

4.5 Summary

The traditional approach to analyse the problem of regenerative machining chatter is revisited for a compliant robot arm that performs grinding. The robot is put into an average machining configuration and its dynamic compliance is measured through modal testing on the end effector. The first vibratory mode from the measured dynamic compliance of the robotic tool holder is used to establish the stability lobes with respect to system gain, i.e., the ratio of cutting rigidity over robot stiffness. *Robotic machining is found located on the far upper right of the "lobes zone" where conventional machining is located on the stability chart. In this region, system gain is about two orders of magnitude larger than for conventional machining inside the lobes zone*. Such large marginal gain values are never met in conventional operations. The characteristic behavior for the operation under study, i.e. the cyclic impacting dynamics of material removal (impact cutting), is invoked to investigate instability in this region with more details.

A SDOF dynamic model for the robot is excited by the impact-cutting force and the stability of the simulated response is verified while increasing the depth of cut. Rigidity of the cut equivalent to the limiting cutting depths is then calculated based upon the linearized impact-cutting model. The margin of system gain plotted using these limiting values for the cutting rigidity is found very close to the margin predicted by the traditional approach. *It is thus concluded that the large marginal gain is typical for the machining practice of a robot*.

The above mentioned findings make intuitive sense since inside the lobes zone, the gain margin is less than unity $\lambda K_{p,\lim} / k_t < 1$. Regenerative chatter has always been discussed inside the lobes zone on the chart of stability because in a conventional CNC machining operation the elements in the machining chain composed from the machine tool, the tool holder, the cutting tool and the workpiece have about the same order of magnitude stiffness. Thereupon, rigidity of the cut is in the same order of magnitude as the tool holder's stiffness which results in less-than-unity marginal gain values for the operation. Tremendous compliance of a robot arm compared to the rest of the machining chain locates the problem

on the far upper right of the first stability lobe where large marginal gain values define the limit of stable cutting. *This is different from the traditional notion in dealing with vibrational instability due to the regeneration mechanism charted by the stability lobes diagram*.

An experimental investigation is carried out to substantiate the new perspective which is drawn for the problem of robotic machining regenerative chatter. The large marginal gain values predicted for the machining practice of a robot are to be verified through a series of robotic grinding experiments. In other words, the objective of the experimental investigation is to validate the existence of regenerative chatter when machining is performed by a compliant arm. A series of single-pass robotic grinding tests are planned such that some are located under the stability borderline, in the stable cutting zone, and some above, in the unstable zone. Deterioration of surface finish throughout the tests, which is an indication of machining chatter by the common sense is demonstrated by visual inspections and surface profile measurements.

CHAPTER 5

A 6-DOF Multi-body Dynamic Model for Vibration Analysis of the Articulated Structure of a Robot in Machining

5.1 Introduction

In the preceding chapters of the work, steady vibratory dynamics of the cutting process was investigated and instability of the vibratory oscillations caused by the regeneration mechanism was studied. After decades of research about chatter vibrations in CNC machining, it is generally accepted that the regenerative effect is the main source of instability as compared to other sources of self-excitation in the material removal processes. However, given the recently started research about chatter vibration in robotic cutting, such conclusive remark is not possible. Considering the robotic machining operation used for this study, there exist applications such as refurbishment of gate wheel tracks (Gagné et al., 2010) in which the machining trajectory does not involve too much variation of the robot arm configuration. The robotized process in such applications is used to grind multiple layers of material from the part. In this kind of application, regeneration can be the main source of instability. This is somehow confirmed by the intuitive sense because in practice, the vibratory situation would be made worse by a greater overlap of grinding trajectories and grinding multiple layers on top of one another.

The part of the work presented in this chapter is focused on a different line of research from the work which was focused on the vibratory dynamics of the cutting process and regenerative instability presented in Chapters 2, 3 and 4. However, the conducted research has still followed the main objective of the thesis, i.e. the study of vibrations and instability in a robotic grinding process.

Another well-known source of vibrational instability in machining operations, as briefly described in Section 1.2.2, is the mode-coupling effect. The effect appears in machining operations which involve at least two degrees of freedom. Robotic tool holders used for machining operations can be challenging examples for such case as well. The articulated multi-body structure of the robot introduces positional coupling at the end-effector point which also varies as the robot travels along task trajectories. The robot changes configuration enormously in order to perform machining along trajectories which access awkward locations or over complex geometries. Accordingly, the vibratory situation in regard to the mode-coupling instability varies which is a challenge for planning a chatter-free machining task. The robotic approach to improve turbine surface finish (Sabourin et al., 2010) or for interventions in hydraulic turbines (Sabourin et al., 2010) are examples for such case from the robotic grinding technology used in this study.

The recently started studies about robotic machining chatter such as (Pan et al., 2006) has indicated that the effect of mode coupling in a robotic machining process might be a major cause for instability. The coupling effect is not considered as a major issue in the studies of the structural dynamics for conventional CNC machine tools. For symmetrical machine tools, cross compliance is irrelevant and therefore, its effect is usually ignored for machine tool vibration analysis (Altintas, 2000a). A robot structure is not symmetric and its cross compliance may reach a considerable percentage of its direct compliance at some configurations. A literature survey related to dynamic analysis of robot manipulators is carried out by (Dwivedy and Eberhard, 2006). There exist some research works focused on multi-degree-of-freedom dynamic analysis of robotic structures with the objective as to investigate the vibrational performance in the robotic processes. Optimizing the compliance design of machining robots is one simple and effective solution to reduce vibrations (Asada and Goldfine, 1985). Using a guide mechanism can also increase robot stiffness so it can achieve higher accuracy under severe dynamic load conditions (Asada and West, 1984). Details of robot stiffness modeling and identification are introduced in (Zhang et al., 2005). They have performed static payload tests to identify robot joints' stiffness by measuring

external forces and corresponding robot deformations in order to estimate and compensate the deformations in real time and improve the overall machining accuracy.

In the current chapter of this thesis, we present a multi-body dynamic model for the robotic structure under study to be used for operational vibration analysis of the machining processes performed by this robot. The model is validated experimentally through modal testing and experimental modal analysis on the robot structure. A discussion is provided about how the developed modeling tool can serve an investigation of mode-coupling chatter in robotic machining.

5.2 Dynamic Model of the Robotic Tool-holder Structure

The track-based kinematic architecture of SCOMPI with six degrees of freedom is shown in Figure 5.1. The first axis is a prismatic joint translating on a track. The other five degrees of freedom are the displacements in the revolute joints numbered from 2 to 6. Two major sources can be considered for the flexibility of the robot structure; links' flexibilities and joints' flexibilities. An experimental investigation showed that nearly 80% of robot end-effector deflection is caused by the joints' deformations and track distortion for SCOMPI. Therefore, in the modeling that follows, we will consider only joints' flexibilities and the links are treated as rigid bodies. On the other hand since joints' flexibilities are measured experimentally, one can assume that the flexibilities of links are somehow included in the dynamic model of robot structure. Lagrangian formulation based on (Spong, Hutchinson and Vidyasagar, 2006) and (Tsai, 1999) was used to derive the equations of motion for SCOMPI in joint space, around $\{\boldsymbol{q_0}\}_{6\times1}$ which is a fixed configuration.

$$[\boldsymbol{D}(\boldsymbol{q_0})]\{\ddot{\boldsymbol{q}}\}+[\boldsymbol{C}]\{\dot{\boldsymbol{q}}\}+[\boldsymbol{K}]\{\boldsymbol{q}\}+\{\boldsymbol{g}(\boldsymbol{q_0})\}=\{\boldsymbol{Q}\} \tag{5.1}$$

$[\boldsymbol{D}(\boldsymbol{q_0})]_{6\times6}$ is the inertia matrix calculated for the fixed configuration, $[\boldsymbol{K}]_{6\times6}$ and $[\boldsymbol{C}]_{6\times6}$ are diagonal matrices of joints' stiffness and damping constants with zero non-diagonal entries,

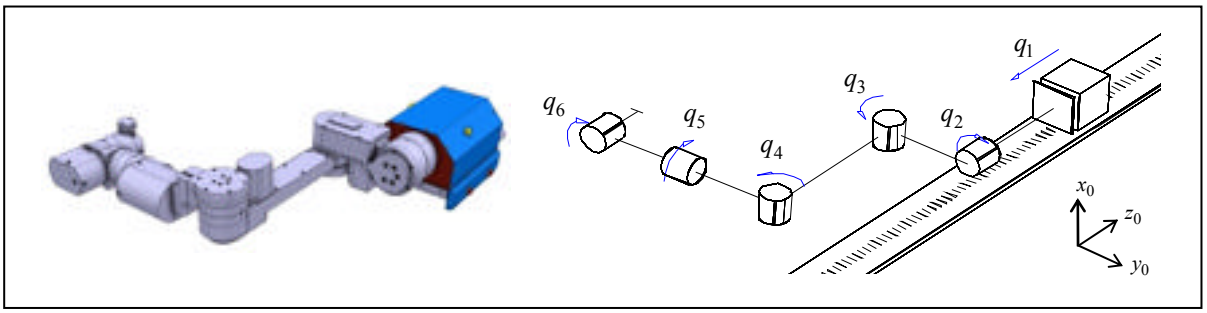

Figure 5.1 Track-based kinematic architecture of SCOMPI with 6-DOF

$\{\boldsymbol{g}(\boldsymbol{q_0})\}_{6\times1}$ is the vector of gravitational generalized forces and $\{\boldsymbol{Q}\}_{6\times1}$ is the vector of generalized forces.

In calculating the inertia matrix, links were approximated as solid members having uniform cross-section with centers of mass considered at geometric centers. Links' masses integrate the mass of the actuator and gearing mechanism. Flexibility is included at the joints based on the methodology suggested by (Spong, 1987). Diagonal values for $[\boldsymbol{K}]_{6\times1}$ are determined through payload tests experiments. The damping matrix is assumed as $[\boldsymbol{C}]=\beta[\boldsymbol{K}]$ where beta is a proportional coefficient. A larger value of beta represents more damping in the joints. In the simulations, a typical value of $\beta=0.001$ is usually used. This parameter can be also varied to observe the damping effect to the dynamic behaviour of the robotic system using simulations. A comparison to its measured behavior can allow us to find a proper value of this coefficient as well. Equations are governing the vibratory motion of robot structure about equilibrium. Nonlinear terms regarding Coriolis and Centrifugal forces are ignored because they only represent dynamics correlated to the slow motion of the arm as compared to high-frequency vibratory dynamics which is the purpose of this study. Details about derivation of dynamic equations for this model can be found in Appendixes A and B.

Joints' stiffness values to be included as the diagonal entries of the stiffness matrix were measured experimentally through payload tests. For the experimental measurement of joints' stiffness values, 4 robots, one from the 2nd generation and three from the 3rd generation of

SCOMPI were studied. For each robot 20 poses (position / orientation) in the workspace of the robot were chosen. At each pose, 4 masses of approximately 2, 4, 6 and 8 *kg* were suspended from the end of the robot and the deformations were measured. Half of the experiments were performed while the rail for the first joint of the robot was horizontal and the other half was performed with a vertical rail. This was to assure that we have better covered the workspace of the robot. A model assuming deformations only at joints was considered and a nonlinear optimization technique was applied to calculate the compliance of each joint. An estimate of the statically measured joint stiffness values are given as follows,

$$[\mathbf{K}] = \begin{bmatrix} 776.4\,kN\cdot m/rad & 0 & 0 & 0 & 0 & 0 \\ 0 & 6.75\,kN/m & 0 & 0 & 0 & 0 \\ 0 & 0 & 11.15\,kN/m & 0 & 0 & 0 \\ 0 & 0 & 0 & 12.72\,kN/m & 0 & 0 \\ 0 & 0 & 0 & 0 & 4.78\,kN/m & 0 \\ 0 & 0 & 0 & 0 & 0 & 3\,kN/m \end{bmatrix} \tag{5.2}$$

More details about the calculation methodology and the payload test experiments can be found in (Swiatek, Liu and Hazel, 2010). Once joints' stiffness values are measured experimentally, one can assume that flexibility of links is somehow included in the model virtually. Furthermore in comparison to methods of measurement of joints' stiffness in which each joint is loaded and measured separately meanwhile other ones are clamped as in (Abele, Rothenbücher and Weigold, 2008; Abele, Weigold and Rothenbucher, 2007), we preferred this method because this way the effect of flexibility of all links and joints are supposedly included in each individual measurement.

5.3 Simulation Results

A SIMULINK model in MATLAB was established to simulate the response of governing equations of motion to different kinds of excitations. These simulations were aimed to check if some initial predictions of the linear model of SCOMPI presented by Equation (5.1) are physically reasonable. Under zero excitation, the model predicted the static position of end-effector after transient parts of the solution were passed which corresponded to the last column of robot's transformation matrix. Static deflection was calculated to check if it

sounds reasonable. The response of model for end-effector position stabilized at a point displaced by 9 *mm* from original position. Under a constant vertical downward force of 200*N* and gravitational forces, response of model stabilized at a point displaced by 12.7 *mm*. These were checked to be very close to experimental observations.

5.3.1 Frequency Response Curves

Exerting only a uniaxial sinusoidal disturbance force, the frequency response curves (FRF) of robot structure as the tool holder mechanism of machining operation were established through the frequency sweeping technique. Figure 5.2 is showing some of such curves for excitation along x_0 and responses measured along x_0, y_0, and z_0 (i.e. FRF_{xx}, FRF_{xy} and FRF_{xz}). Simulation is done for the configuration shown in Figure 5.3 which is also used for experimental modal testing on the robot structure. Frequency response plots of the tool holder mechanism play the role of a dynamic characteristic for machining operation and can be used excessively in chatter vibration studies of the robotic grinding process. It is therefore

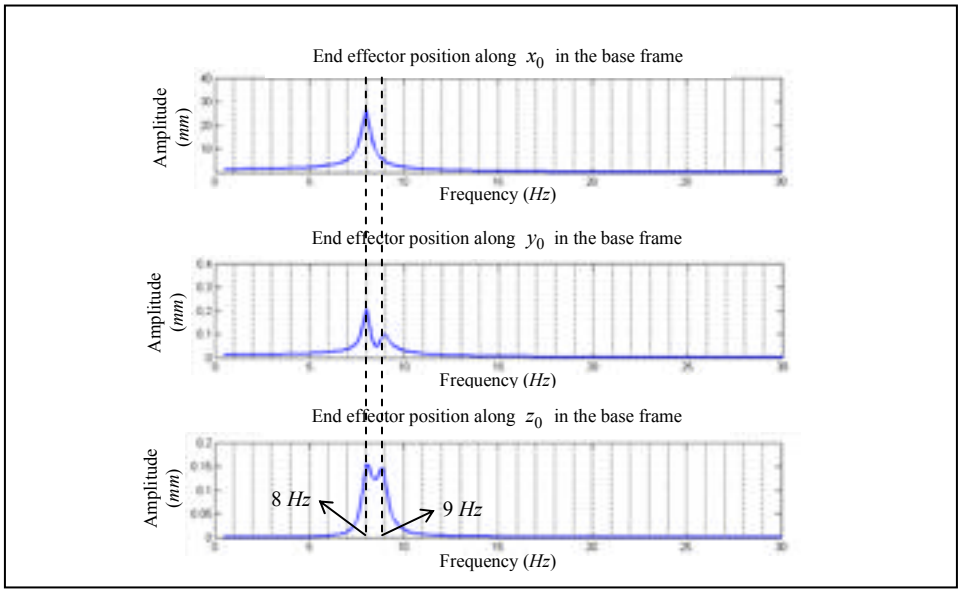

Figure 5.2 Simulated FRF plots for SCOMPI with sinusoidal disturbance excitation along x_0

Figure 5.3 Configuration of SCOMPI for modal testing experiment

very important for a dynamic model of the robotic grinding process to predict reasonable FRFs which match well with experimental measurements to whatever extent it is possible.

5.3.2 Mode Shapes

Experimental verification of the 6 natural modes of vibration predicted by the analytical model of SCOMPI will be addressed in Section 5.4. Investigating the match between model's predictions of these modes with measurements will assure us about the capabilities of the dynamic model to predict structure's dynamic behavior. The model is predicting only vibrating modes due to deflection of joints and more specifically, vibratory deflections only along articulations. This will be further discussed when comparing experimental measurements with analytical predictions but to this end, the eigenvectors of Equation (5.1) as the mode shapes of the structure are established as shown in Figure 5.4.a and Figure 5.5.a.

The vector of natural frequencies predicted by the model is $[8 \quad 8.93 \quad 21.02 \quad 29.85 \quad 162.28 \quad 327.99]Hz$. The mode shapes together with their corresponding natural frequencies will be compared to experimental measurements to assure

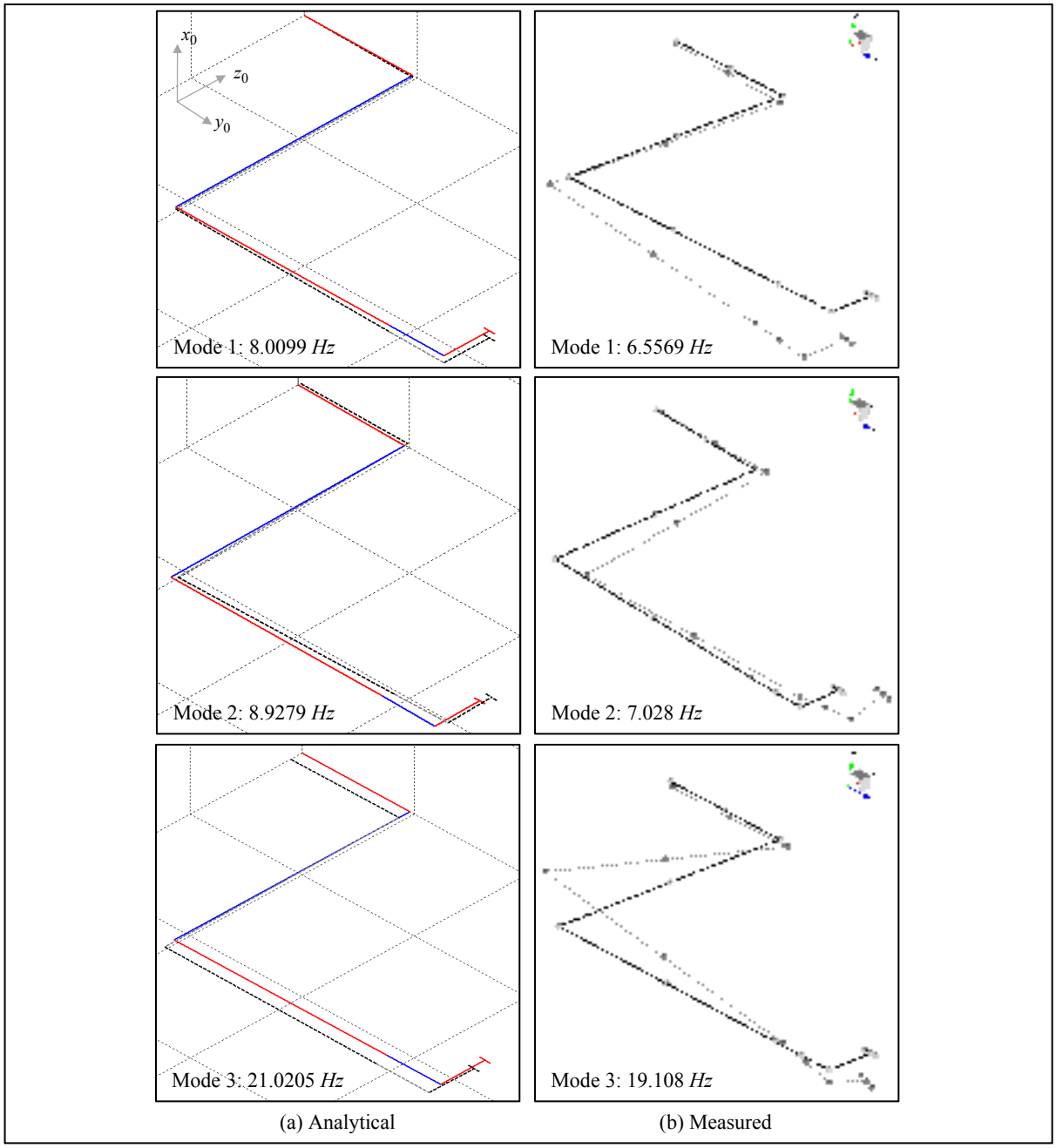

Figure 5.4 Analytical and experimentally measured mode shapes (modes 1-3)

us that the measured natural frequency is that of a mode which is due to deformations of joints along their joint variables, i.e., the modes which we were looking for. Experimental results about mode shape measurements are discussed in the following section.

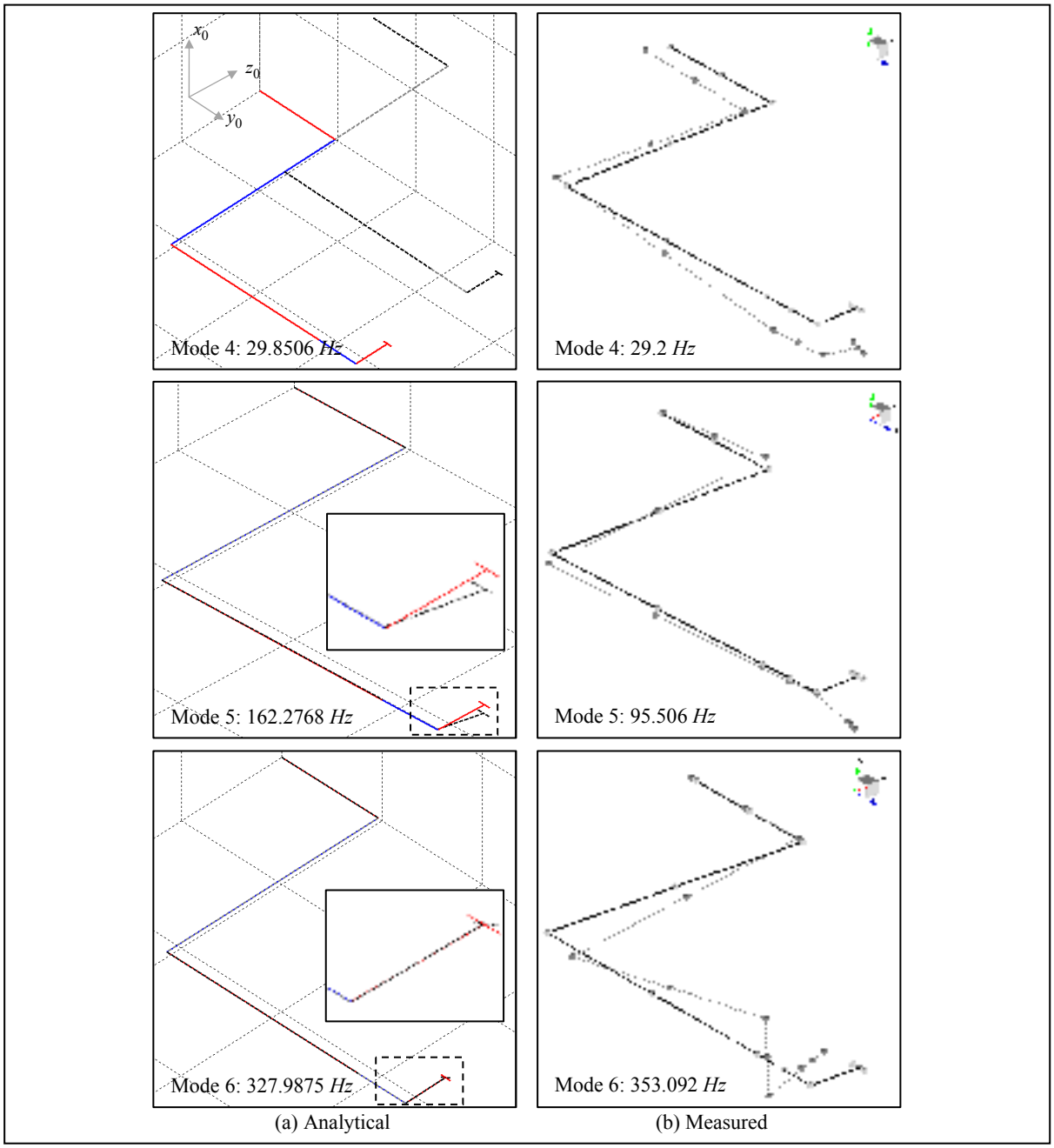

Figure 5.5 Analytical and experimentally measured mode shapes (modes 4-6)

5.4 Modal Testing on the Robot Structure

The dynamic model of the robot presented in the preceding sections of this chapter is developed for vibration analysis of the robot arm when it performs machining along trajectories which dictate considerable configuration changes. There are infinite number of vibratory degrees of freedom for a machine tool structure in cutting as shown schematically by Figure 5.6. Each vibratory mode i contributes into the oscillations of the cutter's end along a specific direction denoted by X_i in this figure. Among the infinite number of vibratory degrees of freedom, six (q_1 to q_6) are correlated to the articulated positions of the joints which define the arm's configuration $\{\mathbf{q_0}\}$ at each location on the robot's trajectory. Flexibilities along the equilibrium articulated degrees of freedom constitute the most compliant and therefore dominant vibratory modes of the system. Contribution of these vibrations at the end-effector point is thus dependent on the configuration of the arm $\{\mathbf{q_0}\}$ which exhibits considerable changes as the robot goes through machining trajectories. This feature is diagrammatically shown in Figure 5.6 by the varying spring elements and the

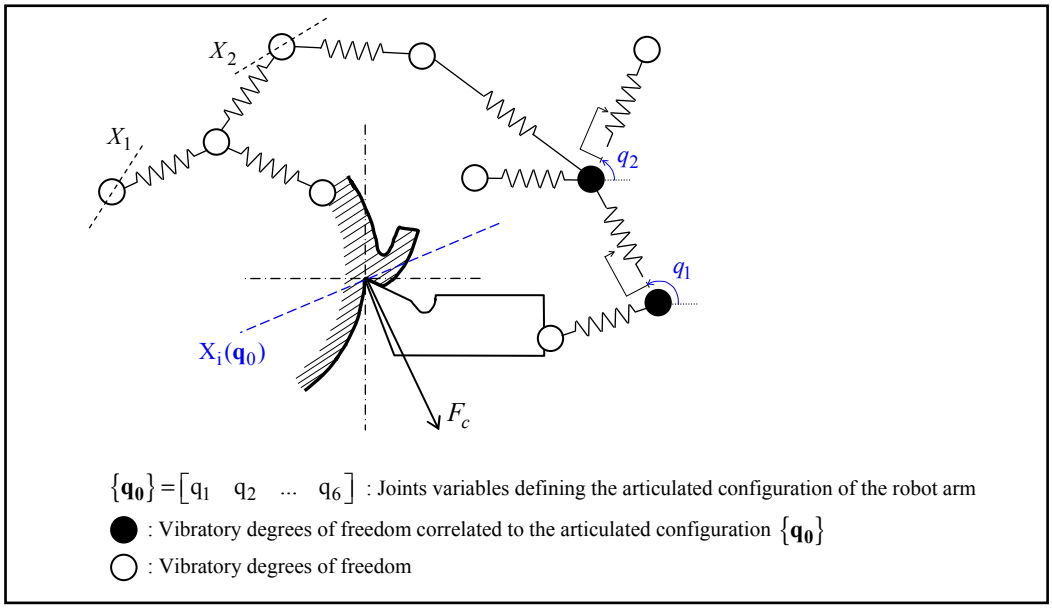

Figure 5.6 Vibrations correlated to the articulated degrees of freedom in a robotic cutting process adapted from (Tlusty and Polacek, 1963)

configuration-dependent mode of oscillation $X_i(\mathbf{q_0})$ at the end-effector point for these degrees of freedom. In order to analyse vibrations correlated to the articulated degrees of freedom, it is therefore important to pinpoint these vibrations from the structural vibrations of the arm. A straightforward method to reach this purpose is to compare the mode shapes of these vibratory oscillations with the mode shapes defined by the dynamic model of the robot because the model only considers the articulated degrees of freedom for vibrational behavior. Such attempt would also validate the dynamic model regarding its predictions of natural frequencies and mode shapes.

The mode shapes of SCOMPI were measured experimentally. An instrumented PCB hammer, PCB piezoelectric accelerometers and the Modal Impact module of an LMS Test.Lab vibration analyser were used for this test. The robot structure was tested at the configuration shown in Figure 5.3. This was the configuration around which the equations of the dynamic model were formulated. The objective was to distinguish the natural frequencies and mode shapes corresponding to the modes resulting only from deflection of joints from others due to links' flexibilities or else. This is a necessary need for the ongoing research work and is briefly discussed in Section 5.5.

In the modal test experiment for measuring mode shapes, for each link, 3 measurement locations, one at the middle and two at both ends were considered. The impacting excitation along the vertical direction at the end-effector point and the layout for attachment of accelerometers in this test is shown in Figure 5.7. At each measurement location, three accelerometers to measure vibrations along x_0, y_0, and z_0 were mounted as close as possible to the cross section of that link. The accelerometers were roved over the structure and by the help of the LMS Test.Lab software, mode shapes were calculated corresponding to all the existing measured peaks in the vibration spectrum of the structure response. From the whole set of measurements, a subset of six modes was selected based on the observed shapes for the vibratory modes due to joints' flexibilities predicted by the 6-DOF dynamic model as discussed in Section 5.3.2. The FRF sum together with its Mode Indicator Function (MIF) for 33 channels of measurement is shown in Figure 5.8 for a bandwidth of 0-500 *Hz*.

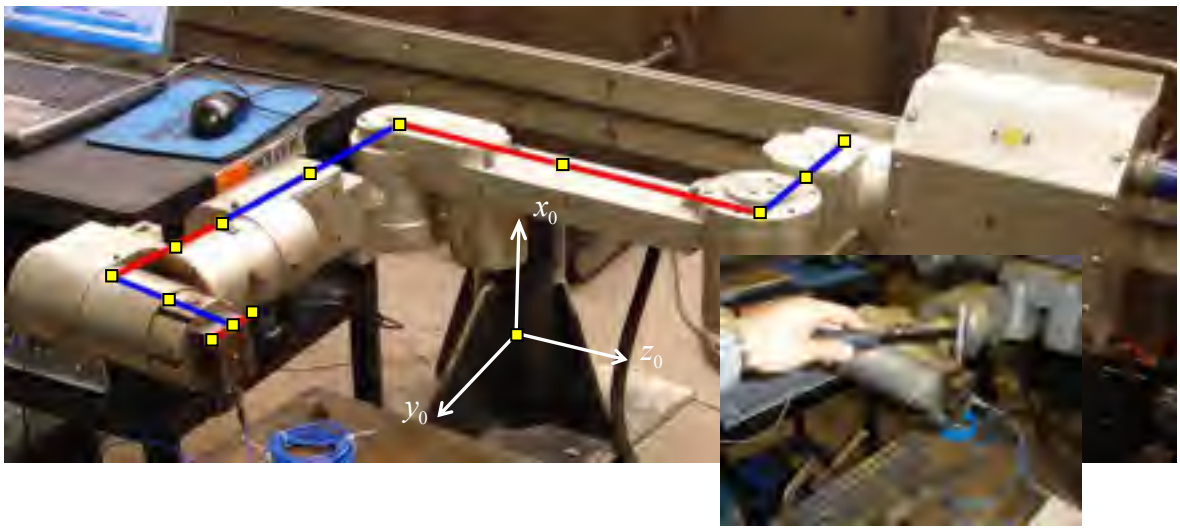

(a) Vertical excitation at the end-effector

(b) Attachment of accelerometers on the robot structure

Figure 5.7 Mode shape measurement on the robot structure

As shown in this figure, several high rising peaks in the FRF sum indicating several natural frequencies of the structure are visible. In among them, those corresponding to a local minimum of the MIF and also the criterion of stability based on consecutive order of

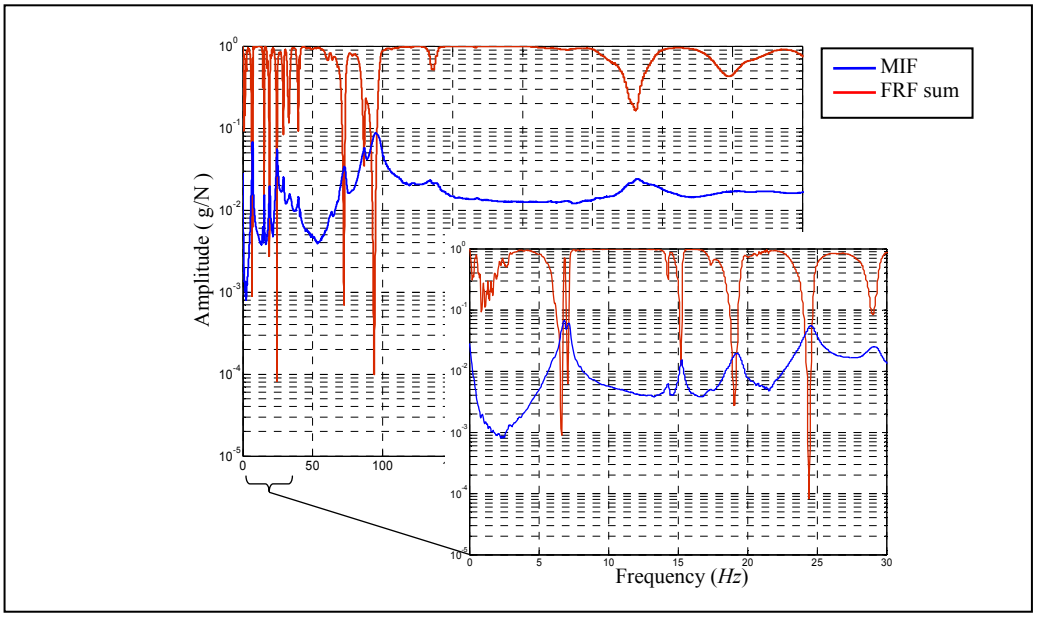

Figure 5.8 FRF sum and MIF for 33 measurement channels of the experimental modal test on SCOMPI

approximation in the stabilization diagram of LMS Test.Lab could have been considered as modes. These mentioned considerations were also further checked by looking at the mode shape itself and comparing it to the analytically predicted ones in Figure 5.4.a and Figure 5.5.a. The experimentally measured mode shapes together with their corresponding natural frequencies are shown in Figure 5.4.b and Figure 5.5.b. It can be seen from this figure that the first three measured vibratory modes are in a perfect match with analytical predictions in Figure 5.4.a and Figure 5.5.a. Both the frequency and the shape are very close to analytical predictions for the first two modes. The natural frequency of mode 4 matches very well with that of the analytical model and regarding its shape, it is also in a good agreement with model's prediction but may be not that much perfect as the first two. Regarding mode 5, the measured shape is very well agreeing with the corresponding analytical mode for that it is showing clearly the sound deflection of joint 5. However its natural frequency deviates somehow from model prediction. Mode 6 is also showing a relatively good match between analytic and measured shapes and natural frequencies. The sounder deflection of joint 6 relative to other joints in this mode is observed in both analytical and experimental illustrations. Based on these observations we can trust our initial multi-body dynamic model

of the robot structure as the tool holder mechanism of the machining operation for dynamic simulations. It is also demonstrated that vibrations correlated to the articulated degrees of freedom of the robot structure could be pinpointed with the help of the mode shapes.

The deviations can be first of all due to imperfections of the model. One of such could be the constant parameters including joint stiffness parameters which were measured by static payload tests as an intuitive estimation to start simulating with the dynamic model. Updating these stiffness values based on dynamic measurements to refine the model in order to predict the natural frequencies measured from experiment can be the next step of this work. Other imperfections of the model could be the many physical features involved in the real physical problem which were not considered in the model such as the flexibility of links or flexibility of joints along axes other than their own axis of excitation. The latter is obviously seen in experimental measurement of the mode shapes.

5.5 Discussion about Eigendirections of a Robot Structure

The structure of a robot distinguishes itself from many other engineering structures in the sense that it involves articulated degrees of freedom. Rigid-body motions of the robot structure including variations in the positions and orientations of the links are made using these degrees of freedom. The vibratory oscillations correlated to these degrees of freedom play the key role in the vibrational behavior of robotic processes. In the dynamic model which was established in this chapter, rigid members representing the links of the robot were assumed connected through spring and damper elements along the articulated degrees of freedom (q_1 to q_6 in Figure 5.9). Experimental validation of the dynamic model was carried out in the previous section through modal testing and analysis by comparing the predicted and measured eigenfrequencies and mode shapes of the structure.

The comparison between the measured mode shapes and predictions of the dynamic model was also aimed at distinguishing the vibratory modes correlated to the articulated degrees of freedom from other vibrational oscillations. As explained in Section 5.4, vibration

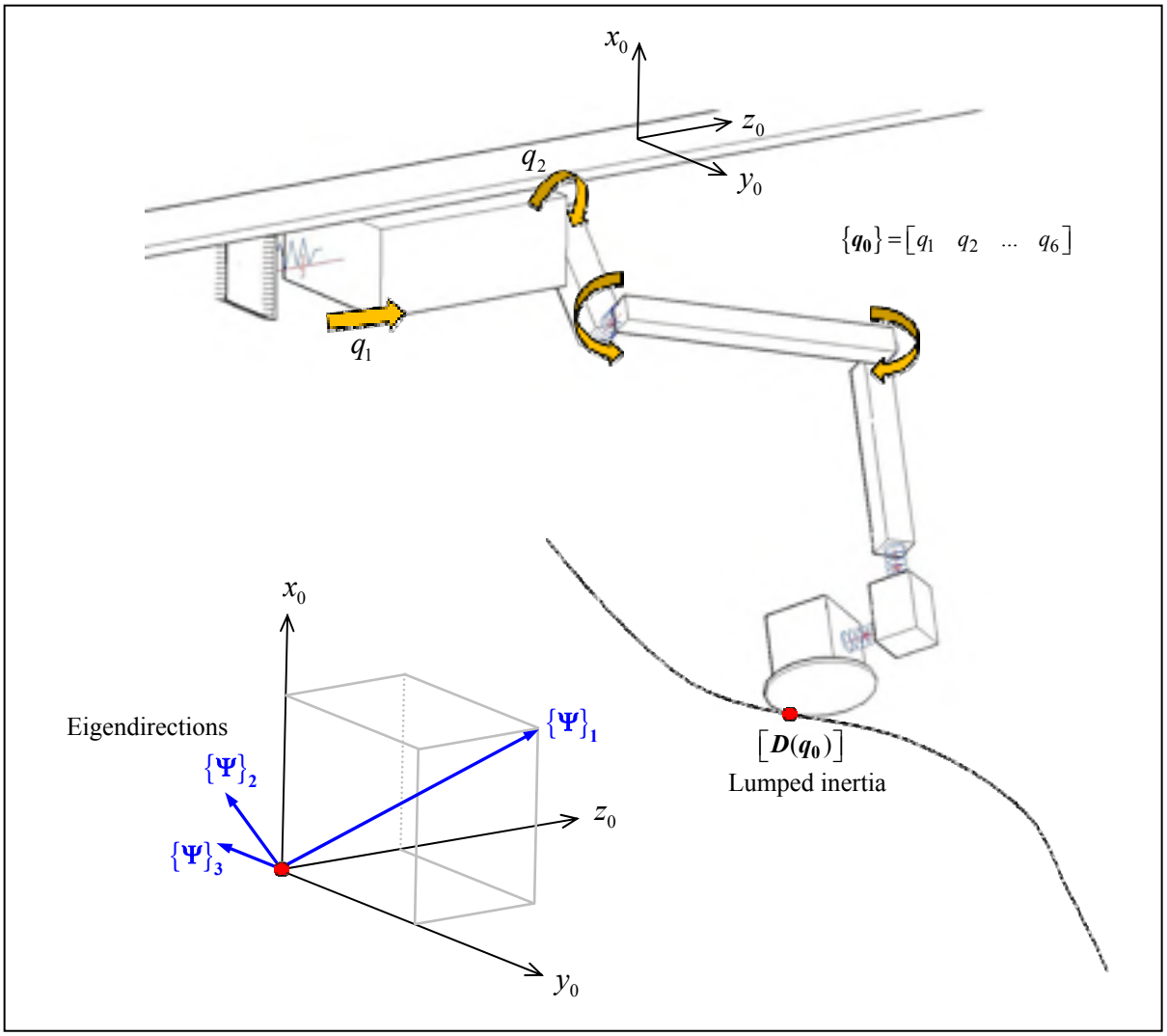

Figure 5.9 The eigendirections $\{\Psi\}_1$, $\{\Psi\}_2$ and $\{\Psi\}_3$ of an articulated multi-body robot structure

measurements over the entire structure of the robot were required for this purpose. Once the dynamic model is transferred into a Cartesian space at the end effector point, a similar procedure can be performed using vibration measurements only at the end-effector point. Inertia, stiffness and damping matrices associated to this point establish a set of dynamic equations that are dependent on the robot's configuration. The 6DOF vibratory oscillations at this point can then be decomposed into a set of decoupled single degree of freedom motion equations through eigendecomposition of dynamic equations. The eigenvectors of the dynamic equations then define three directions $\{\Psi\}_1$, $\{\Psi\}_2$ and $\{\Psi\}_3$ for the robot structure

at the cutter's end as shown schematically by Figure 5.9. As the robot moves along machining trajectories which dictate considerable variations of robot configuration, these eigendirections vary accordingly. Methods of operational modal analysis can be applied on the measured vibration signals captured on the end-effector point in order to identify these directions during the material removal process. Instead of dealing with the shapes for the robot structure's vibratory modes, as done in conventional modal analysis (Section 5.4), experimental analysis of eigendirections is proposed as an alternative which suits machining applications specifically. Eigendecomposition of systems and establishment of system theory based on eigenvalues and eigenvectors of vector spaces is used in many contexts. It has also been used to investigate mode-coupling instability (Gasparetto, 2000) for machine tool structures. Instability caused by the mode-coupling effect (see Section 1.2.2) is influenced by the orientation of the directions of the vibratory modes with respect to the cutting force. Varying structural modal properties in a robotic machining application makes this issue even more challenging. The developed modeling tool in this chapter can be used to extend this kind of analysis to deal with the vibrations of a robot's end-effector point in machining.

It should be emphasized that the part of the study which was presented in this chapter, unlike the work presented in Chapters 2, 3 and 4 is not considering grinding as the process being performed. The modeling tool and the understandings which were provided in Chapter 5 can be used in any material removal operation performed by the robot.

5.6 Summary

The structural dynamics of the robotic tool holder is studied in this chapter. A 6-DOF multi-body dynamic model was established for the robot manipulator under study. Main features were flexibility and damping at the joints with the links assumed to be solid members. Joints' flexibilities were measured experimentally by static payload tests. Predictions of the model under the action of some known forcing functions were checked to be reasonable. Natural frequencies and mode shapes of the robot structure as the tool holder mechanism of the machining operation were calculated based on this model. Modal testing experiments were

performed to measure the 6 natural frequencies and mode shapes of the robotic structure. *The predictions of the dynamic model from the vibrational behavior of the robot were found to be in a good agreement with experimental measurements*.

A discussion is provided at the end of the chapter using the understandings which were developed throughout dynamic modeling and experimental modal analysis of the robot structure. A so called “Eigendirection analysis” approach is proposed, as a customization to traditional modal analysis, in order to investigate the robotic tool holder’s structural dynamics during machining. In this approach, dynamic equations of the robot in the joints’ space for a given configuration of the arm, are transferred into a Cartesian frame defined at the tip of the cutting tool. The eigenvectors of the dynamic equations will then define eigendirections for the robot structure. Experimental modal testing and analysis can be used to identify these eigendirections for the robot structure rather than the shapes of the vibratory modes. The orientation of these eigendirections with respect to cutting force defines if the system becomes unstable under the effect of mode-coupling when machining.

CONCLUSION

This thesis presented a study on the vibrations and instabilities of the grinding process performed by a robot arm. The process is a new application which is under development at Hydro-Québec's research institute for maintenance tasks on hydropower equipment. The application is a high force task for heavy grinding operations aimed at profiling and reshaping of large parts/complex geometries. A compliant robotic tool holder is used in this process to provide the maneuverability which is needed to access awkward locations through its unique architecture. The everlasting challenge about vibrations in material removal processes is thus more serious in this application. The process is designed with special considerations in this regard then. For example, the grinding products used for manual operations are employed in this application because they are resistive to significant vibratory conditions. The strategy of controlled material removal rate is considered in process control rather than the strategy of position control generally used in conventional grinding performed by rigid machine tools. Robot manipulators are low force capacity tool holders which encounter serious challenges about vibrations when conducting the high force task of material removal. The grinding application under study is even a heavy material removal operation compared to conventional grinding processes. A trend of research has been started to bridge this gap by incorporating the vibratory dynamics present in the operation into the control strategy in order to overcome the existing challenges. The research work presented by this thesis contributes into this trend by providing a knowledge basis about the vibratory dynamics of the process and investigation of vibrational instability.

The effect of robot's low stiffness and natural frequency on the steady vibrations of the robotized cutting process was investigated in Chapters 2 and 3. The experimental study substantiated by numerical simulations revealed that due to the compliance of the robot arm, material removal is governed by cyclic impacting oscillations between the cutter and the workpiece. An experimental characterization was carried out on the "impact-cutting" material removal behavior which led to correlating the metal removal rate to the measured drop in the spindle's instantaneous angular speed during chip removal. In Chapter 3, an

impact-cutting model for material removal was validated experimentally with observations from robotic grinding tests. It was demonstrated that a uniform cut can be achieved in presence of high-amplitude vibro-impact dynamics of the process. The limit of stable impact-cutting operation defined by the regenerative self-excitation mechanism was investigated in Chapter 4. The investigation resulted into understanding that the tremendous compliance of the robot arm locates the problem of robotic grinding regenerative chatter out of the "lobes zone" and on the far upper right of the first stability lobe where large gain values define the limit of stable cutting. The cyclic impacting dynamics of the cut was invoked to explain the high gain values in this region for the robotic grinding operation under study.

A second line of research was conducted on the robotic tool holder's structural dynamics presented in Chapter 5. A 6-DOF multi-body dynamic model was developed for the articulated structure of the robot arm. Experimental modal analysis on the robot structure was used to validate the mode shapes and natural frequencies predicted by the dynamic model. A discussion was provided about how the modeling tool can be used for an investigation of mode-coupling chatter in robotic machining.

Contributions and Industrial Impacts

The contributions of this thesis together with the practical significance of the obtained results are listed in this section.

i. *Experimental investigation and characterization of the instantaneous dynamics of the grinding process performed by a compliant robot arm using angular analysis.*

The instantaneous cutting process performed by a compliant grinder robot was investigated experimentally. It was observed that the substantial compliance of the robotic holder makes robotic grinding an interrupted cutting operation governed by cyclic impacting dynamics in material removal ("impact cutting"). The investigation revealed that the discrete cutting events take place within a very short interval of the spindle period and for the rest of the revolution, the cut is interrupted. Unlike the common perception about cutting interruption as

a nonlinearity which occurs when the cutting tool vibrates unstably, it is concluded that the interruption of the cut happens frequently, on a regular impacting basis and thus can be considered as the steady vibratory dynamics of the process.

The impact-cutting behavior was characterized using the measured instantaneous rotational frequency mapped into a representation where revolutions during grinding could be compared regarding the angular position of the cutting impacts ("impact cutting map"). A plausible hypothesis for uniform disk wear in presence of the impact-cutting material removal process was verified experimentally.

The experimental methodology was proved capable of capturing the instantaneous variation in the spindle's angular speed during each cutting impact. The measured drop in angular speed was very well correlated to the grinding power which is an indicator of the metal removal rate. The setup can provide ongoing measurements of this transient at each revolution cycle. The practical significance of this result is considered as to integrate the real-time measurement of the speed drop and the number of impacts per spindle revolutions into the robot control strategy in order to improve the metal removal estimation.

ii. *Experimental validation of an impact-cutting model for material removal and performing a uniform cut in presence of the vibro-impact oscillations in the process.*

A conceptual analogy was drawn between the impacting nature of the interrupted cutting process and the vibro-impact dynamics of a generic impact pair. The qualitative analysis ascertained that the impact-cutting behavior present in the robotic grinding operation under study is inherent to the mechanical operation.

A modeling tool was then introduced to formulate the grinding force and consequently the required grinding power based on the impacting dynamics of material removal. Parameters of this impact-cutting model were identified experimentally. The target grinding power in the

controlled material removal rate strategy of the robot was set based on the estimation of the model. The impact-cutting model provided a very close fit with the observations from representative long-run robotic grinding tests performed iteratively. The model incorporates physical parameters from the impacting dynamics of the cut such as the number of cutting impacts per revolutions. Once real-time measurement of such parameter is obtained, the modeling tool can estimate the material removal rate during the process to be used in the robot control strategy. Appropriate knowledge from the vibratory dynamics of material removal increases the confidence level when task planning to remove the excess material in robotized surface profiling.

A detailed investigation was carried out on the grooves created during single-pass robotic grinding tests in order to verify the capability of the robotic grinding operation to achieve a uniform cut, i.e., a cut with a target depth, a target rate of metal removal and an acceptable surface waviness. It was shown that even in presence of significant vibro-impact oscillations, acceptable tolerance levels can be achieved on the machined part. Practical significance of this result is that robotic grinding tasks aimed at very fine tolerances can be achieved using the controlled material removal rate strategy coupled with an accurate measurement system that scans the ground surface profile in an iterative measuring/grinding approach.

The publication work related to contributions (i) and (ii) can be found in (Hazel, Rafieian and Liu, 2011; Rafieian et al., 2014; Rafieian, Hazel and Liu, 2013).

iii. *Investigation of the limits of stable impact cutting defined by regenerative chatter and experimental confirmation of the margin for stable operation.*

The knowledge about the steady vibro-impact dynamics of the cut in the robotic grinding operation under study is used as the basis for chatter analysis. The traditional approach to analyse the problem of regenerative machining chatter is revisited for the compliant robot arm that performs grinding. Stability lobes are plotted with respect to system gain, i.e. the

ratio of cutting rigidity over robot stiffness. The robotic grinding operation is found located on the far upper right of the first stability lobe. In this region, system gain is about two orders of magnitude larger than what is experienced inside the “lobes zone” where conventional machining is located. Such large gain values are never met in conventional operations.

The impact-cutting process is simulated numerically using a SDOF dynamic model for the robot structure. Regenerative self-excitation is considered with a single delay term accounting for the overlap of successive cutting impacts. The limits of stable robotic grinding within the practical range for spindle speed were obtained. System gain was plotted at these limits and it was found very close to the boundary defined by the stability lobes obtained from the traditional approach. It is thus concluded that the large gain is typical for the grinding process performed by the compliant robot arm. The findings make intuitive sense since inside the lobes zone, the system gain is less than unity. Regenerative chatter is usually discussed inside the lobes zone on the chart of stability because in a conventional CNC machining operation the elements in the machining chain have about the same order of magnitude stiffness. Thereupon, rigidity of the cut is in the same order of magnitude as the tool holder’s stiffness which results in less-than-unity gain values for the operation. Tremendous compliance of the robot arm compared to the rest of the machining chain locates the problem on the far upper right of the lobes zone where large gain values define the limit of stable cutting.

A new perspective is drawn for the problem of robotic grinding regenerative chatter with the understandings invoked from the cyclic impacting dynamics of the process. A series of robotic grinding tests are conducted in order to verify the margin for stable operation defined by regenerative self-excitation experimentally.

The publication work related to contribution (iii) can be found in (Rafieian, Hazel and Liu, 2014).

iv. *Development of a 6-DOF multi-body dynamic model for the articulated structure of a robotic tool holder in machining and model validation with experimental modal analysis.*

A 6-DOF multi-body dynamic model was established for the robot manipulator under study. Main features were flexibility and damping at the joints with the links assumed to be solid members. Joints' flexibilities were measured experimentally by static payload tests. Natural frequencies and mode shapes of the robot structure as the tool holder mechanism of the machining operation were calculated based on this model. Modal testing experiments were performed to measure the 6 natural frequencies and mode shapes of the robotic structure. *The predictions of the dynamic model from the vibrational behavior of the robot were found to be in an excellent agreement with experimental measurements*.

A discussion is provided about how the modeling tool can be used for an investigation of mode-coupling instability in robotic machining. Eigendirection analysis is proposed as a customization to traditional modal analysis on engineering structures in order to investigate the articulated multi-body structure of a robot arm during machining. In this approach, dynamic equations of the robot in the joints space are transferred into a Cartesian frame defined at the tip of the cutting tool. An inertia matrix will be thus associated to the end-effector point. Stiffness and damping matrices associated to this point represent the flexibilities and damping elements for the vibratory degrees of freedom. Eigendecomposition of dynamic equations defines eigendirections at the end-effector point of the robot structure. The orientation of eigendirections with respect to cutting force defines if the system becomes unstable under the effect of mode-coupling in machining.

The publication work related to contribution (iv) can be found in (Rafieian, Liu and Hazel, 2009). A study on the operational vibration analysis of the robot structure has also been conducted (Mokdad et al., 2011) related to this line of research.

Through items (i)-(iii), this research work contributed into understanding the vibro-impact dynamics that govern the process of grinding performed by a compliant robot. The origin of

the behavior was studied through dynamic modeling. The cyclic impacting oscillatory behavior was characterized experimentally with the help of angular analysis. A modeling tool which formulates the instantaneous impact-cutting force was validated experimentally. Robotized precision profiling of surfaces in presence of stabilized impacting oscillations is proved possible. Unstable impact-cutting condition caused by the regenerative effect was studied based upon the steady vibro-impact dynamics of the cut. Through item (iv), the thesis contributed into understanding the robot's structural dynamics that influence the vibratory oscillations of the robotized process. A multi-body dynamic model of the robot structure was developed and verified experimentally. The needed insight for investigation of mode-coupling instability with the help of this model was provided as well. The developed understandings and the analysis tools constitute a knowledge basis which serves the development of the new application under study. The research work is thus contributing into the development of robotized surface profiling for large/complex parts, with high accuracy level and involving heavy material removal. Several industrial sectors such as manufacturers of turbine runners and hydropower equipment as well as the maintenance operators of hydraulic utilities can be considered as the end-users of the research avenue suggested by this thesis.

RECOMMENDATIONS

The research work presented by this thesis might be continued through the recommendations listed in this part.

a) Cyclostationarity analysis of impact-cutting material removal in robotic grinding.

The impact-cutting regime of material removal may remain quasi-stationary regarding the number of cutting impacts per spindle revolution or the angular position of the discrete cutting events. However, due to the physical continuous kinematics of grinding, these are subject to random dynamics and cyclostationarity. Cyclostationarity is recognized as the characteristic of processes in which energy is conveyed on a cyclic basis based upon a generic variable. The strategy of controlled material removal rate employed in robot control for the operation under study is based on the grinding energy which is conveyed on the cyclic basis of the vibro-impact response period. The period is assumed to be commensurate to the spindle's revolution period. A great deal of information, useful for task planning, is hidden in this periodicity of the energy flow. The transients excited by the cutting impacts are another useful information source for identification purposes. The measured drop in the spindle's instantaneous angular speed correlated to the metal removal rate was one example of such transients (see Section 2.6). Another example is the natural torsional oscillations of the grinder's rotor during the flight times (the time between the sequential cutting impacts). These suggest that cyclostationarity analysis of impact-cutting material removal exhibited in robotic grinding can shed a much-needed light on these dynamic effects and provide new avenues for ongoing research.

b) In-process identification of the cutting force using a dynamic model for the grinder's rotor structure and the measured instantaneous angular speed.

The developed experimental methodology for the measurement of instantaneous angular speed may still be improved. The measurement precision with the current setup ($\approx 0.3\%$) is in the same order of magnitude as what is to be studied about the drop in angular speed during cutting impacts ($\approx 1\%$). Even though the results could clearly indicate the major impacting regime of material removal once per spindle revolution in the process, it is still difficult to discuss the minor impacts based on these readings. This line of research should be pursued toward increasing the precision of the setup. With a higher-precision test setup, it might be possible to capture the impact response of the grinder's rotor structure after each cutting impact. Once a dynamic model of the rotor structure is established in the angular domain, its parameters can be identified from the online measurement of torsional oscillations. The experimentally identified model from operational measurements together with the measured torsional response can then be used to estimate the cutting force instantaneously during the operation. If the robot control strategy is established based on the instantaneous grinding force rather than the grinding power, a more precise measure of the metal removal process will be used. The chance for having better control results will be higher which consequently reduces the number of grinding/measuring iterations to reach the desired tolerance level on the finished surface.

c) Nonlinear analysis on the periodic motions of the cutter as an impact oscillator

The cutter held by a compliant robot arm in a robotic machining operation is the limit case of a bilinear oscillator, i.e., an impact oscillator. Bilinear oscillators describe the dynamics of engineering systems in which the return forces have different magnitudes in tension and compression. The periodicity of impact times, the structure of resonances, instabilities, modeling of impact forces and generally speaking, the nonlinear dynamics of impact oscillators have been the subject of extensive theoretical and experimental research work in the past. The reason is, a wide range of applications is described by the strongly nonlinear non-smooth differential equation of the impact oscillator. The time scale of impact in all applications is much smaller than the time scale of the natural frequency oscillations of the oscillator. The existing research work can be well adopted to further investigate the dynamics

present in the impact-cutting material removal process in the robotic grinding operation under study.

d) Implementation of the impact-cutting map as a chatter monitoring tool during robotic grinding tasks to investigate the dynamic evolutions in the regime of material removal.

The impact-cutting map which was established in Section 2.4.4 using the measured rotational frequency during two-pass robotic grinding tests provides, in one look, a measure of the impacting regime of material removal occurring once per spindle revolution. Once the procedure for creating this map from the measured data is equipped with high computational power, the map can be used as an online monitoring tool during long-run robotic grinding tasks. It will be then possible to observe the dynamic evolutions in the impacting regime of metal removal and correlate the observations to the aggressive chattering conditions developed while robotic grinding.

e) Study of the effect of multiple and time-varying delay terms on regenerative chatter in the robotic grinding process under study.

From the practice of robotic grinding with SCOMPI, it is known that the vibrational situation and the issue of instability become worse when grinding is performed along more overlapping grooves. Vibrational behavior progressively deteriorates when grinding layers of material on top of one another. The machining trajectory and thus robot configuration remain unchanged under such conditions. This suggests further investigation on the effect of regenerative self-excitation in the robotic grinding process. In this thesis, a single delay term that represented the overlapping cutting impacts occurring once per spindle revolution was presented when dealing with the problem of regenerative chatter. Overlapping cuts of several other forms exist in reality which can be the source of instability observed in operation. Multiple delay terms represent overlapping of a cutting impact with the preceding impacts. Time-varying delay terms represent overlapping of two grinding passes as robot travels along

the grinding trajectory. They can also represent grinding layers of material on top of one another.

f) Investigation of mode-coupling instability in robotic machining using experimental eigendirection analysis on the articulated robotic structure in machining.

The study of mode-coupling instability in machining deals with the orientation of the vibratory modes of the machine tool with respect to the dynamics of the cutting process. For the fairly invariant structure of a CNC machine tool, these orientations are identified through experimental modal analysis and chatter-free machining tasks are designed based on the fair assumption of invariant tool-holder's vibratory dynamics. The work presented in Chapter 5 of this thesis proposed defining eigendirections for an articulated robot structure with similar functionality as mode shapes generally defined for structural dynamic analysis of engineering structures. Experimental modal analysis is extensively used to identify the modal properties of machine tool structures with the aim as to study mode-coupling instability. The approach can be customized to identify eigendirections rather than mode shapes for the robot structure. Instability caused by the mode-coupling effect can be avoided once these directions are identified from vibration measurements during the machining process.

APPENDIX A

6-DOF Multi-body Dynamic Model for the Articulated Structure of the SCOMPI Robot

In this appendix, some details about the derivation of the 6-DOF multi-body dynamic model for the articulated structure of the SCOMPI robot based on (Spong, Hutchinson and Vidyasagar, 2006) and (Tsai, 1999) are presented. The model has been used for vibration analysis of the robotic structure as presented in Chapter 5 of the thesis. The analytical natural frequencies and mode shapes shown in Figure 5.4 and Figure 5.5 are calculated using the dynamic equations of this model as presented in this Appendix.

A.1 DH Parameters and Coordinate Systems

The schematic diagram of Figure A. 1 is showing coordinate frame assignments and the corresponding parameters based on the DH convention method for SCOMPI. In this figure, d_1, q_2, q_3, q_4, q_5 and q_6 are joint variables corresponding to one prismatic and five

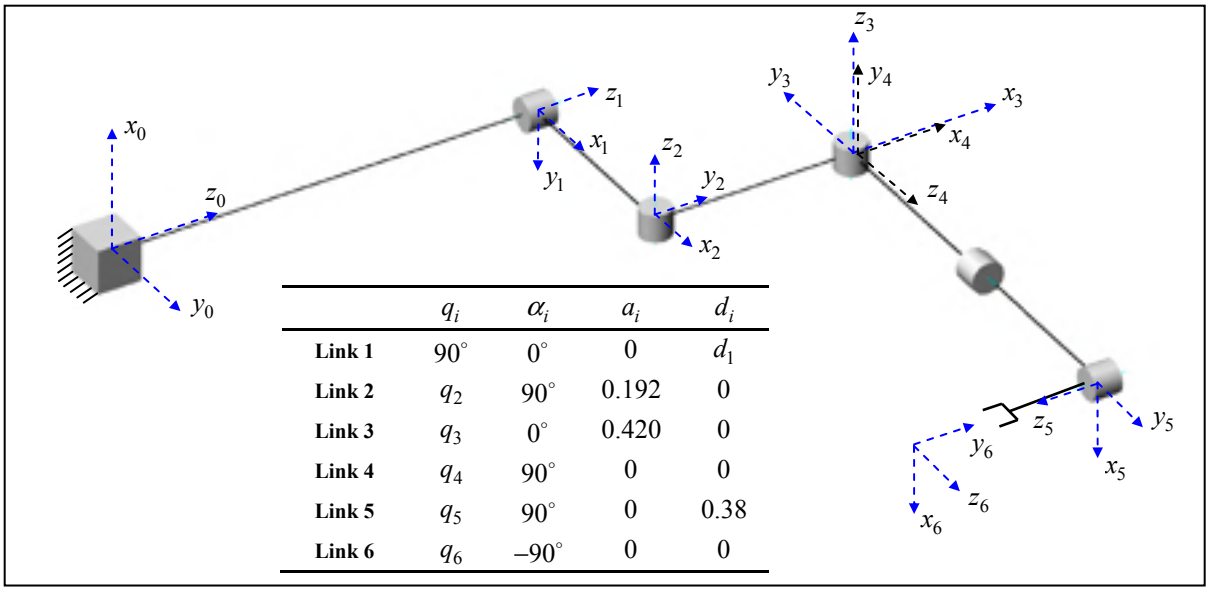

	q_i	α_i	a_i	d_i
Link 1	90°	0°	0	d_1
Link 2	q_2	90°	0.192	0
Link 3	q_3	0°	0.420	0
Link 4	q_4	90°	0	0
Link 5	q_5	90°	0	0.38
Link 6	q_6	–90°	0	0

Figure A. 1 Assignment of DH parameters for the SCOMPI robot

revolute joints. The configuration around which the governing equations of motion (see Equation (5.1) of Chapter 5) are solved is:

$$\{\boldsymbol{q_0}\} = \begin{bmatrix} d_1 & q_2 & q_3 & q_4 & q_5 & q_6 \end{bmatrix}^T = \begin{bmatrix} 0 & -15^\circ & 75^\circ & 5^\circ & -90^\circ & 0^\circ \end{bmatrix}^T \quad \text{(A. 1)}$$

Transformation matrix from end effector's frame to the base, and the Jacobian matrix for the 6DOF manipulator are then calculated as;

$$[\boldsymbol{T}]_6^0 = \begin{bmatrix} -0.9659 & 0.0449 & 0.2549 & 0.1747 \\ 0.2588 & 0.1677 & 0.9513 & 0.6519 \\ 0 & 0.9848 & -0.1736 & 0.3397 \\ 0 & 0 & 0 & 1 \end{bmatrix} \quad \text{(A. 2)}$$

$$[\boldsymbol{J}] = \begin{bmatrix} 0 & -0.6519 & -0.0879 & 0.0171 & 0 & 0 \\ 0 & 0.1747 & -0.3281 & 0.0637 & 0 & 0 \\ 1 & 0 & 0.4829 & 0.3742 & 0 & 0 \\ 0 & 0 & 0.9659 & 0.9659 & 0.2549 & -0.0449 \\ 0 & 0 & -0.2588 & -0.2588 & 0.9513 & -0.1677 \\ 0 & 1 & 0 & 0 & -0.1736 & -0.9848 \end{bmatrix} \quad \text{(A. 3)}$$

The complete list of links' transformation matrices and some details about calculation of the Jacobian matrix can be found in Appendix B.

A.2 Dynamic Equations

The general form for the dynamic equations of motion in the joints space for a robot derived through the Euler-Lagrange method is given by (Spong, Hutchinson and Vidyasagar, 2006) as,

$$[\boldsymbol{D}(\boldsymbol{q_0})]\{\ddot{\boldsymbol{q}}\} + [\boldsymbol{C}(\boldsymbol{q}, \dot{\boldsymbol{q}})]\{\dot{\boldsymbol{q}}\} + \{\boldsymbol{g}(\boldsymbol{q_0})\} = \{\boldsymbol{Q}\} \quad \text{(A. 4)}$$

In which $\{\boldsymbol{q_0}\}_{6\times1}$ is the vector of joints' variables (generalized coordinates) at the equilibrium configuration. It is important to note that $\{\boldsymbol{q}\}$ in the above is not the actual generalized coordinate of the system but it virtually represents vibratory *displacements* (angular and linear) of joints' variables from their equilibrium positions ($\{\boldsymbol{q}\}=[\delta d_1 \quad \delta q_2 \quad \delta q_3 \quad \delta q_4 \quad \delta q_5 \quad \delta q_6]^T$).

Matrix $[\boldsymbol{C}(\boldsymbol{q},\dot{\boldsymbol{q}})]$ including *Centrifugal* ($\dot{q}_i^2$) and *Coriolis* ($\dot{q}_i\dot{q}_j$ where $i \neq j$) terms, where the coefficients may also depend on $\{\boldsymbol{q}\}$, is neglected in this study for simplicity.

$[\boldsymbol{D}(\boldsymbol{q_0})]$, the inertia matrix, and $\{\boldsymbol{g}(\boldsymbol{q_0})\}$, the gravitational generalized force, are evaluated at the given configuration of Equation (A. 1) and $\{\boldsymbol{Q}\}$ is the vector of generalized forces resulting from excitations. Details of evaluating these terms are given as follows.

In this model, links are assumed to be rigid members with no flexibility. The potential energy then arises only due to gravity. Flexibility and damping of joints which are neglected in this basic model will be added through the following sections. The finalized governing equation of motion used for the simulations in this thesis with its basic assumptions is then presented at the end of this section.

A.2.1 Inertia Matrix

The inertia matrix, $[\boldsymbol{D}(\boldsymbol{q_0})]$, results from differentiation of kinetic energy of the system ($K.E.=\frac{1}{2}\{\dot{\boldsymbol{q}}\}^T[\boldsymbol{D}(\boldsymbol{q_0})]\{\dot{\boldsymbol{q}}\}$) w.r.t. joints velocities $\{\dot{\boldsymbol{q}}\}$ in the Lagrange formulation. For SCOMPI with the 6 links approximated by solid cubes and prisms to simplify the evaluation of links' inertia matrices, and the vector of links' masses as

$[14.76 \quad 5.38 \quad 4.78 \quad 4.12 \quad 2.88 \quad 1.29](kg)$, the inertia matrix is calculated for the vibratory motion of robot around its equilibrium position as,

$$[\boldsymbol{D}(\boldsymbol{q}_0)] = \begin{bmatrix} 38.2100 & 0 & 5.7038 & 3.9251 & -0.0019 & 0.0003 \\ 0 & 5.3553 & -0.0028 & 0.0027 & -0.0274 & -0.0228 \\ 5.7038 & -0.0028 & 4.4353 & 1.5486 & -0.0008 & 0.0008 \\ 3.9251 & 0.0027 & 1.5486 & 1.4256 & -0.0007 & 0 \\ -0.0019 & -0.0274 & -0.0008 & -0.0007 & 0.0133 & 0.0003 \\ 0.0003 & -0.0228 & 0.0008 & 0 & 0.0003 & 0.0106 \end{bmatrix} \tag{A. 5}$$

Numerical evaluation of $[\boldsymbol{D}(\boldsymbol{q}_0)]$ is based on,

$$[\boldsymbol{D}(\boldsymbol{q}_0)] = \sum_{i=1}^{6} \left\{ m_i \left[\boldsymbol{J}\boldsymbol{v}_{c,i}(\boldsymbol{q}_0)\right]^T \left[\boldsymbol{J}\boldsymbol{v}_{c,i}(\boldsymbol{q}_0)\right] + \left[\boldsymbol{J}\boldsymbol{\omega}_{c,i}(\boldsymbol{q}_0)\right]^T [\boldsymbol{R}_i(\boldsymbol{q}_0)][\boldsymbol{I}_i][\boldsymbol{R}_i(\boldsymbol{q}_0)]^T \left[\boldsymbol{J}\boldsymbol{\omega}_{c,i}(\boldsymbol{q}_0)\right] \right\} \tag{A. 6}$$

In which, m_i is the mass of link (i), $[\boldsymbol{R}_i(\boldsymbol{q}_0)]$ is the rotation matrix from link (i) to the base frame and $[\boldsymbol{I}_i]$ is the tensor of inertia for link (i) expressed in its attached frame. $\left[\boldsymbol{J}\boldsymbol{v}_{c,i}(\boldsymbol{q}_0)\right]$ and $\left[\boldsymbol{J}\boldsymbol{\omega}_{c,i}(\boldsymbol{q}_0)\right]$ are links' sub-Jacobian matrices (Tsai, 1999) as detailed in Appendix B, Section B.4. These matrices relate the linear and angular velocities of center of mass for each link ($\{\boldsymbol{v}_{c,i}\}$, $\{\boldsymbol{\omega}_{c,i}\}$) to the vector of joints' velocities ($\{\dot{\boldsymbol{q}}\}$) as,

$$\{\boldsymbol{v}_{c,i}\}_{3\times1} = \left[\boldsymbol{J}\boldsymbol{v}_{c,i}(\mathbf{q}_0)\right]_{3\times6} \{\dot{\mathbf{q}}\}_{6\times1} \tag{A. 7}$$

$$\{\boldsymbol{\omega}_{c,i}\}_{3\times1} = \left[\boldsymbol{J}\boldsymbol{\omega}_{c,i}(\mathbf{q}_0)\right]_{3\times6} \{\dot{\mathbf{q}}\}_{6\times1} \tag{A. 8}$$

Some details about the calculation of links' inertia tensors and sub-Jacobian matrices are included in Appendix B.

A.2.2 Gravitational Generalized Force

Assuming rigid members for links without flexibility, the potential energy of the system (without the effect of joints' flexibilities) is due to gravity only. The effect of joints'

flexibilities in the potential energy of the system will be added later in Section A.2.4. Presently, the potential energy of the system can be written as,

$$P.E. = \sum_{i=1}^{6} m_i \{\boldsymbol{g}\}^T \{\boldsymbol{r}_{c,i}\} \tag{A. 9}$$

In which, m_i is the mass of link (*i*), $\{\boldsymbol{g}\} = [-9.81 \quad 0 \quad 0](m/s^2)$ is the acceleration of gravity expressed in the base frame (0) and $\{\boldsymbol{r}_{c,i}\}$ is the position vector for center of mass of link (*i*).

For a fixed configuration $\{\boldsymbol{q}_0\}$ the linear velocity relation of center of mass for link (*i*) will be,

$$\{\boldsymbol{v}_{c,i}\}_{3\times1} = [\boldsymbol{Jv}_{c,i}(\boldsymbol{q}_0)]_{3\times6} \{\dot{\boldsymbol{q}}\}_{6\times1} \tag{A. 10}$$

The fixed configuration $\{\boldsymbol{q}_0\} = const.$ implements that $[\boldsymbol{Jv}_{c,i}(\boldsymbol{q}_0)] = const.$ which consequently results into,

$$\{\boldsymbol{r}_{c,i}\}_{3\times1} = [\boldsymbol{Jv}_{c,i}(\boldsymbol{q}_0)]_{3\times6} \{\boldsymbol{q}_0\}_{6\times1} \tag{A. 11}$$

Therefore the position vector of center of mass for link (*i*) is simply calculated by multiplying the link's sub-Jacobian matrix at the given configuration by the vector of generalized coordinates itself. The potential energy of the system can therefore be written as,

$$P.E. = \sum_{i=1}^{6} m_i \{\boldsymbol{g}\}_{3\times1}^T [\boldsymbol{Jv}_{c,i}(\boldsymbol{q}_0)]_{3\times6} \{\boldsymbol{q}_0\}_{6\times1} \tag{A. 12}$$

In the Euler-Lagrange formulation, the differentiation of potential energy with respect to each generalized coordinate $\partial(P.E.)/\partial(q_j)$ is needed which can be derived from Equation (A. 12). The vector of generalized gravitational force is therefore given by,

$$\{\boldsymbol{g}(\boldsymbol{q}_0)\} = \begin{Bmatrix} \dfrac{\partial(P.E.)}{\partial(q_1)} \\ \vdots \\ \dfrac{\partial(P.E.)}{\partial(q_6)} \end{Bmatrix} = \begin{Bmatrix} \sum_{i=1}^{6} m_i \{\boldsymbol{g}\}^T \left[\boldsymbol{Jv}_{c,i}(:,1)\right] \\ \vdots \\ \sum_{i=1}^{6} m_i \{\boldsymbol{g}\}^T \left[\boldsymbol{Jv}_{c,i}(:,6)\right] \end{Bmatrix} = \begin{Bmatrix} 0 \\ -92.2042 \\ -14.9542 \\ 1.9004 \\ 0.3243 \\ 0.1681 \end{Bmatrix} \quad \text{(A. 13)}$$

In which $\left[\boldsymbol{Jv}_{c,i}(:,j)\right]_{3\times1}$ is the j^{th} column of $\left[\boldsymbol{Jv}_{c,i}\right]$.

A.2.3 Excitation: Vector of Generalized Forces

Several kinds of excitations were considered for the purpose of simulation in this thesis. For each type of excitation, the forcing vector expressed in the base frame $\{\mathbf{Q}\}_{6\times1}$ is constructed first. The vector of generalized forces then is made by,

$$\{\mathbf{Q}\}_{6\times1}^{generalized} = [\boldsymbol{J}]^T \{\boldsymbol{Q}\}_{6\times1} \quad \text{(A. 14)}$$

This is a simple transformation into the joints' space by the transpose of manipulator's Jacobian matrix.

A.2.4 Joints' Stiffness

Flexibility of joints which has been ignored in the formulation until present, is added in this section based upon the model proposed by (Spong, 1987). Figure A. 2 shows the flexible joint proposed by their study schematically. Flexibility of joint resulting from gearing mechanism between rotors of actuators and links is modeled by simple torsional spring elements. The spring can also account for the torsional flexibility of the Flexspline element in the harmonic drive mechanisms.

A robot with flexible joints modeled with this approach, has fictitious links. These are rotors of actuators which add additional degrees of freedom to the system because they are rigid

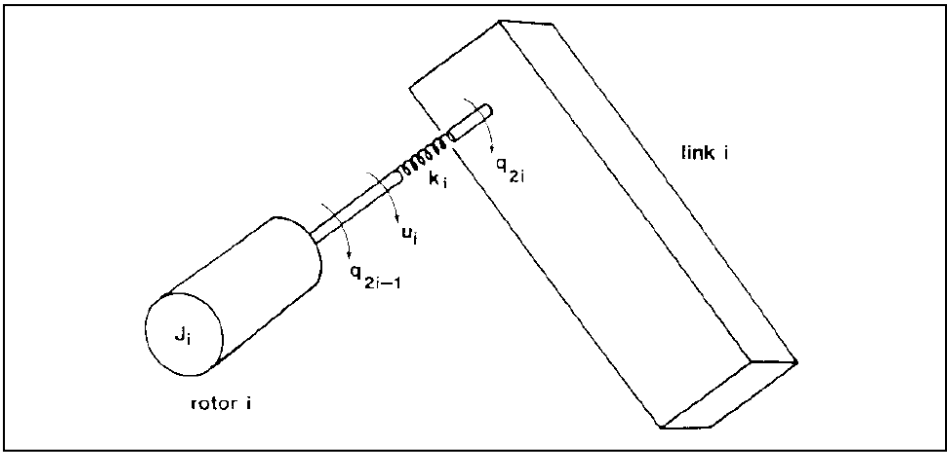

Figure A. 2 Elastic coupling between an actuator's rotor and the link taken from (Spong, 1987)

bodies with their own inertias. If $\{\boldsymbol{q}\}$ represents joints' variables (generalized coordinates) of the robot and $\{\boldsymbol{p}\}$ is the angular displacement of the actuators of rotors, the torsional displacements of the springs $\{\boldsymbol{q}\}-\{\boldsymbol{p}\}$ will add up an elastic potential energy term $\frac{1}{2}(\{\boldsymbol{q}\}-\{\boldsymbol{p}\})^T[\boldsymbol{K}](\{\boldsymbol{q}\}-\{\boldsymbol{p}\})$ to Equation (A. 9). The diagonal matrix $[\boldsymbol{K}]$ includes joints' flexibilities on its diagonal. Since the equations of motion for SCOMPI are simulated for a fixed configuration $\{\boldsymbol{q}_0\}$ and $\{\boldsymbol{q}\}$ actually represents vibratory displacements of the joints from equilibrium, positions of actuators in the fixed configuration is considered as reference and therefore $\{\boldsymbol{p}\}=\{0\}$ in the term for the elastic potential energy.

The elastic potential energy term now has the form $\frac{1}{2}\{\boldsymbol{q}\}^T[\boldsymbol{K}]\{\boldsymbol{q}\}$. It is differentiated with respect to the generalized coordinates q_j in the Euler-Lagrange formulation for the equation of motion governing each of the generalized coordinates. This will result into $[\boldsymbol{K}]$ multiplied by $\{\boldsymbol{q}\}$ in the matrix form of the dynamic equations. The matrix of joints' flexibilities considered for the simulations of dynamic behavior for SCOMPI in this thesis is identified

from payload test experiments as briefly described in Section 5.2. The diagonal matrix is as follows,

$$[\boldsymbol{K}]=\begin{bmatrix} 776.4\,kN\cdot m/rad & 0 & 0 & 0 & 0 & 0 \\ 0 & 6.75\,kN/m & 0 & 0 & 0 & 0 \\ 0 & 0 & 11.15\,kN/m & 0 & 0 & 0 \\ 0 & 0 & 0 & 12.72\,kN/m & 0 & 0 \\ 0 & 0 & 0 & 0 & 4.78\,kN/m & 0 \\ 0 & 0 & 0 & 0 & 0 & 3\,kN/m \end{bmatrix} \quad \text{(A. 15)}$$

More details about the payload tests and the identification procedure of the stiffness matrix can be found in (Swiatek, Liu and Hazel, 2010).

A.2.5 Joints' Damping

If viscous damping elements are also considered at joints parallel to the spring elements, robot's motion will be resisted by forces whose magnitudes are proportional to joints' velocities $\{\dot{\boldsymbol{q}}\}$. The Rayleigh's dissipation function will therefore be,

$$R_E=\frac{1}{2}\{\dot{\boldsymbol{q}}\}^T[\boldsymbol{C}]\{\dot{\boldsymbol{q}}\} \quad \text{(A. 16)}$$

Damping matrix $[\boldsymbol{C}]$ includes viscous damping elements on its main diagonal. Lagrange equations in this case include additional terms of $\partial R_E/\partial\dot{q}_j$ accounting for dissipative forces. This will result into an additional term, $[\boldsymbol{C}]\{\dot{\boldsymbol{q}}\}$, in the matrix form of the dynamic equations of motion. Proportional damping with the coefficient β is considered for SCOMPI in simulations presented in this thesis as,

$$[\boldsymbol{C}]=\beta[\boldsymbol{K}] \quad \text{(A. 17)}$$

The dynamic equations for the vibrational behavior of the multi-body articulated structure of the SCOMPI robot is therefore,

$$[\boldsymbol{D}(\boldsymbol{q}_0)]\{\ddot{\boldsymbol{q}}\}+[\boldsymbol{C}]\{\dot{\boldsymbol{q}}\}+[\boldsymbol{K}]\{\boldsymbol{q}\}+\{\boldsymbol{g}(\boldsymbol{q})\}=\{\boldsymbol{Q}\} \quad \text{(A. 18)}$$

in which $[\boldsymbol{D}(\boldsymbol{q}_0)]$, $[\boldsymbol{C}]$, $[\boldsymbol{K}]$, $\{\boldsymbol{g}(\boldsymbol{q})\}$ and $\{\mathbf{Q}\}$ are matrices which were explained in the preceding sections. In this model links are assumed to be rigid members and flexibility and damping is included at joints. The following basic assumptions are embedded into the formulation of this dynamic model;

i. Equations of motion are governing the vibratory oscillations of robot structure about a fixed equilibrium configuration. This is the fixed configuration at which experimental modal analysis was carried out on the robot structure (see Figure 5.3).

ii. Given the fact that joints' flexibilities are measured experimentally, a plausible assumption can be made that links' flexibilities are partially included into the flexibilities of joints.

iii. Rotors of actuators at the articulated joints are assumed to be members without inertia.

iv. In calculating the inertia matrix, members are approximated by solid links with uniform cross-sections and their centers of mass are considered at their geometric centers. Mass of each member is also assumed to integrate the mass of its actuator and gearing mechanism.

The nonlinear terms regarding Coriolis and Centrifugal forces are ignored for simplicity.

APPENDIX B

Transformation Matrices, Jacobian Matrix and the Links' Inertia Tensors for the SCOMPI Robot

This appendix explains some details about the calculation of the transformation matrices, the Jacobian matrix and the inertia tensors for the links of SCOMPI based on (Spong, Hutchinson and Vidyasagar, 2006) and (Tsai, 1999).

B.1 Links' Transformation matrices

Considering the DH parameters assigned to the SCOMPI robot structure as shown in Figure A. 1 and the given configuration as in Equation (A. 1), links' transformation matrices, $[A_i]$ and $\left[T_i^0\right]$ are calculated using the following formulations.

The transformation matrix from link (*i*) to (*i-1*) is calculated from,

$$[A_i]=\begin{bmatrix} \cos q_i & -\sin q_i.\cos\alpha_i & \sin q_i.\sin\alpha_i & a_i.\cos q_i \\ \sin q_i & \cos q_i.\cos\alpha_i & -\cos q_i.\sin\alpha_i & a_i.\sin q_i \\ 0 & \sin\alpha_i & \cos\alpha_i & d_i \\ 0 & 0 & 0 & 1 \end{bmatrix} \quad \text{(B. 1)}$$

in where the values for α_i, a_i, d_i and q_i associated to links $i=1-6$ can be found in Section A.1.

The transformation matrix for each link with respect to the base frame is thus given by,

$$\left[T_i^0\right]=[A_1][A_2].....[A_{i-1}][A_i] \quad \text{(B. 2)}$$

The two matrices calculated for each of the six links of the robot are listed as follows,

$$[A_1]=\begin{bmatrix}0 & -1 & 0 & 0\\ 1 & 0 & 0 & 0\\ 0 & 0 & 1 & 0\\ 0 & 0 & 0 & 1\end{bmatrix} \qquad \left[T_1^0\right]=\begin{bmatrix}0 & -1 & 0 & 0\\ 1 & 0 & 0 & 0\\ 0 & 0 & 1 & 0\\ 0 & 0 & 0 & 1\end{bmatrix} \tag{B. 3}$$

$$[A_2]=\begin{bmatrix}0.9659 & 0 & -0.2588 & 0.1855\\ -0.2588 & 0 & -0.9659 & -0.0497\\ 0 & 1 & 0 & 0\\ 0 & 0 & 0 & 1\end{bmatrix} \quad \left[T_2^0\right]=\begin{bmatrix}0.2588 & 0 & 0.9659 & 0.0497\\ 0.9659 & 0 & -0.2588 & 0.1855\\ 0 & 1 & 0 & 0\\ 0 & 0 & 0 & 1\end{bmatrix} \tag{B. 4}$$

$$[A_3]=\begin{bmatrix}0.2588 & -0.9659 & 0 & 0.1087\\ 0.9659 & 0.2588 & 0 & 0.4057\\ 0 & 0 & 1 & 0\\ 0 & 0 & 0 & 1\end{bmatrix} \quad \left[T_3^0\right]=\begin{bmatrix}0.0670 & -0.2500 & 0.9659 & 0.0778\\ 0.2500 & -0.9330 & -0.2588 & 0.2905\\ 0.9659 & 0.2588 & 0 & 0.4057\\ 0 & 0 & 0 & 1\end{bmatrix} \tag{B. 5}$$

$$[A_4]=\begin{bmatrix}0.9962 & 0 & 0.0872 & 0\\ 0.0872 & 0 & -0.9962 & 0\\ 0 & 1 & 0 & 0\\ 0 & 0 & 0 & 1\end{bmatrix} \quad \left[T_4^0\right]=\begin{bmatrix}0.0449 & 0.9659 & 0.2549 & 0.0778\\ 0.1677 & -0.2588 & 0.9513 & 0.2905\\ 0.9848 & 0 & -0.1736 & 0.4057\\ 0 & 0 & 0 & 1\end{bmatrix} \tag{B. 6}$$

$$[A_5]=\begin{bmatrix}0 & 0 & -1 & 0\\ -1 & 0 & 0 & 0\\ 0 & 1 & 0 & 0.3800\\ 0 & 0 & 0 & 1\end{bmatrix} \quad \left[T_5^0\right]=\begin{bmatrix}-0.9659 & 0.2549 & -0.0449 & 0.1747\\ 0.2588 & 0.9513 & -0.1677 & 0.6519\\ 0 & -0.1736 & -0.9848 & 0.3397\\ 0 & 0 & 0 & 1\end{bmatrix} \tag{B. 7}$$

$$[A_6]=\begin{bmatrix}1 & 0 & 0 & 0\\ 0 & 0 & 1 & 0\\ 0 & -1 & 0 & 0\\ 0 & 0 & 0 & 1\end{bmatrix} \quad \left[T_6^0\right]=\begin{bmatrix}-0.9659 & 0.0449 & 0.2549 & 0.1747\\ 0.2588 & 0.1677 & 0.9513 & 0.6519\\ 0 & 0.9848 & -0.1736 & 0.3397\\ 0 & 0 & 0 & 1\end{bmatrix} \tag{B. 8}$$

B.2 Jacobian matrix

Linear and angular velocities of the end-effector point relative to the base frame ($\{\boldsymbol{v}_6^0\}$ and $\{\boldsymbol{\omega}_6^0\}$) are related to joint velocities $\{\dot{\boldsymbol{q}}\}_{6\times1}$ through the Jacobian matrix of the robot $[\boldsymbol{J}]_{6\times6}$ as,

$$\begin{bmatrix} \boldsymbol{v}_6^0 \\ \boldsymbol{\omega}_6^0 \end{bmatrix}_{6\times1} = \begin{bmatrix} \begin{bmatrix} \boldsymbol{J}_v \\ \boldsymbol{J}_\omega \end{bmatrix}_1 & \cdots & \begin{bmatrix} \boldsymbol{J}_v \\ \boldsymbol{J}_\omega \end{bmatrix}_6 \end{bmatrix}_{6\times6} \{\dot{\boldsymbol{q}}\}_{6\times1} \tag{B. 9}$$

In where the i^{th} column of the Jacobian matrix is calculated from,

$$[\boldsymbol{J}]_i = \begin{cases} \begin{bmatrix} \boldsymbol{Z}_{i-1}^0 \times (\boldsymbol{O}_6^0 - \boldsymbol{O}_{i-1}^0) \\ \boldsymbol{Z}_{i-1}^0 \end{bmatrix} & revolute(i) \\ \begin{bmatrix} \boldsymbol{Z}_{i-1}^0 \\ \{\boldsymbol{0}\} \end{bmatrix} & prismatic(i) \end{cases} \tag{B. 10}$$

In the above, $\{\boldsymbol{O}_6^0\}$ is the center of the end-effector frame (6) expressed in base frame (0), $\{\boldsymbol{O}_{i-1}^0\}$ is the center of frame $(i-1)$ expressed in base frame (0) and $\{\boldsymbol{Z}_{i-1}^0\}$ is the axis of joint (i) expressed in the base frame (0).

Based on the above, columns of the Jacobian matrix are calculated as follows.

$$[\boldsymbol{J}]_1 = \begin{bmatrix} \boldsymbol{Z}_0^0 \\ \{\boldsymbol{0}\} \end{bmatrix} = \begin{bmatrix} 0 \\ 0 \\ 1 \\ 0 \\ 0 \\ 0 \end{bmatrix} \tag{B. 11}$$

$$[\boldsymbol{J}]_2 = \begin{bmatrix} \boldsymbol{Z}_1^0 \times (\boldsymbol{O}_6^0 - \boldsymbol{O}_1^0) \\ \boldsymbol{Z}_1^0 \end{bmatrix} = \begin{bmatrix} \begin{Bmatrix} 0 \\ 0 \\ 1 \end{Bmatrix} \times (\begin{Bmatrix} 0.1747 \\ 0.6519 \\ 0.3397 \end{Bmatrix} - \begin{Bmatrix} 0 \\ 0 \\ 0 \end{Bmatrix}) \\ \begin{Bmatrix} 0 \\ 0 \\ 1 \end{Bmatrix} \end{bmatrix} = \begin{bmatrix} -0.6519 \\ 0.1747 \\ 0 \\ 0 \\ 0 \\ 1 \end{bmatrix} \quad \text{(B. 12)}$$

$$[\boldsymbol{J}]_3 = \begin{bmatrix} \boldsymbol{Z}_2^0 \times (\boldsymbol{O}_6^0 - \boldsymbol{O}_2^0) \\ \boldsymbol{Z}_2^0 \end{bmatrix} = \begin{bmatrix} \begin{Bmatrix} 0.9659 \\ -0.2588 \\ 0 \end{Bmatrix} \times (\begin{Bmatrix} 0.1747 \\ 0.6519 \\ 0.3397 \end{Bmatrix} - \begin{Bmatrix} 0.0497 \\ 0.1855 \\ 0 \end{Bmatrix}) \\ \begin{Bmatrix} 0.9659 \\ -0.2588 \\ 0 \end{Bmatrix} \end{bmatrix} = \begin{bmatrix} -0.0879 \\ -0.3281 \\ 0.4829 \\ 0.9659 \\ -0.2588 \\ 0 \end{bmatrix} \quad \text{(B. 13)}$$

$$[\boldsymbol{J}]_4 = \begin{bmatrix} \boldsymbol{Z}_3^0 \times (\boldsymbol{O}_6^0 - \boldsymbol{O}_3^0) \\ \boldsymbol{Z}_3^0 \end{bmatrix} = \begin{bmatrix} \begin{Bmatrix} 0.9659 \\ -0.2588 \\ 0 \end{Bmatrix} \times (\begin{Bmatrix} 0.1747 \\ 0.6519 \\ 0.3397 \end{Bmatrix} - \begin{Bmatrix} 0.0778 \\ 0.2905 \\ 0.4057 \end{Bmatrix}) \\ \begin{Bmatrix} 0.9659 \\ -0.2588 \\ 0 \end{Bmatrix} \end{bmatrix} = \begin{bmatrix} 0.0171 \\ 0.0637 \\ 0.3742 \\ 0.9659 \\ -0.2588 \\ 0 \end{bmatrix} \quad \text{(B. 14)}$$

$$[\boldsymbol{J}]_5 = \begin{bmatrix} \boldsymbol{Z}_4^0 \times (\boldsymbol{O}_6^0 - \boldsymbol{O}_4^0) \\ \boldsymbol{Z}_4^0 \end{bmatrix} = \begin{bmatrix} \begin{Bmatrix} 0.2549 \\ 0.9513 \\ -0.1736 \end{Bmatrix} \times (\begin{Bmatrix} 0.1747 \\ 0.6519 \\ 0.3397 \end{Bmatrix} - \begin{Bmatrix} 0.0778 \\ 0.2905 \\ 0.4057 \end{Bmatrix}) \\ \begin{Bmatrix} 0.2549 \\ 0.9513 \\ -0.1736 \end{Bmatrix} \end{bmatrix} = \begin{bmatrix} 0 \\ 0 \\ 0 \\ 0.2549 \\ 0.9513 \\ -0.1736 \end{bmatrix} \quad \text{(B. 15)}$$

$$[\boldsymbol{J}]_6 = \begin{bmatrix} \boldsymbol{Z}_5^0 \times (\boldsymbol{O}_6^0 - \boldsymbol{O}_5^0) \\ \boldsymbol{Z}_5^0 \end{bmatrix} = \begin{bmatrix} \begin{Bmatrix} -0.0449 \\ -0.1677 \\ -0.9848 \end{Bmatrix} \times \left(\begin{Bmatrix} 0.1747 \\ 0.6519 \\ 0.3397 \end{Bmatrix} - \begin{Bmatrix} 0.1747 \\ 0.6519 \\ 0.3397 \end{Bmatrix} \right) \\ \begin{Bmatrix} -0.0449 \\ -0.1677 \\ -0.9848 \end{Bmatrix} \end{bmatrix} = \begin{bmatrix} 0 \\ 0 \\ 0 \\ -0.0449 \\ -0.1677 \\ -0.9848 \end{bmatrix} \quad \text{(B. 16)}$$

B.3 Links' Inertia Tensors

The inertia tensor of each link approximated by solid members which have uniform cross sections is evaluated in the attached frame to that link and around its center of mass. The inertia tensors are then expressed in base frame using Equation (A. 18) by pre and post multiplying with the rotation matrix of link (*i*) and its transpose.

The masses of links are taken from the specification of the robot as $m_1 = 14.76(kg)$, $m_2 = 5.38(kg)$, $m_3 = 4.78(kg)$, $m_4 = 4.12(kg)$, $m_5 = 2.88(kg)$ and $m_6 = 1.29(kg)$. The lengths of the links are also taken as $l_1 = 80(mm)$, $l_2 = 192(mm)$, $l_3 = 420(mm)$, $l_4 = 380(mm)$, $l_5 = 95(mm)$ and $l_6 = 80(mm)$ from the robot's specification. The matrices of moments of inertia for links considered as members of uniform density $7800(kg/m^3)$ are thus estimated as shown in Figure B. 1. Coordinates are parallel with the frames attached to the links.

$$H_1 = \sqrt[3]{V_1}\ ,\ L_1 = W_1 = H_1$$

$$I_{xx} = I_{yy} = I_{zz} = \frac{1}{12} m_1 (H_1^2 + W_1^2)$$

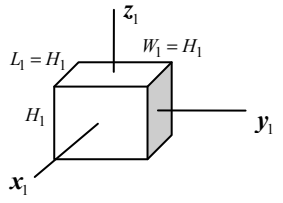

(a) Approximation of link (1) by a solid cube

$$V_2 = m_2 / \rho = L_2 H_2^2$$

$$H_2 = \sqrt{V_2 / L_2}\ ,\ W_2 = H_2$$

$$I_{xx} = \frac{1}{12} m_2 (H_2^2 + W_2^2)\ ,\ I_{yy} = \frac{1}{12} m_2 (L_2^2 + W_2^2)\ ,\ I_{zz} = \frac{1}{12} m_2 (L_2^2 + H_2^2)$$

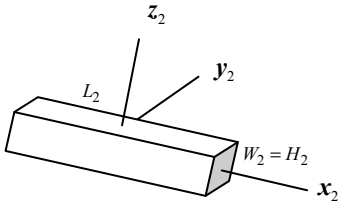

(b) Approximation of link (2) by a rectangular prism

$$V_3 = m_3 / \rho = L_3 H_3^2$$

$$H_3 = W_3 = \sqrt{V_3 / L_3}$$

$$I_{xx} = \frac{1}{12} m_3 (H_3^2 + W_3^2)\ ,\ I_{yy} = \frac{1}{12} m_3 (L_3^2 + W_3^2)\ ,\ I_{zz} = \frac{1}{12} m_3 (L_3^2 + H_3^2)$$

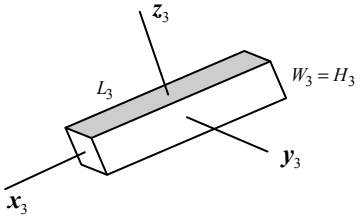

(c) Approximation of link (3) by a rectangular prism

$$V_4 = m_4 / \rho = L_4 H_4^2$$

$$H_4 = W_4 = \sqrt{V_4 / L_4}$$

$$I_{xx} = \frac{1}{12} m_4 (L_4^2 + W_4^2)\ ,\ I_{yy} = \frac{1}{12} m_4 (L_4^2 + H_4^2)\ ,\ I_{zz} = \frac{1}{12} m_4 (H_4^2 + W_4^2)$$

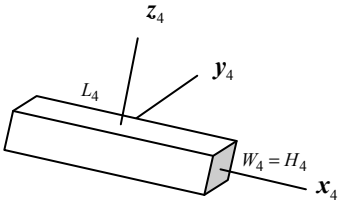

(d) Approximation of link (4) by a rectangular prism

$$V_5 = m_5 / \rho = L_5 H_5^2$$

$$H_5 = W_5 = \sqrt{V_5 / L_5}$$

$$I_{xx} = \frac{1}{12} m_5 (L_5^2 + W_5^2)\ ,\ I_{yy} = \frac{1}{12} m_5 (W_5^2 + H_5^2)\ ,\ I_{zz} = \frac{1}{12} m_5 (H_5^2 + L_5^2)$$

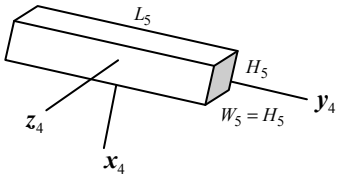

(e) Approximation of link (5) by a rectangular prism

$$V_6 = m_6 / \rho = L_6 H_6^2$$

$$W_6 = H_6 = \sqrt{V_6 / L_6}$$

$$I_{xx} = \frac{1}{12} m_6 (L_6^2 + W_6^2)\ ,\ I_{yy} = \frac{1}{12} m_6 (W_6^2 + H_6^2)\ ,\ I_{zz} = \frac{1}{12} m_6 (H_6^2 + L_6^2)$$

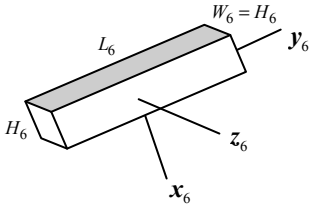

(f) Approximation of link (6) by a rectangular prism

Figure B. 1 Moments of inertia estimated for the links of SCOMPI

B.4 Links' Sub-Jacobian matrices

Derivation of the links' sub-Jacobian matrices which were used in Section A.2.1 for calculation of the inertia matrix are described in the current section. These matrices relate the linear and angular velocities of the center of mass for each link to the vector of joints' velocities. The position of the centers of mass for the six links of SCOMPI in their own local coordinate frame is given by;

$$[\boldsymbol{P}_c] = \begin{bmatrix} 0.02250 & -0.03490 & -0.15940 \\ -0.08810 & 0.00370 & 0.00330 \\ -0.15000 & 0 & -0.01460 \\ -0.02180 & 0.01370 & 0.13900 \\ 0 & -0.02780 & 0.02150 \\ -0.00030 & 0.01530 & 0.00290 \end{bmatrix} \tag{B. 17}$$

Linear and angular velocities of center of mass for link (i) relative to base frame $\{\boldsymbol{v}_{c,i}^0\}$ and $\{\boldsymbol{\omega}_{c,i}^0\}$ are related to joints' velocities $\{\dot{\boldsymbol{q}}\}_{6\times1}$ through the sub-Jacobian matrix $[\boldsymbol{J}_{c,i}]_{6\times6}$ as,

$$\begin{bmatrix} \boldsymbol{v}_{c,i}^0 \\ \boldsymbol{\omega}_{c,i}^0 \end{bmatrix}_{6\times1} = \left[\begin{bmatrix} \boldsymbol{J}_{vc,1} \\ \boldsymbol{J}_{\omega c,1} \end{bmatrix}_1 \quad \cdots \quad \begin{bmatrix} \boldsymbol{J}_{vc,i} \\ \boldsymbol{J}_{\omega c,i} \end{bmatrix}_i \quad \begin{bmatrix} \{\boldsymbol{0}\} \\ \{\boldsymbol{0}\} \end{bmatrix}_{i+1} \quad \cdots \quad \begin{bmatrix} \{\boldsymbol{0}\} \\ \{\boldsymbol{0}\} \end{bmatrix}_6 \right]_{6\times6} \{\dot{\boldsymbol{q}}\}_{6\times1} \tag{B. 18}$$

in where the j^{th} column of the sub-Jacobian matrix is calculated from,

$$[\boldsymbol{J}]_j = \begin{cases} \begin{bmatrix} \boldsymbol{Z}_{j-1}^0 \times (\boldsymbol{O}_{c,i}^0 - \boldsymbol{O}_{j-1}^0) \\ \boldsymbol{Z}_{j-1}^0 \end{bmatrix} & revolute(j) \\ \begin{bmatrix} \boldsymbol{Z}_{j-1}^0 \\ \{\boldsymbol{0}\} \end{bmatrix} & prismatic(j) \end{cases} \tag{B. 19}$$

In Equation (B. 19), $\{\boldsymbol{O}_{c,i}^0\}$ is the center of mass for link (i) expressed in the base frame (0) which is calculated by multiplying the transformation matrix of link (i) by the vector of position of the center of mass expressed in its local coordinate frame as $\{\boldsymbol{O}_{c,i}^0\} = [\boldsymbol{T}_i^0][\boldsymbol{P}_{c,i}^i]$. The center of frame ($j-1$) expressed in the base frame (0) is shown by $\{\boldsymbol{O}_{j-1}^0\}$ and $\{\boldsymbol{Z}_{j-1}^0\}$ is the axis of joint (j) expressed in base frame (0).

In calculating the sub-Jacobian matrix for link (*i*), columns with the index $j > i$ are put to zero. This is based on the assumption that when calculating the velocity of center of mass for link (*i*), the motion of links $j = (i+1),(i+2),....,6$ do not have any effect on the kinematics of point C_i (center of mass for link (*i*)). The calculated sub-Jacobian matrices are listed as follows.

- **Joint 1:** Prismatic joint

$$\left[\boldsymbol{J}_{c,1}\right] = \begin{bmatrix} \boldsymbol{Z}_0^0 & \{\boldsymbol{0}\} & \{\boldsymbol{0}\} & \{\boldsymbol{0}\} & \{\boldsymbol{0}\} & \{\boldsymbol{0}\} \\ \{\boldsymbol{0}\} & \{\boldsymbol{0}\} & \{\boldsymbol{0}\} & \{\boldsymbol{0}\} & \{\boldsymbol{0}\} & \{\boldsymbol{0}\} \end{bmatrix} = \begin{bmatrix} 0 & 0 & 0 & 0 & 0 & 0 \\ 0 & 0 & 0 & 0 & 0 & 0 \\ 1 & 0 & 0 & 0 & 0 & 0 \\ 0 & 0 & 0 & 0 & 0 & 0 \\ 0 & 0 & 0 & 0 & 0 & 0 \\ 0 & 0 & 0 & 0 & 0 & 0 \end{bmatrix} \tag{B. 20}$$

- **Joint 2:** Revolute joint

$$\left[\boldsymbol{J}_{c,2}\right] = \begin{bmatrix} \boldsymbol{Z}_0^0 & \boldsymbol{Z}_1^0 \times (\boldsymbol{O}_{c,2}^0 - \boldsymbol{O}_1^0) & \{\boldsymbol{0}\} & \{\boldsymbol{0}\} & \{\boldsymbol{0}\} & \{\boldsymbol{0}\} \\ [0] & \boldsymbol{Z}_1^0 & \{\boldsymbol{0}\} & \{\boldsymbol{0}\} & \{\boldsymbol{0}\} & \{\boldsymbol{0}\} \end{bmatrix} = \begin{bmatrix} 0 & -0.0995 & 0 & 0 & 0 & 0 \\ 0 & 0.0301 & 0 & 0 & 0 & 0 \\ 1 & 0 & 0 & 0 & 0 & 0 \\ 0 & 0 & 0 & 0 & 0 & 0 \\ 0 & 0 & 0 & 0 & 0 & 0 \\ 0 & 1 & 0 & 0 & 0 & 0 \end{bmatrix} \tag{B. 21}$$

- **Joint 3:** Revolute joint

$$\left[\boldsymbol{J}_{c,3}\right] = \begin{bmatrix} \boldsymbol{Z}_0^0 & \boldsymbol{Z}_1^0 \times (\boldsymbol{O}_{c,3}^0 - \boldsymbol{O}_1^0) & \boldsymbol{Z}_2^0 \times (\boldsymbol{O}_{c,3}^0 - \boldsymbol{O}_2^0) & \{\boldsymbol{0}\} & \{\boldsymbol{0}\} & \{\boldsymbol{0}\} \\ \{\boldsymbol{0}\} & \boldsymbol{Z}_1^0 & \boldsymbol{Z}_2^0 & \{\boldsymbol{0}\} & \{\boldsymbol{0}\} & \{\boldsymbol{0}\} \end{bmatrix} = = \begin{bmatrix} 0 & -0.0995 & -0.0675 & 0 & 0 & 0 \\ 0 & 0.0301 & -0.2519 & 0 & 0 & 0 \\ 1 & 0 & 0.0699 & 0 & 0 & 0 \\ 0 & 0 & 0.9659 & 0 & 0 & 0 \\ 0 & 0 & -0.2588 & 0 & 0 & 0 \\ 0 & 1 & 0 & 0 & 0 & 0 \end{bmatrix} \tag{B. 22}$$

- **Joint 4:** Revolute joint

$$\left[\boldsymbol{J}_{c,4}\right] = \begin{bmatrix} \boldsymbol{Z}_0^0 & \boldsymbol{Z}_1^0 \times (\boldsymbol{O}_{c,4}^0 - \boldsymbol{O}_1^0) & \boldsymbol{Z}_2^0 \times (\boldsymbol{O}_{c,4}^0 - \boldsymbol{O}_2^0) & \boldsymbol{Z}_3^0 \times (\boldsymbol{O}_{c,4}^0 - \boldsymbol{O}_3^0) & \{\boldsymbol{0}\} & \{\boldsymbol{0}\} \\ \{\boldsymbol{0}\} & \boldsymbol{Z}_1^0 & \boldsymbol{Z}_2^0 & \boldsymbol{Z}_3^0 & \{\boldsymbol{0}\} & \{\boldsymbol{0}\} \end{bmatrix} =$$

$$= \begin{bmatrix} 0 & -0.4155 & -0.0932 & 0.0118 & 0 & 0 \\ 0 & 0.1255 & -0.3478 & 0.0441 & 0 & 0 \\ 1 & 0 & 0.2418 & 0.1331 & 0 & 0 \\ 0 & 0 & 0.9659 & 0 & 0 & 0 \\ 0 & 0 & -0.2588 & 0 & 0 & 0 \\ 0 & 1 & 0 & 0 & 0 & 0 \end{bmatrix} \tag{B. 23}$$

- **Joint 5:** Revolute joint

$$\left[\boldsymbol{J}_{c,5}\right]=\begin{bmatrix} \boldsymbol{Z}_0^0 & \boldsymbol{Z}_1^0\times(\boldsymbol{O}_{c,5}^0-\boldsymbol{O}_1^0) & \boldsymbol{Z}_2^0\times(\boldsymbol{O}_{c,5}^0-\boldsymbol{O}_2^0) & \boldsymbol{Z}_3^0\times(\boldsymbol{O}_{c,5}^0-\boldsymbol{O}_3^0) & \boldsymbol{Z}_4^0\times(\boldsymbol{O}_{c,5}^0-\boldsymbol{O}_4^0) & \{\mathbf{0}\} \\ \{\mathbf{0}\} & Z_1^0 & Z_2^0 & Z_3^0 & Z_4^0 & \{\mathbf{0}\} \end{bmatrix}=$$

$$=\begin{bmatrix} 0 & -0.6219 & -0.0837 & 0.0213 & -0.0208 & 0 \\ 0 & 0.1666 & -0.3123 & 0.0795 & 0.0056 & 0 \\ 1 & 0 & 0.4518 & 0.3431 & 0 & 0 \\ 0 & 0 & 0.9659 & 0.9659 & 0.2549 & 0 \\ 0 & 0 & -0.2588 & -0.2588 & 0.9513 & 0 \\ 0 & 1 & 0 & 0 & -0.1736 & 0 \end{bmatrix} \quad \text{(B. 24)}$$

- **Joint 6:** Revolute joint

$$\left[\boldsymbol{J}_{c,6}\right]=\begin{bmatrix} \boldsymbol{Z}_0^0 & \boldsymbol{Z}_1^0\times(\boldsymbol{O}_{c,6}^0-\boldsymbol{O}_1^0) & \boldsymbol{Z}_2^0\times(\boldsymbol{O}_{c,6}^0-\boldsymbol{O}_2^0) & \boldsymbol{Z}_3^0\times(\boldsymbol{O}_{c,6}^0-\boldsymbol{O}_3^0) & \boldsymbol{Z}_4^0\times(\boldsymbol{O}_{c,6}^0-\boldsymbol{O}_4^0) & \boldsymbol{Z}_5^0\times(\boldsymbol{O}_{c,6}^0-\boldsymbol{O}_5^0) \\ \{\mathbf{0}\} & \boldsymbol{Z}_1^0 & \boldsymbol{Z}_2^0 & \boldsymbol{Z}_3^0 & \boldsymbol{Z}_4^0 & \boldsymbol{Z}_5^0 \end{bmatrix}=$$

$$=\begin{bmatrix} 0 & -0.6572 & -0.0917 & 0.0133 & 0.0148 & 0.0027 \\ 0 & 0.1764 & -0.3422 & 0.0497 & -0.0040 & -0.0010 \\ 1 & 0 & 0.4884 & 0.3797 & -0.0003 & 0.0001 \\ 0 & 0 & 0.9659 & 0.9659 & 0.2549 & -0.0449 \\ 0 & 0 & -0.2588 & -0.2588 & 0.9513 & -0.1677 \\ 0 & 1 & 0 & 0 & -0.1736 & -0.9848 \end{bmatrix} \quad \text{(B. 25)}$$

REFERENCES

Abele, E., S. Rothenbücher and M. Weigold. 2008. « Cartesian compliance model for industrial robots using virtual joints ». *Production Engineering,* vol. 2, p. 339-343.

Abele, E., M. Weigold and M. Kulok. 2006. « Increasing the accuracy of a milling industrial robot ». *Production Engineering,* vol. XIII, n° 2, p. 221-224.

Abele, E., M. Weigold and S. Rothenbucher. 2007. « Modeling and Identification of an Industrial Robot for Machining Applications ». *CIRP Annals - Manufacturing Technology,* vol. 56, n° 1, p. 387-390.

Akbari, A., and S. Higuchi. 2000. « Autonomous tool adjustment in robotic grinding ». In *The International conference on Precision Engineering(ICoPE)*. p. 121-126.

Akbari, Ali Akbar, and Shizuichi Higuchi. 2002. « Autonomous tool adjustment in robotic grinding ». *Journal of Materials Processing Technology,* vol. 127, n° 2, p. 274-279.

Altintas, Y. 2000a. « Chatter Stability lobes ». In *Manufacturing automation: Metal cutting mechanics, machine tool vibrations, and CNC design*. p. 110-116. Cambridge University Press.

Altintas, Y. 2000b. « Chatter vibrations in cutting ». In *Manufacturing automation: Metal cutting mechanics, machine tool vibrations, and CNC design*. p. 97-104. Cambridge University Press.

Altintas, Y. 2000c. *Manufacturing automation: Metal cutting mechanics, machine tool vibrations, and CNC design*. Cambridge University Press.

Altintas, Y. 2000d. « Mechanistic modeling of cutting forces ». In *Manufacturing automation: Metal cutting mechanics, machine tool vibrations, and CNC design*. p. 13-17. Cambridge University Press.

Altintas, Y., and E. Budak. 1995. « Analytical prediction of stability lobes in milling ». *Annals of the ClRP* vol. 44, n° 1.

Antoni, J., F. Bonnardot, A. Raad and M. El Badaoui. 2004. « Cyclostationary modelling of rotating machine vibration signals ». *Mechanical Systems and Signal Processing,* vol. 18, n° 6, p. 1285-1314.

Arnold, R. N. 1946. « The mechanism of tool vibration in the cutting of steel ». *Proceedings of the Institution of Mechanical Engineers,* vol. 154, n° 1, p. 261-284.

Asada, H. , and N. Goldfine. 1985. « Optimal compliance design for grinding robot tool holders ». In *IEEE International Conference on Robotics and Automation*. (St. Louis, MO, USA, March 25-28).

Veuillez sélectionner un type de document autre que « Generic » afin de faire afficher la référence bibliographique.

Bayly, P.V., J.E. Halley, B.P. Mann and M.A. Davies. 2003. « Stability of interrupted cutting by temporal finite element analysis ». *ASME Journal of Manufacturing Science and Engineering,* vol. 125, n° 2, p. 220-225.

Braun, S. 2011. « The synchronous (time domain) average revisited ». *Mechanical Systems and Signal Processing,* vol. 25, n° 4, p. 1087-1102.

Braun, S. G. 1975. « The extraction of periodic waveforms by time domain averaging ». *Acustica,* vol. 32, p. 69-77.

Chen, Y., and F. Dong. 2013. « Robot machining: recent development and future research issues ». *The International Journal of Advanced Manufacturing Technology,* vol. 66, n° 9-12, p. 1489-1497.

Comparin, R. J., and R. Singh. 1989. « Non-linear frequency response characteristics of an impact pair ». *Journal of Sound and Vibration,* vol. 134, n° 2, p. 259-290.

Dai, H., K. M. Yuen and M. A. Elbestawi. 1993. « Parametric modelling and control of the robotic grinding process ». *The International Journal of Advanced Manufacturing Technology,* vol. 8, n° 3, p. 182-192.

Das, M. K., and S. A. Tobias. 1967. « The relation between the static and the dynamic cutting of metals ». *International Journal of Machine Tool Design and Research,* vol. 7, n° 2, p. 63-89.

Davies, M. A., J. R. Pratt, B. S. Dutterer and T. J. Burns. 2000. « The stability of low radial immersion milling ». *CIRP Annals - Manufacturing Technology,* vol. 49, n° 1, p. 37-40.

Davies, M.A., J.R. Pratt and B. Dutterer. 2002. « Stability prediction for low radial immersion milling ». *ASME Journal of Manufacturing Science and Engineering,* vol. 124, n° 2, p. 217-225.

Doi, S., and S. Kato. 1956. « Chatter vibration of lathe tools ». In. Vol. 78. Trans. ASME.

Dwivedy, S. K., and P. Eberhard. 2006. « Dynamic analysis of flexible manipulators, a literature review ». *Mechanism and Machine Theory,* vol. 41, n° 7, p. 749-777.

Ferretti, G., G. Magnani and P. Rocco. 1999. « Force Oscillations in Contact Motion of Industrial Robots: An Experimental Investigation ». *IEEE Trans. Mechatronics,* vol. 4, n° 1, p. 86-91.

Gagné, J.L., L. Bédard-T, L. Lavoie, B. Hazel, J. Côté, Y. Laroche and P. Mongenot. 2010. « Robotic refurbishment of gate wheel tracks ». In *IEEE 1st International Conference on Applied Robotics for the Power Industry (CARPI)*. (Montreal, Canada).

Ganguli, A., A. Deraemaeker and A. Preumont. 2007. « Regenerative chatter reduction by active damping control ». *Journal of Sound and Vibration,* vol. 300, n° 3–5, p. 847-862.

Gasparetto, A. 2000. « Eigenvalue analysis of mode-coupling chatter for machine-tool stabilization ». *Journal of Vibration and Control,* vol. 7, n° 2, p. 181-197.

Girardin, F., D. Rémond and J.F. Rigal. 2010. « Tool wear detection in milling-An original approach with a non-dedicated sensor ». *Mechanical Systems and Signal Processing,* vol. 24, n° 6, p. 1907-1920.

Giroux, A. M., S. Houde, Y. Laroche and R. Dubois. 2008. « Improving the performance of a 20 year-old Francis turbine using numerical simulations and robotized intervention ». In *24th Symposium on Hydraulic Machinery and Systems*. (Iguassu, Brazil, October 27-31).

Hahn, R. S. 1953. « Metal cutting chatter and its elimination ». *Trans. ASME*.

Hazel, B., J. Côté, Y. Laroche and P. Mongenot. 2012a. « Field repair and construction of large hydropower equipment with a portable robot ». *Journal of Field Robotics,* vol. 29, n° 1, p. 102-122.

Hazel, B., J. Côté, Y. Laroche and P. Mongenot. 2012b. « A portable, multiprocess, track-based robot for in situ work on hydropower equipment ». *Journal of Field Robotics,* vol. 29, n° 1, p. 69-101.

Hazel, B., F. Rafieian and Z. Liu. 2011. « Impact cutting and regenerative chatter in robotic grinding ». In *ASME International Mechanical Engineering Congress & Exposition (IMECE)*. (Denver, Colorado, USA, 11-17 Nov., 2011).

Huang, H., Z. M. Gong, X. Q. Chen and L. Zhou. 2002. « Robotic grinding and polishing for turbine-vane overhaul ». *Journal of Materials Processing Technology,* vol. 127, n° 2, p. 140-145.

Kaneko, T, H Sato, Y Tani and M O-hori. 1984. « Self-excited chatter and its marks in turning ». *Trans. ASME, Journal of Engineering for Industry,* vol. 106, n° 3, p. 222-236.

Kegg, R. L. 1965. « Cutting dynamics in machine tool chatter: Contribution to machine-tool chatter research—3 ». *Journal of Engineering for Industry,* vol. 87, n° 4, p. 464-470.

Kita, Y., M. Ido and S. Hata. 1978. « The mechanism of metal removal by an abrasive tool ». *Wear,* vol. 47, n° 1, p. 185-193.

Kunieda, M., and T. Nakagawa. 1985. « Robot-polishing of curved surface with magneto-pressed tool and magnetic force sensor ». In *25th International Machine Tool Design and Research Conference*. (Birmingham, UK, 22–24 April), p. 193-200.

Li, Y., F. Gu, G. Harris, A. Ball, N. Bennett and K. Travis. 2005. « The measurement of instantaneous angular speed ». *Mechanical Systems and Signal Processing,* vol. 19, n° 4, p. 786-805.

Lin, F., and T. Lü. 2005. « Development of a robot system for complex surfaces polishing based on CL data ». *The International Journal of Advanced Manufacturing Technology,* vol. 26, n° 9-10, p. 1132-1137.

Liu, L., B.J. Ulrich and M.A. Elbestawi. 1990. « Robotic grinding force regulation: Design, implementation and benefits ». In *IEEE International Conference on Robotics and Automation*. (Cincinnati, USA, 13-18 May). Vol. 1, p. 258–265.

Malkin, S., and C. Guo. 2008. « Empirical relashionships ». In *Grinding technology - Theory and applications of machining with abrasives (2nd Edition)*. p. 152-153. Industrial Press.

Marui, E, S Kato, M Harashimoto and T Yamada. 1988a. « The mechanism of chatter vibration in a spindle-workpiece system: Part 2-Characteristics of dynamic cutting force and vibration energy ». *ASME Journal of Engineering for Industry,* vol. 110, p. 242-7.

Marui, E, S Kato, M Hashimoto and T Yamada. 1988b. « The mechanism of chatter vibration in a spindle-workpiece system: Part 1-Properties of self-excited chatter vibration in spindle-workpiece system ». *ASME Journal of Engineering for Industry,* vol. 110, p. 236-241.

Marui, E., S. Kato, M. Hashimoto and T. Yamada. 1988c. « The mechanism of chatter vibration in a spindle-workpiece system: Part 3—Analytical considerations ». *Journal of Engineering for Industry,* vol. 110, n° 3, p. 248-253.

Matsuoka, S., K. Shimizu, N. Yamazaki and Y. Oki. 1999. « High-speed end milling of an articulated robot and its characteristics ». *Journal of Materials Processing Technology,* vol. 95, n° 1-3, p. 83-89.

Merchant, M. E. 1944. « Basic mechanics of the metal cutting process ». *Journal of Applied Mechanics,* vol. 11, n° A, p. 168-175.

Merritt, H.E. 1965. « Theory of self-excited machine-tool chatter: Contribution to machine-tool chatter research—1 ». *Transactions of the ASME Journal of Engineering for Industry,* vol. 87, n° 4, p. 447-454.

Moerlein, Alex. 2007. « Modeling size change as a function of force during precision cylindrical plunge grinding ». Pennsylvania State University.

Mokdad, F., V. H. Vu, M. Thomas, F. Rafieian, Z. Liu and B. Hazel. 2011. « Online modal analysis of a flexible robot during grinding ». In *International Operational Modal Analysis Conference (IOMAC)*. (Istanbul, Turkey, 9-11 May 2011).

Olgac, Nejat, and Martin Hosek. 1998. « A new perspective and analysis for regenerative machine tool chatter ». *International Journal of Machine Tools and Manufacture,* vol. 38, n° 7, p. 783-798.

Pan, Z., H. Zhang, Z. Zhu and J. Wang. 2006. « Chatter analysis of robotic machining process ». *Journal of Materials Processing Technology,* vol. 173, n° 3, p. 301-309.

Pan, Zengxi, and Hui Zhang. 2007. « Analysis and suppression of chatter in robotic machining process ». In *International Conference on Control, Automation and Systems, . ICCAS '07.* (COEX, Seoul, Korea, Oct. 17-20), p. 595-600.

Quintana, G., and J. Ciurana. 2011. « Chatter in machining processes: A review ». *International Journal of Machine Tools and Manufacture,* vol. 51, n° 5, p. 363-376.

Rafieian, F., F. Girardin, Z. Liu, M. Thomas and B. Hazel. 2014. « Angular analysis of the cyclic impacting oscillations in a robotic grinding process ». *Mechanical Systems and Signal Processing,* vol. 44, n° 1-2, p. 160-176.

Rafieian, F., B. Hazel and Z. Liu. 2013. « Vibro-impact dynamics of material removal in a robotic grinding process ». *International Journal of Advanced Manufacturing Technology,* vol. (submitted).

Rafieian, F., B. Hazel and Z. Liu. 2014. « Regenerative instability of impact-cutting material removal in the grinding process performed by a flexible robot arm ». In *6th CIRP Conference on High Performance Cutting (HPC)*. (University of California, Berkely, California, USA, 23-25 June). Vol. (submitted).

Rafieian, F., Z. Liu and B. Hazel. 2009. « Dynamic model and modal testing for vibration analysis of robotic grinding process with a 6DOF flexible-joint manipulator ». In *IEEE International Conference on Mechatronics and Automation (ICMA)*. (Changchun, China, 9-12 August), p. 2793-2798.

Remond, D., and J. Mahfoudh. 2005. « From transmission error measurements to angular sampling in rotating machines with discrete geometry ». *Shock and Vibration,* vol. 12, n° 2, p. 149-161.

Ren, X., B. Kuhlenkötter and H. Müller. 2006. « Simulation and verification of belt grinding with industrial robots ». *International Journal of Machine Tools and Manufacture,* vol. 46, n° 7–8, p. 708-716.

Sabourin, M., F. Paquet, B. Hazel, J. Côté and P. Mongenot. 2010. « Robotic approach to improve turbine surface finish ». In *IEEE 1st International Conference on Applied Robotics for the Power Industry (CARPI)*. (Montreal, Canada, 5-7 October).

Shin, Y. C., Y. T. Chen and S. Kumara. 1992. « Framework of an intelligent grinding process advisor ». *Journal of Intelligent Manufacturing,* vol. 3, n° 3, p. 135-148.

Shumsheruddin, and Tobias S. 1962. « Dynamic metal cutting ». In *Third International Machine Tool Design and Research Confrence*. (September 26).

Siddhpura, M., and R. Paurobally. 2012. « A review of chatter vibration research in turning ». *International Journal of Machine Tools and Manufacture,* vol. 61, n° 0, p. 27-47.

Smith, J. D., and S. A. Tobias. 1961. « The dynamic cutting of metals ». *International Journal of Machine Tool Design and Research,* vol. 1, n° 4, p. 283-292.

Spong, M. W. 1987. « Modeling and control of elastic joint robots ». *Transactions of the ASME Journal of Dynamic Systems, Measurement, and Control,* vol. 109, p. 310-319.

Spong, M. W., S. Hutchinson and M. Vidyasagar. 2006. *Robot modeling and control*.

Stander, C. J., and P. S. Heyns. 2005. « Instantaneous angular speed monitoring of gearboxes under non-cyclic stationary load conditions ». *Mechanical Systems and Signal Processing,* vol. 19, n° 4, p. 817-835.

Swiatek, G., Z. Liu and B. Hazel. 2010. « Dynamic simulation and configuration dependant modal identification of a portable flexible-link and flexible-joint robot ». In *28th seminar on machinery vibration (CMVA)*. (October 27-29).

Szalai, R., and G. Stepan. 2006. « Lobes and lenses in the stability chart of interrupted turning ». *ASME Journal of Computational and Nonlinear Dynamics,* vol. 1, n° 3, p. 205-211.

Tahvilian, A. M., Z. Liu, H. Champliaud and B. Hazel. 2013. « Experimental and finite element analysis of temperature and energy partition to the workpiece while grinding

with a flexible robot ». *Journal of Materials Processing Technology,* vol. 213, n° 12, p. 2292-2303.

Takeuchi, Y., D. Ge and N. Asakawa. 1993. « Automated polishing process with a human-like dexterous robot ». In *IEEE International Conference on Robotics and Automation*. (2-6 May). Vol. 3, p. 950-956.

Tlusty, J., and F. Ismail. 1981. « Basic non-linearity in machining chatter ». *CIRP Annals - Manufacturing Technology,* vol. 30, n° 1, p. 299-304.

Tlusty, J., and M. Polacek. 1963. « The stability of the machine tool against self-excited vibration in machining ». *International research in production engineering, ASME*, p. 465-474.

Tobias, S. A., and W. Fishwick. 1958. « Theory of regenerative machine tool chatter ». *Engineering,* vol. 205, n° 16-23.

Tsai, L. W. 1999. *Robot analysis. The mechanics of serial and parallel manipulators*. New York: John Wiley & Sons Inc.

Wang, J., H. Zhang and Z. Pan. 2006. « Machining with flexible manipulators: Critical issues and solutions ». In *Industrial Robotics: Programming, Simulation and Applications*, sous la dir. de Huat, Low Kin. p. 515-536. Pro Literatur Verlag, Germany / ARS, Austria.

Wiercigroch, M., and E. Budak. 2001. « Sources of nonlinearities, chatter generation and suppression in metal cutting ». *Philosophical Transactions of the Royal Society of London. Series A: Mathematical, Physical and Engineering Sciences,* vol. 359, n° 1781, p. 663-693.

Yang, J., L. Pu, Z. Wang, Y. Zhou and X. Yan. 2001. « Fault detection in a diesel engine by analysing the instantaneous angular speed ». *Mechanical Systems and Signal Processing,* vol. 15, n° 3, p. 549-564.

Zhang, H., J. Wang, G. Zhang, Z. Gan, Z. Pan, H. Cui and Z. Zhu. 2005. « Machining with flexible manipulator: Toward improving robotic machining performance ». In *IEEE/ASME International Conference on Advanced Intelligent Mechatronics*. (Monterey, California, USA, 24-28 July), sous la dir. de Jianjun, Wang, p. 1127-1132.